First Measurements of Inclusive Muon Neutrino Charged Current Differential Cross Sections on Argon at 0.8 GeV Average Neutrino Energy with the MicroBooNE Detector

Marco Del Tutto

St Hilda's College

University of Oxford

A thesis submitted in fulfilment of the requirements for the degree of

Doctor of Philosophy

Hilary Term, 2019

First Measurements of Inclusive Muon Neutrino Charged Current Differential Cross Sections on Argon at 0.8 GeV Average Neutrino Energy with the MicroBooNE Detector

Marco Del Tutto

St. Hilda's College
University of Oxford

A thesis submitted in fulfilment of the requirements for the degree of
Doctor of Philosophy

Hilary Term, 2019

Abstract

Current and next-generation precision neutrino oscillation experiments aim to determine the neutrino mass ordering, to measure the extent of CP violation in the lepton sector and to probe beyond Standard Model physics, such as sterile neutrinos. These experiments rely on models for neutrino interactions with matter that are complicated by nuclear effects and final state interactions. To date, these effects cannot be modelled precisely, especially for heavy target nuclei, typically used in modern neutrino experiments. Many future experiments will employ detectors based on the liquid argon time projection chamber technology. As a consequence, neutrino-argon cross-section measurements are of the outmost importance, especially given the relative scarcity of neutrino-argon data, due to the novelty of the technology.

This thesis presents the first measurement of muon-neutrino charged-current inclusive cross section on argon at a mean neutrino energy of 0.8 GeV. Data were collected using the MicroBooNE liquid argon time projection chamber in the Fermilab Booster neutrino beam during a period of six months, corresponding to an exposure of 1.6×10^{20} protons on target. The measured cross section is presented as a function of the outgoing muon momentum, using multiple Coulomb scattering as a measurement technique, as well as the muon angle with respect to the beam direction. A comparison of the measured cross section obtained with two different configurations of the GENIE neutrino event generator is performed, and better agreement is found when using nuclear-effect modelling in the theoretical calculations. Additionally, the total flux integrated cross section is measured to be $0.693 \pm 0.010\,(\text{stat.}) \pm 0.165\,(\text{syst.}) \times 10^{-38}\,\text{cm}^2$.

Statement of Originality

This thesis and the work presented in it are my own and were produced by me as a result of my own original research. Results and figures from published works by others have been clearly attributed, and this work has not been submitted for another qualification at this or any other university.

After a brief introduction in Chapter 1, Chapters 2 and 3 give some background information about the theory motivating the work presented in this thesis, and Chapter 4 describes the MicroBooNE experiment whose data was analysed in this work. These chapters represent my summary of the work of others, and all relevant papers and documents have been cited. However, some elements of the interpretations of how neutrino interactions affect oscillation analysis and on the importance of neutrino interaction measurements (Sections 2.5 and 3.3) are my own.

Chapter 5 discusses the event reconstruction used for the analysis in this thesis. The algorithms that lead to track/shower reconstruction, the muon momentum measurement and part of the optical reconstruction and flash matching were developed by others, and the relevant technical reports have been referenced. My contributions to the work presented in this chapter are all the cosmic ray tagging algorithms that make use of the detector geometry and optical information, as well as those that identify cosmic ray tracks piercing the sides of the detector and cosmic ray muons that enter and stop in the detector. Moreover, considerable parts of the optical reconstruction and flash matching were developed by me.

The event selection performed to select muon neutrino candidate events detailed in Chapter 6 is all my own work. The measurements of the total, single- and double-differential muon-neutrino charged-current inclusive cross-sections described in Chapter 7 were all done by me. The implementation, study and propagation of all the systematic uncertainties that affect the measurement, described Chapter 8, are all my original work. The entire analysis framework used for this analysis was developed by me.

The results, as well as the hypothesis testing between two different theoretical models in Chapter 9, the interpretations presented in Chapter 10, as well as all the appendices, are all my own work.

Acknowledgements

I would like to thank my DPhil supervisor, Roxanne Guenette, for her constant support. She has been a wonderful supervisor from whom I have learned a lot. I would like to thank her in particular for all the opportunities she has given me, for being extremely approachable and for her kindness: she sets the standard of what a supervisor should be. Thank you to my co-supervisor, Giles Barr, who has always been available to support me.

I certainly would not have been able to complete this work without the advice and support of Anne Schukraft. She is an incredible scientist and she represents all the good things I love about Fermilab. A special thanks also goes to Sam Zeller, for all her invaluable feedback and for always being available to help.

I am honoured to have been part of Oxford Physics and would like to thank all the people I interacted with in past years, especially the Oxford neutrino group I worked with: Roberto Soleti, Wouter Van De Pontseele and Matt Bass.

I have been very fortunate to work at Fermilab for part of my DPhil, and would like to thank who on MicroBooNE helped me throughout my time on the experiment, especially Corey Adams and Kazu Terao. I learned so much from them. Thank you also to Colton Hill and Adam Lister, for being part of this journey and for all the lovely moments spent together at Fermilab.

I would also like to thank my parents. I owe so much to them for their constant support throughout my DPhil and my entire life. Finally, my biggest thank you goes to who has been standing by my side during the past years. Thank you Cecilia. There is no way I could have managed this without you.

To Cecilia

Contents

List of Figures

List of Tables

Chapter 1

Introduction

Particle physics studies the building blocks of our Universe and the elementary forces that bind them together and make them interact to form all the matter that we know of: from the particles on Earth to the far-away stars. Remarkably, all the elementary particles and forces are consistently described by a single theory: the Standard Model (SM) of particle physics. The SM is able to explain all the particles that have currently been discovered, the way they obtain their mass thanks to the Higgs field, and the way they interact with one another. For all of this, it is definitely one of the most significant achievements of humankind.

At the same time, from cosmological and astrophysical studies it is known that matter only constitutes 5% of the known universe. The remaining 95% is made by the so-called dark matter (25%) and dark energy (70%). The SM, in its current formulation, does not predict other particles that could explain dark matter. Many other questions exist that make physicists wonder about the correctness, or at the least on the completeness, of the SM. Fixing, or completing the SM is extremely challenging, as it makes remarkable predictions of all the experimentally observed phenomena. For example, the SM has been confirmed at the level of one part per trillion precision by looking at the comparison between the measured and predicted

magnetic moment of the electron [1]. This is the most accurately verified prediction in the history of physics.

The SM predicts the existence of antimatter, that arises as a direct consequence of combining two of the most fundamental known concepts in physics, the theory of relativity and quantum mechanics. On the other hand, the atoms in our local region of the Universe are formed from electrons, protons and neutrons rather than their equivalent antiparticles. The possibility that there are galaxies or regions of space dominated by antimatter can be excluded by the astronomical searches of photons from the e^+e^- annihilation process that would occur at the interfaces between matter and antimatter dominated regions of the Universe [2]. The predominance of matter is believed to have arisen in the early evolution of the Universe, and this asymmetry between matter and antimatter is among the most pressing open questions in particle physics.

Moreover, several other questions remain unanswered: how to unify the forces? Why are there three generations of particles? Why the observed pattern of particles masses? And more.

Ultimately, the SM is in fact just a model: while it can predict all the discovered particles and their interactions, it still has 28 parameters that are not fixed but need to be measured by experiments (like the particle masses and the interaction strengths).

Current and future experiments will aim to address these open questions and neutrinos seem very promising to solve many of the great puzzles of physics. Despite being the most abundant particles just after photons, neutrinos remain the least understood ones. Indeed, several neutrino properties are still unknown, like their absolute mass, the number of species, or their exact nature. The SM predicts neutrinos as massless particles, but experiments [3, 4] have demonstrated the

existence of neutrino oscillations, where neutrinos have been observed changing in one another, implying neutrinos as massive particles. This is already strongly challenging the SM.

The asymmetry between matter and antimatter could be explained by a symmetry being broken in our Universe. In the SM, this symmetry is called CP: if CP symmetry is violated, that means that physics draws a distinction between matter and antimatter, and could explain what causes our universe to be matter-dominated. While CP violation has been observed in the quark sector, it is not strong enough to justify the current matter/antimatter asymmetry. Alternatively, CP symmetry is yet to be observed in the neutrino sector, and this is an auspicious place to look.

An essential missing piece in the understanding of neutrinos is the knowledge of the neutrino mass, but especially the knowledge of the mechanism that gives origin to this mass. Mass mechanisms require that neutrinos are either "Dirac" or "Majorana" in nature. Understanding their nature is therefore of fundamental importance as it has direct implications on the understanding of the neutrino mass.

To unravel all these mysteries around neutrinos, precision neutrino oscillation experiments are needed. In the near future, these experiments will be able to answer most of the above questions and to search for physics beyond the SM. Precision measurements require incredibly high-resolution detectors that are able to resolve all the subatomic particles produced from a neutrino interaction. Liquid Argon Time Projection Chambers (LArTPCs) are cutting-edge detectors now employed for neutrino physics, and their technology allows one to track particles produced by neutrino interactions to unprecedented, millimetre scale, 3D resolution.

Precision neutrino experiments, in turn, require precise knowledge of neutrino interactions with matter. While these have been studied for a long time, modern detectors like LArTPC use complex nuclei as target material, which complicate

the study of neutrino interactions. Many of the current neutrino experiments dedicate a considerable effort in the study of neutrino interactions, which will then be a crucial point in the study of neutrino oscillations. MicroBooNE, a neutrino detector at Fermilab (U.S.A.), employs the LArTPC detector technology for the study of neutrinos and can measure neutrino-argon interactions with unprecedented precision.

This thesis presents the first measurement of muon neutrino charged current interactions on argon at low neutrino energy ($E_\nu \sim 0.8$ GeV). Most of the future neutrino experiments will use argon as target material, and this measurement is of fundamental importance for the successful completion of these experiments. The analysis described in this thesis uses data collected by the MicroBooNE experiment from February to October 2016.

Chapter 2

Neutrino Physics

Neutrino history is deeply rooted in the discovery of weak interactions [5]. In 1914, Chadwick demonstrated that the spectrum of electrons released in β-decays was continuous, in contrast to α- and γ-ray spectra, which were unique in energy. In order to solve this problem, W. Pauli argued that the existence of a neutral weakly interacting fermion emitted in β-decay could address the issue. He called this neutral fermion a neutron, with a mass of the order of the electron. When J. Chadwick discovered in 1932 the neutron as it is known today, E. Fermi renamed the Pauli particle the *neutrino*. The first published reference to the neutrino is in the Proceedings of the Solvay Conference of October 1933.

The first milestone in a comprehensive theory of weak interactions was established in 1934 when Fermi formulated a theory of β-decay, now known as Fermi theory, in analogy with quantum electrodynamics. Although the remarkable success of the Fermi theory left few in doubt of the neutrino's existence, this particle had yet to be observed. In fact, predicting the strength of interactions, H. Bethe and R. Peierls claimed in 1934 that it might never be observed [6]. As it will be shown in this chapter, neutrinos have now been discovered with the main difference between the particle known today and the particle that was described in Fermi's

theory being its mass. Fermi's neutrino was massless, as the neutrino in the SM of particle physics, but the observation of neutrino oscillations leads to the conclusion that neutrinos have non-zero mass. The Nobel Prize was awarded in 2015 for measurements by the Super-Kamiokande [3] and SNO [4] experiments confirming that neutrinos have mass, and although the precise masses of the neutrinos are yet to be measured, it has been demonstrated that they are non-zero.

In this chapter, Section 2.1 gives a brief historical overview of neutrinos and neutrino oscillations, Sections 2.2 and 2.3 introduce neutrino oscillations in vacuum and matter respectively, while Section 2.4 provides an overview of the different types of neutrino oscillation experiments. Finally, Section 2.5 describes what are the current challenges in neutrino oscillation experiments, highlighting the need for a better understanding of neutrino-nucleus interaction models, which will then be described in Chapter 3.

2.1 The Discovery of Neutrinos and Oscillations

Fermi's theory accurately accounted for almost all the observed properties of beta decay, and its success was taken as convincing evidence for the neutrino. Advised by B. Pontecorvo in the early 1950s, F. Reines and C.L. Cowan searched for a way to measure inverse β-decay, in which an anti-neutrino can produce a positron according to the reaction:

$$\bar{\nu}_e + p \rightarrow n + e^+.$$

They settled on using the large flux of *electron anti-neutrinos* from a nuclear reactor at the Savannah River Nuclear Plant and 10 ton of equipment, including 1400 litres of liquid scintillators. This experiment was the first reactor-neutrino

experiment. In June of 1956, Reines and Cowan sent a telegram informing Pauli of the discovery [7].

In 1962, *muon neutrinos* were discovered by Lederman, Schwartz, Steinberger and coworkers at the Brookhaven National Laboratory. This experiment used a beam of protons focused toward a beryllium target. The resulting interaction produced a large number of pions which decayed to muons and muon neutrinos [8].

In 1973, the Gargamelle experiment at CERN discovered the weak neutral current interaction via $\nu_\mu + N \rightarrow \nu_\mu + \text{hadrons}$ and $\bar{\nu}_\mu + N \rightarrow \bar{\nu}_\mu + \text{hadrons}$, where N is a nucleon in the detector [9].

Much later in 2001, the *tau neutrinos* were detected by the DONUT experiment, which collided 800 GeV protons with a block of tungsten [10]. This collision produced D_S mesons that subsequently decayed into tau-leptons which then produced tau neutrinos.

These and the experiments which followed confirmed the existence of three neutrino flavours: the electron neutrino (ν_e), the muon neutrino (ν_μ), and the tau neutrino (ν_τ).

As a branch of the neutrino history, in 1968 there was the first clue of neutrino oscillation: the Homestake experiment by Davis and coworkers measured the flux of neutrinos from the sun and detected a deficit when compared with the prediction of Bahcall's Standard Solar Model [11]. This discrepancy was referred to as the *solar neutrino problem*. The Homestake experiment used a chlorine-based detector and radiological techniques to measure the flux of solar neutrinos interacting in the detector. This solar experiment was detecting electron neutrinos.

A deficit was also observed with muon neutrinos in atmospheric experiments. This happened in 1988 with the Kamiokande experiment [12]. In 1998, the Super-Kamiokande experiment used a cylindrical stainless steel tank with 50 ktons of

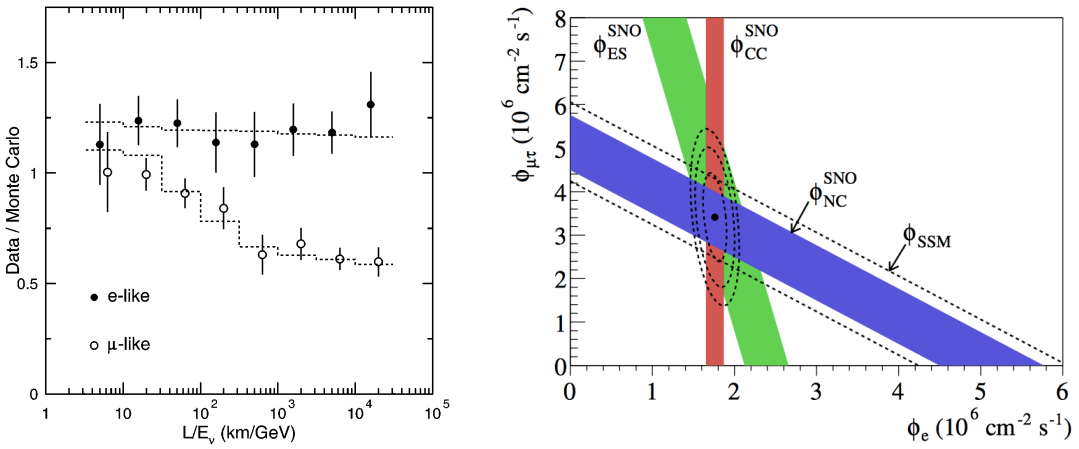

(a) (b)

Figure 2.1: (a) The ratio of number of data events to predicted number of events without neutrino oscillations (from Monte Carlo) as a function of L/E_ν in Super-Kamiokande. The points show the ratio of data to prediction, and the dashed lines show the expected shape when accounting for $\nu_\mu \to \nu_\tau$ oscillation. Figure source: [3]. (b) The solar neutrino fluxes measured by SNO. The flux of muon plus tau neutrinos v.s. the flux of electron neutrinos is shown. The solid bands show the CC, NC and ES flux measurements. The dashed line shows the Solar Standard Model prediction. The best fit point is shown with 68%, 95% and 99% contours. Figure source: [4].

water surrounded by 11,146 Photo Multiplier Tube (PMT) to detect neutrinos coming from the sun and the atmosphere [13]. Neutrino oscillations explained the revealed deficit in the angular and energy distribution from atmospheric muon neutrinos. Figure 2.1a shows the ratio of measured to predicted number of events as a function of distance, L (calculated from the angle of the incoming atmospheric neutrino), and neutrino energy, E_ν, in Super-Kamiokande. This is shown for both electron-like and muon-like signals, corresponding to ν_e and ν_μ interactions respectively. At high L/E_ν, the observed ν_μ flux is around 50% of the prediction – clear evidence for ν_μ disappearance.

In 2002, the Sudbury Neutrino Observatory (SNO) experiment made precise measurements of solar neutrinos. SNO is a heavy water Cherenkov detector in a nickel mine in Ontario (Canada) at a depth of 204 m of rock. The detector

contained 1000 tons of D_2O [4]. This experiment measured the electron and non-electron component of the solar neutrino spectrum by comparing the Charged Current (CC), Neutral Current (NC) and Elastic Scattering (ES) neutrino reactions on deuterium. The result from this experiment was a detailed confirmation of the flavour changing signature of solar neutrinos, although this is explained by adiabatic flavour conversion of neutrinos in the matter of the Sun and not by neutrino oscillations [14]. Figure 2.1 shows the allowed fluxes determined by the CC, NC and ES measurements. The intersection of the three bands allows resolution of the fluxes of the muon and tau neutrinos and shows the consistency of the three measurements. No L/E_ν dependence was observed in SNO and mechanism of the neutrino transformation was not identified. After the SNO results, a number of solutions of the solar neutrino problem still existed [14]: matter effects conversion (see Section 2.3), resonant spin-flavour precession, Lorentz symmetry violation, decoherence, neutrino decay, and others.

In 2002, KamLAND selected the unique solution of the solar neutrino problem and showed that non-zero neutrino mass is behind the SNO result. The KamLAND experiment found the first evidence for reactor $\bar{\nu}_e$ oscillations. The experiment consists in a liquid scintillator anti-neutrino detector that measured the $\bar{\nu}_e$ flux from nuclear reactors at an average distance of 180 km [15]. This experiment observed 258 events with an expected 365 ± 24 events for the case of no oscillations. The L/E_ν dependence of the survival probability has also been observed.

In 2010, the observation of a ν_τ particle in a ν_μ beam was announced by the OPERA experiment [16]. The OPERA experiment has been designed to search for $\nu_\mu \rightarrow \nu_\tau$ oscillations in appearance mode through the detection of the τ-lepton produced in the ν_τ CC interactions. The detector is located at Gran Sasso, 730 km away from the source in Geneva.

No experiments that have been performed so far have detected conclusive deviations from the SM, except neutrino oscillation experiments, which have shown that neutrinos are massive. In the SM, this is not the case. This discovery has confirmed that the SM in an effective theory of the yet unknown theory beyond the SM.

The phenomenon of neutrino oscillation has been observed for neutrinos from many sources, the sun, reactors, Cosmic Ray (CR) interactions, and accelerator beams [17]. While these experiments provide information about neutrino mixing angles and differences in the square of their masses, complete knowledge of neutrinos is still missing. Remaining questions are mainly the absolute mass of neutrinos (since oscillations are only sensitive to the difference of the square of the masses), whether there is CP violation in the neutrino sector, the neutrino mass ordering and if they are Dirac ($\nu \neq \bar{\nu}$) or Majorana ($\nu = \bar{\nu}$) particles.

2.2 Neutrino Oscillations

Neutrino oscillations are generated by the interference of different massive neutrinos, which are produced and detected coherently because of their very small mass differences.

Neutrinos ν_α with flavour $\alpha = e$, μ, τ are produced in particle decay or in CC weak interactions processes. Neutrinos of any flavour can also be produced in the NC weak interaction process $Z \to \nu\bar{\nu}$. The CC processes are generated by the CC leptonic interaction Lagrangian [18]:

$$\mathscr{L} = -\frac{g}{2\sqrt{2}} \left(J^\rho W_\rho + J^{\rho\dagger} W_\rho^\dagger \right). \tag{2.1}$$

where g is the coupling constant, W_ρ is the W boson field and J^ρ is the leptonic CC:

$$J^\rho = 2 \sum_{\alpha=e,\mu,\tau} \sum_k U^*_{\alpha k} \bar{\nu}_k \gamma^\rho l_\alpha. \tag{2.2}$$

The leptonic current J^ρ in Equation (2.1) generates a superposition of massive neutrinos whenever the energies and momenta of the particles involved in the neutrino production process are not measured with a degree of accuracy allowing the determination, through energy-momentum conservation, of the emitted massive neutrino. This is the case for neutrino oscillations, in which a flavour neutrino ν_α is a superposition of massive neutrinos ν_k with weights proportional to $U^*_{\alpha k}$.

Let us consider a neutrino with flavour α and momentum $\mathbf{p}$, produced in a CC weak interaction from a charged lepton l_α. In the standard theory of neutrino oscillations, the neutrino flavour state is described by:

$$|\nu_\alpha\rangle = \sum_k U^*_{\alpha k} |\nu_k\rangle , \tag{2.3}$$

where U is the unitary mixing matrix, called PMNS (Pontecorvo, Maki, Nakagawa and Sakata) matrix. In the case of three mass eigenstates and three flavour eigenstates, U takes the form:

$$U = \begin{pmatrix} U_{e1} & U_{e2} & U_{e3} \\ U_{\mu 1} & U_{\mu 2} & U_{\mu 3} \\ U_{\tau 1} & U_{\tau 2} & U_{\tau 3} \end{pmatrix} . \tag{2.4}$$

The 3×3 PMNS matrix can be parameterised in terms of three mixing angles θ_{12},

θ_{13}, and θ_{23} and three CP-violating phases δ_{CP}, α_1, and α_2:

$$U = \underbrace{\begin{pmatrix} 1 & 0 & 0 \\ 0 & c_{23} & s_{23} \\ 0 & -s_{23} & c_{23} \end{pmatrix}}_{\text{Atmospheric}} \underbrace{\begin{pmatrix} c_{13} & 0 & s_{13}e^{-i\delta_{\mathrm{CP}}} \\ 0 & 1 & 0 \\ -s_{13}e^{i\delta_{\mathrm{CP}}} & 0 & c_{13} \end{pmatrix}}_{\text{Cross-mixing}} \underbrace{\begin{pmatrix} c_{12} & s_{12} & 0 \\ -s_{12} & c_{12} & 0 \\ 0 & 0 & 1 \end{pmatrix}}_{\text{Solar}} \underbrace{\begin{pmatrix} e^{i\frac{\alpha_1}{2}} & 0 & 0 \\ 0 & e^{i\frac{\alpha_2}{2}} & 0 \\ 0 & 0 & 1 \end{pmatrix}}_{\text{Majorana}}. \tag{2.5}$$

U has been decomposed into four component matrices in Equation (2.5) to make it easier to read and interpret, and because different mixing angles are measured by different types of experiment. The first matrix includes only the mixing angle θ_{23}. The third matrix includes only the mixing angle θ_{12}, which dominates the mixing of solar neutrinos. The second matrix is known as the cross-mixing matrix, and depends on two parameters: the mixing angle θ_{13} and the CP-violating phase δ_{CP}. A non-zero δ_{CP} will lead to a complex matrix U and different probabilities for the CP-conjugate oscillations $P(\nu_\alpha \to \nu_\beta) \neq P(\bar{\nu}_\alpha \to \bar{\nu}_\beta)$, which would be a significant finding.

The final matrix in Equation (2.5) contains the so-called "Majorana" CP-violating phases. These lead to physical effects only for the case of Majorana neutrinos (i.e. where neutrinos are their own antiparticle) and do not conserve lepton number. Even in the case of Majorana neutrinos, these CP-violating phases do not affect the oscillation probability, which (as in Equation (2.14)) depends on $\sum_i U^*_{\alpha i} U_{\alpha j}$, so the Majorana phases cancel. It is not possible to determine whether neutrinos are their own antiparticles from oscillation measurements; other experiments (such as the search for neutrinoless double beta decay being conducted or planned by the MAJORANA [19], GERDA [20], CUORE [21], SNO+ [22], NEXT [23] and nEXO [24] collaborations, among others) are needed to answer this question. If the neutrinos are instead different from anti-neutrinos, they are "Dirac"

particles and acquire their mass in a similar way as other fermions in the SM do.

Considering orthonormal massive neutrino states ($\langle\nu_k|\nu_j\rangle = \delta_{kj}$), the unitary of the mixing matrix implies that also the flavour states are orthonormal: $\langle\nu_\alpha|\nu_\beta\rangle = \delta_{\alpha\beta}$. Since the massive neutrino states ν_k are eigenstates of the Hamiltonian, $\mathscr{H}\,|\nu_k\rangle = E_k\,|\nu_k\rangle$, with energy

$$E_k = \sqrt{\mathbf{p}^2 + m_k^2}, \tag{2.6}$$

then the Schrodinger equation

$$i\frac{d}{dt}\,|\nu_k(t)\rangle = \mathscr{H}\,|\nu_k(t)\rangle\,, \tag{2.7}$$

implies that the massive neutrino states evolve in time as plane waves:

$$|\nu_k(t)\rangle = e^{-iE_k t}\,|\nu_k\rangle\,. \tag{2.8}$$

Considering now a flavour state $|\nu_\alpha(t)\rangle$ which describes a neutrino created with a definite flavour α at time $t = 0$. From Equations (2.3) and (2.8), the time evolution of this state is given by

$$|\nu_\alpha(t)\rangle = \sum_k U^*_{\alpha k} e^{-iE_k t}\,|\nu_k\rangle\,, \tag{2.9}$$

such that

$$|\nu_\alpha(0)\rangle = |\nu_\alpha\rangle\,.$$

The massive states can be expressed in terms of flavour states inverting Equa-

tion (2.3):

$$|\nu_k\rangle = \sum_\alpha U_{\alpha k} |\nu_\alpha\rangle , \tag{2.10}$$

where the relation $U^\dagger U = \mathbf{1}$ has been used. Substituting the last relation into Equation (2.9) one gets:

$$|\nu_\alpha(t)\rangle = \sum_{\beta=e,\mu,\tau} \left(\sum_k U^*_{\alpha k} e^{-iE_k t} U_{\beta k} \right) |\nu_\beta\rangle . \tag{2.11}$$

Hence, the superposition of massive neutrino states $|\nu_\alpha(t)\rangle$, and the pure flavour state given in Equation (2.3) at $t = 0$, becomes a superposition of different flavour states at $t > 0$. The transition probability of $|\nu_\alpha\rangle \to |\nu_\beta\rangle$ as a function of time is given by:

$$P_{\nu_\alpha \to \nu_\beta}(t) = |\langle \nu_\beta | \nu_\alpha \rangle|^2 = \sum_{k,j} U^*_{\alpha k} U_{\beta k} U_{\alpha j} U^*_{\beta j} e^{-i(E_k - E_j)t}. \tag{2.12}$$

For ultra-relativistic neutrinos, one could expand Equation (2.6) considering $m_k \sim 0$ to obtain $E_k \simeq E + m_k^2/2E$, where $E = |\mathbf{p}|$. Given the mass difference Δm^2_{kj} it is possible to write:

$$E_k - E_j \simeq \frac{\Delta m^2_{kj}}{2E}. \tag{2.13}$$

In neutrino oscillation experiments, the propagation time t is not measured. What is known is the distance L between the source and the detector. Since ultra-relativistic neutrinos propagate almost at the speed of light, it is possible to approximate $t = L$. Therefore, the transition probability can be approximated by:

$$P_{\nu_\alpha \to \nu_\beta}(t) = \sum_{k,j} U^*_{\alpha k} U_{\beta k} U_{\alpha j} U^*_{\beta j} e^{-i\frac{\Delta m^2_{kj} L}{2E}}. \tag{2.14}$$

The oscillation probability thus depends both on quantities fixed by nature

(PMNS matrix elements and differences of the square of the masses Δm^2) and on parameters fixed by experiments (the path the neutrino travels L, i.e. the source-detector distance, and the neutrino energy E). Moreover, oscillation experiments are only sensitive to the difference of the squares of the masses and not to the absolute neutrino mass.

The now well-accepted picture of neutrino mixing involves three underlying mass states, with three mixing angles defining the linear superpositions that make up each of the three weak, or flavour, states. The magnitude of the mass-squared splitting between states ν_1 and ν_2 is known from the KamLAND reactor experiment [15], and the much-larger splitting between the third, ν_3 state and the $\nu_1 - \nu_2$ pair is known from atmospheric and long-baseline experiments [17]. However, pure neutrino oscillations are sensitive only to the magnitude of the mass splitting, not to its sign. Defining the ν_1 state as having the largest admixture of the electron flavour eigenstate, the sign of the mass splitting between states ν_2 and ν_1 is determined to be positive ($\Delta m^2_{21} > 0$) using the pattern of neutrino oscillations through the varying-density solar medium [17]. However, the corresponding sign of $\Delta m^2_{32} \sim \Delta m^2_{31}$ remains unknown. That is, there are two potential orderings, for the neutrino mass states: the so-called *normal ordering*, in which ν_3 is the heaviest, and the *inverted ordering*, in which ν_3 is the lightest, as shown in Figure 2.2.

2.3 Neutrino Oscillations In Matter

Neutrinos propagating in matter are subject to a potential due to the coherent forward elastic scattering with the particles in the medium (electrons and nucleons). Coherent scattering happens when the neutrino wave function interacts with the matter as a whole, such as the scattered waves from the nuclei in the matter

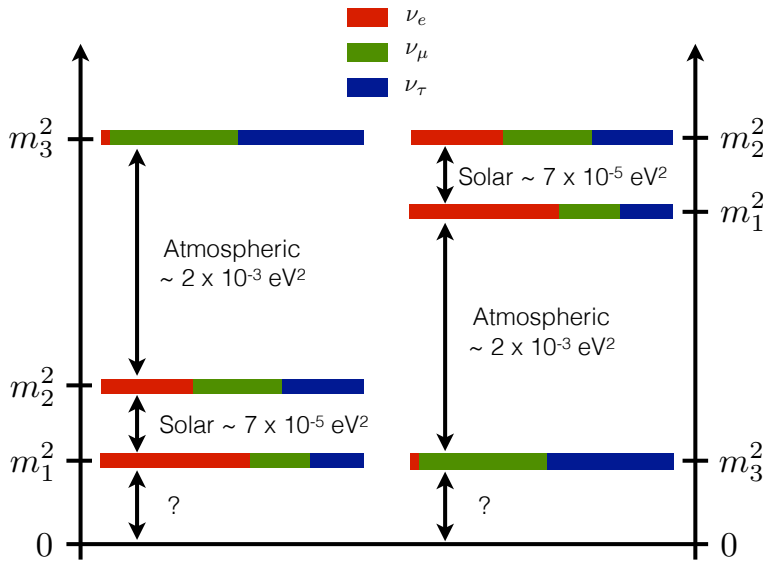

Figure 2.2: Pictorial representation of the possible neutrino mass orderings. Note: Δm^2_{atm} is equivalent to Δm^2_{32} and Δm^2_{sol} is equivalent to Δm^2_{21}.

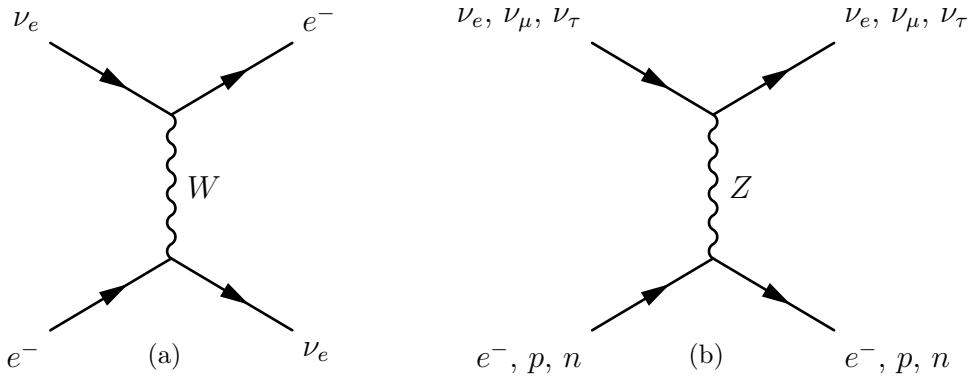

Figure 2.3: Feynman diagrams of the coherent forward elastic scattering processes.

interfere with each other.

When active flavour neutrinos propagate in matter, their evolution equation is affected by both CC and NC scatterings [11]. The Feynman diagrams of CC and NC scattering are shown in Figure 2.3. This phenomenon was first proposed by Wolfenstein [25] and is now known as the Mikheyev-Smirnov-Wolfenstein (MSW) effect.

A full account of how exactly these matter effects alter neutrino oscillation probabilities is beyond the scope of this thesis (although it is well described in

other sources, e.g. [11]).

An important implication of matter effects in neutrino oscillations is that their impact is different for neutrinos and antineutrinos (since the CC interaction shown in Figure 2.3a is not available for antineutrinos) due to the lack of positrons in the Earth. This can mimic a CP violation $P(\nu_\alpha \to \nu_\beta) \neq P(\bar{\nu}_\alpha \to \bar{\nu}_\beta)$ effect which does not say anything interesting about matter-antimatter asymmetry at a fundamental level. It is therefore essential to account for matter effects when attempting to determine δ_{CP} to identify genuine neutrino-sector CP violation.

Moreover, whilst vacuum oscillations are only sensitive to the square of the neutrino mass splitting, matter effects are sensitive to the signs of the mass splittings. Current and future experiment will have sensitivity to a mass ordering measurement. While T2K [26] has very little sensitivity to the ordering, due to the shorter baseline, NOνA [27] has the potential to make a measurement at the $2-3\sigma$ level, if the value of the CP phase parameter δ_{CP} is maximal. A combination of current experiments at different baselines (e.g. T2K+NOνA) could help to further disentangle the competing effects of CP violation and matter-induced neutrino-anti-neutrino differences. However, the future DUNE [28] experiment will identify the mass ordering, removing the ambiguities.

There are several motivations as to why to determine the neutrino mass ordering. Once the ordering is understood, the uncertainty on a measurement of the CP-violating phase, δ_{CP}, is significantly reduced. Knowledge of the mass ordering would define the scope for future neutrinoless double beta decay experiments, seeking to resolve the mass nature of the neutrino, by limiting the domain for observation of a signal. In combination with cosmological measurements, which are sensitive to the sum of neutrino masses, knowledge of the mass ordering could also

be used to determine the absolute mass scale of neutrinos. Furthermore, it will allow constraining many of the grand unification theories [17] and will help in the understanding of core-collapse supernovae. For these many reasons, determination of the neutrino mass ordering is thus a fundamental step towards completion of the SM of particle physics.

2.4 Overview of Neutrino Oscillation Experiments

Neutrino oscillation experiments are classified based on the different sources of neutrinos that have been used.

Reactor Neutrino Experiments These experiments exploit the large isotropic fluxes of electron anti-neutrinos produced in nuclear reactors by β decays of heavy nuclei (mainly fission fragments of ^{235}U, ^{238}U, ^{239}Pu, ^{241}Pu). Typical energy of reactor ν_e's is of the order of a few MeV.

Atmospheric Neutrino Experiments Primary CR interact with the upper layers of the atmosphere producing a large flux of pions and kaons which decay in the atmosphere into muons and muon neutrinos. Many muons further decay into electrons and muon neutrinos before hitting the ground. Atmospheric neutrino experiments are designed to detect these ν_μ. The energy of detectable atmospheric neutrinos covers a very wide range, from about 500 MeV to about 100 GeV, and even higher are possible in a large detector like IceCube [29]. The source-detector distance ranges from about 20 km for neutrinos coming from above, to about 10^4 km for neutrinos coming from below, initially produced on the other side of the Earth. Atmospheric neutrino experiments are sensitive to Δm^2 of the order of $10^{-3}\,\mathrm{eV}^2$ and the current best measurement is $\Delta m^2_{32} = 2.56^{+0.13}_{-0.11} \times 10^{-3}\,\mathrm{eV}^2$ [17], as previously

shown in Figure 2.2.

Solar Neutrino Experiments These experiments detect the electron neutrinos generated in the core of the Sun by the thermonuclear reactions that power the Sun. Solar neutrino experiments are designed to detect these ν_e and are sensitive to extremely small values of Δm^2 ($\Delta m^2_{21} = 7.37^{+0.59}_{-0.44} \times 10^{-5}\,\text{eV}^2$ [17]), much smaller than the sensitivity of the other experiment discussed above.

Accelerator Experiments These experiments make use of beams of muon neutrinos produced by the decay of pions, kaons, and muons created by a proton beam hitting a target. They are further classified into *appearance* experiments if they look at electron neutrinos oscillated from the initial muon neutrinos, or *disappearance* experiments if they look at the reduction in muon neutrino events due to oscillations. These experiments are the focus of this thesis and will be better described in the next section.

Since the value of Δm^2 is fixed by nature, different experiments can be designed to be sensitive to different values of Δm^2, by choosing appropriate values of the ratio L/E. From Equation (2.14), the value of Δm^2 for which

$$\frac{\Delta m^2 L}{2E} \simeq 1$$

is called the sensitivity to Δm^2 of an experiment. Different types of neutrino oscillation experiments are then classified depending on the average value of the ratio L/E. Short baseline experiments ($L/E \lesssim 1\,\text{km/GeV}$) are sensitive to $\Delta m^2 \gtrsim 1\,\text{eV}^2$. Some experiments of this type which have been performed in the past are BEBC [30], CDHSW [31], CHARM [32], CHORUS [33], NOMAD [34], LSND [35] and MiniBooNE [36]. Long baseline experiment ($\frac{L}{E} \lesssim 10^3\,\text{km/GeV}$) are sensitive to

$\Delta m^2 \gtrsim 10^{-3}$. Some experiments of this type which have been performed in the past and in the present are ICARUS [37], OPERA [16], T2K [26], MINOS [38] and NOνA [39].

2.5 Challenges in Neutrino Oscillation Experiments

Accelerator long-baseline neutrino experiments can measure muon neutrino disappearance (and are particularly sensitive to the oscillation parameters θ_{23} and Δm^2_{23}) and electron neutrino appearance (are sensitive to the oscillation parameters θ_{13} and δ_{CP}). These experiments consist of a far detector, positioned close to the oscillation maximum, and a near detector, placed just after the neutrino beam production point, to constrain the properties of the neutrino beam and neutrino interactions.

Oscillation experiments measure event rates as a function of energy in their detectors. For a $\nu_\alpha \to \nu_\beta$ oscillation, the event rate in their far detector can be naively computed as

$$N_{\text{FD}}^{\alpha\to\beta}(E_{\text{reco}}) = \int \phi_\alpha^{\text{FD}}(E_{\text{true}})\, P_{\alpha\to\beta}(E_{\text{true}})\sigma_\beta(E_{\text{true}})\epsilon_\beta(E_{\text{true}})U^{\text{FD}}(E_{\text{true}}, E_{\text{reco}})dE_{\text{true}}, \tag{2.15}$$

where $N_{\text{FD}}^{\alpha\to\beta}(E_{\text{reco}})$ is the number of events as a function of reconstructed neutrino energy, $\phi_\alpha^{\text{FD}}(E_{\text{true}})$ is the neutrino flux of flavour α, $P_{\alpha\to\beta}(E_{\text{true}})$ is the oscillation probability, $\sigma_\beta(E_{\text{true}})$ is the cross section for flavour β, and $U^{\text{FD}}(E_{\text{true}}, E_{\text{reco}})$ is the detector response function, describing how E_{true} is reconstructed in E_{reco}.

Experiments depend upon a model of the neutrino-nucleus interaction to disentangle neutrino event rates in their detectors. It is clear from Equation (2.15) that in order to reliably measure the neutrino oscillation probability, $P_{\alpha\to\beta}$, the unoscillated flux, the detector response and neutrino interaction cross sections must

be well understood. If any of these components are not well modelled the extracted oscillation parameters may be biased and large uncertainties on these components will limit the sensitivity of the experiment.

Neutrino oscillation experiments often employ a near detector to measure the unoscillated rate of interactions. Here, the number of events can be naively computed as

$$N^{\alpha}_{\mathrm{ND}}(E_{\mathrm{reco}}) = \int \phi^{\mathrm{ND}}_{\alpha}(E_{\mathrm{true}})\, \sigma_{\alpha}(E_{\mathrm{true}}) \epsilon_{\alpha}(E_{\mathrm{true}}) U^{\mathrm{ND}}(E_{\mathrm{true}}, E_{\mathrm{reco}}) dE_{\mathrm{true}}, \tag{2.16}$$

and experiments may either fit the near detector data to constrain model parameters, or correct the energy distribution according to the near detector data and then extrapolate to the far detector. These methods allow to reduce systematic uncertainties as the flux, cross section, detector response and efficiency are usually highly correlated. However, even when near detector data is used in long-baseline experiments, it does not remove all dependence on the cross-section model. Because event rates correspond to a convolution of the flux and cross section, determinations of oscillation parameters rely on the model to relate near and far detector measurements. In fact, despite the critical role of the near detectors, the near-far cancellation can never be complete for several reasons. First of all, the two detectors might employ different target materials, which require the cross-section extrapolation from one material to another. Moreover, the flux at the near detector cannot be the same as the oscillated one at the far detector as Equation (2.15) contains the unknown oscillation probability $P_{\alpha\to\beta}$. The fluxes also differ because the near and far detectors are in two different locations: the near detector sees a line source of neutrinos (pion decays take place along the decay pipe, which typically has a length of a few hundred meters), while the far detector essentially sees a point source. This implies that the acceptance of particles is different at the

two detectors.

Another way the cross-section model affects an oscillation analysis is through the efficiencies $\epsilon_\alpha(E_{\text{true}})$ in Equations (2.15) and (2.16). These efficiencies include both the acceptance of the detector and the efficiency of selection cuts applied to select signal and reject background. Although the efficiency should be independent of any interaction model, in practice it is calculated by taking simulated particles from a neutrino simulator, which generates events according to a particular model. See for example Section 6.7 for the efficiency calculated for the analysis presented in this thesis. The difference between the near and far detectors leads to uncertainties that do not cancel exactly.

Finally, another challenge for oscillation experiments is the estimation of the neutrino energy as the oscillation probability in Equation (2.14) depends on it. The true neutrino energy is not an observable and what is actually measured is a reconstructed neutrino energy, that must account for unobserved energy deposition, including particles below detection threshold, inactive material, and escaping neutral particles. In practice, assumptions about these effects are based on the cross-section model. The determination of the reconstructed neutrino energy depends on the detector technology used and can be roughly divided into two different methods [40]: kinematical and calorimetric. With the kinematical method, the energy is reconstructed assuming the interaction is CC Quasi-Elastic (QE), neglecting the unmeasured recoil momentum of the system and approximating the interaction energy ϵ of the initial state nucleon by a constant $E_i^n = M - \epsilon$ [41], where M is the mass of the nucleon, so that:

$$E_\nu^{\text{kin}} = \frac{2(M-\epsilon)E_l + M^2 - (M-\epsilon)^2 - m_l^2}{2(M - \epsilon - E_l + |\mathbf{k}_l|\cos\theta)}, \tag{2.17}$$

where m_l is the mass of the outgoing charged lepton, E_l and k_l are its energy and

momentum, and θ is the angle between the outgoing lepton and the direction of the neutrino beam. This reconstruction method works well if the true nature of the event was indeed a CC QE process, but this is rarely the case as many processes contribute to a selected topology. For example, events with one pion in the final state where the pion is absorbed in the nuclear medium, or events with two-nucleon knockout, as will be shown in Section 3.2.3. Moreover, this method assumes a fixed interaction energy ϵ, while in reality the struck nucleon's momentum is drawn from a distribution characteristic of the target nucleus, see Section 3.2.1. Cherenkov detectors usually employ this method. Detectors like liquid scintillators, magnetised iron detectors, or Liquid Argon Time Projection Chambers usually employ the calorimetric method. In this case, the energy is reconstructed by summing up the reconstructed energy of all the visible particles coming out of the interaction vertex [40]:

$$E_{\nu}^{\text{calo}} = E_l + \epsilon + \sum_{i=1}^{n} T_i + \sum_{j=1}^{m} E_j, \tag{2.18}$$

where T_i is the kinetic energy of the i^{th} nucleon, and E_j is the energy of the j^{th} meson in the final state. For nucleons, only the kinetic energies contribute as they pre-exist and are knocked out of the target nucleus while mesons are produced during the interaction process. This energy reconstruction procedure can be applied to non-QE events as well as to QE events but also this procedure is not free from systematic uncertainties affecting the determination of the incident neutrino energy. Each particle in the interaction must be properly identified and reconstructed, but the accurate reconstruction of hadrons poses a formidable experimental challenge. In particular, neutrons typically escape detection, and any undetected meson results in energy underestimation by at least the value of the pion mass, 140 MeV. This makes low detection and tracking thresholds a key requirement for a calorimetric detector.

Source of uncertainty	ν_e CC [%]
Flux and common cross sections	
(w/o ND280 constraint)	26.0
(w ND280 constraint)	3.2
Independent cross sections	4.7
SK	2.7
FSI + SI (+PN)	2.5
Total	
(w/o ND280 constraint)	26.8
(w ND280 constraint)	6.8

Source of uncertainty	ν_e CC [%]
Cross sections and FSI	7.7
Normalisation	3.5
Calibration	3.2
Detector response	0.67
Neutrino flux	0.63
ν_e extrapolation	0.36
Total systematic uncertainty	9.2

Table 2.1: Relative uncertainty (1σ) on the predicted rate of ν_e signal at T2K (left) and NOνA (right), tables are from [26] and [42] respectively.

In summary, with the current limited understanding of the microphysics of neutrino-nucleus interactions, the neutrino energy scale cannot be determined reliably in future experiments like DUNE. As an example, Table 2.1 summaries the uncertainties on the ν_e CC event prediction at T2K (left) and NOνA (right). Uncertainties have significant components from cross-section systematic uncertainties which do not cancel in the near/far extrapolation (4.7% for T2K and 7.7% for NOνA). A better understanding of neutrino-nucleus interactions is then needed, and many experiments are performing measurements, like the one presented in this thesis, to constrain nuclear models.

Chapter 3

Neutrino Interactions

While the previous chapter described neutrino oscillations and the challenges for current and future neutrino oscillation experiments due to neutrino-nucleus interactions, this chapter focuses on neutrino interactions, describing the approximations used and the models employed in neutrino simulations. The different neutrino interaction modes are described in Section 3.1, and the nuclear effects due to the neutrino-nucleus interaction are shown in Section 3.2. Finally, Section 3.3 shows a summary and the need for more measurements, introducing the ν_μ CC measurement on argon that will be described in this thesis.

3.1 Neutrino Interaction Modes

The description of neutrino scattering between $0.1 - 20$ GeV can be described by several distinct neutrino scattering mechanisms [43]. The possibilities fall into three main categories, also shown in Figure 3.1:

Elastic and Quasi-Elastic Scattering Neutrinos can elastically scatter off an entire nucleon liberating a nucleon (or multiple nucleons) from the target. In the case of CC neutrino scattering, this process is referred to as "QE

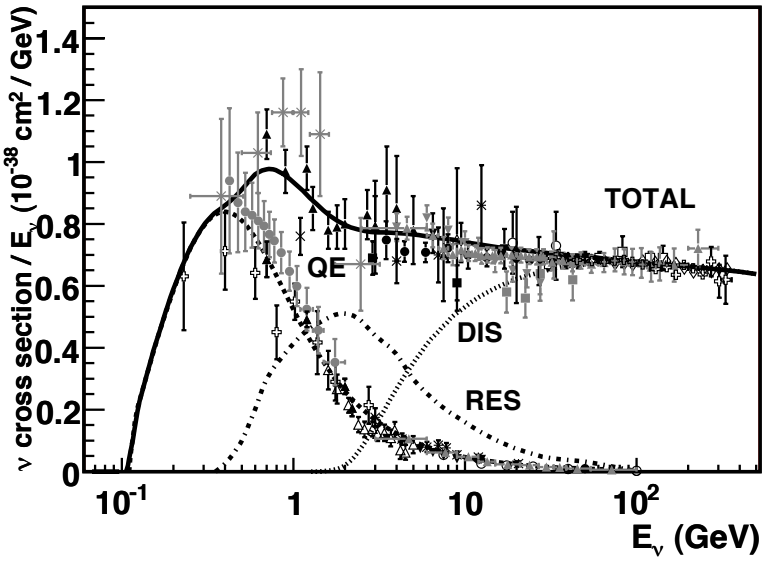

Figure 3.1: Total neutrino per nucleon CC cross sections (for an isoscalar target) divided by neutrino energy and plotted as a function of energy. The data points show the results of different experiments, as described in [43]. Also shown are the various contributing processes that will be described in the next sections. These contributions include QE scattering (dashed), resonance production (dot-dash), and DIS scattering (dotted). Example predictions for each are provided by the NUANCE generator [44]. Source: [43].

scattering" because neutrinos become charged leptons in the final state. For NC scattering, this is traditionally referred to as "elastic scattering", although the "quasi elastic" terminology is also used for NC interactions, and it refers to when the final state nuclear targets are not in their ground states. These mechanisms are described in Section 3.1.1.

Resonance Production Neutrinos can excite the target nucleon to a resonance state. The resultant baryonic resonance decays to a variety of possible mesonic final states producing combinations of nucleons and mesons. This is described in Section 3.1.2.

Deep Inelastic Scattering Given enough energy, the neutrino can resolve the individual quark constituents of the nucleon. This is called Deep Inelastic Scattering (DIS) and manifests in the creation of a hadronic shower. This is

described in Section 3.1.3.

Examples of these types of interaction are shown in Figure 3.2, as they appear in a LArTPC detector. As a results of all these processes, the products of neutrino interactions include a variety of final states ranging from the emission of nucleons to more complex final states including pions, kaons, and collections of mesons. Other interaction processes, like coherent pion production and kaon production, are also present, and they will be briefly discussed in Section 3.1.4.

Looking at Figure 3.1, and considering that neutrinos at the MicroBooNE detector have energy from a few tens of MeV to ~ 2 GeV, the relevant interaction processes for the measurement in this thesis are QE scattering and resonance production, with a small contribution from DIS events.

3.1.1 Quasi-Elastic Interactions

At neutrino energies between ~ 0.1 and ~ 1.5 GeV, the primary way in which neutrinos interact with matter is via QE interactions, as shown in Figure 3.3. These interactions will now be discussed in details, as MicroBooNE deals with neutrinos mainly at these energies. This section focuses on CC interactions, which include the following processes:

$$\nu_l + n \rightarrow l^- + p, \qquad \bar{\nu}_l + p \rightarrow l^+ + n, \tag{3.1}$$

for lepton flavour l, a neutron n and proton p.

Starting from Equation (2.1), an effective CC Lagrangian can be written by requiring that the squared momentum transferred being smaller than the W mass squared, $q^2 \ll M_W^2$, and so integrating out the W boson, and by working at the

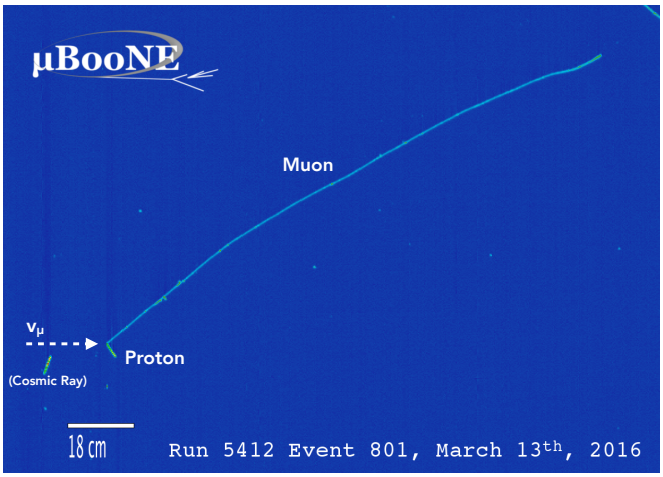

(a) ν_μ CC QE candidate event.

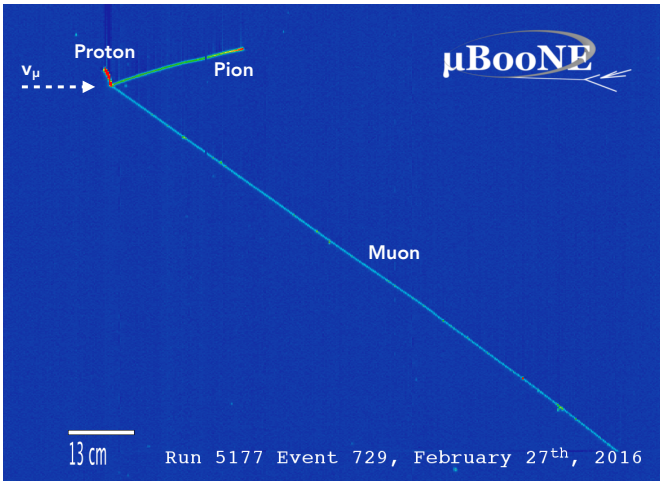

(b) ν_μ CC resonance candidate event.

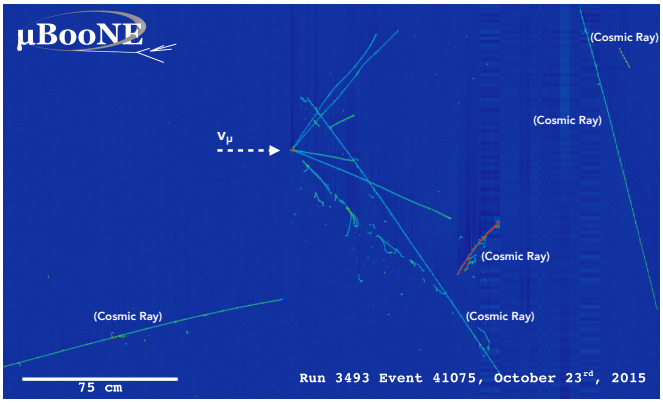

(c) ν_μ CC DIS candidate event.

Figure 3.2: Events recorded by the MicroBooNE detector showing QE (a), resonance (b), and DIS (c) events. The images show a 2D projection of the events, and display the final state particles coming from the neutrino interactions. Neutrinos come from the left. More details on the MicroBooNE event display are given in Section 4.2.2.

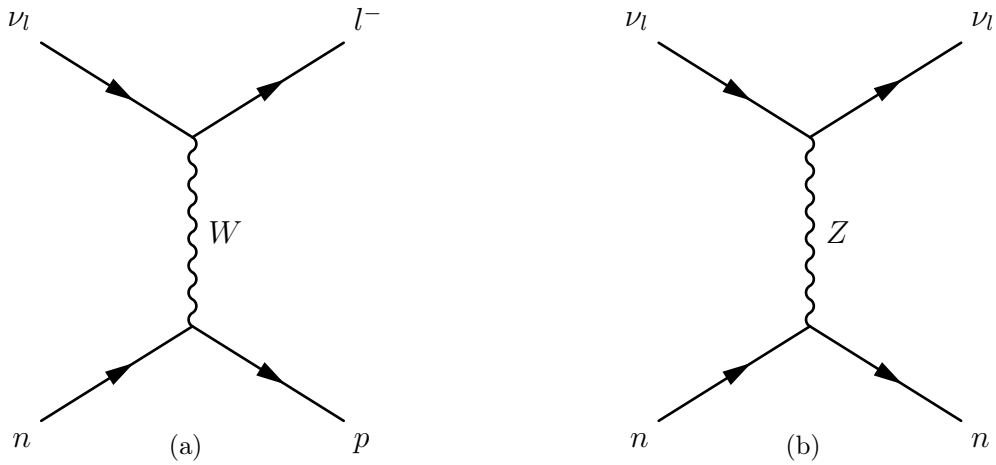

Figure 3.3: Example of Feynman diagrams of QE interactions. A CC with a W exchange (a), and a NC one, with a Z exchange (b).

first order in perturbation theory [18]:

$$\mathcal{L}_{\text{eff}} = -\frac{G_F}{\sqrt{2}} \left(J^\mu {J_\mu}^\dagger \right), \tag{3.2}$$

where G_F is the Fermi constant. The current J^μ is given by

$$J^\mu = \sum_l \bar{\nu}_l \gamma^\mu (1-\gamma^5) l + \sum_{ij} V_{ij}^{\text{CKM}} \bar{U}_i \gamma_\mu (1-\gamma_5) D_j, \tag{3.3}$$

where ν_l and l are the neutrino and lepton spinors with flavour l, V^{CKM} is the Cabibbo–Kobayashi–Maskawa (CKM) matrix for the quark mixing, and U and D denote the up- and down-type quark spinors respectively.

The above Lagrangian describes the quark-level interaction as shown in Figure 3.4a, but in reality, it is not possible to study neutrino interactions with free quarks, but rather with neutrons or protons. While the lepton current can be calculated exactly, this is not the case for the hadronic current. Problems arise in this case given the ignorance on the internal structure of the nucleons, and the inability to solve Quantum Chromodynamics (QCD) at low energies. Cross sections

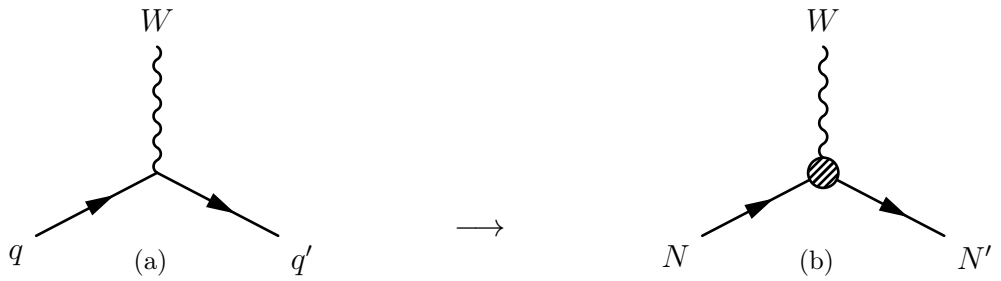

Figure 3.4: W interacting with a quark (a) and with a nucleon (b). It is not possible to solve QCD at low energies and effective interactions, schematically shown as a blob in the picture, are considered when a W interacts with a nucleon.

are then parametrised with "form factors" which effectively take into account the internal structure of the nucleons as well as their coupling with the lepton current, as schematically shown in Figure 3.4b.

The hadronic matrix element $\langle p(p_2)|\, J_\mu\, |n(p_1)\rangle$ can then be expressed in terms of the most general Lorentz-invariant form factors:

$$\begin{aligned}\langle p(p_2)|\, J_\mu\, |n(p_1)\rangle = \bar{u}^{(p)}(p_2)[\gamma_\mu F_V^1(q^2) + \frac{i\sigma_{\mu\nu}q^\nu}{2M}F_V^2(q^2) + \frac{q_\mu F_V^3(q^2)}{M} + \\ \gamma_\mu\gamma_5 F_A(q^2) + \frac{q_\mu\gamma_5}{M}F_P(q^2) + \frac{i\sigma_{\mu\nu}q^\nu\gamma_5}{2M}F_A^2(q^2)]u^{(n)}(p_1),\end{aligned} \tag{3.4}$$

where $q = k_1 - k_2 = p_1 - p_2$ is the momentum transfer, M is the nucleon mass, $F_V^{1,2,3}(q^2)$ are called vector form factors, $F_A(q^2)$ and $F_A^2(q^2)$ axial form factors and $F_P(q^2)$ pseudo-scalar form factor.

These form factors can be naively interpreted as the Fourier transform of the internal charge distribution of the nucleus [18]. Assuming that this charge is distributed as $\rho(r) = \rho_0 e^{-Mr}$, the form factors assume the form of a dipole: $F(q^2) \propto (1 + q^2/m^2)^{-2}$, where m is a parameter that needs to be measured experimentally.

The two form factors $F_V^3(q^2)$ and $F_A^2(q^2)$ are set to zero as they violate G-parity. $F_V^1(q^2)$ and $F_V^2(q^2)$ can be related via Conserved Vector Current (CVC) to electromagnetic form factors which are measured over a broad range of kinematics

in electron elastic scattering experiments. These observations have found that the dipole form works well for $Q^2 < 2.0\,\mathrm{GeV}^2$, but deviations are seen at larger Q^2 (see, e.g. [45]). Extensions to $F_V^1(q^2)$ and $F_V^2(q^2)$, which parametrise these deviations, are typically used by the neutrino scattering community. One of the most recent parametrisations, called "BBBA05" form factors, are used in this work, which are defined in [46].

Two form factors remain: the pseudo-scalar $F_P(q^2)$ and the axial vector $F_A(q^2)$. The pseudo-scalar form factor is assumed to have the form suggested by the partially conserved axial current (PCAC) hypothesis [47], which leaves the axial form factor $F_A(q^2)$ as the sole remaining unknown quantity. A dipole form is usually assumed for $F_A(q^2)$:

$$F_A(q^2) = \frac{F_A(0)}{\left(1 + q^2/M_A^2\right)^2}. \tag{3.5}$$

$F_A(0)$ is well known from measurements of neutron beta decay ($F_A(0) = g_A$) and the q^2 dependence (parametrised by M_A, often referred to as "axial mass") of this form factor can only be determined in neutrino experiments and has been the focus of a large amount of experimental work over several decades.

Usually, the Llewellyn Smith formulation is used for the neutrino-nucleon cross section, which is given by [47]:

$$\frac{d\sigma}{dQ^2} = \frac{G_F^2 M^2 |V_{ud}|^2}{8\pi E_\nu^2} \left[A(Q^2) \pm \frac{(s-u)}{M^2} B(Q^2) + \frac{(s-u)^2}{M^4} C(Q^2) \right], \tag{3.6}$$

where the $(-)+$ refers to (anti)neutrino scattering, M is the nucleon mass, Q^2 is the four-momentum transfer ($Q^2 = -q^2 > 0$), E_ν is the incident neutrino energy and $(s-u) = 4ME_\nu - Q^2 - m^2$, m being the lepton mass. A, B and C are functions of Q^2 built from the vector ($F_V^{1,2}$), axial vector (F_A) and pseudoscalar (F_P) nucleon form factor [47].

As the NC equivalent to CC QE interactions, neutrinos can undergo NC elastic scatters, typically ejecting a nucleon from the nucleus. The available neutrino interaction modes are:

$$\begin{aligned} \nu_\mu\, p &\rightarrow \nu_\mu\, p, \\ \nu_\mu\, n &\rightarrow \nu_\mu\, n. \end{aligned} \tag{3.7}$$

As the hadronic current is similar, they are modelled very similarly to CC QE interactions.

3.1.2 Resonance Production

Given enough energy and if the neutrino-nucleus centre of mass energy exceeds the mass of a delta baryon, neutrinos can send the struck nucleon to an excited state. In this case, the neutrino interaction produces a baryon resonance (N^*). The baryon resonance quickly decays, most often to a nucleon and single pion final state:

$$\nu_l + N \rightarrow l + N^* \rightarrow l + \pi + N', \tag{3.8}$$

where $N, N' = n, p$. Other higher multiplicity decay modes are also possible as baryonic resonances created in neutrino-nucleon interactions can potentially decay to multi-pion final states. At the lowest energies, the process is dominated by production of the $\Delta(1232)$, as shown for example in Figure 3.5a.

In scattering off of free nucleons, there are seven possible resonant single pion reaction channels. Only listing the ones for neutrinos, resonance production can

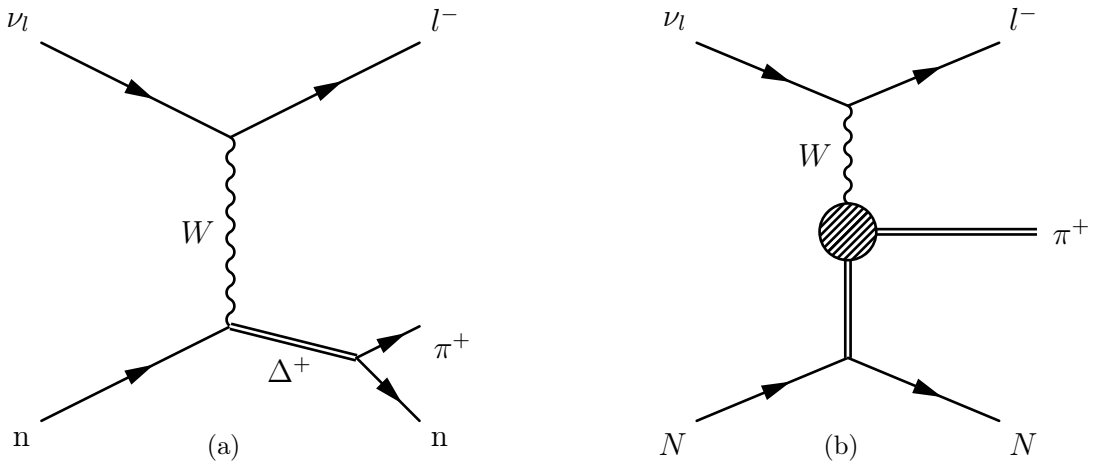

Figure 3.5: Two examples of Feynman diagrams of pion production interactions: resonance (a) and coherent (b).

happen in both CC (left) and NC (right) interactions:

$$\nu_\mu p \to \mu^- p \pi^+, \qquad \nu_\mu p \to \nu_\mu p \pi^0,$$
$$\nu_\mu n \to \mu^- p \pi^0, \qquad \nu_\mu p \to \nu_\mu n \pi^+,$$
$$\nu_\mu n \to \mu^- n \pi^+, \qquad \nu_\mu n \to \nu_\mu n \pi^0,$$
$$\nu_\mu n \to \nu_\mu p \pi^-.$$

To describe such resonance production processes, neutrino experiments most commonly use calculations from the Rein and Sehgal model [48, 49] and this is, in fact, the model used in the analysis presented in this thesis.

As for QE interactions, the hadronic current is parameterised with form factors, both the vector and axial form factors are assumed to have a dipole form. Two parameters cannot be taken be taken from electron scattering, those are the equivalent as $F_A(0)$ and M_A in Equation (3.5), which have to be measured experimentally.

The analysis in this thesis also uses the Berger-Sehgal model [50], which improves upon the Rein-Seghal one in using the available data on differential and total pion cross sections. In general, the pion scattering cross-section is significantly reduced

compared to pion-nucleus Rein-Sehgal approximations in the $E_\pi < 1$ GeV region.

NC π^0 production is often the largest ν_μ-induced background in experiments searching for $\nu_\mu \to \nu_e$ oscillations, as the photons coming from the π^0 decay may mimic the signature of an electron neutrino interaction.

3.1.3 Deep Inelastic Scattering

In deep inelastic scattering (see Figure 3.6), the neutrino scatters off a quark in the nucleon via the exchange of a virtual W or Z boson producing a lepton and a hadronic system in the final state. This breaks apart the nucleon, producing a jet of hadrons in an interaction mode known as DIS. This is the dominant neutrino interaction mode for neutrinos with energy above about 10 GeV. Both CC and NC processes are possible:

$$\nu_\mu N \to \mu^- X, \qquad \nu_\mu N \to \nu_\mu X. \tag{3.9}$$

There are only a few neutrinos undergoing DIS interactions at MicroBooNE energies, and for this reason, this interaction mode is not described in details here. Details on these interactions can be found in [18, 43] and in this thesis they are modelled according to the GENIE neutrino simulator, which employs a leading order model using the modifications suggested in [51] to describe scattering at low momentum transfer [52].

3.1.4 Other Interaction Modes

In addition to resonance production, neutrinos can also coherently produce single pion final states. In this case, the neutrino coherently scatters from the entire nucleus N, transferring negligible energy to the target, as shown in Figure 3.5b.

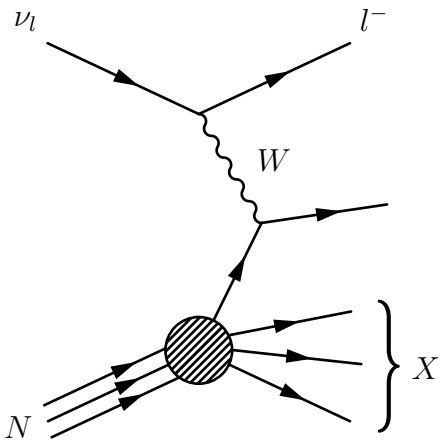

Figure 3.6: Feynman diagram for CC neutrino DIS process.

The nucleus recoils but does not fragment, leaving it in the same final state as initial state. Both CC and NC coherent pion production processes are possible:

$$\nu_\mu N \to \mu^- N \pi^+, \qquad \nu_\mu N \to \nu_\mu N \pi^0. \tag{3.10}$$

The Rein-Sehgal is again the model mostly used in event generators, with the Berger-Sehgal model being an improvement as discussed in the previous section.

Neutrino interactions can also produce final states involving strange quarks. At neutrino energies below 2 GeV, Cabibbo suppressed single kaon production $\nu_\mu N \to \mu^- K^+ N$ is the dominant K^+ production mechanism [53]. At higher energies, K^+ mesons arise via associated production accompanied by strangeness $= -1$ baryons (Λ, $\Sigma^\pm$) or mesons (K^-, $\bar{K}^0$) such that there is no net change in strangeness ($\Delta S = 0$). This can occur through an intermediate resonance state or in DIS by hadronisation, the production of mesons and baryons from the struck quark. Measuring neutrino-induced kaon production is of interest primarily as a source of potential background for proton decay searches. Proton decay modes containing a final state kaon, $p \to K^+ \nu$, have large branching ratios in many SUSY GUT models [43]. Because there is a non-zero probability that an atmospheric neutrino interaction can mimic such a proton decay signature, estimating these background

rates has become an increasingly important component to such searches.

3.2 Nuclear Effects

The sections above described neutrinos interacting with free nucleons but in reality nucleons are aggregated in nuclei and nuclear effects alter the interactions and the products. In general, there are initial state effects that need to be taken into account as the nucleons are bound in the nucleus, as well as final state effects as the particles produced in the interactions need to pass through the nuclear matter to exit from the nucleus. While in the past neutrino experiments mainly used deuterium as target material, modern-day experiment use more complex nuclei to increase the overall interaction rates and because modern detector technologies require heavier elements (for example in the case of LArTPC detectors). When dealing with more complex nuclei, nuclear effects are no longer negligible and need to be taken into account. As a result, Equation (3.6) is no longer valid, as it describes the interaction with a free nucleon. If the nucleon is bounded in a nucleus, it is important to take into account nuclear effects that produce sizeable modifications to Equation (3.6). Finally, there will also be brand new interactions processes which are not present for free nucleons, as it will be described in the next sections.

3.2.1 Basic Approximations and Fermi Motion

In the majority of the cases, the Impulse Approximation (IA) is the most commonly adopted to describe the interaction with a nucleus [54]. The IA approximation is based on the assumptions that at large enough momentum transfer the target nucleus is seen by the W or Z probe as a collection of individual nucleons

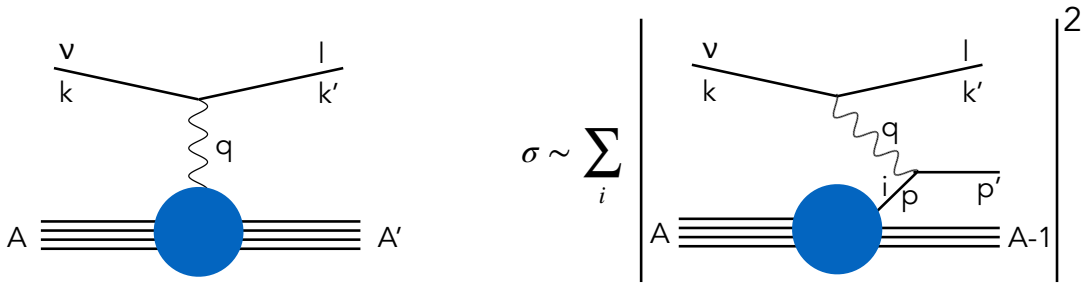

(a) (b)

Figure 3.7: (a) Feynman diagram for the process $\nu_l + A \to l^- + A'$. (b) shows the IA used to calculate the cross section for the process.

and that the particles produced at the interaction vertex and the recoiling nucleon system evolve independently (see Figure 3.7 for a pictorial representation of the IA picture). As a result of this, the final cross section can be written as a cross section describing the neutrino-nucleon interactions, integrated all over possible states of the nucleon, weighted by a Spectral Function (SF):

$$\frac{d^2\sigma_{\text{IA}}}{dQ^2} = \int d^3p\, dE\, P(\mathbf{p}, E)\, \frac{d^2\sigma_{\text{elem}}}{dQ^2}, \tag{3.11}$$

where $d^2\sigma_{\text{elem}}/dQ^2$ corresponds to the one in Equation (3.6). The function $P(\mathbf{p}, E)$ is the target SF, i.e. the probability distribution of finding a nucleon with momentum $\mathbf{p}$ and removal energy E in the target nucleus. It then encodes all the information about the initial (struck) particle.

In this approximation, the Fermi motion is embedded in the SF $P(\mathbf{p}, E)$, which needs to be characterised. A simple and commonly used spectral function model is the global Relativistic Fermi Gas (RFG) model [55]. Here, nucleons within the nucleus are modelled as non-interacting fermions inside a pervading nuclear potential, such that all momentum states are filled from the ground state upwards. The highest momentum state has momentum p_F, known as the Fermi momentum,

which depends on the number of nucleons in a nucleus. This means that the SF can be written as $P(\mathbf{p}, E) \propto \theta(p_F - |\mathbf{p}|)$, which then needs a Dirac δ-function that ensures the conservation of energy. The energy of the struck nucleon (off-shell) can be written as:

$$E_{\mathbf{p}} = \sqrt{\mathbf{p}^2 + M^2} - \epsilon(\mathbf{p}), \tag{3.12}$$

where M is the nucleon mass and ϵ is the so-called interaction energy. The Smith–Moniz approach to the FG model [55] is to approximate $\epsilon(\mathbf{p})$ by the constant average value $\bar{\epsilon}$, and conserve energy only on average. In this way, the spectral function takes the form

$$P(\mathbf{p}, E) = N\,\delta(\sqrt{\mathbf{p}^2 + M^2} - \bar{\epsilon} - M + E)\theta(p_F - |\mathbf{p}|), \tag{3.13}$$

where N is a normalisation constant. Overall, the Heaviside function gives rise to a sharp end in the SF distribution, as can be seen from the green curve in Figure 3.8, which shows the nucleon momentum distribution, defined as

$$n(\mathbf{p}) = \int dE\, P(\mathbf{p}, E). \tag{3.14}$$

The RFG spectral function treats all nucleons as feeling the same constant binding potential, whilst in reality this depends upon the local density of the nucleus. More sophisticated Local Fermi Gas (LFG) spectral functions use the local nuclear density $\rho(r)$ to build a nuclear potential that depends on the radial position of a nucleon within the nucleus r, following the density profile of the nuclear matter [56].

Although a LFG model is more realistic than an RFG model, nucleons are still treated as non-interacting fermions (other than via the local nuclear potential).

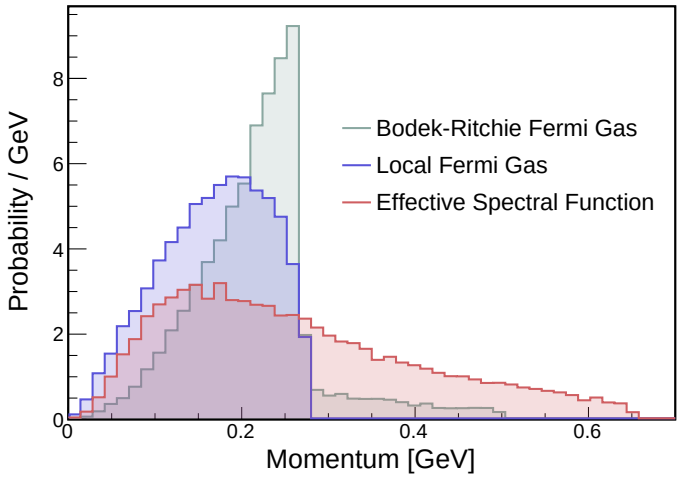

Figure 3.8: Nucleon momentum distributions in an argon nucleus for several spectral functions as implemented in the GENIE neutrino event generator. The Bodek-Ritchie Fermi gas, relativistic Fermi gas and effective spectral function are shown. The distribution shown is $4\pi|\boldsymbol{p}|^2 n(|\boldsymbol{p}|)$ as a function of $|\boldsymbol{p}|$, with $n(\boldsymbol{p})$ given by Equation (3.14) and with normalisation condition given by $4\pi \int d|\boldsymbol{p}||\boldsymbol{p}|^2 n(|\boldsymbol{p}|) = 1$.

However, it is well known from electron scattering data that nucleon-nucleon interactions inside the nuclear medium can significantly alter the distribution of the initial state nucleon momenta [57, 58]. Nucleon-nucleon correlations introduce a high-momentum tail in the SFs. There are variations of the RFG and LFG that allow to include these correlations, one example is the Bodek-Ritchie modification to the RFG model [59]. This is shown in Figure 3.8, and is the main model used in this thesis.

Beyond the energy conserving Dirac-δ shown above, these models are not explicitly functions of the removal energy E. More sophisticated SF can be extracted by taking into account two and three-nucleon interaction potentials which give rise to nucleon-nucleon correlations. These SF, for examples the ones derived in [54], depend explicitly on E, and have a high momentum tail.

Effective SF have also been calculated [60] that are able to reproduce the predictions obtained by the superscaling variable [61]. This SF also has a high

momentum tail, as shown in Figure 3.8.

In general, Fermi gas models need an additional modification to take into account the effect of Pauli blocking. Since nucleons are fermions, they follow Fermi-Dirac statistics which allows only two nucleons per energy level. Scattering which would take the nucleon to a new state already occupied by other nucleons are not allowed. For QE interactions, which change a neutron to a proton, enough energy has to be transferred to the proton to avoid this problem or the reaction does not take place. In the GENIE simulator [62], used in MicroBooNE and in the work presented in this thesis, a suppression factor is included based on the simple requirement that the momentum of the outgoing nucleon exceeds the Fermi momentum k_F for the nucleus in question.

A summary of the nuclear models used in this thesis is shown in Section 4.5.

3.2.2 Final State Interactions

As described in the previous section, many generators employed by neutrino experiments adopt the IA in which neutrinos scatter on individual quasi-free nucleons. In this picture any neutrino-nucleus interaction can be factorised in a two-step process: in the first step, the neutrino scatters on a bound nucleon, and in the second step Final State Interactions (FSI) affect the hadrons produced in the first step. FSI happen as pions and protons rescatter before exiting the nucleus. As an example, Figure 3.9 shows how pions can be absorbed, can be scattered elastically, can produce new pions, or can exchange electric charge with nucleons.

Simulations used in major neutrino oscillation experiments, in their description of FSI effects, rely on the model of Intra-Nuclear Cascade (INC) [64]. These cascade models assume the nucleus is an ensemble of quasi-free nucleons and the incident particle interacts in a series of encounters with single nucleons called a cascade (see

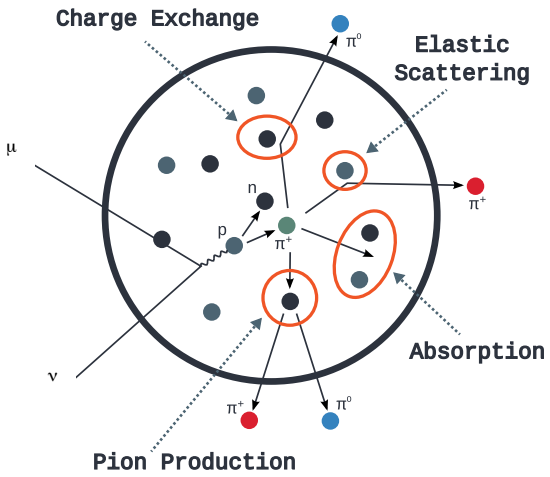

Figure 3.9: Hadrons produced at the neutrino interaction vertex must still traverse the dense nuclear matter and they are then subject to FSI before appearing in the detector. The image shows how pions can be absorbed, scattered, produce new pions or exchange electric charge with other nucleons. A similar picture can be drawn for nucleons. Image credit: [63].

Figure 3.9). All interactions are governed by the cross section for the free processes, and the probability of interaction is governed by a mean free path $\lambda = 1/(\sigma \cdot \rho(r))$. The probability for a multitude of different interactions (e.g. elastic scatter, charge exchange, absorption) is calculated at each step based on the local nuclear density and, if necessary, such an interaction is simulated. This continues until the hadron leaves the nucleus. These cascade models have some limitations, they use a simple Fermi gas model to describe the distribution of the nucleons, effects of nucleon correlations must be included empirically and both the struck nucleon and the scattered hadron are likely to be off-shell, while they are treated as free particles.

FSIs contribute significantly to the systematic uncertainties in neutrino oscillation measurements as they are extremely difficult to model or constrain with experimental data. In the simulation used in this thesis (GENIE), the intranuclear transport is handled by a subpackage called INTRANUKE and the model used for the INC is called `hA` [52]. Rather than calculate a cascade of hadronic interactions as is done in a complete INC model, the `hA` model uses the total cross section for

each possible nuclear process for pions and nucleons. This is an empirical and data-driven model [52] which uses data from Fe targets and extrapolates to other targets.

To conclude this section, it is important to note the nucleus will also affect the lepton in the final state. For targets with atomic number Z greater than one, the effect of the electric field of the nucleus on the scattered lepton must be considered. Corrections due to this electric field are called Coulomb corrections. The corrections result in an acceleration (for l^+) or deceleration (for l^-) of the scattered lepton l, thus resulting in a variation of its momentum.

In this work, the measured neutrino cross sections at MicroBooNE will be compared to two GENIE simulations: one which includes the `hA` cascade model and no Coulomb corrections, and another that includes an updated cascade model called `hA2014` [65] (which includes a wide range of data [66] for other nuclei than Fe for $\pi^{\pm}$ so that much less extrapolation is needed), and Coulomb corrections as calculated by Nieves et al. [67, 68].

3.2.3 Nucleon-Nucleon Correlations and the Random Phase Approximation

MiniBooNE neutrino cross-section measurements [36] were much larger than the theoretical predictions. This is shown in Figure 3.10, where the MiniBooNE and the NOMAD measurements, both on carbon, appear to differ in normalisation by about 30%. The low energy MiniBooNE results are higher than expected from the Fermi Gas model with more sophisticated impulse approximation calculations assuming an axial mass $M_A = 1.0$ GeV from deuterium-based measurements. Indeed, a large nucleon axial mass of $M_A = 1.35 \pm 0.17$ GeV was needed to describe these data. Such large values for M_A were in clear conflict with other electron and neutrino

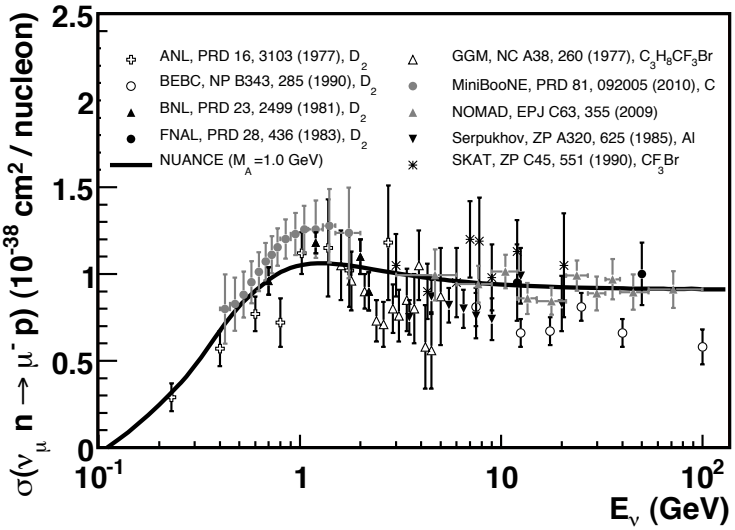

Figure 3.10: Existing measurements of the ν_μ QE-like scattering cross section, $\nu_\mu n \to \mu^- p$, as a function of neutrino energy on a variety of nuclear targets. The free nucleon scattering prediction assuming $M_A = 1.0$ GeV is shown for comparison. Figure from [43].

experiments which result in a value very close to 1 GeV ($M_A = 1.014 \pm 0.014$ GeV [69]). This is shown in Figure 3.11, where data from MiniBooNE now show the measured differential cross section as a function of the muon kinetic energy, and the black line shows the prediction with an axial mass of 1.32 GeV. This is the so-called MiniBooNE M_A puzzle.

It is currently believed that nuclear effects beyond the impulse approximation approach are responsible for the discrepancies noted in the experimental data. A more theoretically sound solution to the puzzle was obtained thanks to the inclusion of some standard nuclear effects such as multinucleon mechanisms [70]. In these mechanisms, the W boson can be absorbed by nucleons belonging to correlated pairs and to two-nucleon currents arising from Meson Exchange Current (MEC) which lead to the excitation of multinucleon or $2p2h$ (2-particles 2-holes) excitations. In these models, a substantial part of the cross section measured corresponds to events in which at least two nucleons are emitted. The consideration of the $2p2h$ nuclear excitations allows to describe the MiniBooNE cross section

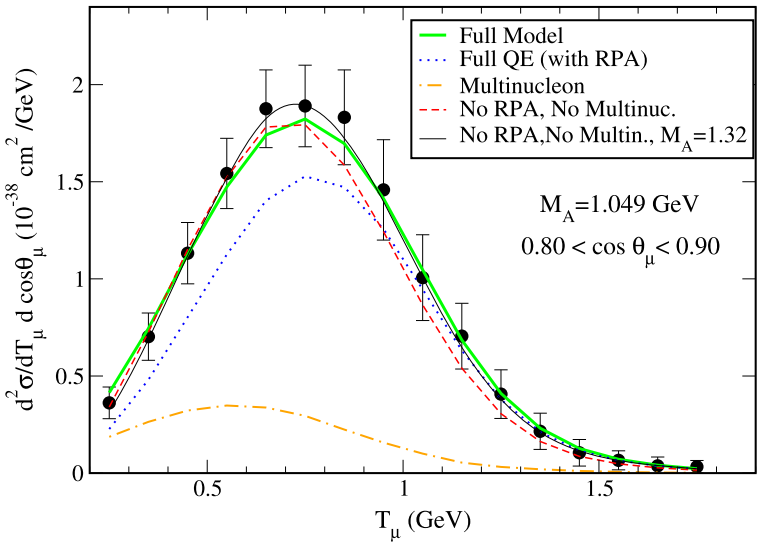

Figure 3.11: The muon angle and energy distribution $d^2\sigma/d\cos\theta_\mu dT_\mu$ for $0.80 < \cos\theta_\mu < 0.90$ from the MiniBooNE experiment [36]. The curves show different model predictions: the black line show the MC obtained by increasing M_A to 1.35 GeV, while the green line shows the model prediction with multinucleon effects and RPA included. The two predictions are similar. Figure from [70].

$d\sigma/dT_\mu/d\cos\theta_\mu$ with values of M_A around 1 GeV, as can been seen from the green curve in Figure 3.11.

However, not only multinucleon mechanisms but also Random Phase Approximation (RPA) corrections [67] turn out to be essential to find that axial masses consistent with the world average lead to a good description of the MiniBooNE data. RPA is a method to describe microscopic quantum mechanical interactions in complex many-body systems. In this case, the many-body system is described by the mutual interactions of nucleons inside the nucleus, which cannot be resolved exactly. The overall effect of RPA correlations is to account for the change of the electroweak coupling strengths, from their free nucleon values, due to the presence of strongly interacting nucleons. RPA corrections are dominant at low Q^2: the W or Z probe has small resolution and sees nucleons embedded in the nuclear potential. While at higher Q^2 RPA corrections are negligible as the probe has high

resolution and sees nucleons as almost free particles.

The cross section measurements presented in this thesis are compared to a default GENIE simulation that does not include RPA and that uses an empirical model for the simulation of MEC events that reproduces MiniBooNE and NOMAD data [71]. Moreover, the measurements are also compared to an alternative configuration of GENIE that uses the Nieves et al. model [67, 68], which folds interactions of correlated pairs and a RPA corrections to describe interactions of many bodies into the calculation.

3.3 Final Remarks

While most of our knowledge of neutrino cross sections around the $\sim$ 1 GeV energy range comes from early experiments that collected relatively small data samples [43], current experiments use heavy nuclei as target material, like hydrocarbon in the T2K and NOνA detectors, and argon in MicroBooNE. As described in the previous sections, nuclear effects seriously complicate the understanding of neutrino interactions and can greatly affect the sensitivity of neutrino oscillation experiments.

Although many of the future experiments, such as DUNE [72, 73, 74] and the SBN program [75], will all employ the Liquid Argon Time Projection Chamber (LArTPC) detection technology with argon as target material, experimental data for the neutrino-argon scattering process is scarce [76, 77].

This thesis presents the first ν_μ CC inclusive measurement on argon at $\sim$ 0.8 GeV of mean neutrino energy. The CC inclusive channel is sensitive to some of the nuclear effects described in the previous sections and will be extremely valuable to future neutrino oscillation experiments. The signal topology for a ν_μ CC inclusive measurement is the presence and identification of a neutrino-induced muon track

with or without accompanying particles. It is, therefore, the most inclusive cross section measurement that one can make, and due to the very clear signal definition allows straight-forward comparisons to theoretical models and other experiments.

It is important to evaluate neutrino cross sections as a function of the kinematics of the outgoing muon as nuclear models will shape these distributions. Neutrino experiments have measured single differential cross sections as a function of the muon momentum ($d\sigma/dp_\mu$) or the cosine of the muon angle w.r.t. the neutrino direction ($d\sigma/d\cos\theta_\mu$). Recently, experiments are also producing double-differential cross sections ($d^2\sigma/dp_\mu d\cos\theta_\mu$) as they provide a better insight in the properties of neutrino interaction with the nucleus and how the angle and the momentum of the lepton are correlated. For this reason, the analysis in this thesis will show both single and double-differential cross sections.

Some other modern experiments have also measured the ν_μ CC inclusive cross section. ArgoNeuT [76, 77] and the T2K on-axis detector INGRID [78, 79] published flux-integrated measurements. ArgoNeuT is the only experiment that published cross sections for neutrino-argon scattering to date, but at higher neutrino energy, around 5 GeV. SciBooNE [80], NOMAD [81], MINOS [82], and MINERvA [83, 84] all published CC inclusive cross sections as a function of a reconstructed neutrino energy. The only experiments with published double-differential data are event distributions from SciBooNE [80] and cross section measurements from the T2K on-axis detector [85], both as a function of muon angle and muon momentum. T2K – which has comparable beam energy to MicroBooNE – was able to bin in four angular and five momentum bins. All flux-integrated or energy-dependent measurements are summarised in Figure 3.12 from the PDG review article [86]. This analysis provides a flux integrated measurement that can be added to a future Figure 3.12, as well as single differential and double differential cross sections as a

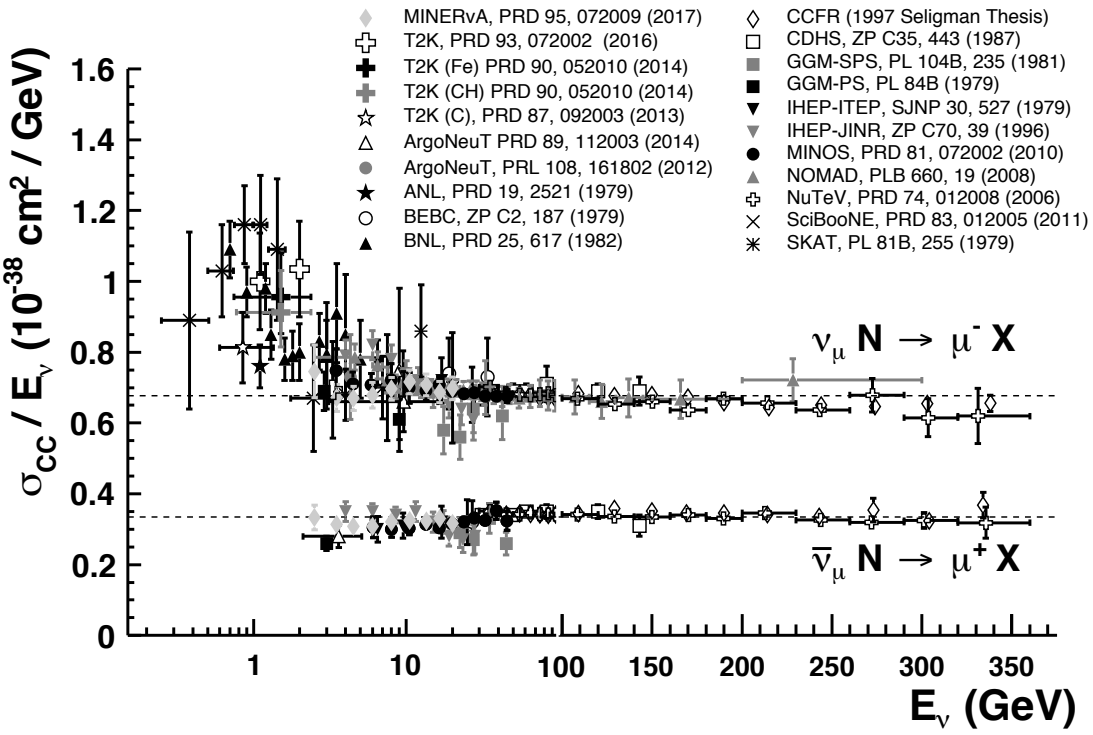

Figure 3.12: Measurements of per nucleon ν_μ and $\bar{\nu}_\mu$ CC inclusive scattering cross sections divided by neutrino energy as a function of neutrino energy. From [86].

function of muon momentum and angle, which allow to test generator predictions.

Chapter 4

The MicroBooNE Experiment

This chapter describes the technical details of the MicroBooNE experiment. Section 4.1 describes the primary beamline from which MicroBooNE receives neutrinos: the Booster Neutrino Beamline (BNB). Details of the MicroBooNE LArTPC detector are then shown in Section 4.2. A comprehension of how a LArTPC works is crucial for understanding the results of the data analysis described in later chapters. This specific detector technology gives rise to certain backgrounds which are relevant to MicroBooNE measurements and not for other experiments that use different detection techniques. Additionally, the knowledge of the neutrino beamline and the detector operation is precursory to the implementation of the neutrino flux and detector modelling uncertainties that affect the analysis presented in the next chapters. Sections 4.3, 4.4, 4.5 and 4.6 will describe details of the trigger, readout electronics, simulation and detector operations, respectively.

4.1 The Booster Neutrino Beamline

The neutrino beam received by the MicroBooNE experiment is produced at the Fermi National Accelerator Laboratory (Fermilab) thanks to the Fermilab

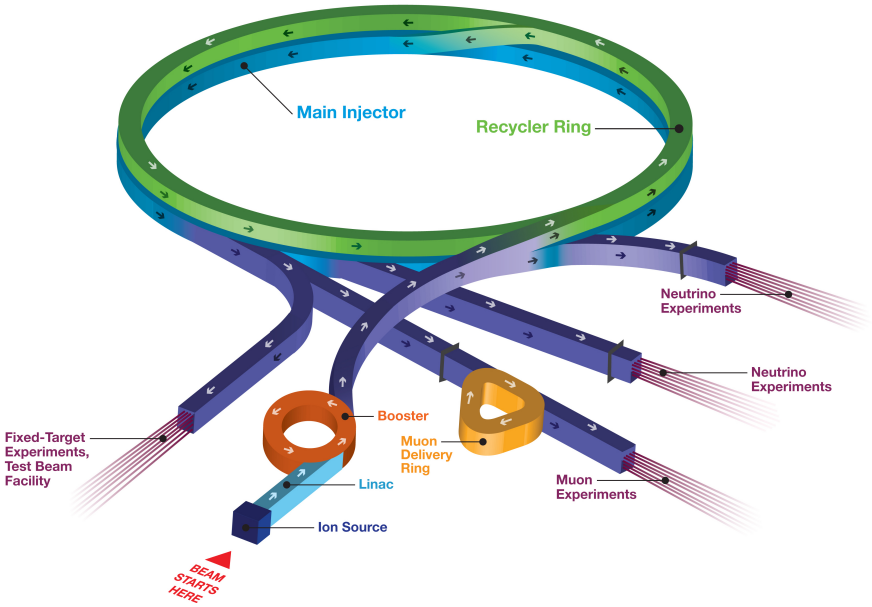

Figure 4.1: The Fermilab accelerator complex. Image source: [87].

accelerator complex. This complex, shown in Figure 4.1, is composed of four accelerators that work in tandem [87]: the linear accelerator (Linac), the Booster, the Recycler, and the Main Injector. These accelerators produce two primary proton beams, a low energy (8 GeV) proton beam from the Booster and a high-energy (120 GeV) beam from the Main Injector. Hitting a target, these proton beams produce secondary beams of pions, kaons, muons and neutrinos that serve a variety of experiments.

This section describes in some detail the production process of neutrinos through the BNB beamline. Three sections will describe the main stages involved: the production and extraction of an 8 GeV proton beam, in Section 4.1.1; the beam target and focusing horn which lead to a secondary meson beam, in Section 4.1.2; and the composition of the neutrino beam reaching the MicroBooNE detector, in Section 4.1.3.

4.1.1 Primary Proton Beam

The Booster proton beam starts as a beam of negatively charged hydrogen ions H^-. The H^- ions are subjected to a linear accelerator using alternating electromagnetic fields that accelerate them to 400 MeV kinetic energy [88]. Electrons are removed from the H^- ions through a carbon foil. The bare protons enter the 474-meter-circumference Booster synchrotron, which operates at a frequency of 15 Hz. Here, the protons are accelerated up to 8.89 GeV momentum. The protons are bunched in "beam spills" containing roughly 4×10^{12} protons spaced throughout a 1.6 μs time window per spill. The protons are then directed toward a thick beryllium target.

The absolute number of Protons on Target (POT) is measured by two toroids upstream of the target which are part of a larger beam monitoring system. The uncertainty on the POT is on the order of 2% [88]. Additional beam characteristics are monitored by beam position monitors, a multi-wire chamber, and a resistive wall monitor. This system measures beam intensity, timing, width, position, and direction of the proton beam.

4.1.2 Beam Target and Focusing Horn

The beryllium target hit by the protons is made up of seven identical cylindrical segments of beryllium, to produce a cylinder 71.1 cm long and 0.51 cm in radius. These are contained within a sleeve (1.37 cm inner radius, 0.9 cm thickness) also made of beryllium, which is connected to each segment via three beryllium fins. The volume of air within the sleeve is circulated to provide cooling for the target.

When the protons hit the target, secondary particles are produced, including pions and kaons, which represent the primary source of neutrinos and anti-neutrinos. To enhance the neutrino beam, these secondaries are focused by a toroidal electro-

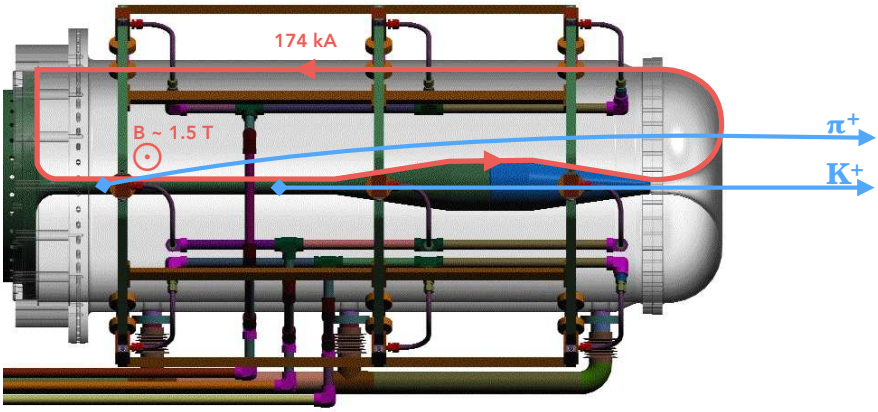

Figure 4.2: The pulsed horn system. The outer conductor (grey) is transparent to show the inner conductor components running along the centre (dark green and blue). The target assembly is inserted into the inner conductor from the left side. In neutrino-focusing mode, the (positive) current flows from left-to-right along the inner conductor, returning along the outer conductor. The plumbing associated with the water cooling system is also shown. Adapted from [88].

magnet (horn) placed around the target. Inside the horn, a toroidal magnetic field provides a restoring force for particles of a certain charge, and defocuses particles of the opposite charge, thus enhancing a ν_μ beam while reducing $\bar{\nu}_\mu$ background (or vice versa) originating from the decay of the secondary particles. The more focused the mesons are before the decay, the more focused will the neutrino beam be once it reaches the detector, enhancing the flux. The focusing horn is made of aluminium and is pulsed with a 174 kA current. A drawing of the horn structure is shown in Figure 4.2. The horn is 185 cm long and is composed of an inner and outer conducting cylinders. A positive current travels down the inner conductor, and arches back towards the front via the outer conductor, producing a magnetic field perpendicular to the beam direction within its volume and falls off as $1/r$. The inner conductor is placed just outside the beryllium target. Right outside the inner conductor, the strength of the magnetic field reaches 1.5 Tesla. Since the horn heats up due to the pulsed current and radiation, during running the inner conductor is being cooled with nozzles that spray water on it. The direction of the

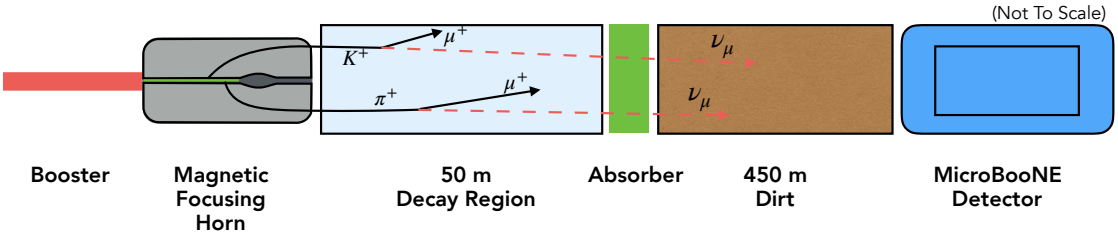

Figure 4.3: Schematic of the Booster Neutrino Beamline.

current can be switched to focus the positively charged secondaries (as shown in Figure 4.2), or the negatively charged secondaries, ultimately producing a beam primarily of neutrinos ("neutrino mode") or antineutrinos ("antineutrino mode"), respectively. The BNB beamline is schematically shown in Figure 4.3. The horn has a small field-free region, called the neck of the horn. The particles can pass through that region without being affected. The neck also allows the remaining proton beam to go through, without hitting the horn.

Focused charged pions and kaons travel through a 50-meter decay region: a cylindrical volume of air, in which pions and kaons decay, producing the tertiary neutrino beam which eventually reaches the detector. Remaining charged particles which have not yet decayed are blocked by an absorber made of concrete. The absorber stops the hadron component of the beam, while neutrinos and some of the muons pass through it. By this point, the beam is composed almost entirely of neutrinos which propagate through the dirt before reaching the detector.

4.1.3 Beam Composition

The analysis described in this thesis makes use of a data set collected when the horn was pulsed with a positive current, resulting in positively charged mesons being focused towards the beam axis, while negatively charged were deflected away. Pions are the most abundant particles produced in the target, and this results in

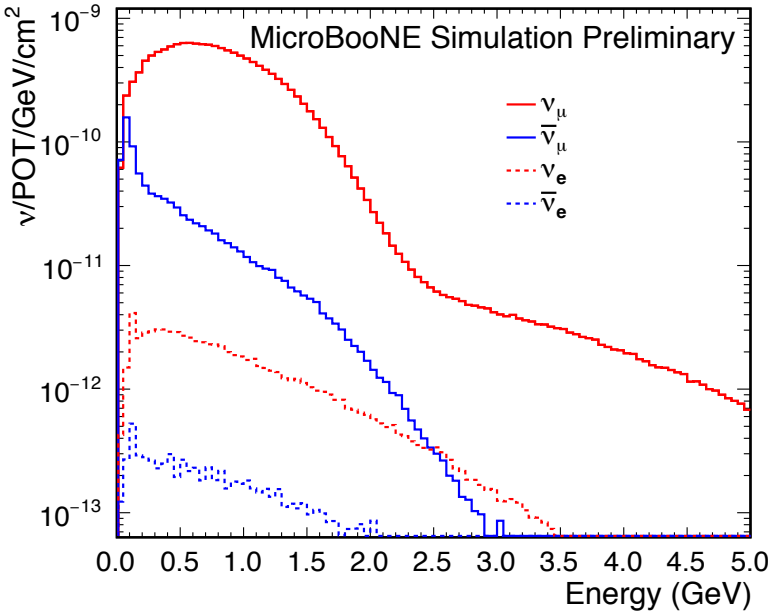

Figure 4.4: Neutrino flux prediction at MicroBooNE. Figure from [89].

a π^+ beam with a small contribution of K^+ and μ^+. In the decay region, these secondary particles are left free to decay. Pions predominantly decay in μ^+ and ν_μ, hence giving rise to the ν_μ beam. At the same time, contamination from other neutrino states in pion decay are caused by either $\bar{\nu}_\mu$ or by ν_e coming from the decay of muons ($\mu^+ \rightarrow e^+ + \bar{\nu}_\mu + \nu_e$). $\bar{\nu}_\mu$ also come from the contamination in the beam from μ^- which are very forward going or very energetic and therefore are not deflected by the horn.

Neutrinos produced by the decay of kaons ($K^\pm$, K^0, K^0_L) also contribute to the flux. Due to the smaller kaon production rate in the target this is a minor contribution to the total neutrino flux. Almost the entire flux of ν_μ with energy below 2.5 GeV is contributed by events which originate from pion decay, while kaons contribute almost exclusively to ν_μ beyond this energy. Most importantly, because of the broader range of decay channels, kaons contribute significantly to the ν_e flux, even at lower energies. A small fraction of $\bar{\nu}_e$ also arises from kaon decay.

In the end, the neutrino beam produced at the BNB is a 93.6% ν_μ beam, with a contamination of $\bar{\nu}_\mu$ (5.86%), ν_e (0.52%) and $\bar{\nu}_e$ (0.05%). Figure 4.4 shows the neutrino flux split in the contributions from the four neutrino states as modelled by the MiniBooNE beam simulation [88] and calculated at the MicroBooNE detector.

4.2 The MicroBooNE Detector

The MicroBooNE detector is located along the BNB beamline, 470 m from the target. It is a 60 metric ton fiducial mass (170 metric ton total mass) LArTPC detector [90], contained within a cylindrical cryostat, where charged particles traversing a volume of highly-purified liquid argon leave trails of ionisation electrons along their paths, and also create prompt ultraviolet scintillation photons. Ionisation electrons drift in an electric field to a system of three anode wire planes. Waveforms originate from drift electrons inducing signals on the three wire planes, as shown in Figure 4.5. The MicroBooNE Time Projection Chamber (TPC) is described in Section 4.2.1. The scintillation photons are observed by PMTs located behind the wire planes, described in Section 4.2.3.

4.2.1 Time Projection Chamber

The TPC used in the MicroBooNE experiment, shown in Figure 4.6, is a rectangular parallelepiped with dimensions 2.3 m (height) × 2.6 m (width) × 10.4 m (length, along the beam direction). The coordinate system adopted is shown in Figure 4.7. The 8256 stainless steel sense wires forming the three anode planes have a plane-to-plane spacing of 3 mm, and the wires on each plane are separated with a 3 mm wire pitch. The wires are connected to application-specific integrated circuits (ASICs) which operate at a liquid argon temperature of 87 K. While crossing the

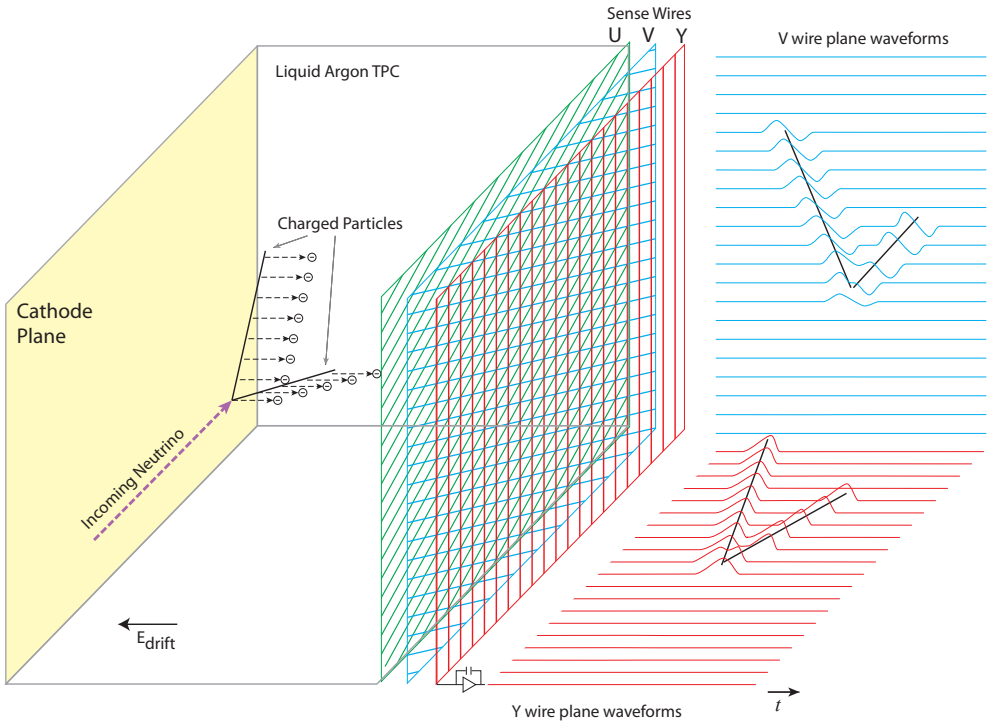

Figure 4.5: Operational principle of the MicroBooNE LArTPC. Ionisation electrons from particles traversing the detector medium are drifted by an electric field past multiple planes of sense wires. The signals on those wires create several two-dimensional images of the event and can be combined to obtain a three-dimensional view of the event. PMTs are also used to collect scintillation light, but are not drawn in this diagram. Image source: [90].

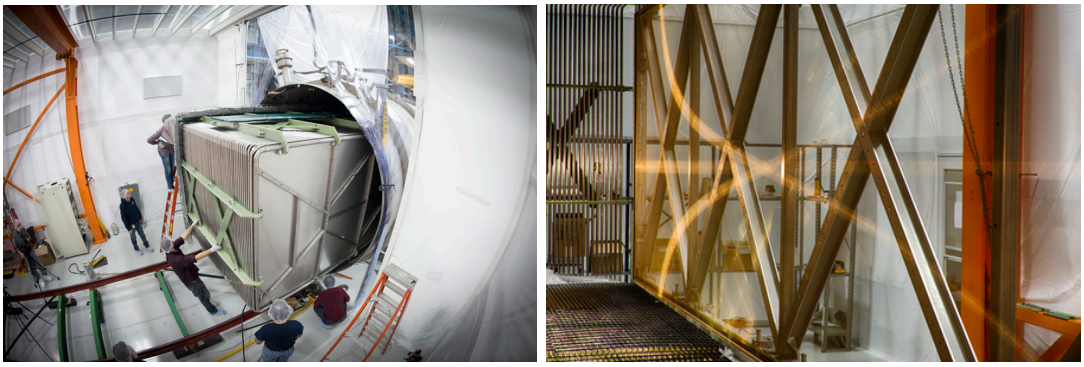

(a) (b)

Figure 4.6: The MicroBooNE TPC when it was inserted in the cryostat (a). The cathode is visible on the front right and the field cage, made of tubes, can also be seen. The inside the TPC (b). The three wire planes are visible along the anode on the right, and the field cage tubes at the back.

first two wire planes, consisting of 2400 wires at angles ±60 degrees relative to the vertical, the electrons induce a signal on them. Subsequently, the electrons are collected by the third plane, made of 3456 vertically-oriented wires. The electric field is created by a series of 64 2.54-cm diameter stainless steel pipes shaped into a rectangular loop, forming the field cage. The negatively charged cathode is held at a high voltage (operating voltage is 70 kV), and this voltage is incrementally stepped down across the field cage tubes with a voltage divider chain, with an equivalent resistance of 250 MΩ between each tube. The distance from centre-to-centre of adjacent field cage loops is 4 cm. This creates a uniform electric field within the LArTPC.

4.2.2 Charge Signal

Ionisation electrons produced in the TPC are detected as induced currents caused by their passage through sense-wires placed on the anode-plane. The same ionisation electrons will produce a signal on wires on all three planes since bias voltages are applied to ensure full transparency of the first two induction planes.

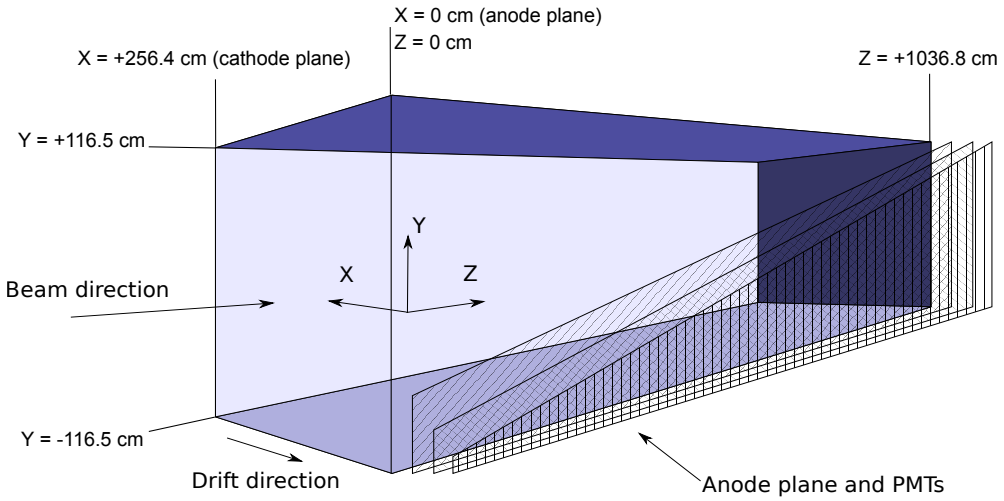

Figure 4.7: Drawing of the MicroBooNE's TPC. The TPC is placed with its longest side in the beam direction. The anode-plane on which wires where signals are formed is on the right-hand side, as seen from the beam. The cathode, where the drift high voltage is applied, is on the left.

As they pass by the first two wire-planes, electrons induce a bipolar signal. The signature on wires on the final plane, on which electrons are collected, is unipolar. Starting with a waveform from a single wire (Figure 4.8, step (a)), it is possible to visualise particles trajectories by displaying such waveform next to the waveforms from all the other wires, as done in steps (b) and (c) of Figure 4.8. This figure only shows part of the detector, where a ν_μ CC candidate vertex was identified. Figure 4.9 shows the complete candidate event, with the final state muon coming o a stop and decaying. In this figure, moving from the left to right, all the waveforms from the collection plane wires are displayed. For a single wire, the y axis shows the recorded waveform in drift-time coordinate. Particle trajectory points visible in the lower part of the image are closer to the anode plane, as it took less time for the electrons originated in those points to drift and be collected by the collection plane wires. The y axis in this figure can then be seen as the drift direction in the detector, while the x axis shows the direction along the neutrino beam, as collection plane wires are displaced perpendicularly to this direction. In summary, Figure 4.9

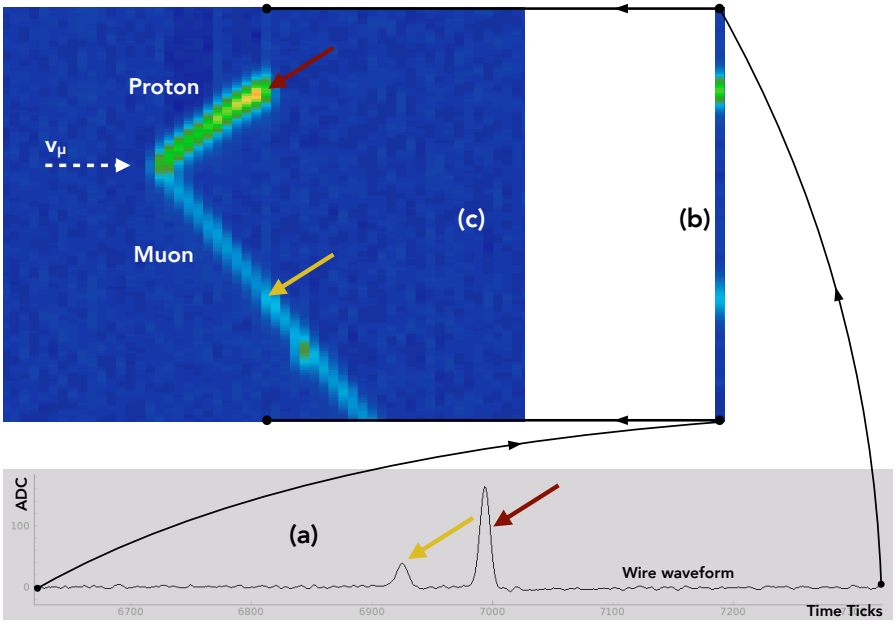

Figure 4.8: Figure (a) shows a waveform from a collection plane wire (after noise filtering [91]). Figures (b) and (c) shows how the MicroBooNE event display is constructed, by displaying waveforms from each wire one next to the other. The display shows a candidate interaction vertex from a ν_μ CC interaction, where the final state proton and muon are visible.

shows a bird-eye view of particles interacting in the MicroBooNE detector.

4.2.3 Light Collection System

Liquid argon is a bright scintillator, and sampling the light produced from interactions in the argon can bring powerful capabilities and information to complement the charge information. Scintillation light is produced by the formation and eventual radiative decay of excited argon dimers (or excimers) and is emitted in an isotropic distribution [92, 93]. Liquid argon produces a large amount of light per unit energy deposited (about 24,000 photons per MeV at 500 V/cm drift field) and is transparent to its own scintillation. The scintillation light has one prompt and one slow component with decay times of about 6 ns and 1.6 μs, respectively. Both components consist of photons with a wavelength of 128 nm (VUV). An example of

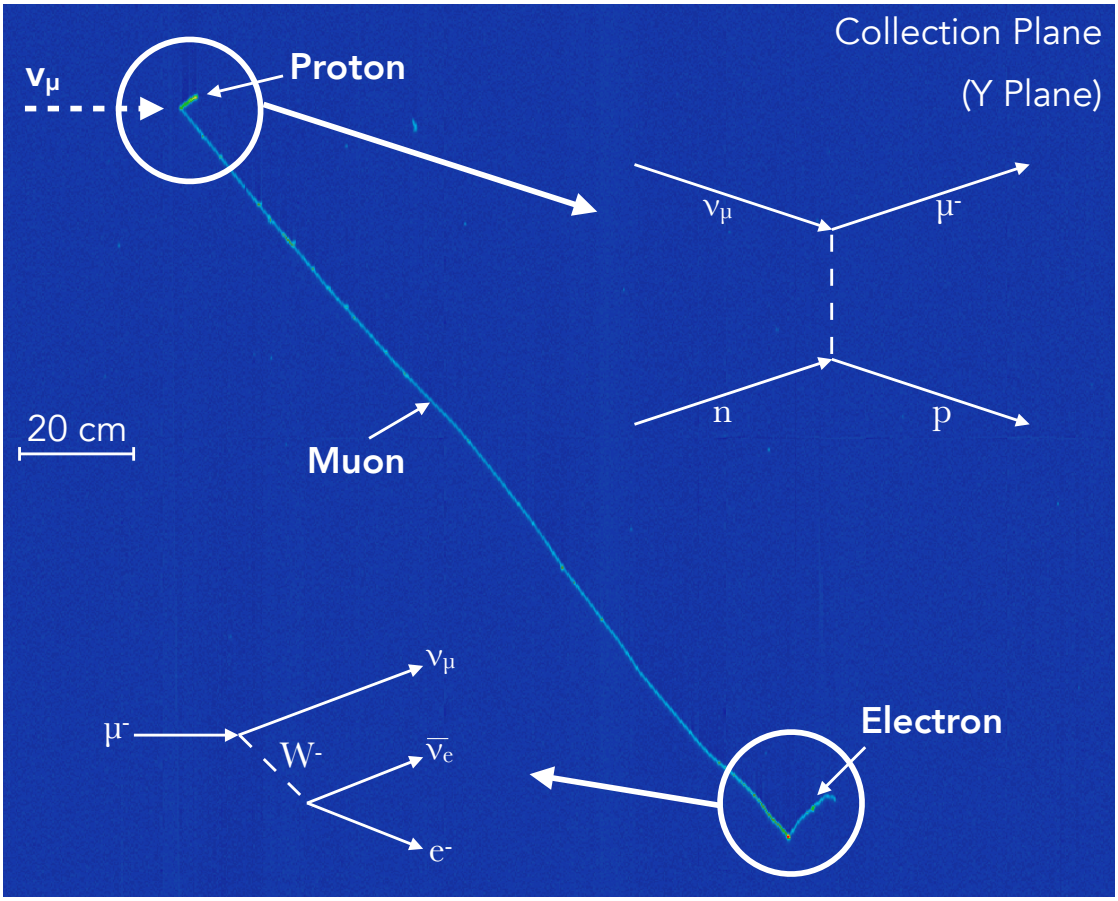

Figure 4.9: Event display showing raw data from a small region of the TPC volume from the collection plane. The display shows a candidate ν_μ CC interactions, where the final state proton and muon are visible. The x axis shows the collection plane wires (increasing wire-number from left to right) and the y axis shows the drift-coordinate (increasing drift-time moving upwards). The scale bar applies to both the horizontal and vertical coordinates. The colour map shows the amount of collected charge on each wire per time tick. In this display the muon candidate is spatially contained in the detector and it decays. The Michel electron coming from the decay is also visible.

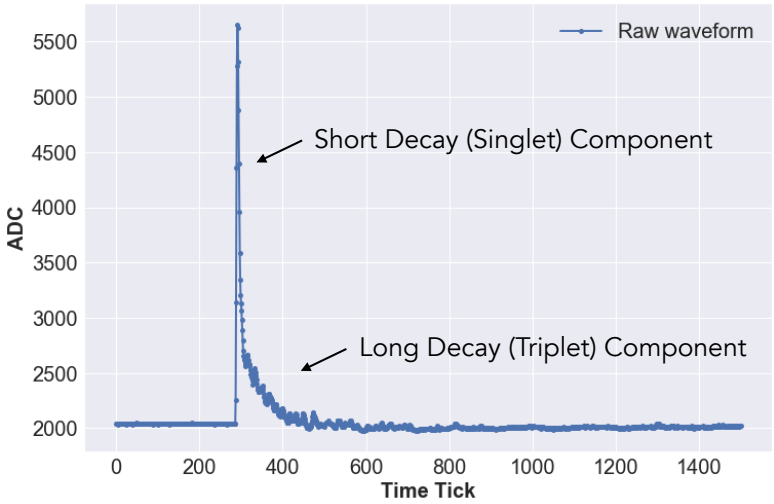

Figure 4.10: A waveform from a MicroBooNE optical detector from the PMT shaper (see Section 4.4). One time-tick corresponds to 15.6 ns.

raw waveform recorded by a single PMT in MicroBooNE from a candidate neutrino interaction is shown in Figure 4.10, where both the fast and slow components are visible.

Scintillation light is an important ingredient to the ultimate 3D reconstruction of particle interactions within a LArTPC. While the wire signals alone suffice to reconstruct 3D interactions, the absolute timing of an interaction (referred to as t_0) is unknown so there is ambiguity in the drift direction. However, measuring the scintillation light allows to clarify this ambiguity to high precision. In fact, the time scale of the production and propagation of the light (nanoseconds) is orders of magnitude faster than the ionisation electrons drift (milliseconds). Furthermore, the scintillation light from interactions is relatively localised, and therefore combining the measured PMT signals with the physical position of the signal allows to match individual flashes of light with different interactions, which may have different interaction times t_0. The description of this flash-to-track matching is provided in Section 5.5. This is important to help tagging and rejecting cosmogenic backgrounds which may occur outside of the expected beam neutrino arrival times.

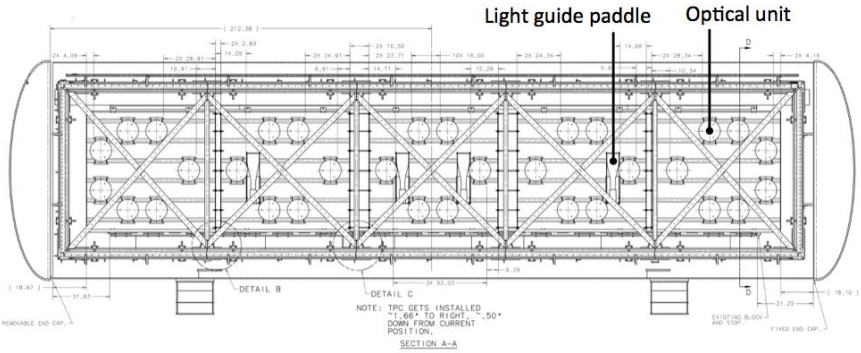

Figure 4.11: The MicroBooNE light collection system consists of a primary system of 32 optical units and a secondary optical system of four light guide paddles [94]. These are mounted behind the anode wire planes such that the view is not obscured by structural cross bars of the LArTPC. Image credit: [90].

The light collection system in MicroBooNE consists of 32 8-inch-diameter Hamamatsu R5912-02mod cryogenic PMTs. These PMTs are mounted in a plane behind the three sense-wire planes. The physical location of these PMTs is shown in Figure 4.11. These 32 PMTs provide 0.9% photocathode coverage. As shown in Figure 4.12, in front of each PMT an acrylic plate is mounted, coated with tetraphenyl-butadiene (TPB), an organic fluor which serves as a wavelength-shifting material. TPB absorbs the VUV scintillation light photons and re-emits it at visible wavelengths detectable by the PMTs, peaked at 425 nm.

4.3 Triggers and Data Streams

Every event in MicroBooNE starts with a hardware trigger. The Fermilab accelerator division sends signals to MicroBooNE every time there is a neutrino beam spill. This trigger, called the "BNB" trigger, causes a window to open the PMT readout that lasts for 23.4 μs, and a window in the TPC readout that lasts 4.8 ms. The beam trigger efficiency is 99.8% [95]. The data sample originating from the trigger is here called "beam-on" data sample.

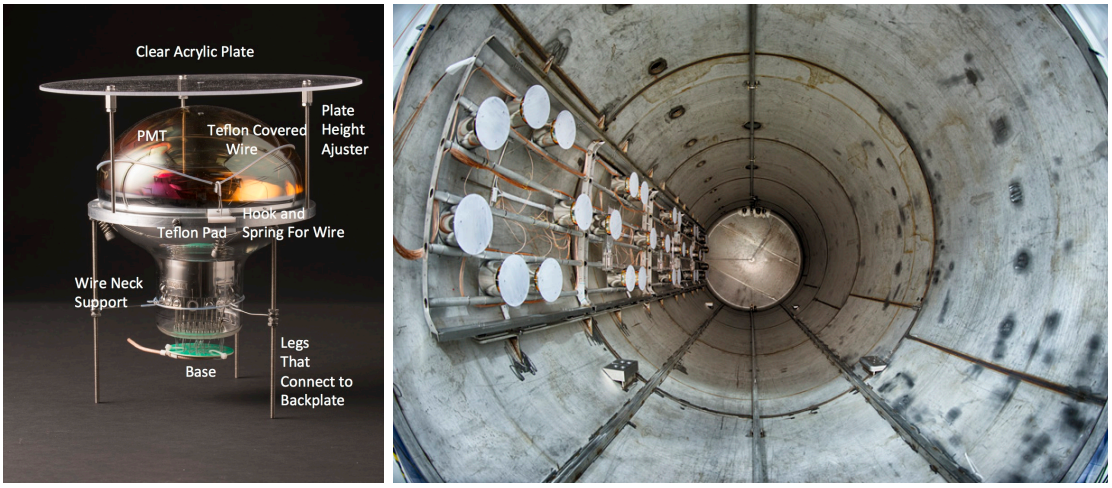

(a) (b)

Figure 4.12: The MicroBooNE optical unit mount internal to the shield, with components labeled (a). Photo credit: [90]. PMTs mounted on the frame inside the MicroBooNE cryostat (b). Photo credit: Reidar Hahn, Fermilab Visual Media Services.

The majority of the spills do not produce a neutrino interaction in the detector. Indeed, simulations show that approximately only 1 in 600 beam spills produces a neutrino interaction in the detector. In order to reduce the amount of recorded data, not every spill is saved. A software trigger looks at light activity on the PMTs in time-coincidence with the 1.6 μs beam spill reaching the detector. This activity may be caused by a neutrino interaction, coincident CR activity, or some other coincident sources. The software trigger reduces the data rate by a factor of 20 [95]. The signal efficiency loss through the trigger condition is negligibly small. Additionally, the trigger cut is superseded by a higher optical light deposition cut, later in the analysis.

An additional trigger used in this work is the so-called "EXT" trigger, that mimics a BNB trigger in the absence of neutrino beam. This trigger allows to record CR data in order to measure the cosmogenic background that will affect the analysis. The data sample collected with this trigger is here called "beam-off" data sample.

In order to reduce the data volume to apply TPC reconstruction algorithms to, an optical pre-filter is also run. This filter checks for optical activity within the time window of the beam and requires a minimum threshold of 20 Photo Electron (PE) in the beam time window (a study on the impact of a PE threshold on the analysis is described in Section 6.1).

The MicroBooNE simulation (described in Section 4.5), only includes simulation of events that contain neutrino interactions and does not contain events with only CRs. In order to be compared to the beam-on data sample, events from the beam-off data stream are added to the simulation, normalising by the number of hardware triggers. The event distributions presented in this thesis will either show simulation compared to beam-on minus beam-off data, or simulation plus beam-off data compared to beam-on data.

4.4 Readout Electronics and Data Format

MicroBooNE's readout electronics are responsible for forming, digitising, and recording signals associated with the TPC and PMT systems.

The MicroBooNE TPC electronics system is separated in "cold" electronics, submerged in liquid argon, and "warm" electronics, located outside of the cryostat. The cold electronics is responsible for amplifying and shaping signals produced on the sense wires. Performing these operations in a cold environment and in close proximity to the wires allows MicroBooNE to obtain a high signal-to-noise ratio, essential to obtain accurate particle identification with low detection thresholds. The warm electronics is responsible for digitising signals, compressing and formatting the data before it is sent to the data acquisition system.

The analogue signals from the 8256 sense wires in the TPC pass through Complementary Metal–Oxide–Semiconductor (CMOS) analogue front end ASICs

which operate on cold motherboards at liquid argon temperatures [90]. The signals are then shaped and amplified by cold intermediate amplifiers before passing through a warm feed-through. The signals are received by custom-designed LArTPC readout modules, which digitise and process them. The TPC wire signals are digitised at 16 MHz and then down-sampled in the digitisation process to 2 MHz (500 ns time-ticks). The TPC system reads out three 1.6 ms frames of wire signal data associated with one event. This time is chosen based on how long it takes for ionisation electrons from the cathode side of the TPC to drift to the anode wires (this time is 1.6 ms with the design drift field of 500 V/cm, but 2.3 ms with the current MicroBooNE drift field of 173 V/cm). One frame before and two frames after the trigger are collected, ensuring enough amount of data to identify a neutrino interaction, as well as all CR signals that arrive soon enough before or after the neutrino which need to be reconstructed in analyses.

Similarly to the TPC, the PMT signals undergo separate shaping with a 60 ns peaking time to allow for digitisation of several samples on the rising edge of a signal for more precise timing reconstruction abilities. The PMT signals are digitised at 64 MHz (15.625 ns time-ticks) and are then split into high-gain and low-gain channels which carry 18% and 1.8% of the total signal amplitude, respectively, to extend the dynamic range of the Analog-to-Digital Converter (ADC). The PMT system records data in two different formats: (*i*) in an unbiased way for a duration of 1500 samples (23.4 μs) which is opened by the beam-gate signal received on the trigger board. Neutrinos are expected to arrive $\sim$ 4 μs after this window is opened; (*ii*) in a discriminated way (called "cosmic discriminator") before and after the 23.4 μs window. This is needed in order to reduce the amount of recorded data. Discriminated waveforms are read out for an interval of 6.4 ms, which well covers the 4.8 ms TPC readout window: $[-1.6, +3.2]$ ms. The cosmic discriminator only

saves waveforms that go above a threshold of 130 ADC ($\sim$ 6.5 effective PE), and it only saves 40 samples ($\sim$ 0.6 μs). A dead-time of 45 samples follows every time a cosmic-discriminated waveform is recorded.

4.5 Simulation

Beamline and detector simulations are intended to represent truth level estimations of neutrino production and interaction processes. These estimations serve as a baseline for comparison with collected data, as well as to estimate the backgrounds in the selected data samples. They are referred to as Monte Carlo (MC) simulations. There are a number of systems to model, and details to account for, to ensure the simulation precisely captures the state of the detector.

The flux of neutrinos at the MicroBooNE detector is simulated using a framework built by the MiniBooNE collaboration [88]. Neutrino interactions in the MicroBooNE detector are simulated using the GENIE event generator [62], which generates the primary interaction inside the argon nucleus, the production of all final-state particles in the nucleus (hadronisation), and the transport and rescattering of the final-state particles through the nucleus (FSI).

Before proceeding with the detector simulation, there is one final step. MicroBooNE is a surface detector and is then subject to a high CR rate, and many CR muons cross the detector as shown in Figure 4.13. The detector is placed in a pit 6 m below the surface with no overburden, and the estimated rate is of 5.5 kHz, which corresponds to an average of 25 CR muons per recorded event. CRs are the dominant background in the analysis documented in this thesis, and this background is here divided into two categories, illustrated Figure 4.14:

- recorded events where no neutrino interacted in the detector (Figure 4.14a).

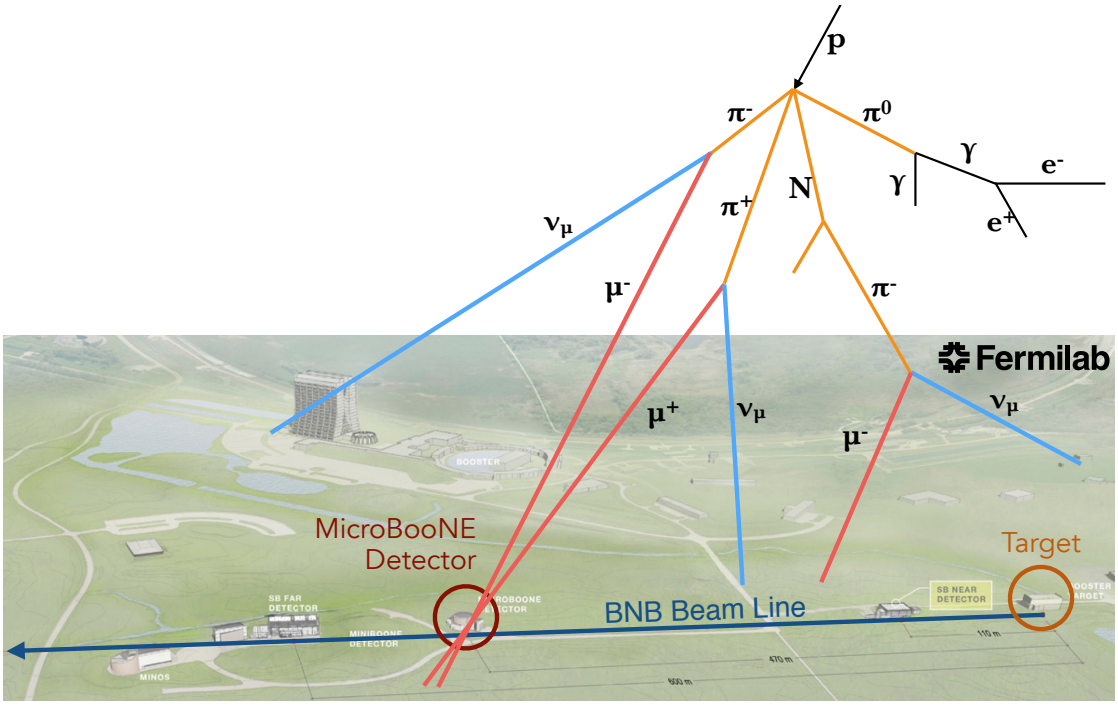

Figure 4.13: Aerial view of Fermilab with the Booster neutrino beamline and the MicroBooNE detector. CRs are the dominant background for many MicroBooNE data analyses.

These events can be estimated directly from data, by recording events when the neutrino beam is off. These events give rise to background events when one of the CR muons interacts in the 1.6 μs beam time window producing a flash that triggers the system, and its topology fakes a neutrino interaction;

- recorded events where one neutrino interacted in the detector (producing a flash that triggers the system) but a CR muon is instead selected (Figure 4.14b).

While the first background does not need to be simulated, as it can be estimated from data events when the neutrino beam is off, the second background needs to be simulated as a neutrino interaction is also present. This is done using the COsmic Ray Simulations for KAscade (CORSIKA) generator [96]. There are a variety of configurable parameters in CORSIKA including primary interaction particle type

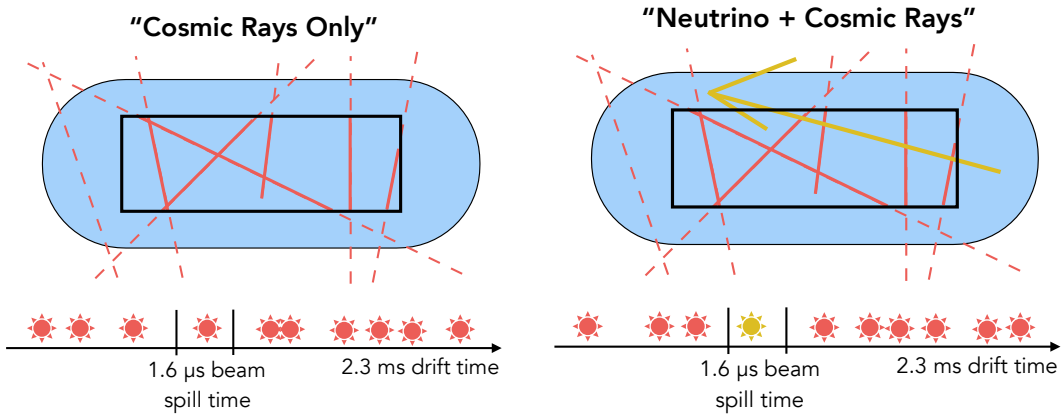

Figure 4.14: Examples of a "Cosmic Rays Only" event (a), where no neutrino interacted in the detector but one CRs muon interacts during the beam spill window, triggering the detector readout, and of a "Neutrino + Cosmic Rays" event (b), where a neutrino inetracts in the detector triggering the readout, but a CR muon can still be selected instead of the neutrino origin muon track.

and low-energy hadronic models that are explored in detail in a MicroBooNE public note [97]. After both neutrino and CR interactions have been simulated, the products of these interactions are ready to be tracked through the detector.

The simulation of the MicroBooNE detector is based on GEANT4 [98] and includes particle propagation, drift of ionisation electrons to the wire planes, as well as propagation of scintillation light to the PMTs. Ionisation due to CRs also leads to a distortion of the electric field within the detector. The effect is the build-up of slow-moving positive ions in a detector which gives rise to the so-called "space charge" effect [99]. This effect leads to a displacement in the reconstructed position of signal ionisation electrons, as well as variations in the amount of charge quenching experienced by ionisation throughout the volume of the TPC. The MicroBooNE detector simulation includes the space-charge effect. All simulation is carried out within the LArSoft framework [100].

The work documented in this thesis uses two different configurations of GENIE, summarised in Table 4.1. The first one, which is the baseline configuration used

Model element	Default GENIE + Emp. MEC	GENIE Alternative
Nuclear Model	Bodek-Ritchie Fermi Gas [101]	Local Fermi Gas [67, 68]
Quasi-Elastic	Llewellyn-Smith [47]	Nieves [67, 68]
Meson-Exchange Currents	Empirical [71]	Nieves [67, 68]
Resonant	Rein-Seghal [48]	Berger-Seghal [50]
Coherent	Rein-Seghal [48]	Berger-Seghal [50]
FSI	hA [52]	hA2014 [52]

Table 4.1: The two GENIE model sets used in the analysis presented in this thesis.

in MicroBooNE, uses the default GENIE configuration in which Fermi motion is described by the Bodek-Ritchie Fermi gas model [101], QE and resonant pion production interactions are modelled according to the Llewellyn-Smith [47] and the Rein-Seghal [48] models respectively, and an additional term is added that enhances QE-like interactions that occur off of correlated nucleon pairs via an empirically driven meson exchange current [71]. The second, alternative configuration, includes the Valencia model for QE interactions paired with a local Fermi gas model [67, 68] and Kuzmin-Lyubushkin-Naumov [102] and Berger-Sehgal model [50] for resonant pion production. The alternative configuration represents a theoretically driven set of models relevant at MicroBooNE energies.

4.6 Detector Operations

The MicroBooNE detector has been recording neutrino beam data since the fall of 2015. Figure 4.15 shows the amount of Protons on Target (POT) collected since the start of operations. The CC inclusive cross-section analysis presented in this thesis utilises 1.6×10^{20} POT of data (called "Run 1"), collected from February to October 2016. More recent data, not used for the analysis in this thesis, benefits from the installation of a CR tagger system [103].

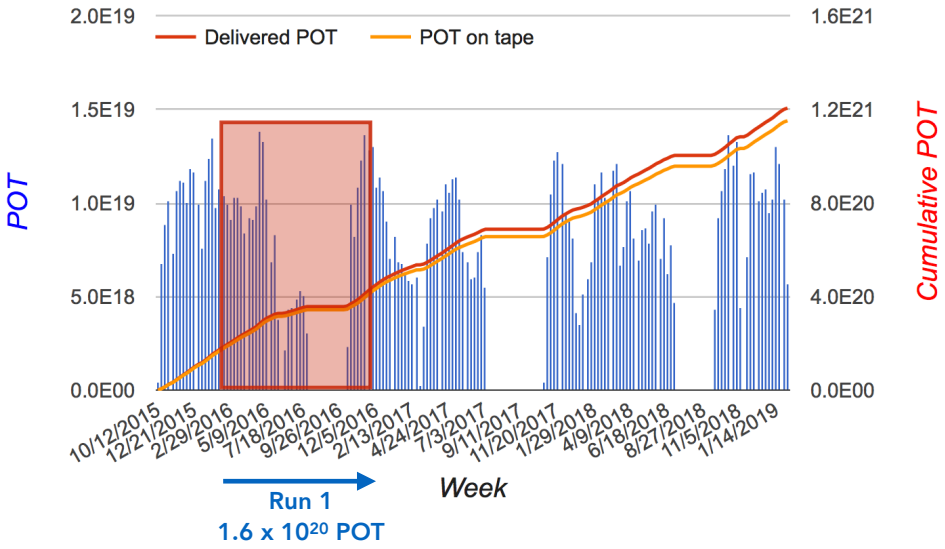

Figure 4.15: Protons on target over MicroBooNE's two year data-taking period. Highlighted in red is the period used for the cross section analysis presented in this thesis.

Chapter 5

Event Reconstruction

This chapter describes the TPC and optical reconstruction that is applied to all data events in order to go from the raw data recorded by the detector (as shown in the previous Chapter) to high-level reconstructed objects, like particles tracks and optical flashes of light, needed for the downstream analysis. Sections 5.1 and 5.2 describe the TPC and optical reconstruction respectively.

Section 5.3 shows techniques for mitigating CRs, the main background for many physics analyses at MicroBooNE. Section 5.4 describes how the TPC reconstruction of neutrino candidate events is done, and Section 5.5 shows how these TPC reconstructed objects are matched to optical information. Finally, Section 5.6 shows how the muon momentum is measured for the analysis in this thesis.

5.1 Optical Reconstruction

The optical reconstruction collects raw waveforms recorded by individual PMTs (as shown in Figure 4.10) and combines them to reconstruct "flashes", which represent optical activity in time across several PMTs, usually caused by a single neutrino or CR interaction in the TPC.

Signal Processing

The first step performed in the optical reconstruction consists in merging the high and low gain channels described in Section 4.4 into a "saturation-corrected" waveform which tries to correct saturating high-gain pulses by using information from the low-gain channel.

Baseline Estimation

The baseline estimation of the waveform is performed in two different ways depending on whether the waveform is coming from the cosmic or the beam discriminator, introduced in Section 4.4. If the waveform comes from the cosmic discriminator, a constant value is used for the baseline, which is simply set to the first ADC value in the first recorded sample. If the waveform comes from the beam discriminator, a more complex algorithm is used. A loop is done over all the waveform ADC recorded values, and the Standard Deviation (STD) of neighbouring values is calculated. If the STD is low, it shows that there is no optical activity in that region. In such regions, the baseline is set to the same waveform ADC values. A loop along the waveform entries is done and, where a region with high STD is found, the baseline is estimated by doing a linear interpolation between the two low-STD adjacent regions. This procedure takes care of estimating the right baseline if there are fluctuations. An example of a waveform with the estimated baseline is shown in Figure 5.1.

Pulse Finding and Flash Reconstruction

Once the baseline is determined, an algorithm that looks at the waveform ADCs going above a configurable threshold is run, in order to find pulses. Then, the flash reconstruction takes the identified pulses associated to each PMT as input. The

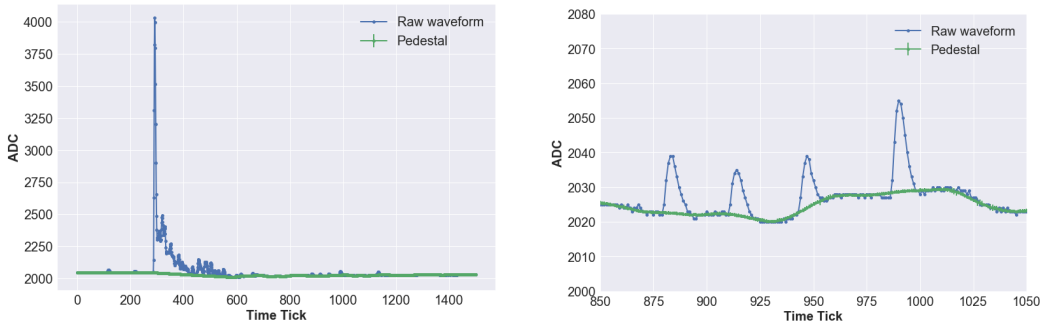

(a) (b)

Figure 5.1: An example of PMT raw waveform from data in blue and the estimated baseline in green (a), and an enlargement of the waveform to show single PE peaks (b).

time range is divided into configurable intervals and pulses falling in the same time interval are identified. Once coincident pulses are found, an integration window of 8 μs is applied in order to collect all the late light. To avoid that another flash is claimed by coincident late light pulses, an 8 μs dead time window is also applied. In the case of two candidate flashes with a time difference smaller than 8 μs, only the one that deposits more PE is saved.

The most interesting flashes are those happening during the 1.6 μs beam spill window, as the majority of them are induced by neutrino interactions. It is not possible to have multiple reconstructed flashes in that time window. In fact, it is smaller than 8 μs dead time window described above. In the case of more than one neutrino interactions or neutrino interactions with one or more CRs happening during the beam spill window, two scenarios are possible. For simplicity, let's assume there are two interactions happening during that time, then: (*i*) if the first interaction deposits less PEs than then second one, the pulses of the first will be ignored, and a flash will be claimed with the pulses of the second one (although late light pulses of the first may contaminate the second claimed pulse), (*ii*) if the first interaction deposits more PEs than the second one, then a flash will be claimed at the time of the first interaction, and the pulses of the second interaction

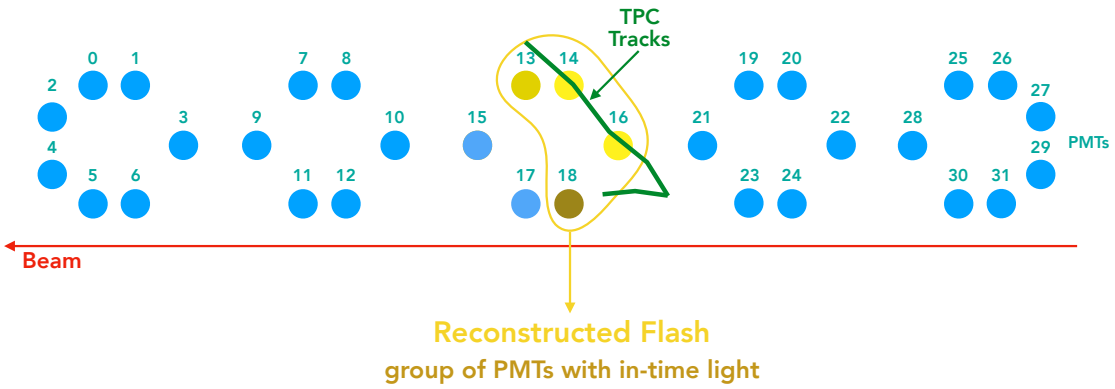

Figure 5.2: Schematic of flash reconstruction. The blue circles represent the MicroBooNE PMTs, and the red line an example of particle track in the detector. The yellow PMTs, that see light in time coincidence coming from the track, are clustered together to form a flash.

will be added to the first claimed pulse.

The flash reconstruction also performs a constant background subtraction of 2 PE per PMT to account for a measured 250 kHz noise, that is then integrated over the 8 μs flash time window. Figure 5.2 shows a sketch of the flash reconstruction.

5.2 TPC Reconstruction

This section briefly describes the reconstruction steps that lead to TPC reconstructed objects like tracks, showers and vertices.

The input data to the TPC reconstruction consists of waveforms in the drift time of charge induced or deposited on the sense wires. These waveforms first pass through a filtering algorithm in order to reduce the noise introduced by the electronics [91]. After noise filtering, an algorithms identifies candidate peaks in the waveforms by requiring that the waveform goes above a configurable threshold. The threshold is currently set at 5 times the RMS noise which is about 300 electrons/tick on average on the collection plane [104, 105]. Candidate peaks in the waveforms are then fitted with a Gaussian shape in order to obtain a "hit" representing the

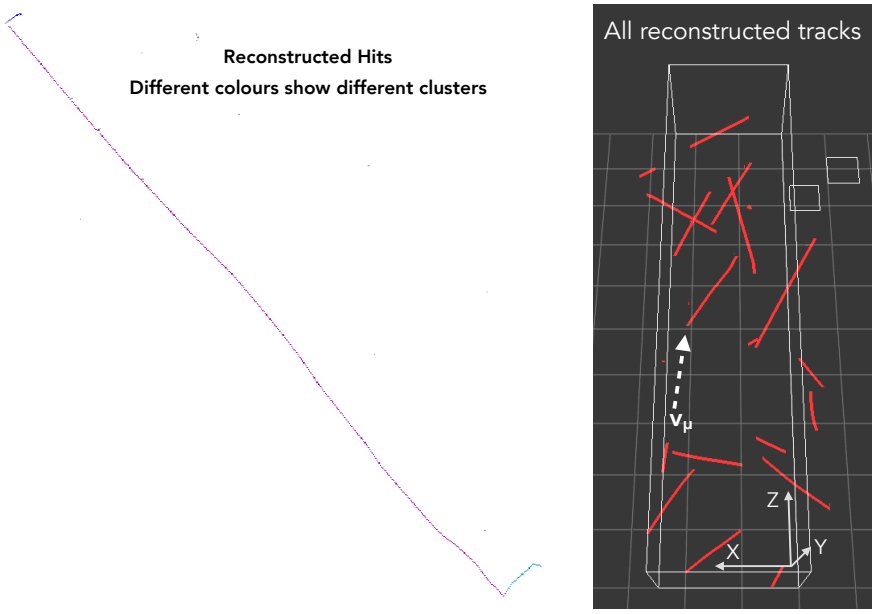

(a) (b)

Figure 5.3: Reconstructed hits and clusters (in different colours for different reconstructed particles) (a) from the raw waveforms displayed in Figure 4.9. Collection plane only. Figure (b) shows a full view of the MicroBooNE TPC with 3D reconstructed track. The event shown is the same as displayed in (a) but zoomed out to show the full detector. Most of the tracks are CR muons. Some tracks exit the detector in the x (drift) direction, as not yet corrected for the interaction time t_0.

charge deposited on a wire by an incident track. Hits are objects with a peak time and width and serve as the basic input to the reconstruction algorithms. Hits reconstructed from the waveforms displayed in Figure 4.9 are shown in Figure 5.3a.

Hits are then grouped into clusters. The purpose of the cluster algorithm is to group hits which correspond to the same particle signature, i.e. a track or a shower. MicroBooNE utilises the Pandora multi-algorithm pattern recognition framework, which handles the clustering of hits, as well as the reconstruction of 3D objects like tracks and showers [106]. The output of the Pandora multi-algorithm pattern recognition is structured in Particle Flow reconstructed particles, called "PFParticles" reconstructed particles, each one corresponding to a distinct track or shower, and their hierarchy, which identifies parent-daughter relationships and

describes the particle flow in the observed interactions. A neutrino is created as part of the hierarchy and forms the primary parent particle for a neutrino interaction. Figure 5.3b shows 3D reconstructed tracks in the full volume of the MicroBooNE detector.

LArTPCs also provide excellent calorimetric information. Calorimetry can be used to make a measurement of a particle energy deposition, which is useful to construct the particle identification (PID). Calorimetry is used in the analysis presented in this thesis to identify stopping CR background muons (see Section 5.3.4), and to distinguish muon candidate tracks from proton candidate tracks (see Section 6.3). It is possible to reconstruct a particle deposited energy per unit of length dE/dx from the waveforms induced by the ionisation electrons, such as the one in Figure 4.8(a). The area below the waveform is divided by the track segment that crosses that particular wire, in order to estimate the particle dQ/dx in ADC/cm. This variable is then calibrated in simulation and data using CR muons [107], so to obtain a dQ/dx in e^-/cm. Additional correction are also applied, that take into account electron lifetime and recombination [108]. In argon, the average energy expended per ion pair (W-value) is 23.6 eV, so that the number of electrons produced per MeV of deposited energy is approximately 42370 e^-/MeV. Using this relation, the particle deposited energy per unit of length dE/dx can be estimated.

The analysis does not make use of the particle dE/dx but uses a reconstructed truncated mean charge deposition along the length of the track $\langle dQ/dx \rangle_{\text{trunc}}$ in e^-/cm, shown in Figure 5.4 both for data and simulation. To calculate the truncated mean, the median m and the standard deviation σ of all the dQ/dx values per hit in the track are calculated. Hits with dQ/dx greater than $m - \sigma$ and smaller than $m + \sigma$ are then selected. Finally, the mean value of the dQ/dx of the selected hits is defined as truncated mean $\langle dQ/dx \rangle_{\text{trunc}}$. The truncated mean is used instead of the

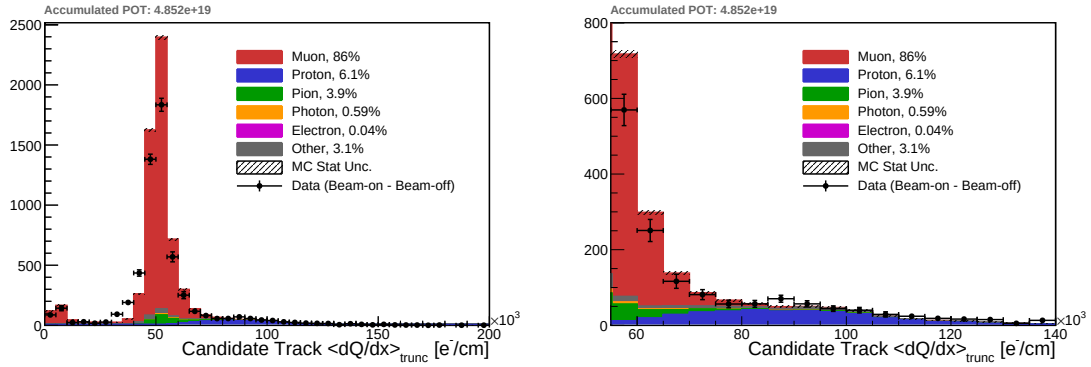

Figure 5.4: Distributions of the truncated mean $\langle dQ/dx \rangle_{\text{trunc}}$ for the muon candidate track (a). Black points are data points. The coloured histograms shows the simulation (stacked). Plot (b) is an enlargement of plot (a), showing that a proton track is selected as muon candidate for higher values of $\langle dQ/dx \rangle_{\text{trunc}}$.

mean or median of the full distribution because it is less sensitive to fluctuations. The truncated mean is obtained per plane, with only the collection plane being used in this analysis. The data and simulation entries at $\langle dQ/dx \rangle_{\text{trunc}} \sim 0$ are due to tracks aligned with the drift direction. In this case, all of the charges arrive on very few collection plane wires, and the hit reconstruction tends to assign this large charge deposition to many hits. This leads to some charge being missed "between" the fitted hits.

5.3 Cosmic Ray Removal

As described in Section 4.5, MicroBooNE is a surface detector and is then subject to constant exposure of cosmogenic radiation from the atmosphere. CR removal is therefore fundamental for any physics analysis.

Immediately after the reconstruction, the hits are passed to the Pandora framework that performs PFParticle reconstruction. Pandora is run in two different modes [106]:

Figure 5.5: Chart showing the steps to remove CRs before the data analysis takes place.

- `PandoraCosmic`, optimised for the reconstruction of CRs and their daughter delta rays;
- `PandoraNu`, optimised for the reconstruction of neutrino interactions.

Pandora is first run in `PandoraCosmic` mode over all reconstructed hits. The output reconstructed particles are analysed by a series of CR tagging algorithms described in the following sections. PFParticles identified as CRs are removed together with their daughter reconstructed particles, as well as their reconstructed hits. By default, `PandoraCosmic` reconstructs CRs as tracks and delta rays as showers. Removing all the hits of the daughter particles avoids leaving the delta ray debris laying around. If a PFParticle shares hits with another reconstructed particle which has not been tagged, the shared hits will not be removed. The remaining hits are passed again to the Pandora framework, which is now run with the `PandoraNu` configuration. The chart in Figure 5.5 shows all these steps. The next sections describe how the CR tagging is performed, while the rest of the analysis, performed with `PandoraNu` reconstructed objects, is described in the following chapters.

5.3.1 Cosmic Tagging Using Geometry and Timing

Tracks which are partially found to lie outside of the beam-spill drift window (before the trigger time and after the trigger time plus one drift length) are removed. These tracks must have entered the TPC at a time which is inconsistent with the trigger time.

CRs can also be identified if their track both enters and exits the TPC. A

Fiducial Volume (FV) contained in the active volume of the TPC within 30 cm from the top and the bottom of the TPC, 10 cm from the TPC borders along the drift direction, and 20 cm from the TPC ends, is defined. A track trajectory is considered to enter or exit the TPC if the track endpoints are outside the FV. The FV borders have been chosen after a dedicated optimisation giving the best CR background reduction. The 30 cm from the top and the bottom are needed to remove most of the CRs whose start and end points are mis-reconstructed and shifted due to space-charge effect. A smaller FV is used in the event selection described in Section 6.5).

5.3.2 Cosmic Tagging Using Optical Information

CRs can also be identified if they are not compatible with the flash reconstructed in the neutrino beam spill window. An algorithm looks at the compatibility between flashes and tracks. The algorithm first selects the flash in the 1.6 μs beam spill window, then takes all the PFParticles reconstructed by the `PandoraCosmic` algorithms and it simulates the associated light patterns expected on the PMTs, introducing a "flash hypothesis". Details on the light simulation will be provided in Section 5.5. The hypothesis flash centre Z_{flash} along the beam direction is calculated averaging the PMT positions of the PMTs that contribute to the flash, weighting for the PE simulated per PMT:

$$Z_{\text{flash}} = \langle Z \rangle = \left(\sum_{i=0}^{32} Z_{\text{PMT}_i} \times \text{PE}_i \right) / \sum_{i=0}^{32} \text{PE}_i. \tag{5.1}$$

Its uncertainty ΔZ_{flash} takes into account the variance of the PMT positions:

$$\Delta Z_{\text{flash}} = \sqrt{\text{Var}(Z)} = \sqrt{\langle Z^2 \rangle - \langle Z \rangle^2}, \tag{5.2}$$

where Z_{PMT_i} is the z coordinate of the i^{th} PMT and PE_i are the photoelectrons detected by that PMT for that particular flash.

If the PFParticle has neutrino origin and represents the whole neutrino interaction in the detector, the reconstructed and hypothesis flashes are expected to agree. If the PFParticle represents only part of the neutrino interaction, the hypothesis flash is expected to be smaller than the reconstructed flash. If the PFParticle has CR origin, the hypothesis and reconstructed flashes should disagree.

The PFParticle is tagged as CR if at least in one PMT the number of the reconstructed PEs (PE_{reco}) and the number of hypothesis PEs (PE_{hypo}) satisfy

$$\frac{PE_{\mathrm{hypo}} - PE_{\mathrm{reco}}}{\sqrt{PE_{\mathrm{hypo}}}} > 3, \tag{5.3}$$

meaning that the hypothesis is 3σ larger than the reconstructed one. In addition, to tag PFParticles as CRs, the z centre of the two flashes must satisfy

$$Z_{\mathrm{hypo}} \notin \left[Z_{\mathrm{reco}} - \Delta Z_{\mathrm{reco}}, Z_{\mathrm{reco}} + \Delta Z_{\mathrm{reco}}\right], \tag{5.4}$$

where Z_{reco} is the reconstructed beam flash. This last check has been added to ensure that neutrino related tracks are not tagged.

5.3.3 Cosmic Tagging Using Anode/Cathode Piercing Tracks

A different algorithm identifies CRs that pierce the two sides of the detector: the anode and the cathode planes. Because of the slow electron drift velocity, reconstructed track information along the drift-coordinate has an offset with respect to the true energy deposition location, as shown in Figure 5.6a. This offset can be corrected only if the time t_0 at which the track enters the detector volume is reconstructed. This section presents a method developed for reconstructing the

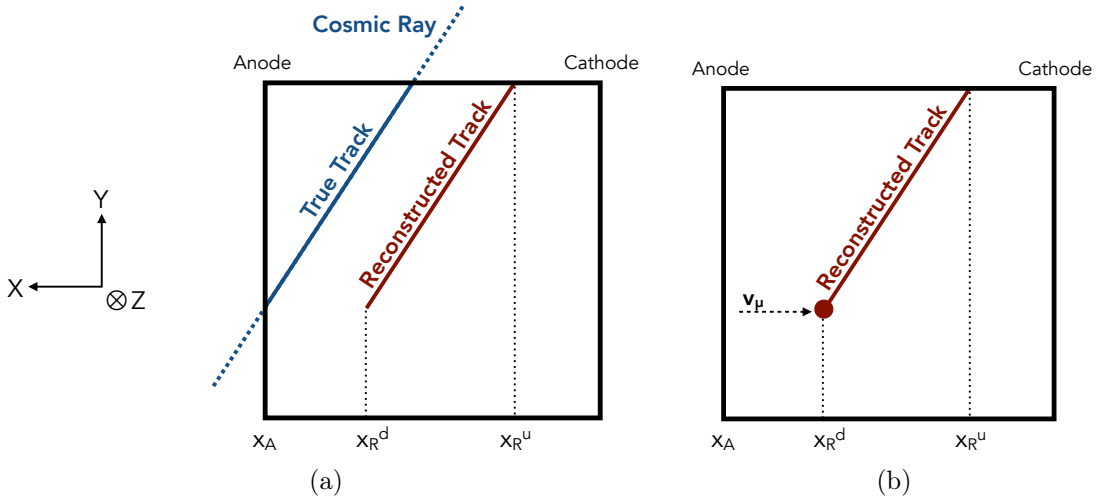

Figure 5.6: Reconstructed tracks need to be corrected for their time offset introduced by the finite velocity of the drifting electrons. In (a), a true CR track enters the detector from the top and exits from the anode plane, but the time offset makes the track look like it is stopping in the FV. In (b), a neutrino interacts in the detector producing a muon that exits from the top. The signature is similar to the CR in (a). In the neutrino case, the offset in the drift direction is small as the detector is triggered when the beam spill arrives.

t_0 of the track for the subset of CR tracks which pierce either the TPC anode- or cathode-plane: Anode or Cathode Piercing Track (ACPT).

The goal is to understand if the track is neutrino induced like in Figure 5.6b, actually originated in the detector and exited, or if it is a CR like in Figure 5.6a that exited from the sides of the TPC, and is shifted due to the slow electron drift velocity. To show how this algorithm works, the particular example illustrated in Figure 5.6a is used, and then generalised. The ACPT algorithm first assumes that the red reconstructed track is a CR. Under this assumption, given the track geometry in the detector, the track must have traversed the anode plane, and the time offset is given by $(x_A - x_R^d)/v_{\text{drift}}$, where $(x_A - x_R^d)$ is the difference between the anode and the last track point in x, and v_{drift} is the electron drift velocity. If this is a CR, a flash recorded with time $t_F = (x_A - x_R^d)/v_{\text{drift}}$ must exist. If such a flash is not found, the track is not a CR, but is neutrino induced. The algorithm

works in a similar way for tracks that enter from the anode and then exit, or if they cross the cathode. Additional checks are performed to ensure that the selected flash has a z centre compatible with the track position, and that the track is down going, as expected for a CR.

5.3.4 Cosmic Tagging of Stopping Muons

A residual CR background arises from CRs that enter and stop in the detector. Some of them are removed by the previous algorithms, but all of those that enter from the top surface or the front and back faces of the detector still remain. Stopping CRs constitute a relevant background because they are usually reconstructed as having the vertex in the FV, from which two reconstructed particles emerge: one being the muon, while the other being the Michel electron.

Stopping muons lead to two different kinds of processes with different topologies, namely *decay* and *absorption* by a neighbouring nucleus. The two kinds of events are easily distinguishable by the presence or absence of an electron/positron track from the decay of the muon. The probability of each of these processes to happen depends on the muon charge sign [109, 110, 111]. Positive muons decay into a positron in 100% of the cases, whereas negative muons are absorbed in about 73% of the cases, and decay into an electron in the remaining cases.

Two distinct algorithms were developed to identify stopping CR muons, the first based on the identification of the ionisation Bragg peak and the Michel electron coming from the muon decay, here called "reconstructed hits method", the second based on Multiple Coulomb Scattering (MCS), here called "multiple Coulomb scattering method".

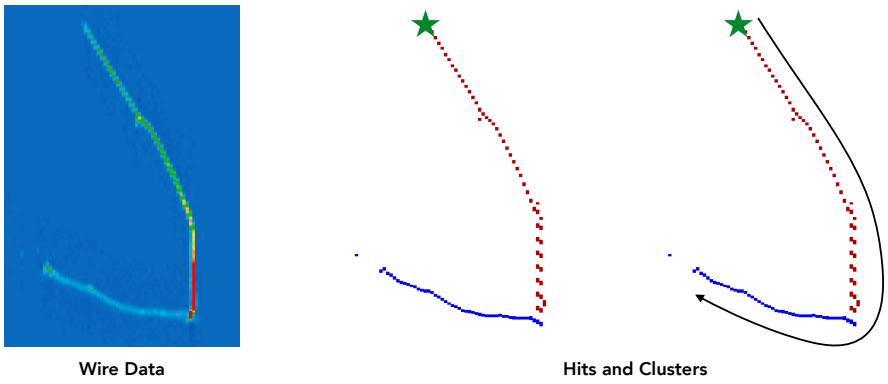

Figure 5.7: (left) Collection plane event display from data (run 5979, event 1467) for a CR muon stopping in the detector. The middle and right figures shows the reconstructed hits (squares) and the clusters from the muon (red) and the electron (blue) made by `PandoraCosmic`. The algorithm first finds the start of the muon (green star) and then orders all the hits (black arrow).

Reconstructed Hits Method

A two-dimensional reconstruction technique was developed to tag stopping CR muons based on the characteristic ionisation Bragg peak of a stopping muon, and/or the spatial kink produced by the outgoing Michel electron, in the case of muon decay. Figure 5.7(left) shows a data event display with a candidate CR muon that comes to a stop and decays. The Bragg peak is identifiable at the end of the muon by the high charge collected on the wires (in red). The kink at the end of the muon shows the separation between the muon and the Michel electron. The following describes the algorithms used to identify these CRs.

Start Hit Finder This algorithm finds the start hit of the cluster. Given the particle track, the upper point of it is taken and projected onto the collection plane. This will give an approximate start position $\tilde{\mathbf{h}}_s$ for the first hit in the cluster. The algorithm then looks at hits in the cluster that are close to this approximate start hit, to find a hit that is at the edge of the cluster. That hit will be the start hit of the cluster, $\mathbf{h_s}$. This is shown as a green star in Figure 5.7.

Hit Orderer This algorithm orders all the hits in the cluster based on their relative distance, starting with $\mathbf{h_s}$. The hits have to be below a certain distance to be ordered together; this is done to ensure that spurious hits due to the noise and delta rays are not considered in the final list of hits. In Figure 5.7 this is shown by the curved arrow.

dQ/dx Calculator This algorithm calculates the quantity dQ/dx hit by hit. For each hit that survived the previous algorithms, the charge dQ is estimated by taking the hit integral value and correcting it with gain calibration constants [107], as described in Section 5.2. The dQ is then divided by the distance dx between the hit and the next hit in the cluster. This dQ/dx gives an indication of how much energy was deposited by the particle per unit of length.

dQ/dx Smoother The quantity dE/dx of a particle is subject to large fluctuations, which in turn become fluctuations in dQ/dx. Delta ray emission also contributes to creating very large spikes in the dQ/dx distribution. This smoothing algorithm is applied to alleviate these fluctuations, in order to focus only on the overall particle dQ/dx, which should be increasing if the particle is coming to a stop. For every hit, this algorithm takes n neighbouring hits, removes the two with the highest and lowest dQ/dx values, and returns the dQ/dx median of the remaining $n-2$ hits. This will be the new dQ/dx value for that hit. The dQ/dx for the event in Figure 5.7 is shown in Figure 5.8a.

Local Linearity Calculator The goal of this last algorithm is to identify the kink point where the muon decays and the Michel electron is produced. For every hit, the algorithm takes five hits before and five hits after, for a

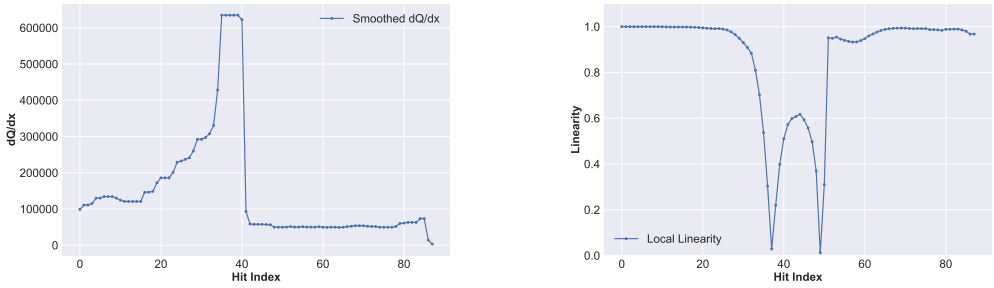

(a) (b)

Figure 5.8: The dQ/dx as a function of hit index (a) for the event shown in Figure 5.7. The dQ/dx increases in the Bragg peak region, and it goes down when the hits belong to the electron. Plot (b) shows the local linearity as a function of the hit index for the same event. The linearity is low in the Bragg peak region (kink).

total of 11 hits. Each of them have two coordinates, wire and time. These two coordinates are divided into two populations: 11 wire numbers $\mathbf{h_w}$, and 11 times $\mathbf{h_t}$. The coefficient of linear correlation between $\mathbf{h_w}$ and $\mathbf{h_t}$, defined as the ratio between the covariance of this two populations and the product of their STD, is calculated:

$$\text{Linearity}(\mathbf{h_w}, \mathbf{h_t}) = \frac{\sigma(\mathbf{h_w}, \mathbf{h_t})}{\sigma(\mathbf{h_w}) \times \sigma(\mathbf{h_t})}, \tag{5.5}$$

where $\sigma(\mathbf{h_w}, \mathbf{h_t})$ is the covariance, and $\sigma(\mathbf{h_w})$ the standard deviation.

After running all the previous algorithms and processing the clusters, a decision is made to understand if that cluster represents a CR muon stopping in the TPC. Two additional algorithms are run to check if the cluster represents a muon stopping and decaying to a Michel electron, or a muon stopping without decaying (absorption) or decaying producing a Michel electron with energy below detection. The two algorithms work in the following way:

StopMuMichel This algorithm first looks for the hit representing the final

Bragg peak, which is accomplished by taking the hit with the largest dQ/dx value. The algorithm then checks that this hit is in a region of low local linearity, indicating that we are in the presence of a kink. Finally, it calculates the average dQ/dx among n hits before the Bragg peak (muon hits) and after it (electron hits). If the muon is coming to a stop, the muon dQ/dx average should be larger than the electron one. The algorithm then checks that the dQ/dx average drops by at least 20% when going from the muon to the Michel electron. If so, the cluster is identified as CR.

StopMuBragg As well as the `StopMuMichel`, this algorithm first looks for the hit representing the final Bragg peak by taking the hit with the largest dQ/dx value. It then checks that the 3D start point (the track highest point) is outside the FV. If so, it checks that the local linearity never goes below threshold (configurable), indicating that no kink is present. Finally, it looks at the dQ/dx along the cluster and calculates the average dQ/dx among n hits at the beginning and at the end of the cluster. If the average dQ/dx increases by more than 30%, then the cluster, the track, and the PFParticle are all tagged as CRs.

Two examples of tracks tagged as CR stopping muons are shown in Figures 5.8 and 5.9.

Multiple Coulomb Scattering Method

Another way of tagging CR stopping muons is by looking at the scattering angle along the muon trajectory. In fact, the scattering angle increases as the particle momentum decreases and the muon comes to a stop.

The scattering can be parametrised in a MCS formula [112], which describes the particle scattering as a function of the particle momentum. The formula can be

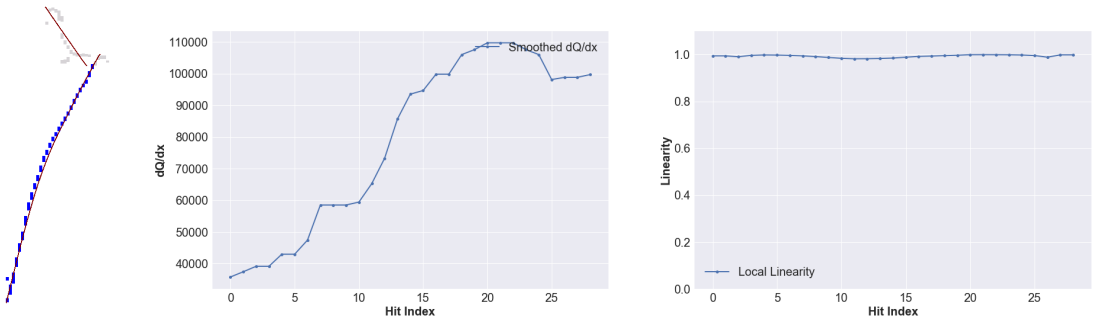

Figure 5.9: In this beam-off event (run: 6069, event: 2744), `PandoraCosmic` fails in reconstructing the CR as a whole object, but it divides it into two hierarchies, one for the muon and one for the Michel electron, which are then reconstructed as separate tracks. The algorithm is still able to tag this object as the dQ/dx increases as a function of the hit index, and local linearity stays flat.

used as a fit along both the forward and the backward direction of the reconstructed tracks. Both fits can be compared to understand the particle direction. Particles are expected to have an increased scattering angle as their momentum decreases and this method works well for stopping CR muons, rather than through-going CR, whose scattering angle is almost constant along their path. Assuming the track is a muon track and its highest y-coordinate is outside the FV, the track scattering is fit using the MCS formula in both directions. The fit (better described in Section 5.6) uses a log-likelihood approach. The MCS log-likelihoods obtained by fitting the MCS hypothesis to the track in the down going and up going direction respectively are here called LL_1 and LL_2 respectively. The difference between these two is considered:

$$\Delta LL = LL_1 - LL_2. \tag{5.6}$$

If the track belongs to a CR moun (or a neutrino induced particle where the neutrino interacted outside the TPC), ΔLL is expected to be negative.

The distribution of ΔLL is shown in Figure 5.10. Plot (a) is area normalised and shows the ΔLL distribution for neutrinos, CRs stopping and all the other CRs.

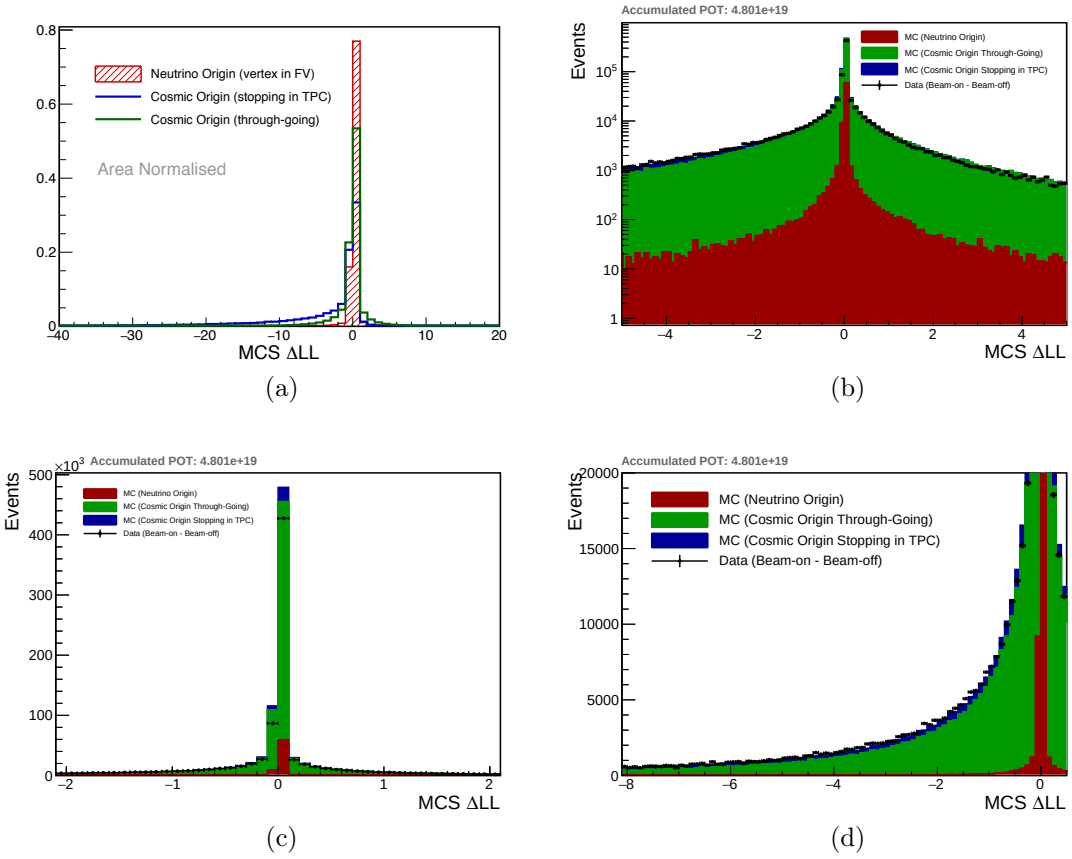

Figure 5.10: Plots show the difference between the MCS log-likelihood in the forward and backward direction applied to all reconstructed tracks. Plot (a) is area normalised and shows the ΔLL distribution for neutrinos (red), CRs stopping (blue) and all the other CRs (green). Plots (b), (c) and (d) show the same distribution, but this time POT normalised for both data (beam-on minus beam-off) and simulation. The bottom right plot is enlarged around the ΔLL cut value (-5).

ΔLL has a bigger negative tail for CR stopping muons, as expected. This allows to place a cut on this distribution to reduce the stopping CR muon background. Plots (b), (c) and (d) show the same distribution, but this time POT normalised for both data (beam-on minus beam-off) and simulation.

An optimal cut is found by maximising the score function $S/\sqrt{S+B}$, with S and B being the number of signal and background events respectively. The best cut is found to be at $\Delta LL = -5$, so that all tracks that have $\Delta LL < \Delta LL_{cut}$ are identified as CRs.

Tagger	% of ν-origin Particles Tagged
Geometry	2.37
Flash	0.31
ACPT	0.76
StopMu	6.46

Table 5.1: Percentage of neutrino induced particles tagged by the different tagging algorithms. The percentage is calculates as (number of events with neutrino induced particles tagged and with neutrino interacting in the FV)/(number of events that have at least one neutrino induced particle reconstructed and neutrino interacting in the FV).

5.3.5 Cosmic Tagging Performances

Table 5.1 shows the percentage of neutrino-induced particles tagged by the different CR tagging algorithms. This percentage is low for the flash and the ACPT tagger. It is around 2% for the geometrical tagger, and this is due to the fact that a misplaced track start or end-point may cause the track to look like it starts or ends outside the borders. This is not an issue, as the FV used in the event selection described in Section 6.5 is smaller than the one used for the CR tagging. The stopping muon tagger tags around 6% of the neutrinos. A closer examination of the tagged neutrino induced PFParticles from this algorithm shows that those are mainly mis-reconstructed tracks, that would not pass the track quality requirements described later in the event selection chapter.

5.4 Neutrino Reconstruction

The hits belonging to the CRs identified by the previous algorithms are removed from the data set and Pandora is run again but this time with the `PandoraNu` configuration. `PandoraNu` reconstruction identifies a neutrino interaction vertex and uses it to aid the reconstruction of all particles emerging from the vertex position. There is careful treatment to reconstruct tracks and showers. A parent

neutrino particle is created and the reconstructed visible particles are added as daughters of the neutrino.

Reconstruction of the neutrino interaction vertex begins with the creation of a list of possible vertex positions. A score is assigned to each vertex and only the one with the highest score is selected. The score is made by the product of three factors [106]: (*i*) the energy kick score, which creates a variable similar to the transverse energy and suppresses vertices with high scores since primary particles produced in the interaction should all point back towards the true interaction vertex; (*ii*) the asymmetry score, which suppresses candidates incorrectly placed along single, straight clusters, by counting the numbers of hits deemed upstream and downstream of the candidate position; (*iii*) the beam weighting score, which uses the beam direction and prefers vertices on the upstream side.

After vertex reconstruction, Pandora reconstructs tracks and showers and returns a list of reconstructed PFParticles. The final step in the `PandoraNu` reconstruction is to organise the reconstructed particles into a hierarchy. The primary particle is the neutrino PFParticle, which has no track nor shower associated but stores the neutrino candidate vertex. Any PFParticles deemed to be associated with the interaction vertex are added as primary daughters of the neutrino particle. Other particles, if exist, are added as daughter to the existing primary daughters of the neutrino PFParticle. Each hierarchy results in a single reconstructed neutrino particle, with the reconstructed daughter particles. More information is available in [106].

Figure 5.11 shows the muon reconstruction efficiency as a function of the muon true momentum after the CR removal. A muon is considered reconstructed if there is at least one PFParticle in the event that has been matched to the true muon. The plot is only made for muons from ν_μ CC interactions. The overall muon

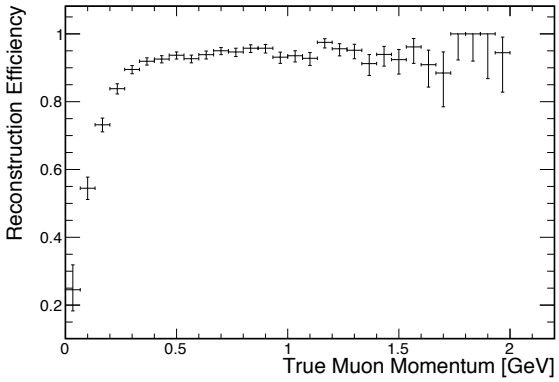

Figure 5.11: ν_μ CC induced muon reconstruction efficiency as a function of the true muon momentum. Only for muons from a ν_μ CC interaction happening in the FV.

reconstruction efficiency is 90%.

While the muon reconstruction efficiency only shows how often a muon is reconstructed, it does not give any information on the quality of the reconstruction. This can be studied by looking at the muon completeness and purity, defined as:

$$\begin{aligned} \text{Completeness} &= \frac{\text{true energy deposited by the muon in the reconstructed particle}}{\text{total true energy deposited by the muon}}, \\ \text{Purity} &= \frac{\text{true energy deposited by the muon in the reconstructed particle}}{\text{total true energy deposited in the reconstructed particle}}. \end{aligned} \tag{5.7}$$

These are shown in Figure 5.12. Figure (a) shows the muon completeness and Figure (b) the muon purity, both as a function of true muon momentum. These figures reflect the high quality of the reconstruction with peaks for the completeness around 85% and for the purity above 95%.

5.5 Flash Matching

The track-to-light matching or Flash Matching (FM) makes full use of the MicroBooNE optical detectors. The MicroBooNE PMTs were already used during

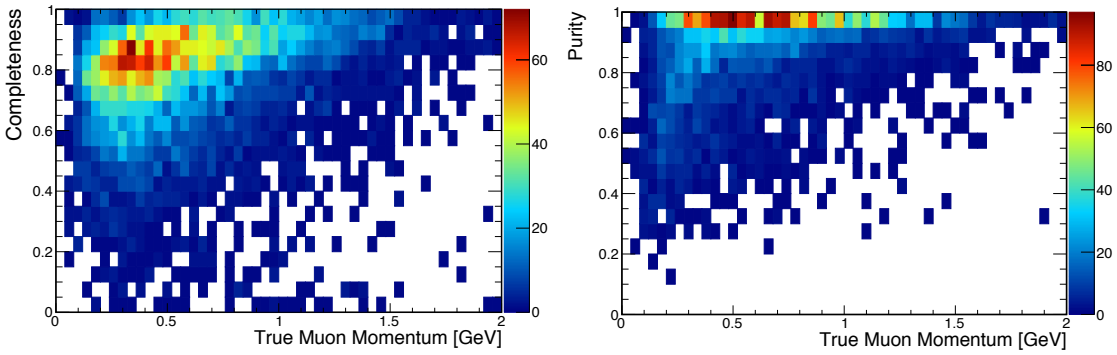

(a) Muon completeness (b) Muon purity

Figure 5.12: Figure (a) shows the muon track completeness, while Figure (b) shows the muon track purity for the neutrino induced muon. The plots include only muons from ν_μ CC interactions.

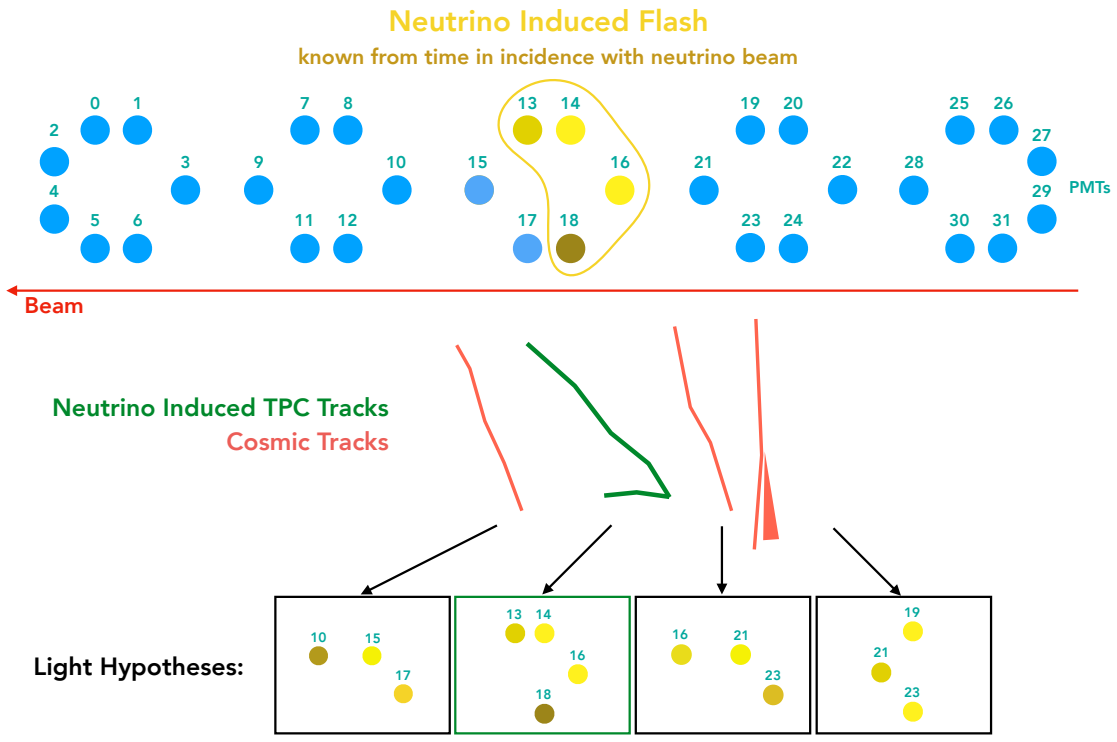

Figure 5.13: A schematic representation of the flash-to-track matching algorithm. The blue circles represent the MicroBooNE PMTs, while the yellow PMTs, that see light in time coincidence during the neutrino beam spill, are clustered together to form the flash originated by the neutrino interaction. The three red lines shows tracks created by CRs, while the green tracks are created by a neutrino interaction. The neutrino flash has to be matched with all the tracks (red and greed) in order to identify the neutrino origin tracks.

the CR tagging stage in Section 5.3.2, but here they are used to uniquely identify a neutrino interaction, by matching the reconstructed flash in the 1.6 μs beam window to a single Pandora-reconstructed neutrino candidate in the TPC that induced that flash. The probability of having two neutrino interactions in the same beam spill is negligible, and the FM has the goal to select one or zero Pandora-reconstructed neutrino candidates, in order to provide a neutrino enriched sample for the downstream analysis.

To accomplish this, the number of PEs per PMT are first simulated for every neutrino candidate in the TPC and then compared to the measured flash. The simulation that matches the best belongs to the neutrino candidate interaction that induced the measured flash. These light simulations are called "flash hypotheses". In the example shown in Figure 5.13, flash hypotheses are constructed for each of the four TPC objects, and then compared with the neutrino-induced flash in the yellow circle. Moreover, since the x position of the TPC tracks is unknown at this stage, the flash hypotheses are constructed for several x positions in the TPC.

Given a neutrino candidate, its track trajectory is first divided into small segments of length $l = 0.5$ cm. The flash hypothesis is then calculated by first looking at the deposited energy for each of these track segments, using the dE/dx for a Minimum Ionising Particle (MIP), currently a default of 2.07 MeV/cm, and assuming a light yield of $y = 29000$ photon/MeV [92, 93]. A Global Quantum Efficiency (GQE) factor is also considered. The GQE is the convolution of the efficiency of the acrylic+TPB plates that convert the 128 nm scintillation light from liquid argon to visible light, the efficiency of the shifted light to reach the photocathode, and the efficiency of the cryogenic PMT. This has been estimated for MicroBooNE using a similar procedure as described in [113], and amounts to $qe = 0.0093$. The solid angle covered by each PMT with respect to each track

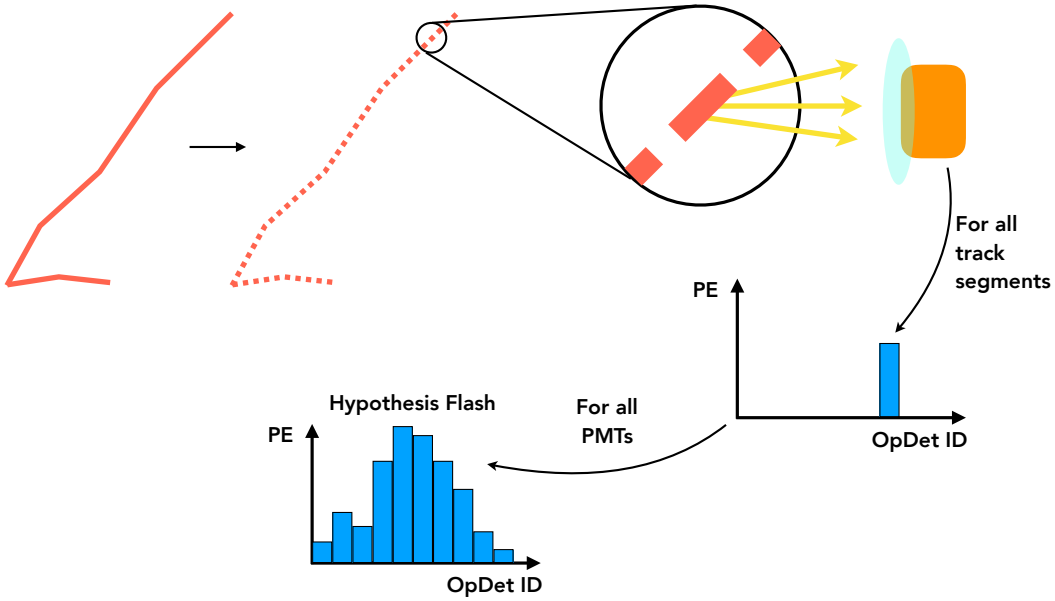

Figure 5.14: A schematic representation of the flash-to-track matching algorithm. A track is first divided into segments. The light that one PMT would see given scintillation created by a certain segment is calculated. The same procedure is repeated for all track segment, and then for all PMTs, in order to create an expected flash ("hypothesis flash").

segment is calculated, and the number of PEs in PMT i is given by:

$$H_i = \sum_{s=0}^{N} \left[l \times \left(\frac{dE}{dx} \right)_{\text{MIP}} \times y \times \text{vis}(s,i) \times qe \right] \tag{5.8}$$

where N is the number of track segments, l is the length of the segment, y is the light yield, $\text{vis}(s,i)$ is the visibility of segment s with respect to PMT i, and qe is the GQE factor. An example is shown in Figure 5.14. The same procedure is repeated for several positions along the TPC drift direction x, to have an hypothesis flash for several x positions: $H_i(x)$.

The flash hypothesis constructed for a neutrino candidate is compared to the reconstructed flash in time with the beam spill. Given a single candidate, the algorithm calculates the following likelihood between the observed and hypothetical

PMT PE spectra at several locations in the drift direction x:

$$-LL(x) = -\sum_{i=1}^{32} \ln\left(Poisson(O_i, H_i(x))\right), \tag{5.9}$$

where $H_i(x)$ is the PE hypothesis and O_i is the PE measurement for PMT i. *Poisson* is implemented by means of Euler's Gamma-function, and the ROOT Minuit MIGRAD algorithm is used to minimise the $-LL(x)$ function.

The $-LL(x_{\text{min}})$ value that is obtained after the minimisation, is used to discriminate the different neutrino candidate in an event: only the one with the smaller value of $-LL(x_{\text{min}})$ is kept for the downstream event selection (see next Chapter), the other neutrino candidates are rejected. An example of FM is shown in Figure 5.15 for MC, and Figure 5.16 for data. Here the measured flash (blue) is compared to the hypothesis flash (green).

The x_{min} position of the selected neutrino candidate estimated by the minimisation of the log likelihood is called $QLLx$. It is also possible to estimate x from the reconstructed time of the measured flash by subtracting $t_F \cdot v_{\text{drift}}$ to the reconstructed track position, where t_F is the time of the measured flash and v_{drift} is the drift velocity. This estimation of x is here called $TPCx$. $QLLx$ and $TPCx$ must agree if the measured flash was matched to the right neutrino candidate, and the next chapter shows how the quantity $QLLx - TPCx$ is used to further reject background.

5.5.1 Performances of the Flash Matching

The PE fractional difference PMT-by-PMT is used to quantify the FM performances:

$$\text{Fractional Difference} = \frac{PE_{\text{hypo}} - PE_{\text{meas}}}{(PE_{\text{hypo}} + PE_{\text{meas}})/2}, \tag{5.10}$$

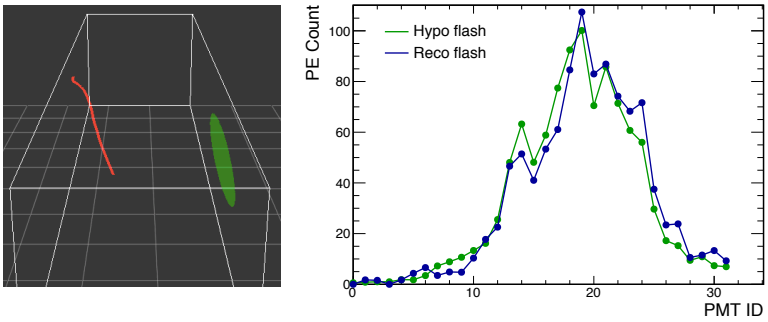

Figure 5.15: A Flash Matching example from MC. The left picture shows a simulated neutrino-induced reconstructed muon track (red) and the reconstructed flash (green). The white borders show the MicroBooNE TPC. The right plot shows the flash hypothesis (PEs per PMT) in green and the reconstructed flash in blue. The flash hypothesis well matches the measured flash. $QLLx$: 163.9 cm. $TPCx$: 165.8 cm. Score: 0.794.

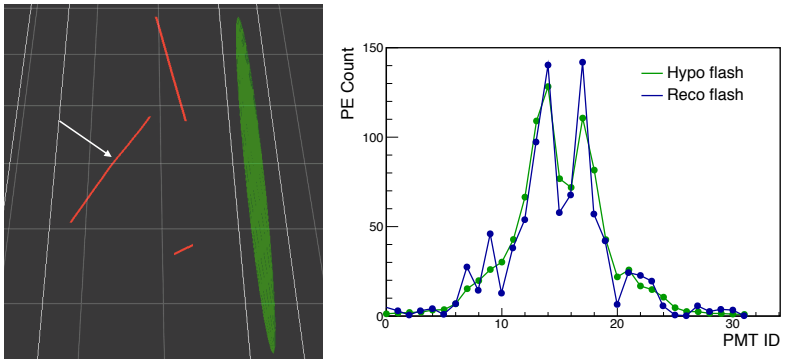

Figure 5.16: A Flash Matching example from data (run 5326 - event 900). The left picture shows a candidate neutrino-induced reconstructed muon track (red) and the reconstructed flash (green) from data. The white borders show the MicroBooNE TPC. The right plot shows the flash hypothesis (PEs per PMT) in green and the reconstructed flash in blue. The flash hypothesis well matches the measured flash. $QLLx$: 116.4 cm. $TPCx$: 112.2 cm. Score: 0.623.

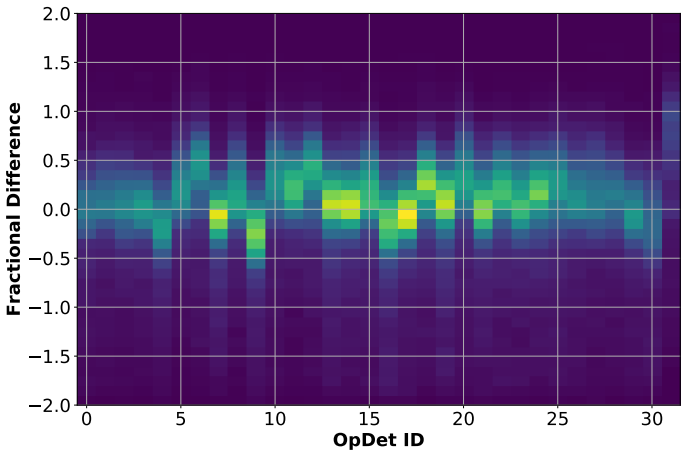

Figure 5.17: Fractional difference (as defined in Equation 5.10) between the simulated PE and reconstructed PE (y axis) and per MicroBooNE PMT (x axis).

where PE_{hypo} and PE_{meas} are the hypothesis and measured PEs for a given PMT. This definition ensures the fractional difference to be between -2 and 2, and so no overflow or underflow entries are present in the histograms. This quantity is shown in Figure 5.17 and indicates the variation between the observed PEs and the predicted PEs for each PMT. It was calculated taking all tracks that were ACPT tagged. Requiring ACPT tagging means that we are looking at tracks and flashes that have already been matched together. This plot is made running over events in the beam-off data stream.

The performances on MC can be seen in Figure 5.18, which shows the same fractional difference plot, this time made running the FM between the flash in the beam spill window and the neutrino candidates in the event. This has been further divided in neutrino origin candidates (5.18a) and all other candidates (5.18b). Neutrino candidates have fractional difference sharply distributed around zero, while there is a very big spread for all the other matches. The matches that are far away from zero usually have a very high $-LL$ and are discarded by the event selection. More details will be given in Chapter 6.

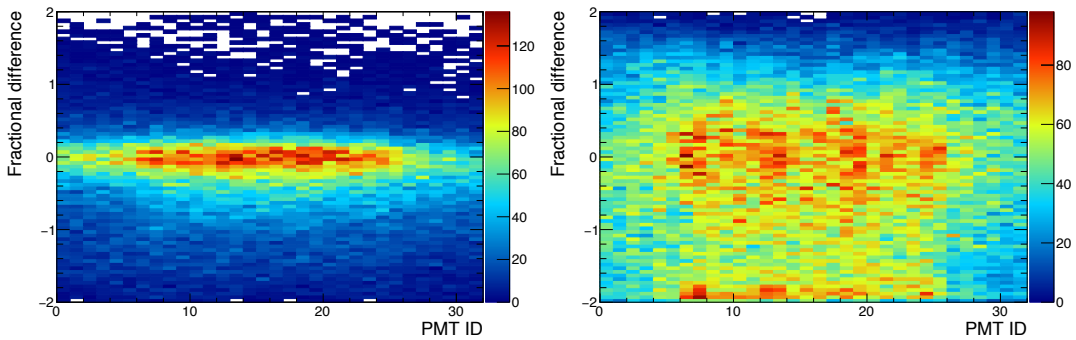

(a) For the good (neutrino) matches.

(b) For all the other matches.

Figure 5.18: Fractional difference (as defined in Equation 5.10) between the simulated PE and reconstructed PE (y axis) and per MicroBooNE PMT (x axis). Only for flash-matched interactions. Plot (a) shows only flashes matched to simulated neutrino interactions, while plot (b) to all other simulated interactions.

The flash matching is only used to identify the best candidate interaction. To understand if the impact of this choice is the same in both data and simulation, the score difference between the first and second best matched candidates for data and simulation are compared in Figure 5.19. The ratio between data and simulation is flat showing that the impact of this choice should be the same in both data and simulation.

5.6 Muon Momentum Reconstruction

In a LArTPC several techniques can be used to measure the muon momentum:

Momentum by Track Length The momentum p can be measured from the muon track length. The relationship between kinetic energy K and muon track length according to [114] is shown in Figure 5.20. The red line shows the interpolation used for this analysis. The particle momentum is obtain by $p = \sqrt{K^2 + 2mK}$ with m being the muon mass. This requires the track to be spatially contained in the TPC.

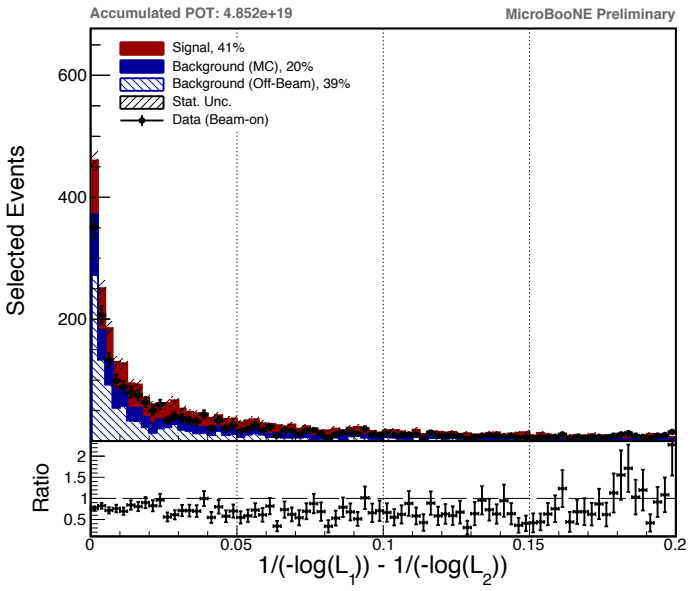

Figure 5.19: Flash matching score difference between the first and second best matched candidates.

Momentum by Calorimetry Information By looking at the deposited charge on the wires, the quantity dE/dx of a particle can be measured along the particle trajectory, and can then be integrated in x to get the energy of the particle, and so the momentum $p = \sqrt{E^2 - m^2}$. This requires the track to be spatially contained in the TPC.

Momentum by Multiple Coulomb Scattering The momentum can be estimated by looking at the amount of muon scatters in argon and comparing it to the theory, then retrieving the RMS of the scattering angle as a function of p [112]. This method is powerful as it can also be applied to muons exiting the TPC.

While the first and second methods can only be applied to tracks that are spatially contained in the detector, the last one can be applied to all tracks. Since a large fraction of muons will exit the detector at the BNB energies, it is important to not restrict the analysis to only contained muons. Momentum by MCS will,

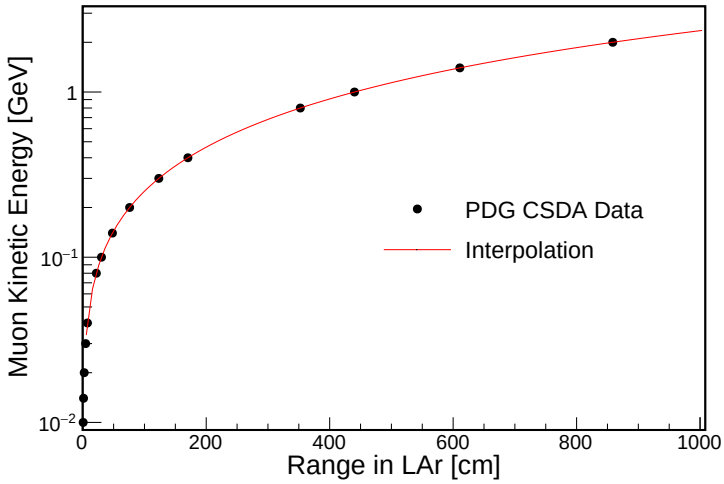

Figure 5.20: Muon kinetic energy vs. range in liquid argon according to the Particle Data Group data [114]. The red line shows the interpolation used for this analysis.

therefore, be used for the analysis in this thesis.

MCS occurs when a charged particle traverses a medium and undergoes electromagnetic scattering off atomic nuclei. This scattering perturbs the original trajectory of the particle within the material, as shown in Figure 5.21. For a given initial momentum p, the angular deflection scatters of a particle in either the x' direction or y' direction (indicated in the figure) are modelled with a Gaussian distribution centred at zero with an RMS width, σ_0^{HL}, given by the Highland formula [115, 116]

$$\sigma_0^{\mathrm{HL}} = \frac{S_2}{p\beta c} z \sqrt{\frac{l}{X_0}} \left[1 + \epsilon \times \ln\left(\frac{l}{X_0}\right) \right], \tag{5.11}$$

where β is the ratio of the particle's velocity to the speed of light (assuming the particle is a muon), l is the distance traveled inside the material, z is the magnitude of the charge of the particle (unity, for the case of muons), and X_0 is the radiation length of the target material (taken to be a constant 14 cm in liquid argon). S_2 and ϵ are parameters determined to be 13.6 MeV and 0.038, respectively.

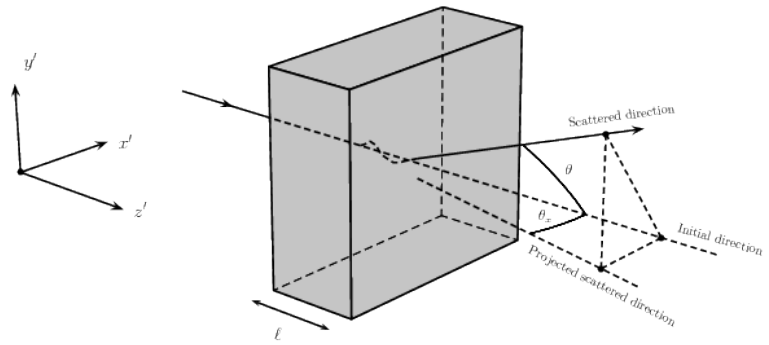

Figure 5.21: The particle's trajectory is deflected as it traverses the material. The angular scatter in the labeled x' direction is shown as θ_x. Image credit: [112].

At MicroBooNE, the S_2 parameter was tuned using a large sample of muons simulated with GEANT4. The result of the tuning, used as a replacement for the S_2 parameter in the Highland formula, is $\kappa(p) = 0.105\,\text{MeV}/(p\,(\text{GeV}))^2 + 11.004\,\text{MeV}$ [112]. Moreover, the Highland formula has been further modified to include a detector-inherent angular resolution term, σ_o^{res}, estimated to be 3 mrad from simulation. For a muon momentum of 4.5 GeV and $l \sim X_0$, Equation (5.11) predicts an RMS angular scatter of 3 mrad, comparable to the detector resolution. The muons studied in this thesis have momenta below 2.5 GeV, making the impact of this detector resolution minimal. In the end, this is the modified Highland formula used in this analysis:

$$\sigma_0 = \sqrt{(\sigma_0^{\text{HL, mod.}})^2 + (\sigma_0^{\text{res}})^2}, \qquad \sigma_0^{\text{HL, mod.}} = \frac{\kappa(p)}{p\beta c} z \sqrt{\frac{l}{X_0}} \left[1 + \epsilon \times \ln\left(\frac{l}{X_0}\right)\right]. \tag{5.12}$$

The MCS momentum is the result of a maximum likelihood method where the likelihood is taken to be the product over all track trajectory segments of the

probability of observing that scattering given the prediction [112]:

$$L(\sigma_{0,1}, \ldots, \sigma_{0,n}; \Delta\theta_1, \ldots, \Delta\theta_n) = \prod_i f(\sigma_{0,i}, \Delta\theta_i), \tag{5.13}$$

where the normal probability distribution with uncertainty σ_0 and mean zero is assumed to be

$$f(\sigma_0, \Delta\theta) = (2\pi\sigma_0^2)^{-1/2} \exp\left[-\frac{1}{2}\left(\frac{\Delta\theta}{\sigma_0}\right)\right]. \tag{5.14}$$

Equation (5.13) includes a $\sigma_{0,i}$ term that changes for consecutive segments because their associated energy is decreasing. The energy of the j^{th} segment is related to the postulated initial energy, E_t, by

$$E_j = E_t - \Delta E_j, \tag{5.15}$$

where ΔE_j is the energy loss upstream of this segment, computed by integrating the muon stopping power curve given by the Bethe-Bloch equation described by in [117] along the length of track upstream of this segment.

The value of the muon momentum that maximises the likelihood is taken as the muon momentum estimation. Figure 5.22 shows the reconstructed momentum as a function of the true momentum for two momentum reconstruction algorithms: MCS and track length. The momentum resolution using the MCS algorithm varies as a function of track length. For spatially contained muons, the resolution improves from about 10% for short tracks ($\sim$ 1 metre long) to 5% for longer (several metre) tracks. For exiting muons the resolution is less than 15%. The momentum resolution for contained tracks using the track-length approach is instead around 3%.

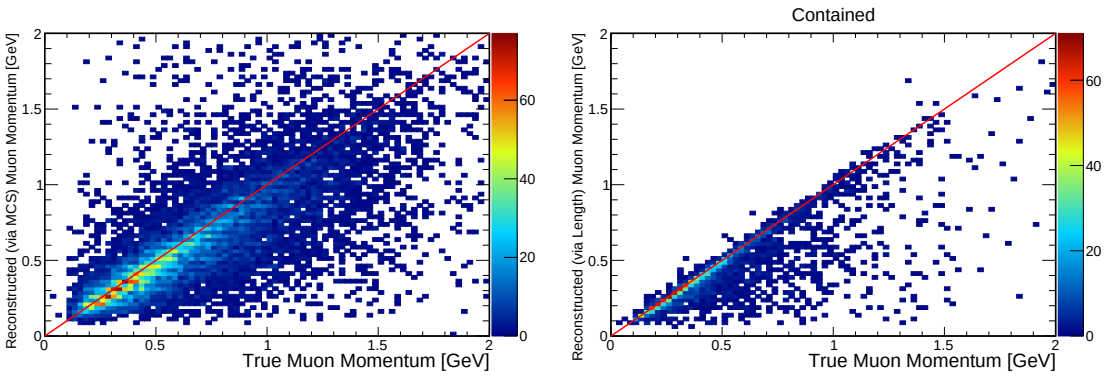

(a) (b)

Figure 5.22: Reconstructed momentum of the muon candidate tracks v.s. generated momentum for muons that are truly originating from neutrino interactions. Figure (a) shows the momentum estimated via MCS (for all tracks), and Figure (b) shows the momentum estimated via track length (only for contained tracks).

Chapter 6

Event Selection

This chapter describes the event selection applied to the data samples to reject background events, while keeping a significant number of selected ν_μ CC events. Since the probability of having two or more neutrino interactions per beam spill is small, the selection aims to select one or zero neutrino candidate interactions per event, together with the muon candidate track. The signal definition for this analysis is ν_μ CC, and all the distributions shown in this chapter that are labeled as "signal" show the distribution of ν_μ CC simulated events. The event selection, that acts on reconstructed variables, aims to get a ν_μ CC enriched sample by requiring at least one muon in the final state. An overview of the selection is shown in Figure 6.1. The selection starts by requiring optical activity in the beam spill window (Section 6.1). Then, all the reconstructed interactions in the event are collected and a flash matching between such interactions and the candidate neutrino flash is performed to select zero or one interaction per event (Section 6.2). In the events where one neutrino candidate is selected, the muon is identified (Section 6.3) and a series of quality cuts are applied to guarantee that the muon is well reconstructed (Sections 6.4). The interaction is then required to have the vertex inside the FV to be selected (Section 6.5). Finally, the selected event distributions

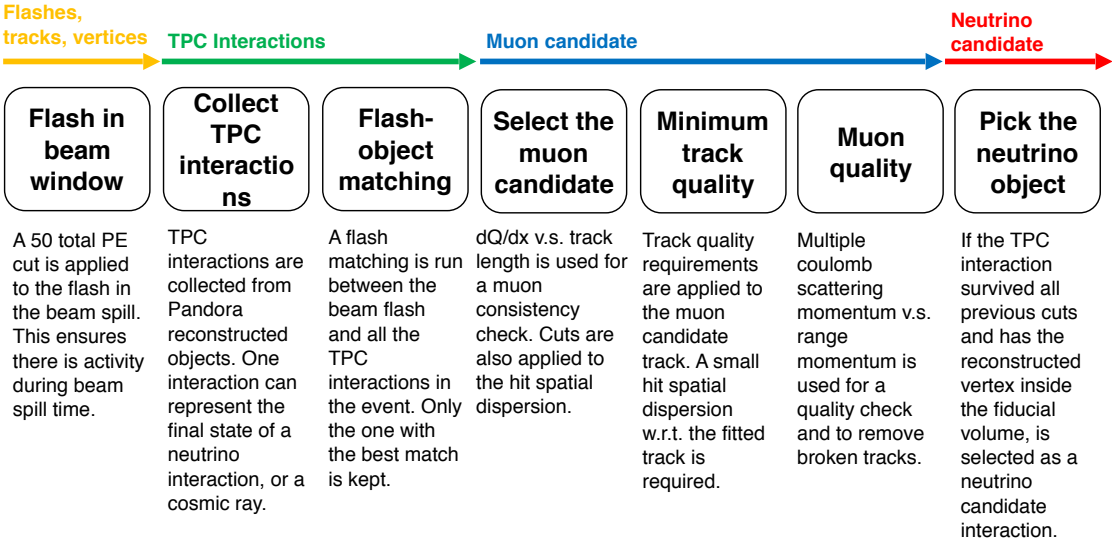

Figure 6.1: Overview of the event selection used in this analysis.

are shown in Section 6.6, and the event selection performances in Section 6.7.

6.1 Beam Spill Flash

The first step in the event selection is to remove events where no optical activities are detected in time with the neutrino beam spill. One reconstructed flash with more than 50 PE is required in the beam spill time window. The beam spill duration is 1.6 μs, and is extended to 1.8 μs to account for the beam timing jitter, which changes the start and end of the beam window by 0.1 μs on an event by event basis.

Figure 6.2a shows the total number of PEs per flash for flashes in the beam spill window. The enlarged plot in Figure 6.2b shows that signal events do not produce any flashes below 50 PE. This is also visible in Figure 6.3, where the signal efficiency as a function of cut applied on the total number of PEs is shown. The efficiency presents a plateau at low PEs, while drops above $\sim$ 80 PE.

Figure 6.4 shows the effect of the cut at 50 PE on the true neutrino energy

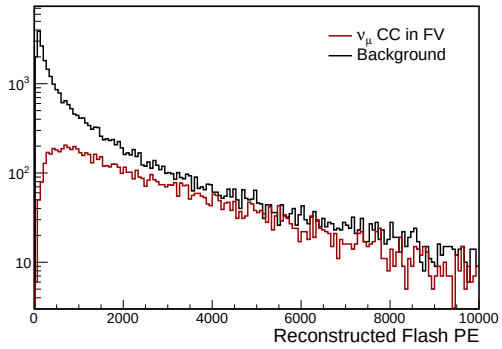

(a) Logarithmic Scale.

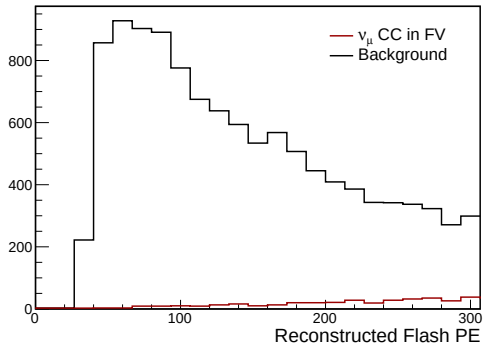

(b) Enlargement in the low PE region.

Figure 6.2: PE distributions of reconstructed flashes, for flashes in the 1.6 μs simulated beam spill time window (a). Red is for signal (ν_μ CC events), black for background (all other events). The plot in (b) is an enlargement in the low PE region.

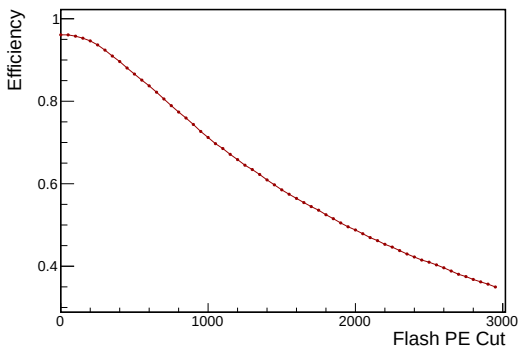

(a)

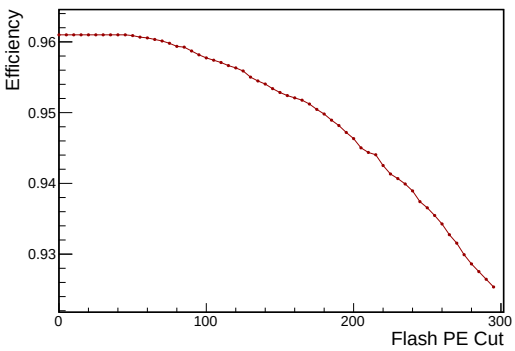

(b) Enlargement in the low PE region.

Figure 6.3: Efficiency of retaining signal events (ν_μ CC events) as a function of the cut applied on the total PE of the flash in the 1.6 μs beam spill (a). The plot in (b) is an enlargement in the low PE region.

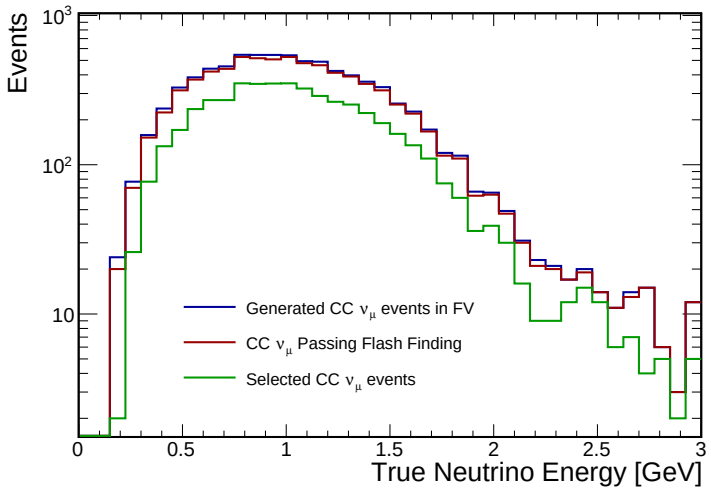

Figure 6.4: Neutrino energy distributions. The blue histogram shows the generated ν_μ CC events, while the red one shows it immediately after the 50 PE cut applied on the beam spill selected flash. For comparison, the green histogram shows the distribution of the final selected signal events.

distribution, estimated from simulations. A small number of neutrinos is lost after the cut is applied, while the energy spectrum remains unchanged in shape. For comparison, the energy distribution obtained for neutrinos passing the final selection is also shown.

6.2 Additional Flash-Matching Cuts

The FM algorithm, described in the Section 5.5, is run with the flash selected with the criterion introduced in the previous section. The neutrino candidate with the best FM score is selected by the algorithm, Two additional cuts are applied. The first is applied to the difference between the predicted x position ($QLLx$) of the candidate interaction reconstructed in the TPC and the x position estimated via the flash time ($TPCx$). The second is applied to the difference between the z position of the hypothesis flash and the z position of the reconstructed flash. The flash z position is calculated according to Equation (5.1). The distributions of these

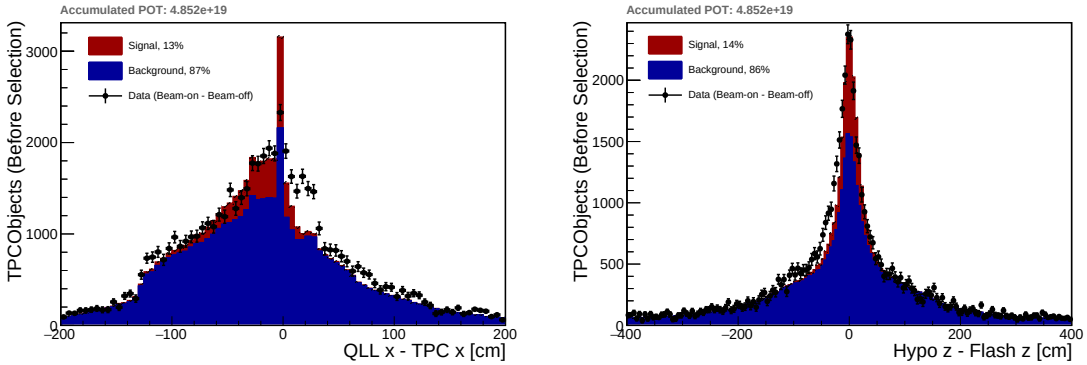

(a) (b)

Figure 6.5: The left figure shows the difference between the predicted x position and the x position estimated via the flash time. The right plot shows the difference between the z position of the hypothesis flash and the z position of the reconstructed flash. The beam-off data has been subtracted from the beam-on data to make this plot. The red distributions shows simulated signal events (ν_μ CC), while the blue ones show the background event (all other events).

quantities before the cut is applied are shown in Figure 6.5. Some disagreements between data and simulation are visible in both distributions. In the distribution of the difference in x, the data is more smeared than the simulation. To take this into account, a loose cut is applied: events pass this cut if they satisfy $-100 \leq QLLx - TPCx \leq 50$ cm. In the distribution of the difference in z, there is a small offset between data and simulation, this is taken into account with a loose cut such that events with $-75 \leq Z_{\text{hypo}} - Z_{\text{meas}} \leq 75$ cm are retained.

6.3 Muon Candidate Selection

Given a flash-matched interaction in the TPC, this interaction is assumed to represent a neutrino interaction in the detector. In order to select CC over NC interactions a muon candidate track has to be identified. In fact, a selected interaction usually contains multiple tracks as well as showers, because neutrino interactions can produce multiple particles in the final state.

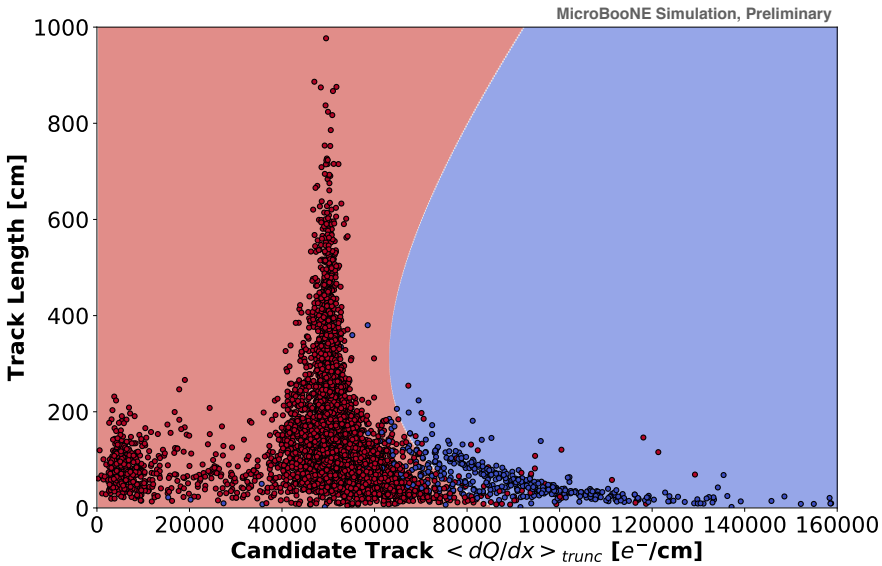

Figure 6.6: Simulated track length as a function of the track $\langle dQ/dx \rangle_{\text{trunc}}$ for the longest track in flash-matched interactions. Red dots are simulated muons, blue ones are simulated protons. The light red and blue regions show the output of the SVM classifier. If a track falls in the blue region, it will not be considered as a muon candidate.

Except rare cases where a pion or proton track is the longest among all final state particles, usually the muon candidate track is the longest one. Combining the track length with the particle $\langle dQ/dx \rangle_{\text{trunc}}$, as previously described in Section 5.2, allows a powerful discrimination between muons and protons. The distribution of $\langle dQ/dx \rangle_{\text{trunc}}$, previously shown in Figure 5.4, shows a good agreement between data and simulation in the proton region (Figure 5.4b), allowing to use this quantity to separate protons from muons. Figure 6.6 shows the track length as a function of the track $\langle dQ/dx \rangle_{\text{trunc}}$ for the longest track in a flash-matched interaction, and displays cases where such track is a simulated muon or a proton. This analysis uses a Support Vector Machine (SVM) [118] algorithm for a muon/proton classification. SVM is a supervised machine learning algorithm which can be used for classification tasks. The algorithm is provided with a training sample, made of vectors $\boldsymbol{x}$ that contain the $\langle dQ/dx \rangle_{\text{trunc}}$ and the track length l, $\boldsymbol{x} = (\langle dQ/dx \rangle_{\text{trunc}}, l)$, as well as labels for muons and protons. Not all the elements of the training sample are used,

but only the ones that are near the muon-proton boundary. These are called the "support vectors", and are denoted as $\bar{\boldsymbol{x}}$. The goal of the algorithm is to identify a decision boundary that separates the muon and proton populations. The decision boundary is characterised by a decision function $D(\boldsymbol{x})$ such that a certain vector $\boldsymbol{x}$ is classified as muon if $D(\boldsymbol{x}) > 0$ or as proton otherwise. The decision function $D(\boldsymbol{x})$ is found by minimising the Euclidean distance between the decision boundary and the support vectors $\bar{\boldsymbol{x}}$. For this particular application, the decision function is chosen to have the form

$$D(\boldsymbol{x}) = \sum_{i=1}^{n} \alpha_i K(\bar{\boldsymbol{x}}_i, \boldsymbol{x}) + \rho, \tag{6.1}$$

where the coefficients α_i and the bias ρ are parameters adjusted by the algorithm during training and K is the so-called Kernel function, here chosen to be

$$K(\bar{\boldsymbol{x}}_i, \boldsymbol{x}) = (\gamma\, \bar{\boldsymbol{x}}_i \cdot \boldsymbol{x} + r)^d\,, \tag{6.2}$$

with $d = 2$, $\gamma = 0.1$ and $r = 0$. Different parameterisations of the kernel function have been tested, and this one turned out to be giving the best performances in terms of the fraction of events that were classified incorrectly. The training of the SVM algorithm, aimed to identify the α_i and ρ parameters, was performed on a separate simulated sample. The output of the classifier is shown Figure 6.6.

To summarise this section, given a flash-matched reconstructed interaction, the candidate muon track is the longest track in such interaction not classified as a proton.

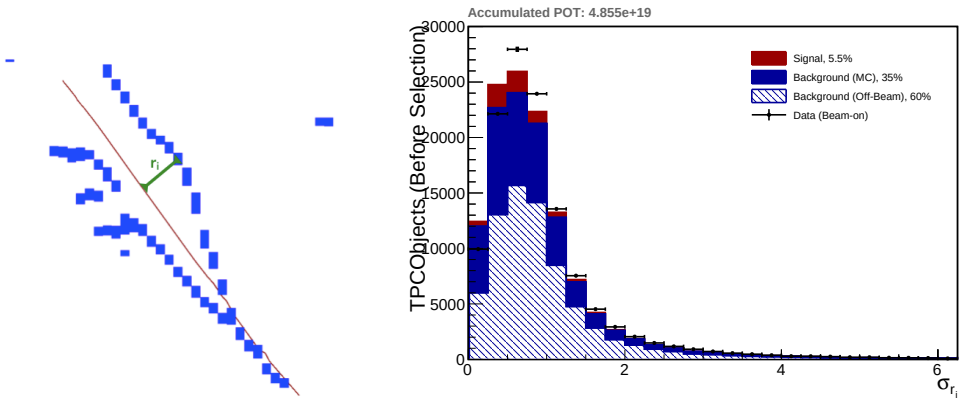

(a) (b)

Figure 6.7: (a) Illustration of how the hit residuals are calculated, taking the projection of the track on the collection plane, and measuring the distance between the hit and the closest track trajectory point. (b) Distribution of the STD of the hit residuals in the collection plane for all flash-matched interactions. Black points are data points. The coloured histograms show the beam-off CR contribution (hashed), the simulated background (blue) and the simulated ν_μ CC signal events (red).

6.4 Selected Track Quality

Since the goal of this analysis is to provide a cross-section measurement as a function of muon momentum and angle, it is very important to ensure that the muon candidate track and the neutrino vertex are well reconstructed. If the track is reconstructed shorter than its true length, the momentum estimation can be affected. If the vertex is in the wrong position, it may give a wrong value for the muon angle. Broken tracks, two separate tracks that come from a single vertex, but represent the same particle, are also an issue. Another issue arises when electrons or photons, producing electromagnetic showers, are reconstructed as tracks. Electrons and photons should be reconstructed as shower objects as they do not produce a track-like signature in the detector. To remove these mis-reconstructed tracks, the distribution of the hits in the collection plane is studied, to check if the hit dispersion along the track is small. If it is large, then the track is most likely

fitting a shower-like object. The hit residuals r_i are defined per each hit as the two dimensional distance between the hit and the closest track trajectory point projected onto the collection plane. Figure 6.7a shows a one-event example, where a track fits a collection of hits from a shower-like particle. For every event, the STD of the residual distribution, σ_{r_i}, is considered, and it is shown in Figure 6.7b for all events at an intermediate stage in the event selection, after the flash matching has been applied, and after the muon candidate track has been selected. Tracks that populate the high σ_{r_i} region have a high hit dispersion with respect to the track trajectory and a cut is applied so that events are selected if they have $\sigma_{r_i} < 2.5$ cm.

The track reconstruction actually takes as input reconstructed three dimensional space points, that are created by matching two dimensional hits from all three wire planes. An additional way to understand if the track is well reconstructed is to look at the number of hits that are associated to space points used for the track fitting. If the particle is not track-like, fewer hits will be associated to space points. The ratio between the number of hits associated to space-points and the total number of hits in the cluster allows to identify mis-reconstructed tracks. Only hits in the collection plane are used. Figure 6.8 shows the hit fraction, f_s. A track-like particle has a f_s close to one. A cut is applied to this distribution such that events are selected if they have $f_s > 0.7$.

The quality of a track can also be understood by comparing the MCS momentum to the range-based momentum (a description of momentum reconstruction is in Section 5.6). This study can only be performed on tracks spatially contained in the detector since the range-based momentum can only be measured for this kind of tracks. This comparison is shown in Figure 6.9a in a two-dimensional histogram with the MCS momentum on the y axis and the range-based momentum on the x axis. This distribution shows a linear agreement between the two momentum

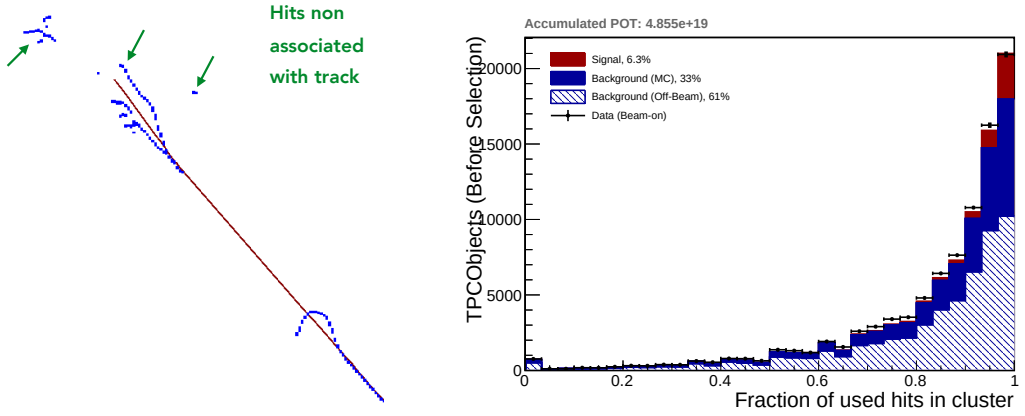

(a) (b)

Figure 6.8: (a) Example of simulated shower hits (blue) that were reconstructed as a track (red). All objects are projected onto the collection plane. Some hits (indicated by the green arrows) are not associated to the reconstructed track. (b) Fraction of hits (f_s) that are present in the collection plane cluster and that are also associated with a track. A good reconstructed track would have this fraction close to one. Black points are data points. The coloured histograms show the beam-off CR contribution (hashed), the simulated background (blue) and the simulated ν_μ CC signal events (red).

estimation algorithms, but there are some off-diagonal points. This is better visible in Figure 6.9b where the difference between the two momentum estimations is shown. There is a large tail in the positive region due to the mis-reconstructed tracks. Usually, these tracks do not reconstruct the full muon length, and so the range-based momentum is underestimated, but the MCS momentum is still able to provide a good estimate for the momentum. The comparison between data and simulation for the difference between the two momentum estimations is shown in Figure 6.10. An additional cut is then applied to further reject mis-reconstructed tracks: the MCS and range-based momenta must agree within 0.2 GeV.

6.5 Fiducial Volume

A FV is chosen in order to reduce the amount of CR muons contamination and also to remove unresponsive detector regions. The FV, shown in Figure 6.11

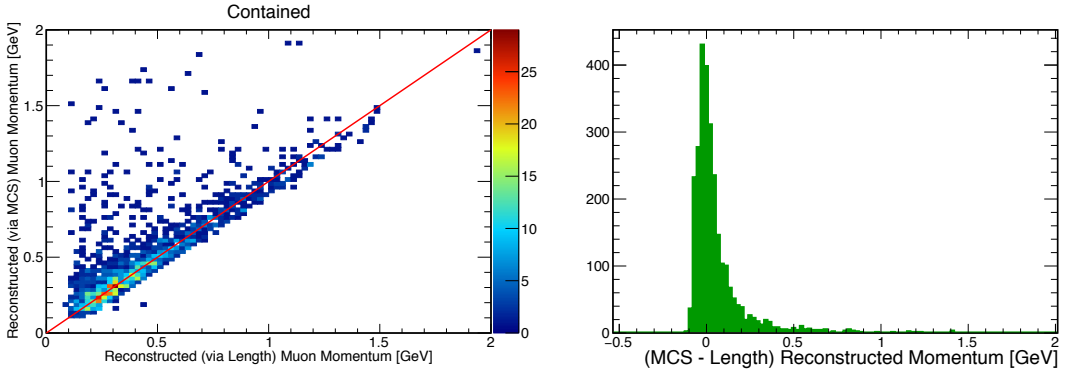

(a) (b)

Figure 6.9: (a) Two-dimensional histogram of the reconstructed muon momentum obtained with the MCS fit (y axis) and with the range-based algorithm (x axis). (b) The difference between the two momentum estimations.

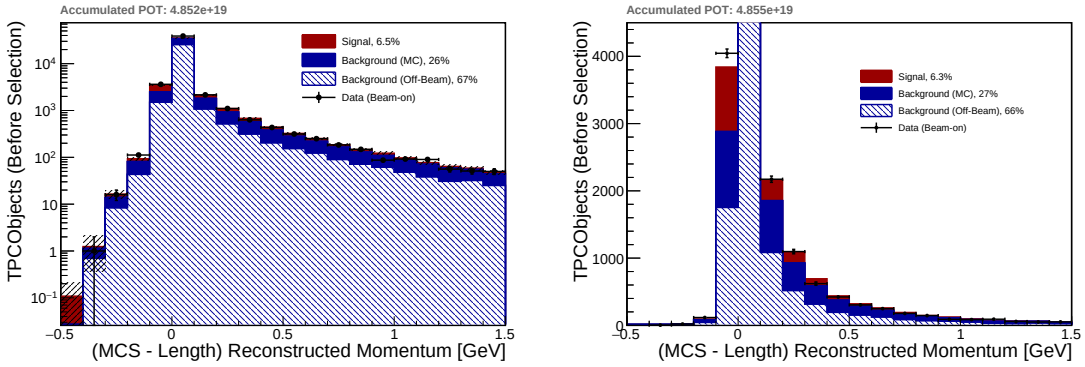

(a) Logarithmic scale. (b) Linear scale, enlarged in the cut region.

Figure 6.10: Similar plot to 6.9b, but this time showing the simulation with the beam-off data (shaded) compared to beam-on data. Plots are POT normalised. Plot (a) is in logarithmic scale, while plot (b) is in linear scale and has been enlarged in the region where the cut is placed (0.2 GeV). The coloured histograms show the beam-off CR contribution (hashed), the simulated background (blue) and the simulated ν_μ CC signal events (red).

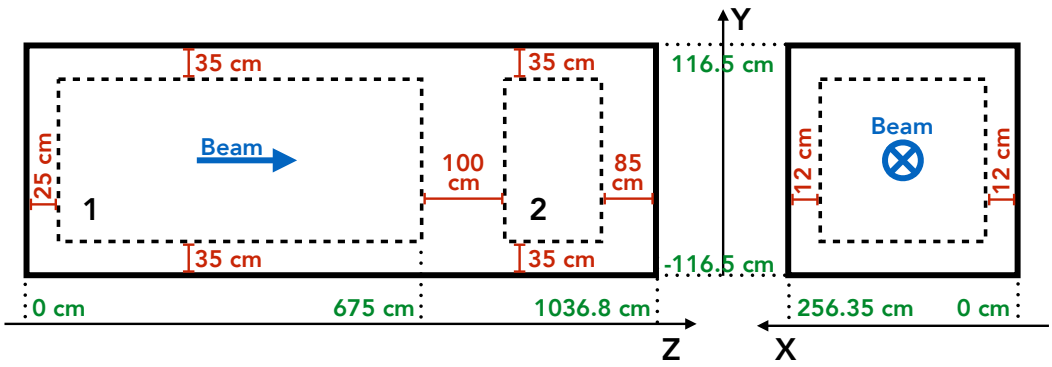

Figure 6.11: The FV used for this analysis. The solid black line is a schematic of the TPC. The FV is shown with a dashed line.

and is a rectangular parallelepiped whose faces are located at a distance of 35 cm from the top and bottom TPC faces. It is defined in order to remove CRs whose start and end positions are either misplaced by the space-charge effect or by mis-reconstruction issues. The FV faces are also 25 cm distant from the front face and 85 cm from the end of the detector, to reject muons interacting in the very end of the TPC that would not leave a substantial track, as they would be exiting immediately. In the drift direction, the faces are 12 cm distant. There is a 100 cm gap along the beam (z) direction that divides the FV in two regions. This is done to exclude a region in the collection plane with unresponsive wires.

As a final cut in the event selection, the reconstructed neutrino vertex is required to be in the aforementioned FV.

6.6 Selected Event Distributions

Figure 6.12 shows the distributions of the most relevant variables of the selected candidate muon track. The data distributions are compared with the two different GENIE configurations described in Section 4.5. However, only the "Default GENIE + Emp. MEC" simulation, being the default MicroBooNE simulation, will be used

for the cross section extraction. The distributions shown are:

- the measured muon momentum p_μ in (a) and (b),
- the measured cosine of the muon angle with respect to the beamline $\cos\theta_\mu$ in (c) and (d),
- the muon track length in (e) and (f),
- the muon angle around the beamline ϕ in (g) and (h),
- the number of reconstructed particles coming from the neutrino interaction vertex in (i) and (j),
- the neutrino reconstructed vertex along the drift direction x in (k) and (l),
- the neutrino reconstructed vertex along the vertical direction y in (m) and (n),
- the neutrino reconstructed vertex along the neutrino beam direction z in (o) and (p).

The angle definitions are shown in Figure 6.13 for reference. The black data points represent beam-on data with statistical uncertainties only shown with vertical bars. Beam-off data is also shown with an hashed histogram, and is stacked together with simulated events, as described in Section 4.5. The data correspond to 1.592×10^{20} POT. The stacked coloured histograms in Figure 6.12 represent the MC simulation for signal events in red and for all the estimated backgrounds. The MC is normalised to the same POT as the data. The different backgrounds are:

Cosmic Rays Events where a neutrino interaction is present (usually producing optical activity in the beam window), but a CR interaction is selected instead. Some CRs will enter the TPC from regions of the detector with unresponsive wires, with the result that the beginning of the track is not reconstructed. This CRs may look as spatially contained tracks.

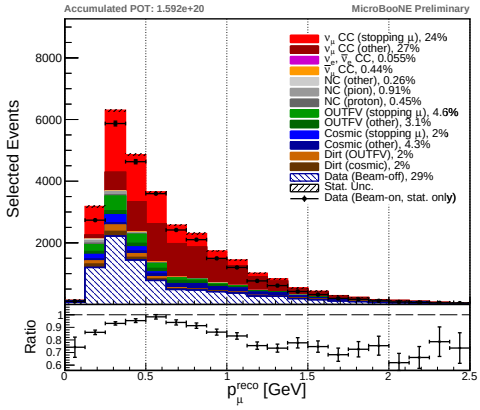

(a) Default GENIE + Emp. MEC.

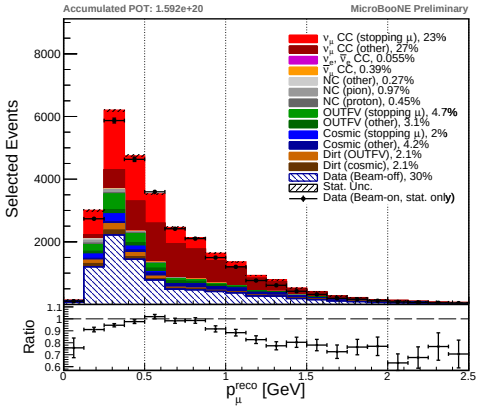

(b) GENIE Alternative.

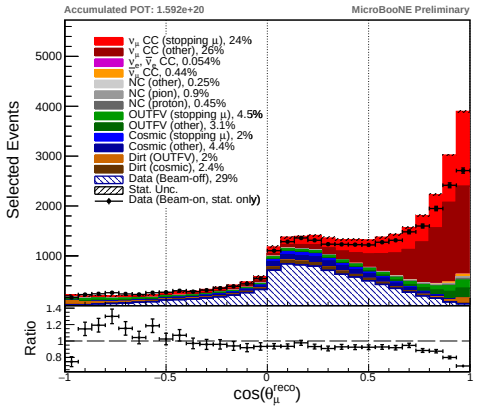

(c) Default GENIE + Emp. MEC.

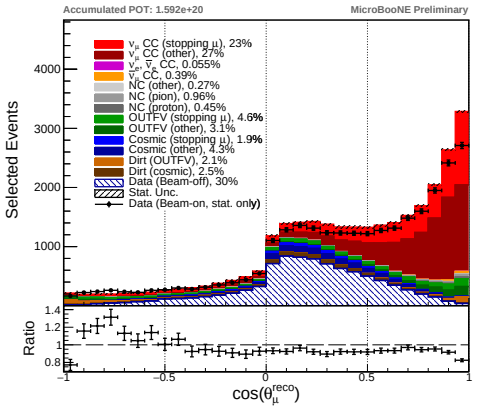

(d) GENIE Alternative.

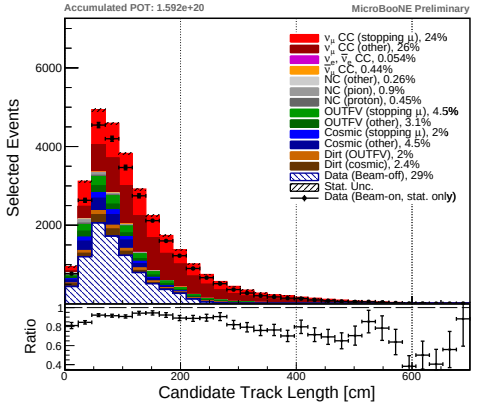

(e) Default GENIE + Emp. MEC.

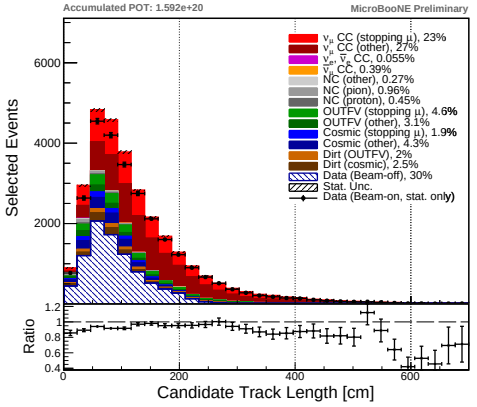

(f) GENIE Alternative.

Figure 6.12: Event distributions of the selected events. The black data points symbolise beam-on data with statistical uncertainties. The stacked coloured histograms represent the simulation, with the shaded bands representing the statistical uncertainty only. The red histograms shows the signal events. The hashed histogram is beam-off data. Data and MC correspond to 1.592×10^{20} POT. Left plots show MC from the "Default GENIE + Emp. MEC" configuration, right ones from the "GENIE Alternative" configuration.

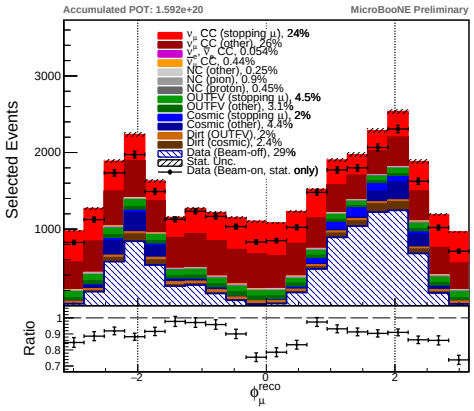

(g) Default Genie + Emp. MEC.

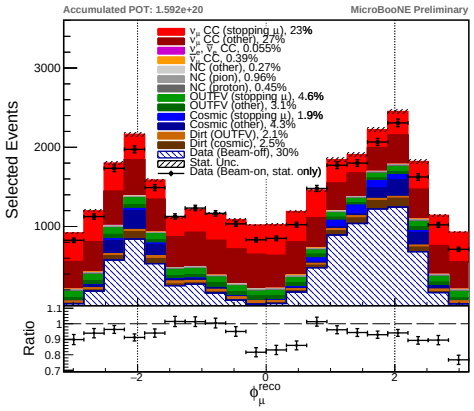

(h) Genie Alternative.

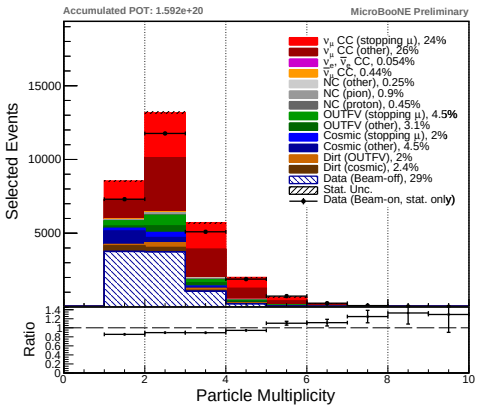

(i) Default Genie + Emp. MEC.

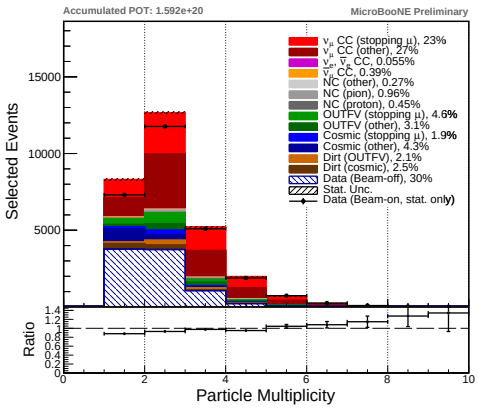

(j) Genie Alternative.

Figure 6.12: *(continues)* Event distributions of the selected events. The black data points symbolise beam-on data with statistical uncertainties. The stacked coloured histograms represent the simulation, with the shaded bands representing the statistical uncertainty only. The red histograms shows the signal events. The hashed histogram is beam-off data. Data and MC correspond to 1.592×10^{20} POT. Left plots show MC from the "Default Genie + Emp. MEC" configuration, right ones from the "Genie Alternative" configuration.

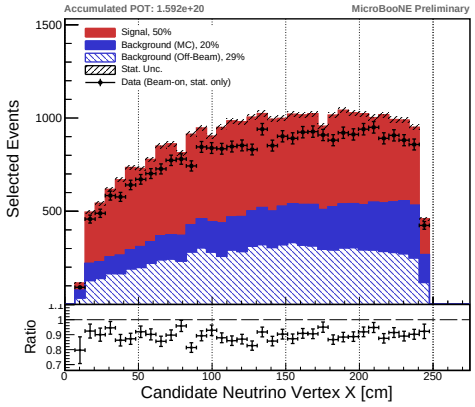

(k) Default GENIE + Emp. MEC.

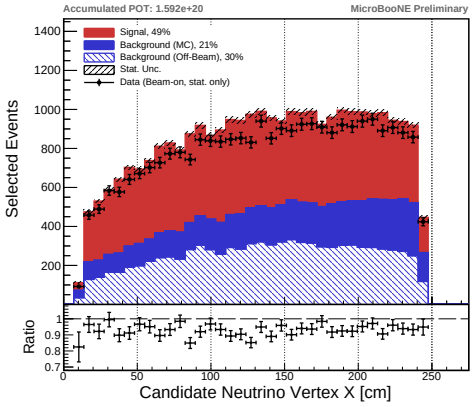

(l) GENIE Alternative.

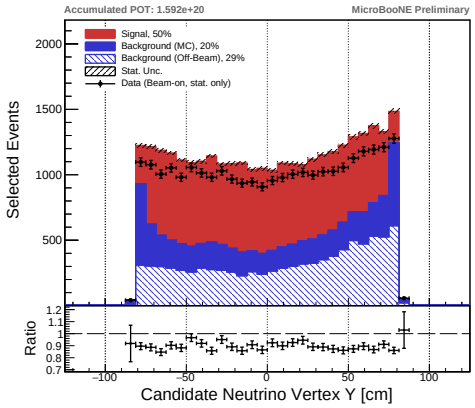

(m) Default GENIE + Emp. MEC.

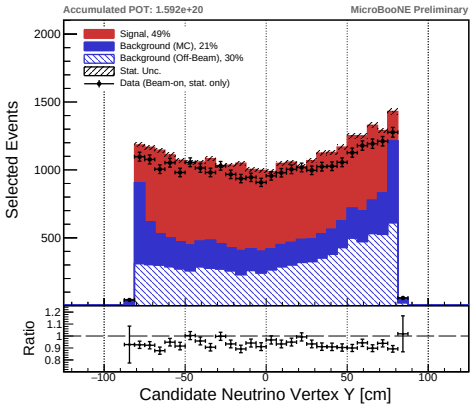

(n) GENIE Alternative.

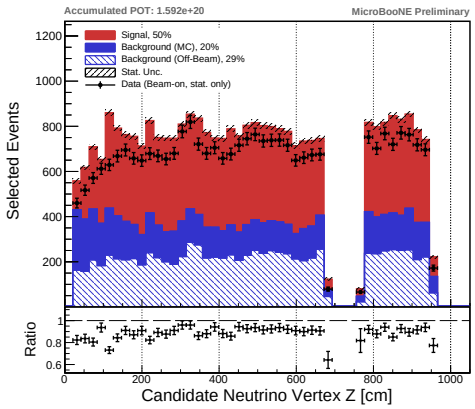

(o) Default GENIE + Emp. MEC.

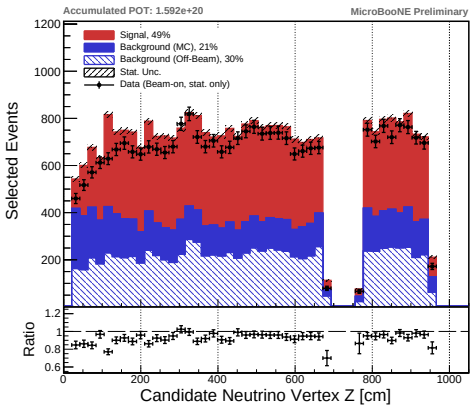

(p) GENIE Alternative.

Figure 6.12: *(continues)* Event distributions of the selected events. The black data points symbolise beam-on data with statistical uncertainties. The stacked coloured histograms represent the simulation, with the shaded bands representing the statistical uncertainty only. The red histograms shows the signal events. The hashed histogram is beam-off data. Data and MC correspond to 1.592×10^{20} POT. Left plots show MC from the "Default GENIE + Emp. MEC" configuration, right ones from the "GENIE Alternative" configuration.

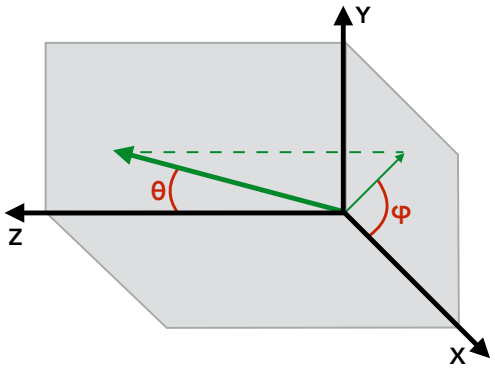

Figure 6.13: MicroBooNE coordinate system showing the definition of the polar angle θ and the azimuthal angle ϕ for a given track (green). The neutrino beam runs along the z axis. The anode is at $x = 0$.

Neutrinos Interacting Outside the Fiducial Volume (OUTFV) Events where the neutrino interacts outside the fiducial volume, but produces a muon that crosses (or stops in) the TPC, that is then selected. In these events the vertex is mis-reconstructed and appears to be in the FV, leading to wrong momentum and angle reconstruction.

Dirt Events coming from the "dirt" simulated sample. They are due to interactions that happen outside the cryostat. The "dirt" contributes to two backgrounds: a CR background (usually because there is a neutrino induced flash, but a CR is selected instead) and an OUTFV background (in which a neutrino origin track is selected).

(Anti-)Electron Neutrinos Events where an electron from a ν_e or a $\bar{\nu}_e$ interaction is selected. ν_e and $\bar{\nu}_e$ are a small contamination in the BNB beam. This usually happens because the electron is reconstructed as a track instead of an electromagnetic shower.

Anti-Muon Neutrinos Events where a muon from a $\bar{\nu}_\mu$ interaction is selected. $\bar{\nu}_\mu$ are a small contamination in the BNB beam. MicroBooNE is not provided

with a magnetic field that help to distinguish a $\bar{\nu}_\mu$ from a ν_μ by the curvature of the μ^+ or μ^- in the final state.

Neutral Current Events where a neutral current event is selected, usually a pion in the final state is selected as muon candidate.

Table 6.1 shows the background contamination percentages, indicating that the main background is from CRs, followed by OUTFV interactions. Some relevant features in the distributions shown in Figure 6.12 are discussed in the next points:

- The $\cos\theta_\mu$ distribution in (c) and (d) shows a bump around $\cos\theta_\mu = 0$. This is caused by CR background. The distribution for CR should be symmetric, but Pandora reconstruction has a bias in placing the neutrino candidate vertex, as described in Section 5.4. A beam weight is applied when choosing the position of the reconstructed vertex so that it is always more likely that a vertex is placed upstream of a reconstructed object, rather than downstream. This bias makes CRs look more forward going.
- In the same $\cos\theta_\mu$ distribution in (c) and (d), there is disagreement in the forward-going region ($\cos\theta_\mu \sim 1$). Several hypotheses have been examined. Coherent noise in the waveforms is mitigated by Coherent Noise Removal (COHNR) algorithms [91] which are applied to data, but not to MC. This might suppress more isochronous tracks in data than in the MC. COHNR was run on a small simulated sample, and the discrepancy in the forward-going region remains. The kaon flux, that contributes to high-energy forward-going neutrinos, was also studied as it could be the cause of the disagreement. Such flux was rescaled by large factors ($\pm 50\%$ of the default values) but the change in the number of selected events remains below 8%, which cannot explain the observed discrepancy. The reason for this discrepancy can be related

to physics rather than detector effects. For example, Continuum Random-Phase Approximation (CRPA) predicts rich physics effects for forward going events [119]. These calculations are done on carbon targets, and the extrapolation of cross sections from carbon to argon is also non-trivial [120].

- The distribution of the candidate neutrino vertex x in (k) and (l) is not flat, but decreases at small x. This shape is created by two effects. One is the space-charge effect, introduced in Section 4.5. The distribution becomes flat in MC if the space-charge effect is not simulated. The space-charge effect pushes reconstructed vertices outside the fiducial volume, so that less candidate neutrino events are not selected. The second effect if due to the flash-matching algorithm, which fails if tracks are close to the PMT plane (that is at $x = 0$). If a track is too close to a single PMT, it deposits most of its light to that PMT, which makes the likelihood estimation described in Section 5.5 to not converge. The shape of the y vertex plot in (m) and (n) is driven by CR stopping muons, that populate the upper region of the detector. This causes the background to increase in this region. For the z distribution in (o) and (p), the spikes seen in simulation are due to simulated unresponsive wires. The simulation uses a static list of unresponsive wires. Many unresponsive wires are in the upstream part of the detector (low z) and cause the spikes in the z vertex distribution because reconstructed vertices pile up at the edges of unresponsive regions. In reality, the number of unresponsive wires in MicroBooNE fluctuates with time (some channels become responsive after some time). This means that the dead regions are not always in the same place, and the spikes that are visible in the simulation are actually smeared in the data distribution.
- There are some discrepancies between data and simulation in the ϕ distri-

Signal and Background	Composition [%]
ν_μ CC in FV (signal)	50
Cosmic in BNB	6.4
OUTFV	7.6
DIRT	4.4
NC	1.6
$\bar{\nu}_\mu$	0.44
ν_e and $\bar{\nu}_e$	0.054
Cosmic Only (data)	29

Table 6.1: The table shows the signal and background composition after the event selection.

bution in (g) and (h). These discrepancies are understood and are covered by a detector systematic uncertainty on the induced-charge effect, as will be described in Section 8.4.

6.7 Event Selection Performances

The performances of the event selection are quantified in terms of efficiency

$$\epsilon = \frac{\text{Selected } \nu_\mu \text{ CC interactions with true vertex in the FV}}{\text{Generated } \nu_\mu \text{ CC interactions with true vertex in the FV}}, \tag{6.3}$$

and purity

$$p = \frac{\text{Selected } \nu_\mu \text{ CC interactions with true vertex in the FV}}{\text{All selected events}}. \tag{6.4}$$

No cut is applied to the neutrino or lepton kinematics in the denominator of the efficiency calculation. The event selection efficiency is shown in Figure 6.14a as a function of true muon momentum and in Figure 6.14b as a function of true muon $\cos\theta_\mu$. The efficiency in the two dimensional space (p_μ, $\cos\theta_\mu$) is also shown in Figure 6.14c. The overall selection efficiency is 57.2%, with a purity of 50.4%.

Cut	MC ν_μ CC in FV	Full MC	Beam-off	Beam-on
Initial	5,810.83	34,597.30	103272	133597
Beam Flash	5,648.25	26,731.80	72975.6	102682
FM	4,203.59	16,347.43	27299.9	44694
FM Δx	4,019.99	12,162.49	15591.2	28226
FM Δz	3,964.90	10,173.96	8760.38	19180
Quality	3,791.25	9,258.22	6529.46	15468
MCS-Length Quality	3,594.25	8,632.98	6270.93	14812
MIP Consistency	3,460.26	7,866.17	5985.75	13706
FV	3,322.22	4,384.67	2011.63	5782

Table 6.2: The table shows passing rates for the described event selection. Numbers are absolute event counts scaled to 3.446×10^{19} POT.

As nuclear models depend on lepton angle and particle multiplicity, this event selection has been carefully designed to minimise biases due to cuts on particle angles and others. Figure 6.14e and 6.14f show the efficiency as a function of the angle around the beam (ϕ) and the GENIE simulated particle multiplicity. The efficiency in particle multiplicity is mostly flat, while the one in ϕ is only shaped by the CR removal stage, which removes some of the neutrinos producing vertical muons ($\phi \sim \pm\pi/2$).

Figure 6.15 shows the efficiency as a function of true neutrino energy for the different GENIE interaction modes: QE, resonance, DIS and MEC. There is also a negligible contribution from CC coherent events not plotted. This plot shows that this event selection allows to select all the interaction modes, making this analysis really inclusive.

The plots in Figure 6.16 show the distribution of true GENIE simulated variables: neutrino energy, muon momentum p_μ, cosine of the muon polar angle $\cos\theta_\mu$, muon azimuthal angle ϕ. These distribution are further divided in different GENIE interaction modes. Apart for a normalisation difference (the efficiency is $\sim 57\%$), one can see that the distributions are not particularly shaped after the selection,

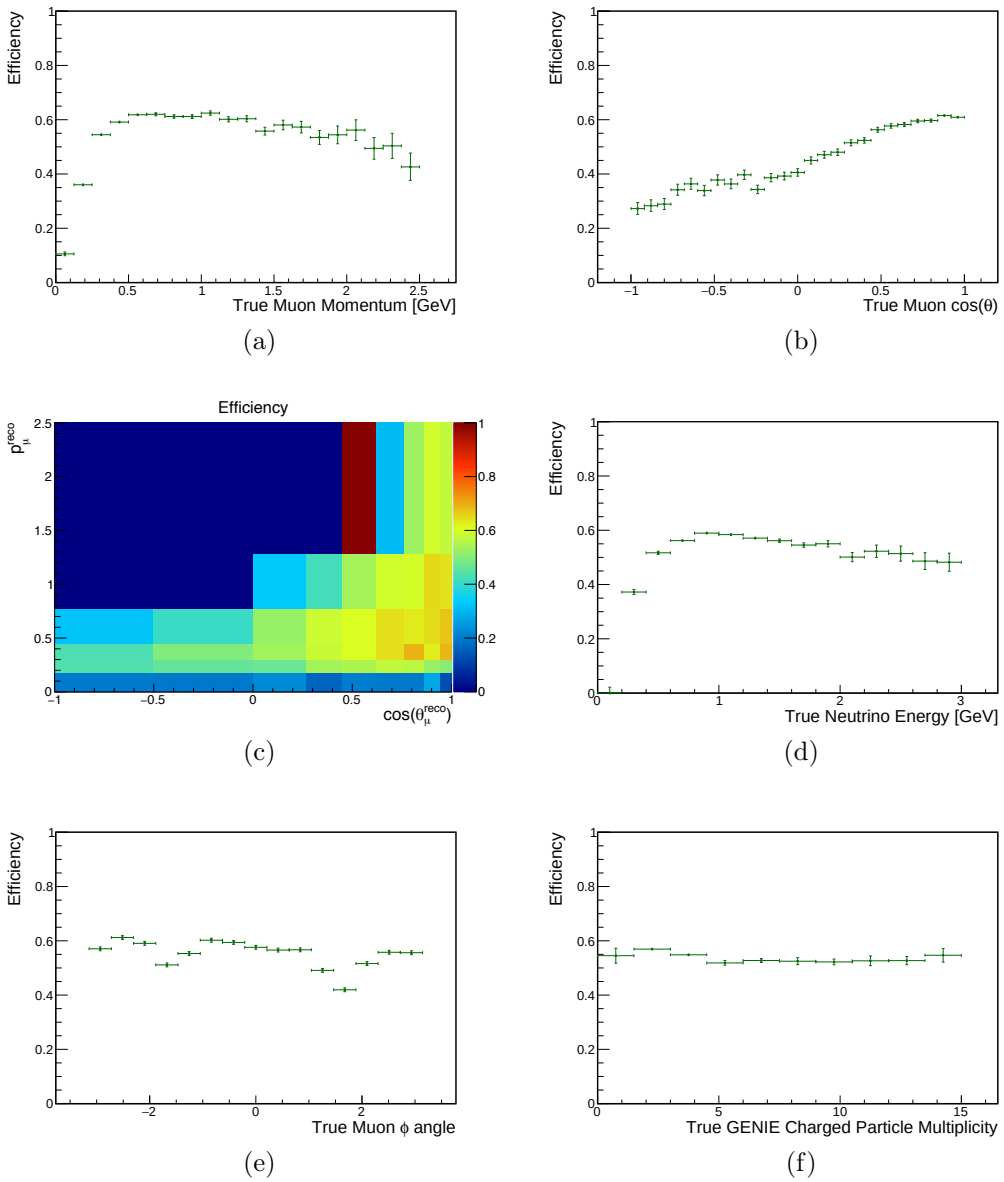

Figure 6.14: Final selection efficiency (efficiency × acceptance) as a function of the true muon momentum (a), cosine of the muon angle with respect to the beam (b), angle and momentum together (c), angle around the beam (e), true initial neutrino energy (d), and true charged particle multiplicity (f) . The overall efficiency is 57.2%.

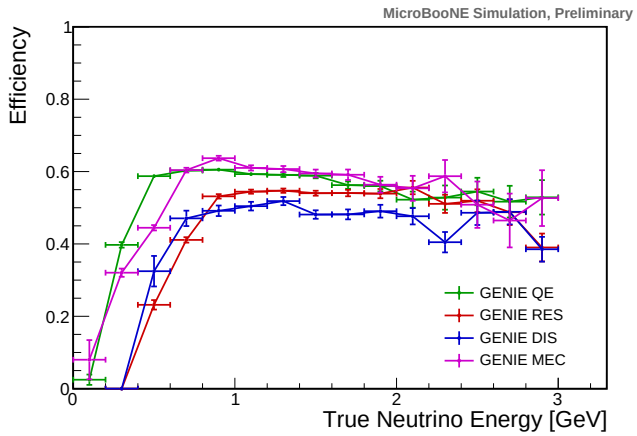

Figure 6.15: Efficiency as a function of true neutrino energy for different GENIE interaction modes. There is a negligible contribution from CC coherent events not plotted.

so that the event selection is not introducing any particular bias.

6.8 Event Selection Summary

This chapter described the event selection used to select ν_μ CC events in the FV. The overall selection efficiency is 57.2%, with a purity of 50.4%. These performances have been estimated by looking at the "Default GENIE + Emp. MEC" configuration, which is the MicroBooNE baseline simulation. The main background is due to CR only events (for which a data driven estimate using beam-off data is used) and from events where neutrino interactions are present, but a CR in the same event is selected (estimated using simulation). The second main background is caused by neutrino interactions outside the FV. The next chapter will use events passing this selection to perform a cross section measurement.

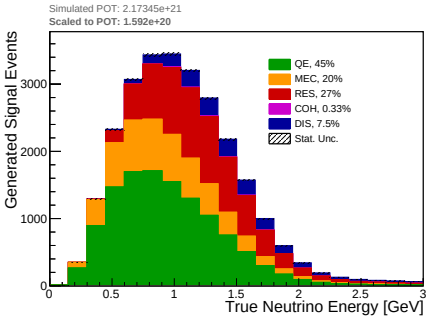

(a) Generated.

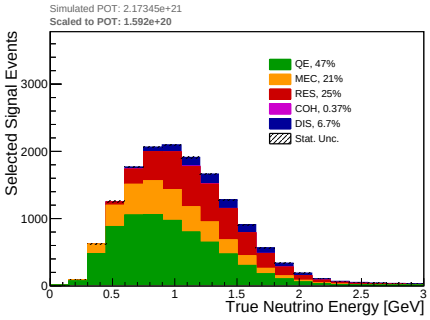

(b) Selected.

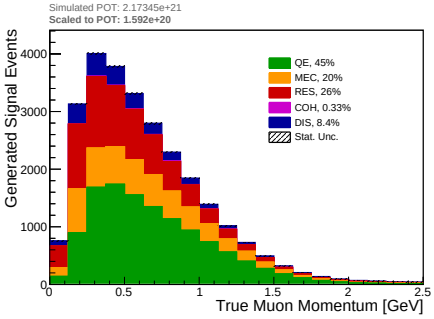

(c) Generated.

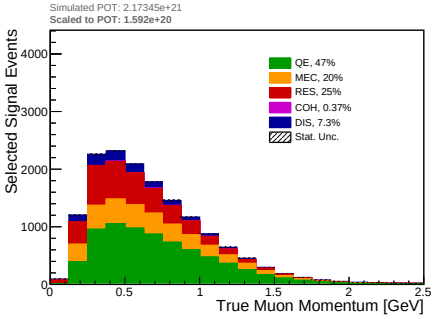

(d) Selected.

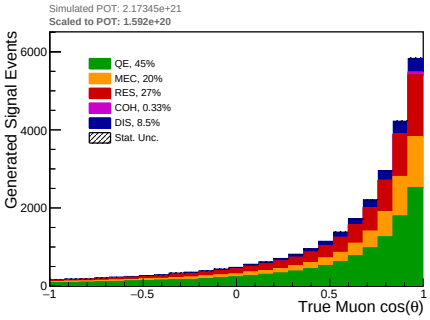

(e) Generated.

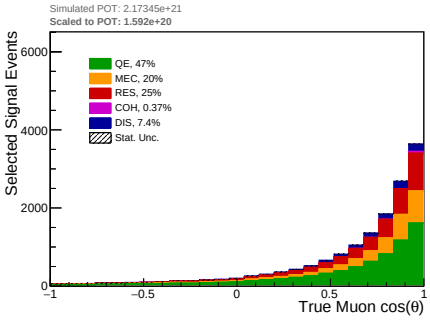

(f) Selected.

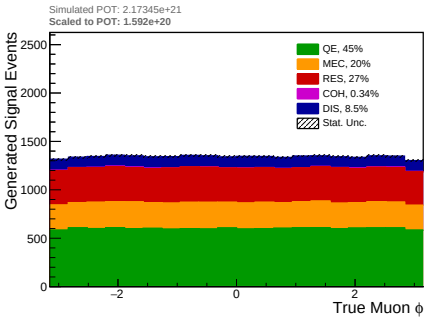

(g) Generated.

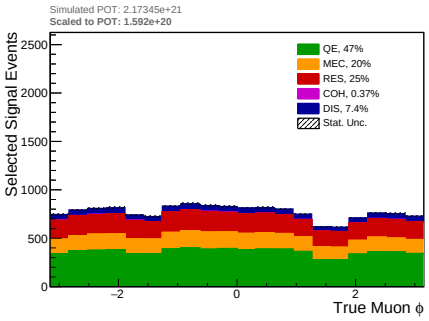

(h) Selected.

Figure 6.16: Distributions of true variables for generated (left) and selected (right) signal events (ν_μ CC in FV). These plots have been made with a 8.9×10^{20} equivalent POT MC. They have then been scaled to 1.6×10^{20} POT, which are the data POT used for this analysis. The coloured histogram are stacked. The distributions are generated with the "Default GENIE + Emp. MEC" configuration.

Chapter 7

Cross-Section Extraction

This chapter describes the full procedure used to calculate the total ν_μ CC inclusive cross section on argon, as well as the single- and double-differential cross sections in muon momentum and angle. Only statistical uncertainties will be taken into account in this chapter. Systematic uncertainties will be discussed in Chapter 8, and the final results are shown in Chapter 9.

The MicroBooNE baseline simulation uses the "Default GENIE + Emp. MEC" configuration, and the cross section will be extracted using the efficiency and the backgrounds estimated according to this simulation. The data extracted cross section will be denoted as σ in the following. Equivalently the cross section from simulation will be denoted as σ_{MC}.

Section 7.1 shows an overview on the cross section calculation, while Section 7.2 describes the extraction of the total cross section. Similarly, Sections 7.3, 7.4 and 7.5 describe the extraction of the two single-differential cross sections and the double-differential cross section in p_μ and $\cos\theta_\mu$ respectively.

7.1 Cross-Section Calculation

The total flux-integrated cross section is calculated using the following equation:

$$\sigma = \frac{N - B}{\epsilon \cdot T \cdot \Phi_{\nu_\mu}}, \tag{7.1}$$

where N is the total number of selected data events, B is the number of selected background events (from simulation and beam-off data), ϵ is the efficiency of the event selection (overall, including acceptance), T is the number of target nucleons and Φ_{ν_μ} is the BNB muon neutrino flux integrated over energy and scaled to the corresponding POT received for the analysis.

In addition to a total cross section, the result is also reported in terms of a differential cross section as a function of muon kinematics, such as the muon momentum p_μ and the cosine of the muon angle θ_μ with respect to the beam direction. In this case, the signal and background event rates, as well as the efficiencies, are binned as a function of muon momentum or angle and the single-differential cross sections in bin i are calculated as

$$\begin{aligned} \left(\frac{d\sigma}{dp_\mu}\right)_i &= \frac{N_i - B_i}{\tilde{\epsilon}_i \cdot T \cdot \Phi_{\nu_\mu} \cdot (\Delta p_\mu)_i}, \\ \left(\frac{d\sigma}{d\cos\theta_\mu}\right)_i &= \frac{N_i - B_i}{\tilde{\epsilon}_i \cdot T \cdot \Phi_{\nu_\mu} \cdot (\Delta \cos\theta_\mu)_i}, \end{aligned} \tag{7.2}$$

where N_i, B_i and $\tilde{\epsilon}_i$ are the number of candidate events, the number of background events and the efficiency in bin i, respectively. $(\Delta p_\mu)_i$ and $(\Delta \cos\theta_\mu)_i$ are the bin widths for bin i in the p_μ and $\cos\theta_\mu$ distributions, respectively.

Similarly, the double-differential cross section is extracted according to

$$\left(\frac{d^2\sigma}{dp_\mu d\cos\theta_\mu}\right)_i = \frac{N_i - B_i}{\tilde{\epsilon}_i \cdot T \cdot \Phi_{\nu_\mu} \cdot (\Delta p_\mu \cdot \Delta\cos\theta_\mu)_i}, \tag{7.3}$$

where $(\Delta p_\mu \cdot \Delta\cos\theta_\mu)_i$ is the i^{th} bin area.

All these cross sections are called "flux integrated" as they include neutrinos with different energies (distributed according to the neutrino spectrum at the detector location). In neutrino interaction differential cross-section measurements, no attempt is usually made to correct for the incoming neutrino flux in each bin of the measurement. Instead, each bin is normalised by the total integrated flux. Because Φ_{ν_μ} is the integrated neutrino flux at the detector location, the result is experiment dependent. Indeed, the shape of the incoming neutrino flux must be made available with the measurement, such that a model can be convoluted with the flux to be comparable to the result.

A specific problem arises in the measurement of a differential cross section that is related to the resolution on p_μ and $\cos\theta_\mu$. If the resolution on these quantities is larger or of the same order than the bin dimension, migration of events between neighbouring bins is expected, affecting the shape of the differential cross section for the reconstructed events. The binning used in this analysis, described below, is made in order to guarantee small bin-to-bin migrations by choosing bin width larger than the resolution. In order to understand the bin-to-bin migrations a smearing matrix S is constructed, allowing to convert the number of true events in a true bin j, to the number of observed events in a reconstructed bin i such that:

$$\nu_i = \sum_{j=1}^{M} S_{ij}\mu_j, \tag{7.4}$$

where S is given by:

$$S_{ij} = P(\text{observed in bin } i \,|\, \text{true value in bin } j), \tag{7.5}$$

and ν_i and μ_j are the number of events in the reconstructed bin i and true bin j, respectively, and M is the total number of bins. Smeared data can be analysed in two ways:

Forward Folding With this approach, the data distribution is presented in reconstructed observables. A theoretical spectrum can be smeared from truth quantities to reconstructed observables, and then be compared directly to the data. The migration matrix, needed to smear the theoretical spectrum, has to be provided alongside the cross-section distributions, in order for people outside the experiment to be able to make model comparisons. This approach does not allow a direct comparison to other experiments, which may provide forward-folded distributions with different smearing matrices, or forward-folded ones.

Unfolding This approach corrects for smearing and other detector effects by trying to deconvolve those effects in order to get to the true underlying distribution. This method allows a direct comparison to unfolded measurements from other experiments.

Although the majority of experiments use the unfolding approach, the cross section presented in this thesis is extracted using the forward-folding method. The unfolding procedure can introduce biases in the cross-section extraction, can add correlations between the data points and presents failures when testing the goodness of a fit to a certain model, as shown in [121]. In this work, a comparison between a predicted theory and the observed data is performed at the level of the smeared theory with

the actual data, rather than between the pure true and the unfolded data. This comparison between theoretical models and data is possible if the smearing matrix is published with the data, as it will be done with this analysis. While the efficiency ϵ_j in true bin j is given by the ratio of the number of selected signal events N_j^{sel} and the number of generated signal events N_j^{gen} in true bin j:

$$\epsilon_j = \frac{N_j^{\text{sel}}}{N_j^{\text{gen}}}, \tag{7.6}$$

for this analysis the true distributions have to be smeared in order to evaluate the efficiency in reconstructed bin i:

$$\tilde{\epsilon}_i = \frac{\sum_{j=1}^{M} S_{ij} N_j^{\text{sel}}}{\sum_{j=1}^{M} S_{ij} N_j^{\text{gen}}}. \tag{7.7}$$

This efficiency is used to extract the cross section using formulas (7.2) and (7.3). where N_j^{sel} is the number of signal selected events in true bin j, and N_j^{gen} is the number of generated signal events in true bin j.

7.1.1 BNB Neutrino Integrated Flux

The BNB ν_μ flux in neutrino mode running is shown in Figure 7.1. The flux is simulated using the MiniBooNE framework as described in [88]. The total integrated flux scaled to 1.592×10^{20} POT is

$$\Phi_{\nu_\mu} = 1.16859 \times 10^{11}\,\text{cm}^{-2}. \tag{7.8}$$

The mean neutrino energy for the BNB flux is

$$\left\langle E_{\nu_\mu} \right\rangle = 823\,\text{MeV}, \tag{7.9}$$

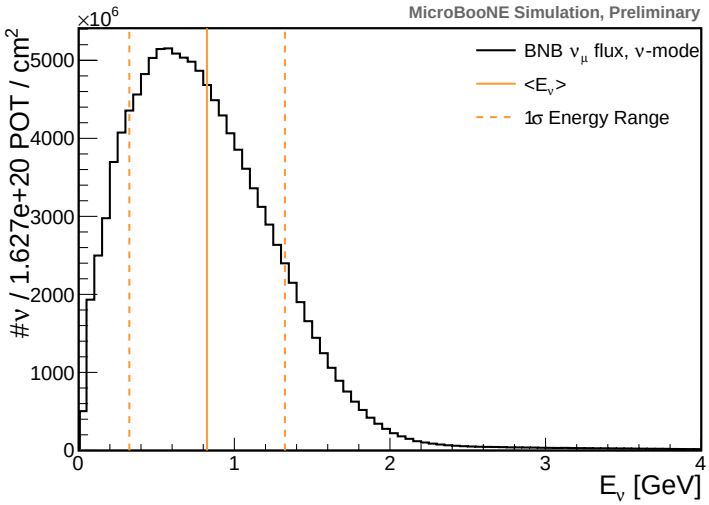

Figure 7.1: BNB ν_μ flux in neutrino mode at the MicroBooNE detector center, scaled to 1.592×10^{20} POT. The lines mark the mean neutrino energy and the 1σ range.

with 68% of the values falling into the energy range of $823 - 498 = 325$ MeV and $823 + 502 = 1325$ MeV. This energy range is not used for the analysis but is used for comparison to other measurements. Tabulated values of the BNB ν_μ flux as a function of neutrino energy are available in [89].

7.1.2 Number of Target Nucleons

The number of target nucleons T in the FV is calculated as

$$T = \frac{\rho_{\mathrm{Ar}} \cdot V \cdot N_A \cdot N_{\mathrm{nucleons}}}{m_{\mathrm{mol}}}, \tag{7.10}$$

where ρ_{Ar} is the liquid argon density, V is the FV, N_A is the Avogadro number, N_{nucleons} is the number of nucleons per argon nucleus, and m_{mol} is the number of grams per mole of argon. The FV is split in two sub-volumes, V_1 and V_2, as previously shown in Figure 6.11. The volume is treated as pure argon as the number of contaminants have been measured to be less than one particle per million [122]. The NIST database at the MicroBooNE measured temperature and pressure was

used to calculate the density of liquid argon. The calculated liquid argon density was found to be slightly different ($< 1\%$ difference) with respect to the simulated one, as simulation uses the design temperature and pressure, and not the measured ones. This leads to two values for the number of targets, one for the data, and one for the simulation. Using

$$\begin{aligned} V_1 &= 2.46175 \times 10^7\,\mathrm{cm}^3, \\ V_2 &= 6.69596 \times 10^6\,\mathrm{cm}^3, \\ \rho_{\mathrm{Ar}}^{\mathrm{data}} &= 1.3836^{+0.0019}_{-0.0002}\,\mathrm{g/cm}^3, \\ \rho_{\mathrm{Ar}}^{\mathrm{MC}} &= 1.3954\,\mathrm{g/cm}^3, \\ m_{\mathrm{mol}} &= 39.95\,\mathrm{g/mol}, \\ N_A &= 6.022140857(74) \times 10^{23}\,\mathrm{molec/mol}, \\ N_{\mathrm{nucleons}} &= 40, \end{aligned} \tag{7.11}$$

the following values for the number of targets are obtained:

$$\begin{aligned} T^{\mathrm{data}} &= 2.6124^{+0.0036}_{-0.0003} \times 10^{31}, \\ T^{\mathrm{MC}} &= 2.6347 \times 10^{31}. \end{aligned} \tag{7.12}$$

T^{data} will be used to extract the data cross section, while T^{MC} will be used for the MC predicted cross section. The uncertainties on the number of targets will be discussed in Section 8.4.1.

7.1.3 Analysis Binning

The binning for the p_μ distribution must be determined before moving to the cross-section extraction. The main strategy used to find the binning is to ensure that the majority of the true values that correspond to the reconstructed values

in one bin, fall in the same reconstructed bin. This is done in order to mitigate bin-to-bin migrations. Moreover, the binning is chosen such that: there are a similar number of events in each reconstructed bin; the statistical uncertainty is comparable in every bin; the change in the expected cross section within a bin is small; the efficiency stays almost flat inside one bin; the efficiency, averaged over one bin, is not less than 30%, to avoid having bins with very small efficiency. The only exceptions are the bins in the backward region of the $\cos\theta_\mu$ distribution ($\cos\theta_\mu < 0$). This region was simply split in two bins, $\cos\theta_\mu \in [-1, -0.5)$ and $\cos\theta_\mu \in [-0.5, 0)$, given the low data statistic in this region. The final bin choice for p_μ is:

$$p_\mu \text{ bins} : [0.00, 0.18, 0.30, 0.45, 0.77, 1.28, 2.50], \tag{7.13}$$

while for $\cos\theta_\mu$ is:

$$\cos\theta_\mu \text{ bins} : [-1.00, -0.50, 0.00, 0.27, 0.45, 0.62, 0.76, 0.86, 0.94, 1.00]. \tag{7.14}$$

Figures 7.2a and 7.2c show the comparison of simulated and reconstructed variables with a fine binning. Figures 7.2b and 7.2d show the same distributions with the final binning, as defined above.

For the double differential cross section, a very similar binning for p_μ and $\cos\theta_\mu$ is used, with some modifications. The same bin boundaries are used, but some of the p_μ bins are merged, especially in the backward region, to ensure enough statistics in each bin. The binning choice is shown in Figure 7.3. The number in each bin represents the bin unique identifier (bin ID). The bin ID will be used for the construction of the smearing matrices and all the covariance matrices. The reader should refer to Figure 7.3 to understand the bins in all the following matrices.

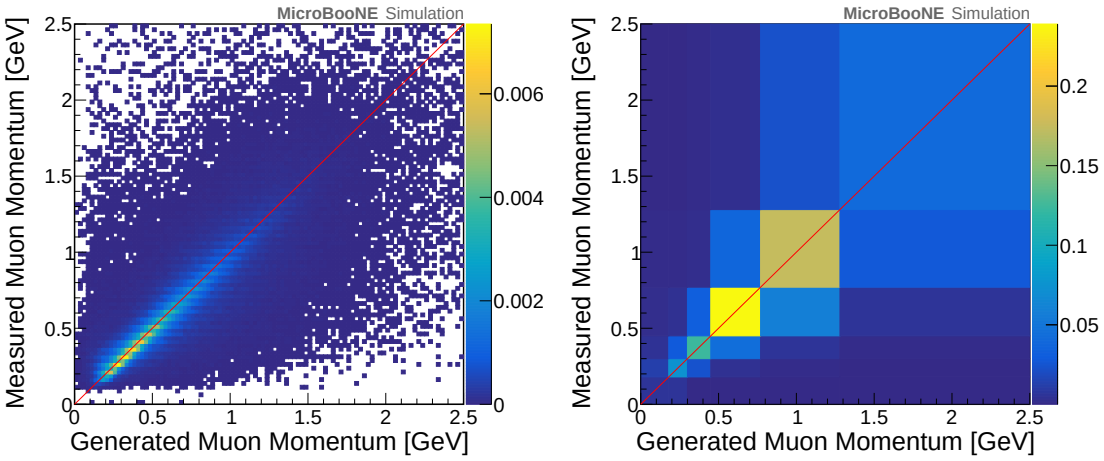

(a) (b)

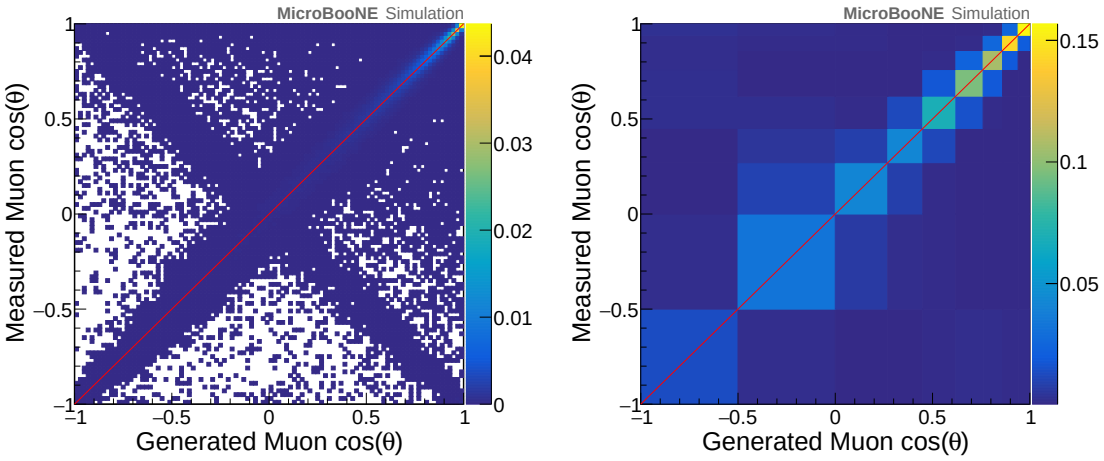

(c) (d)

Figure 7.2: Distribution of the measured v.s. generated muon momentum and cosine of the muon angle in (a) and (c), respectively. The right plots (b) and (d) are the same as the left ones but using the new binning defined for the cross section extraction.

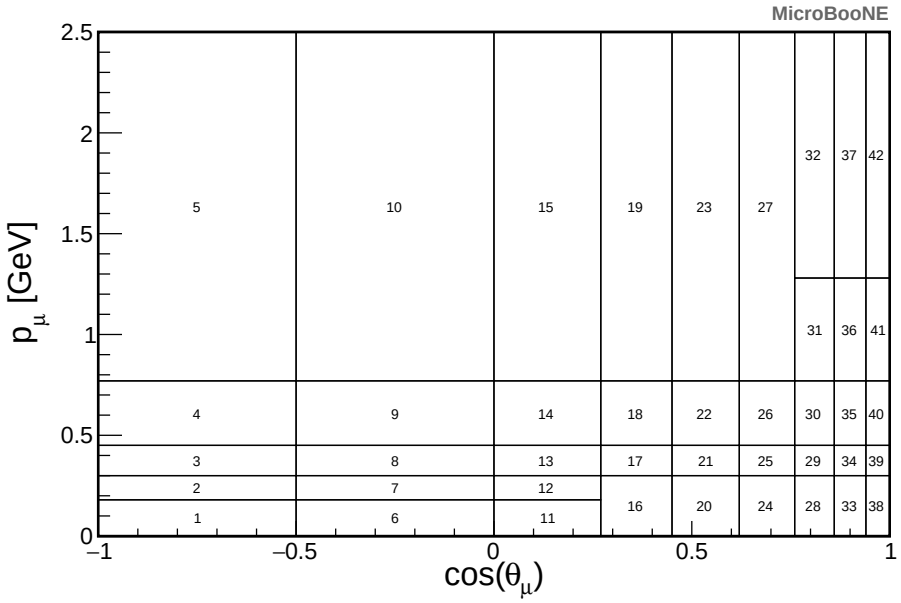

Figure 7.3: The figure shows the binning choice for the double-differential cross section in p_μ and $\cos\theta_\mu$. The numbers inside the bins show the bin ID, which is used to identify the bins in the following matrices.

7.2 Total Cross Section

The total cross section can be calculated according to Equation 7.1 and the quantities needed for this calculation are summarised in Table 7.1 and 7.2. With $N = 27197 \pm 164$ selected data events and $B = 15099 \pm 69$ estimated background

Name	Variable	Value
ν_μ BNB Flux	Φ_{ν_μ}	$1.16859 \times 10^{11}\,\mathrm{cm}^{-2}$
Number of Targets Data	T^{data}	$2.6124^{+0.0036}_{-0.0003} \times 10^{31}$
Number of Targets MC	T^{MC}	2.6347×10^{31}
Efficiency	ϵ	$0.57173 \pm 0.00082\,(\mathrm{stat.})$

Table 7.1: Parameters used for the flux integrated cross-section calculation. The integrated flux corresponds to an exposure of 1.592×10^{20} POT. The uncertainties on the flux and the number of targets will be discussed in the next chapter.

Name	Variable	Event Number
Measured Event Number	N	27197 ± 164
ν_μ CC Events	S	15348 ± 34
Cosmic Only (from off-beam)	-	8868 ± 66
Cosmic in BNB (from MC)	-	1961 ± 12
OUTFV (from MC)	-	2308 ± 13
NC (from MC)	-	488.5 ± 6.0
ν_e and $\bar{\nu}_e$ (from MC)	-	16.5 ± 1.0
$\bar{\nu}_\mu$ (from MC)	-	133.9 ± 3.2
Dirt (from MC)	-	1322.1 ± 8.8
Total Background	B	15099 ± 69

Table 7.2: Number of events used to calculate the flux integrated cross section. The numbers correspond to an exposure of 1.592×10^{20} POT.

events, the data extracted cross section per nucleon is

$$\sigma(\nu_\mu + \mathrm{Ar} \to \mu^- + X) = 0.693 \pm 0.010\,(\mathrm{stat.}) \times 10^{-38}\,\mathrm{cm}^2. \tag{7.15}$$

The MC cross section predicted by GENIE can be obtained by

$$\sigma_{\mathrm{MC}} = \frac{S}{\epsilon \cdot T^{\mathrm{MC}} \cdot \Phi_{\nu_\mu}}, \tag{7.16}$$

where S is the number of selected signal events, $S = 14657 \pm 51$, which gives

$$\sigma_{\mathrm{MC}} = 0.871 \pm 0.002\,(\mathrm{stat.}) \times 10^{-38}\,\mathrm{cm}^2. \tag{7.17}$$

The percental difference between the two cross sections is $(\sigma - \sigma_{\mathrm{MC}})/\sigma_{\mathrm{MC}} = -20.4\%$, which is covered by the total systematic uncertainty as will be shown in the next chapters. The total cross section from data and MC is also shown in Figure 7.4. Note that the cross section is divided by the neutrino energy in this plot. The horizontal bars on the x axis come from the width of the neutrino energy spectrum,

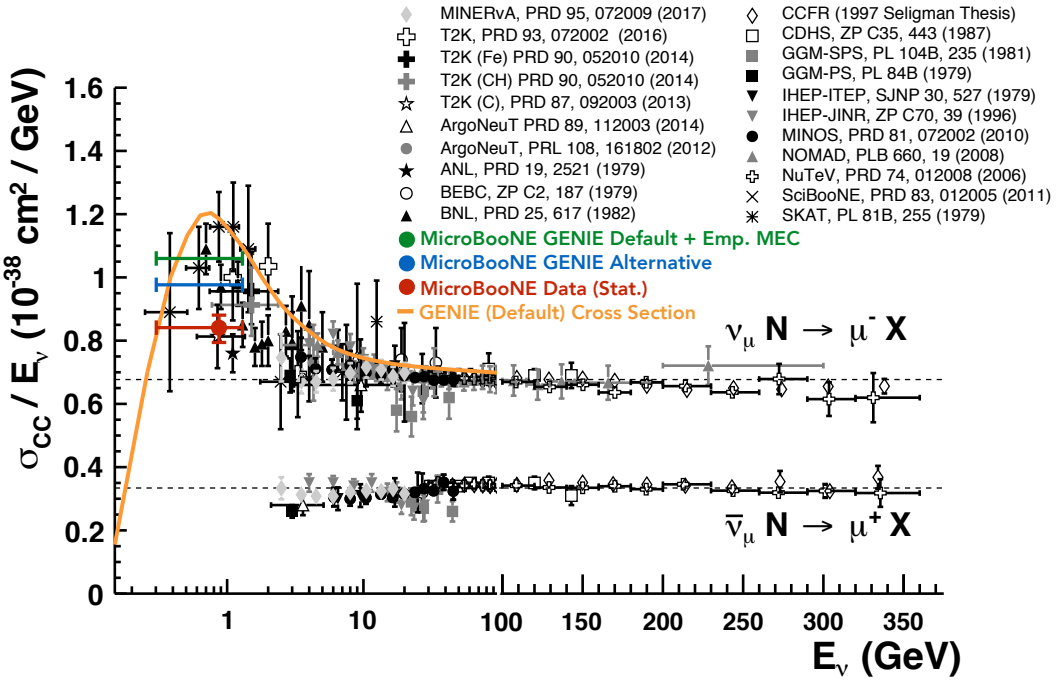

Figure 7.4: CC inclusive measurements for ν_μ and $\bar{\nu}_\mu$ from different experiments with different nuclear targets in black and grey. The green and blue points show the MC predicted cross section by the GENIE default and alternative configurations, respectively. The red point shows the data extracted cross section from the analysis presented in this thesis. Only statistical uncertainties are shown. The orange curve shows the GENIE default initial cross section as a function of neutrino energy.

shown in Section 7.1.1.

7.3 Differential Cross Section in Muon Momentum

This section presents the calculation of the single differential cross section in muon momentum p_μ. The cross section is calculated according to Equation (7.2) and the number of events per bin is shown in Table 7.3.

The simulated distributions must be smeared in order to calculate the efficiency as a function of reconstructed muon momentum, using Equation (7.7). The

Bin	Data		MC						
	Selected Events	Cosmic Only	ν_μ CC Signal	Cosmic in BNB	OUTFV	DIRT	NC	ν_e and $\bar{\nu}_e$	$\bar{\nu}_\mu$
1	728 ± 26	374 ± 13	201.8 ± 3.8	80.1 ± 2.4	77.3 ± 2.3	65.1 ± 1.9	77.9 ± 2.4	2.40 ± 0.37	1.54 ± 0.33
2	4213 ± 64	1748 ± 29	1786 ± 11	286.7 ± 4.6	480.9 ± 5.9	293.5 ± 4.1	184.1 ± 3.6	5.0 ± 0.55	12.41 ± 0.96
3	6670 ± 81	2303 ± 33	3193 ± 15	336.0 ± 4.9	636.8 ± 6.8	347.4 ± 4.4	126.0 ± 3.0	4.49 ± 0.52	21.1 ± 1.2
4	8126 ± 90	1853 ± 30	5241 ± 19	381.4 ± 5.3	633.3 ± 6.8	250.1 ± 3.8	61.2 ± 2.1	2.83 ± 0.44	39.3 ± 1.7
5	5351 ± 73	1496 ± 27	3758 ± 16	506.9 ± 6.1	352.9 ± 5.1	121.9 ± 2.6	25.5 ± 1.4	1.18 ± 0.28	42.4 ± 1.8
6	1905 ± 43	944 ± 21	1101.0 ± 8.9	313.4 ± 4.8	113.5 ± 2.8	122.1 ± 2.6	10.9 ± 0.8	0.61 ± 0.20	16.72 ± 1.2

Table 7.3: The table shows the number of selected events per p_μ reconstructed bin and different categories. Only statistical uncertainties are shown.

migration matrix was estimated from simulation and is found to be

$$S_{ij} = \begin{bmatrix} 0.210 & 0.0546 & 0.00343 & 0.00133 & 0.000822 & 0.000555 & 0.000442 \\ 0.467 & 0.640 & 0.130 & 0.0141 & 0.00593 & 0.00324 & 0.00434 \\ 0.190 & 0.247 & 0.671 & 0.134 & 0.0219 & 0.0152 & 0.0201 \\ 0.0739 & 0.0380 & 0.175 & 0.723 & 0.222 & 0.0818 & 0.0867 \\ 0.0390 & 0.0122 & 0.014 & 0.116 & 0.660 & 0.357 & 0.214 \\ 0.0161 & 0.00655 & 0.00524 & 0.00923 & 0.0856 & 0.522 & 0.539 \\ 0.0039 & 0.00134 & 0.00104 & 0.00139 & 0.00345 & 0.0202 & 0.135 \end{bmatrix}. \tag{7.18}$$

The migration matrix is also illustrated in Figure 7.5. Note that entries $i = 7, \forall j$ and $j = 7, \forall i$ show the overflow values (muon momentum above 2.5 GeV).

Figure 7.6a shows the distribution of the true muon momentum for all generated muons from ν_μ CC interactions in the FV and for selected events. The ratio of these two distributions is shown in Figure 7.6c, which corresponds the efficiency as a function of the true muon momentum. This is the same as the one shown in the previous chapter, but now with the final binning.

On the right side of Figure 7.6, the smeared distributions for both the selected and generated events (7.6b), and the new efficiency $\tilde{\epsilon}$ as a function of the reconstructed muon momentum (7.6d) are shown. This efficiency will be used for the

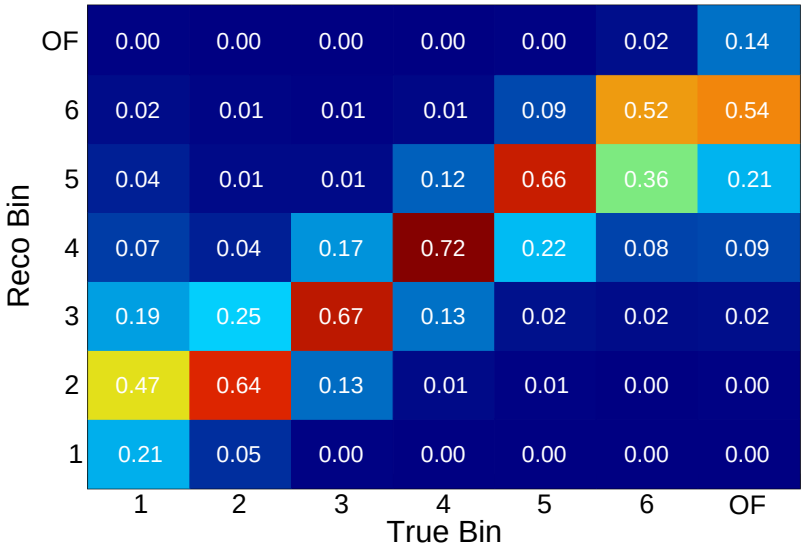

Figure 7.5: Smearing matrix for the p_μ distributions. It shows the probability that an event in a true bin is observed in a reconstructed bin. "OF" shows the overflow bin (muon momentum above 2.5 GeV).

cross-section calculation.

Putting all the quantities calculated in the previous sections into Equation (7.2), the ν_μ CC inclusive differential cross section on argon as a function of muon momentum is extracted and shown in Figure 7.7.

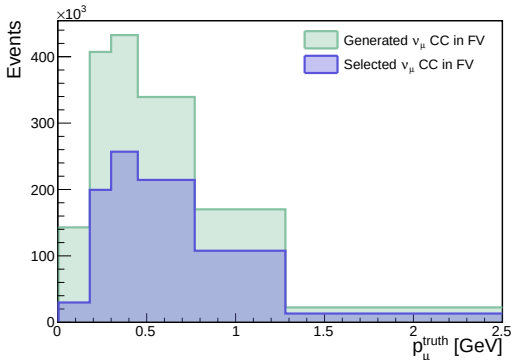

(a) Before smearing.

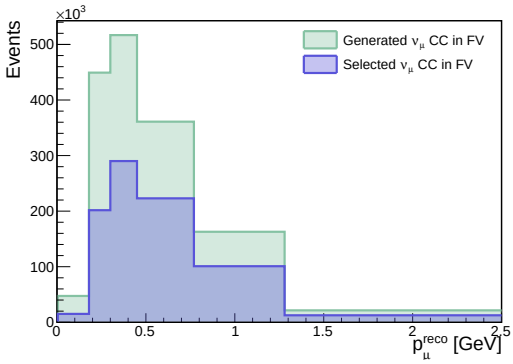

(b) After smearing.

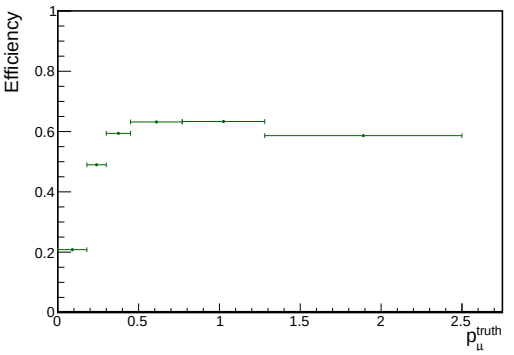

(c) Before smearing.

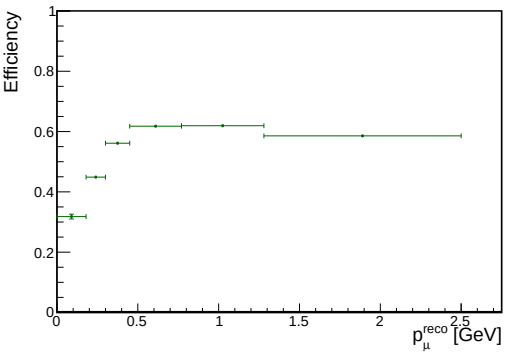

(d) After smearing.

Figure 7.6: Top: distributions of the generated (green) and selected (blue) signal events in terms of the simulated variable p_μ^{truth} (a) and, after smearing, in terms of the reconstructed variable p_μ^{reco} (b). Bottom: ratio of the distributions above, meaning the efficiency in p_μ^{truth} (c) and in p_μ^{reco} (d).

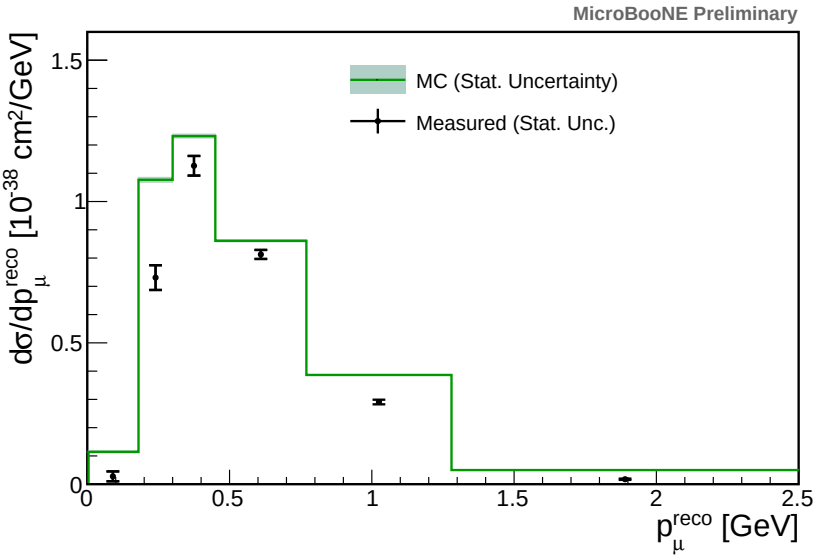

Figure 7.7: ν_μ CC inclusive differential cross section on argon per nucleon as a function of the reconstructed muon momentum. The black data points show the data extracted cross section, while the green curve shows the MC predicted cross section. The data error bars and the MC error bands show statistical uncertainties only. Systematic uncertainties are treated in Chapter 8.

Bin	Data		MC						
	Selected Events	Cosmic Only	ν_μ CC Signal	Cosmic in BNB	OUTFV	DIRT	NC	ν_e and $\bar{\nu}_e$	$\bar{\nu}_\mu$
1	1739 ± 42	363 ± 13	388.2 ± 5.4	77.6 ± 2.4	374.9 ± 5.3	322.4 ± 4.3	55.2 ± 2.0	1.17 ± 0.26	3.22 ± 0.49
2	2755 ± 52	1433 ± 26	715.6 ± 7.3	275.0 ± 4.5	218.0 ± 4.0	171.8 ± 3.1	51.4 ± 2.0	1.89 ± 0.34	2.39 ± 0.42
3	5128 ± 72	3187 ± 40	975.7 ± 8.5	647.6 ± 7.0	246.4 ± 4.3	289.7 ± 4.1	53.7 ± 2.0	1.81 ± 0.35	3.40 ± 0.50
4	3303 ± 57	1745 ± 29	1071 ± 8.9	413.4 ± 5.5	177.3 ± 3.6	161.3 ± 3.0	39.6 ± 1.7	1.28 ± 0.27	6.19 ± 0.68
5	3190 ± 56	1187 ± 24	1603 ± 11	295.1 ± 4.7	202.9 ± 3.9	104.1 ± 2.4	50.2 ± 1.9	1.58 ± 0.31	7.96 ± 0.77
6	3037 ± 55	579 ± 17	2151 ± 12	158.8 ± 3.4	229.9 ± 4.1	66.1 ± 1.9	56.9 ± 2.1	1.64 ± 0.32	14.3 ± 1.0
7	2702 ± 52	250 ± 11	2418 ± 13	63.3 ± 2.2	237.4 ± 4.2	42.8 ± 1.5	56.8 ± 2.1	2.02 ± 0.36	19.1 ± 1.2
8	2883 ± 52	92.5 ± 6.7	3063 ± 15	24.5 ± 1.3	303.7 ± 4.8	57.9 ± 1.8	59.8 ± 2.1	2.55 ± 0.42	31.9 ± 1.5
9	2460 ± 50	30.8 ± 3.9	2962 ± 15	6.06 ± 0.67	317.7 ± 4.8	106.1 ± 2.4	64.9 ± 2.2	2.61 ± 0.41	45.2 ± 1.9

Table 7.4: Number of selected events per $\cos\theta_\mu$ reconstructed bin and different categories. Only statistical uncertainties are shown.

7.4 Differential Cross Section in Muon Angle

This section presents the calculation of the single differential cross section in muon angle $\cos\theta_\mu$. The cross section is calculated according to Equation (7.2) and the number of events per bin is shown in Table 7.4.

As it was done for the cross section as a function of p_μ, the true distributions need to be smeared in order to calculate the efficiency as a function of reconstructed muon angle, using Equation 7.7. The migration matrix obtained is

$$S_{ij} = \begin{bmatrix} 0.462 & 0.0389 & 0.00706 & 0.00605 & 0.0151 & 0.0156 & 0.0113 & 0.00796 & 0.00829 \\ 0.0631 & 0.565 & 0.112 & 0.0296 & 0.0139 & 0.00517 & 0.00459 & 0.00314 & 0.00254 \\ 0.0229 & 0.176 & 0.659 & 0.129 & 0.0105 & 0.00725 & 0.00554 & 0.00412 & 0.00435 \\ 0.0234 & 0.0832 & 0.139 & 0.612 & 0.108 & 0.0067 & 0.00429 & 0.00397 & 0.00300 \\ 0.0812 & 0.0429 & 0.0171 & 0.177 & 0.653 & 0.108 & 0.0066 & 0.00339 & 0.00237 \\ 0.0970 & 0.0161 & 0.0145 & 0.0129 & 0.171 & 0.676 & 0.117 & 0.00502 & 0.00245 \\ 0.0732 & 0.0171 & 0.0125 & 0.0114 & 0.011 & 0.165 & 0.678 & 0.101 & 0.00311 \\ 0.0744 & 0.0233 & 0.0194 & 0.0111 & 0.00888 & 0.00966 & 0.166 & 0.743 & 0.111 \\ 0.103 & 0.0372 & 0.0197 & 0.0116 & 0.00842 & 0.00606 & 0.00718 & 0.129 & 0.863 \end{bmatrix}. \tag{7.19}$$

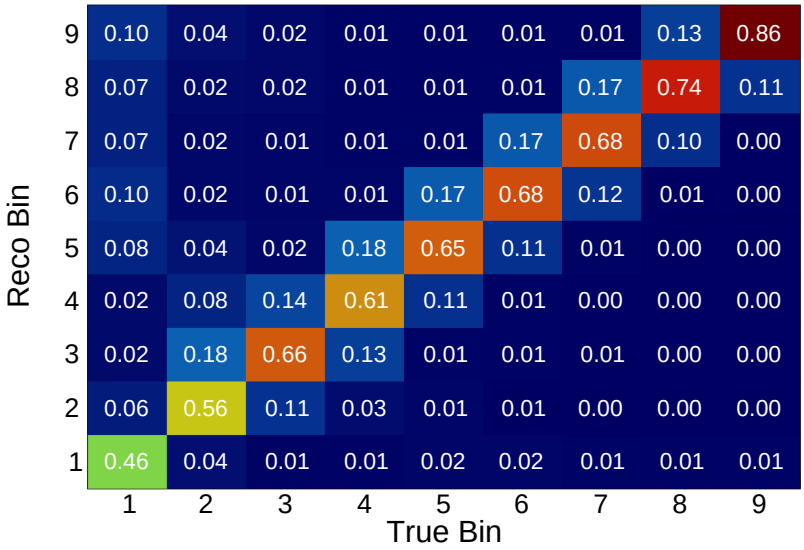

Figure 7.8: Smearing matrix for the $\cos\theta_\mu$ distributions. It shows the probability that an event in true bin j is observed in reconstructed bin i.

It is also illustrated in Figure 7.8. There are no entries showing overflow values in this matrix, as there are no overflows: $-1 \leq \cos(\theta) \leq 1$.

Figure 7.9a shows the distributions of the true muon momentum for all generated muons from ν_μ CC interactions in the FV and for the selected ones. The ratio of these two distributions is shown in Figure 7.9c, which represents the efficiency as a function of the true muon angle. This corresponds to the efficiency shown in the previous chapter, but here using the final binning.

On the right side of Figure 7.9, the smeared distributions for both the selected and generated events (7.9b) are shown, and the new efficiency $\tilde{\epsilon}$ as a function of the reconstructed muon angle (7.9d). This efficiency will be used for the cross-section calculation.

Putting all the quantities calculated in the previous sections into Equation (7.2), the ν_μ CC inclusive differential cross section on argon in muon angle is extracted and shown in Figure 7.10.

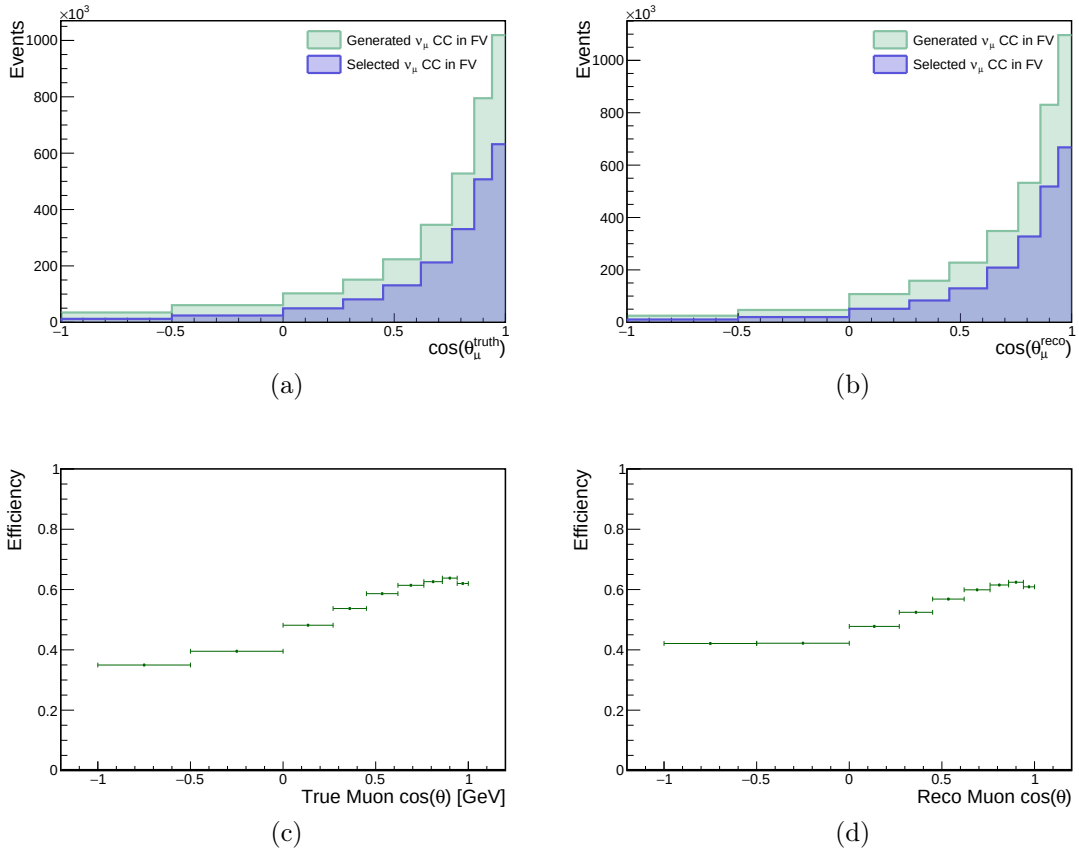

Figure 7.9: Top: distributions of the generated (green) and selected (blue) signal events in terms of the simulated variable $\cos\theta_\mu^{\text{truth}}$ (a) and, after smearing, in terms of the reconstructed variable $\cos\theta_\mu^{\text{reco}}$ (b). Bottom: ratio of the distributions above, meaning the efficiency in $\cos\theta_\mu^{\text{truth}}$ (c) and in $\cos\theta_\mu^{\text{reco}}$ (d).

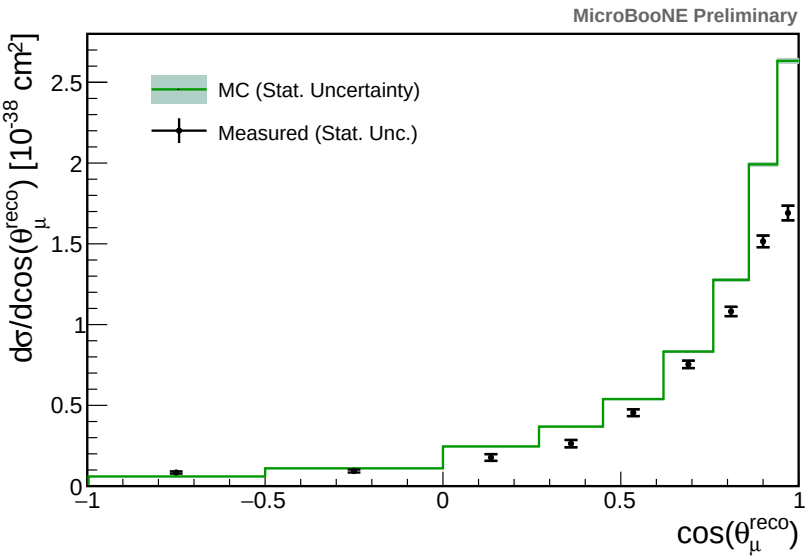

Figure 7.10: ν_μ CC inclusive differential cross section on argon per nucleon as a function per nucleonof the cosine of the reconstructed muon polar angle (angle w.r.t. the beam). The black data points show the data extracted cross section, while the green curve shows the MC predicted cross section. The data error bars and the MC error bands show the statistical uncertainty only, for data and MC respectively. Systematic uncertainties are treated in Chapter 8.

7.5 Double-Differential Cross Section

This section shows the calculation of the double-differential cross section in muon momentum p_μ and cosine of the muon angle $\cos\theta_\mu$. The cross section is calculated according to Equation (7.3) and the number of events per bin is shown in Table 7.5.

As done for the single differential cross sections, the true distributions need to be smeared in order to calculate the efficiency as a function of reconstructed muon momentum and muon angle, using Equation (7.7). The migration matrix is calculated according to this formula and is illustrated in Figure 7.11. The GENIE simulator does not simulate events in the region of phase space covered by true bin 5 and 10. By looking at Figure 7.3, this is a region of phase space where the muon is emitted in the opposite direction compared to the neutrino one, and has high momentum. The simulator does not produce such events as they would violate the conservation of momentum. For this reason, the value of the matrix for those specific bins is set to $S_{5,5} = S_{10,10} = 1$ and $S_{i,5} = 0\,\forall i \neq 5$ and $S_{i,10} = 0\,\forall i \neq 10$.

Figure 7.12a shows the distributions of the true muon momentum for all generated muons from ν_μ CC interactions in the FV and Figure 7.12c shows the same distribution only for the selected events. The ratio of these two distributions is shown in Figure 7.12e, which shows the efficiency as a function of the true muon momentum.

On the right side of Figure 7.12, the smeared distributions for both the selected and generated events (7.12b, 7.12d), and the new efficiency $\tilde{\epsilon}$ as a function of the reconstructed muon momentum (7.12f) are shown. This 2-dimensional efficiency will be used for the cross-section calculation.

Putting all the quantities calculated in the previous sections into Equation 7.3, the ν_μ CC inclusive double-differential cross section on argon is extracted, as shown

Bin	Data		MC						
	Selected Events	Cosmic Only	ν_μ CC Signal	Cosmic in BNB	OUTFV	DIRT	NC	ν_e and $\bar{\nu}_e$	$\bar{\nu}_\mu$
1	120 ± 10	38.1 ± 4.3	26.5 ± 1.4	9.44 ± 0.83	13.5 ± 1.0	13.64 ± 0.89	12.00 ± 0.96	0.42 ± 0.15	0.36 ± 0.16
2	489 ± 22	82.2 ± 6.3	173.3 ± 3.5	15.5 ± 1.0	86.2 ± 2.5	96.3 ± 2.3	24.8 ± 1.3	0.44 ± 0.17	1.46 ± 0.32
3	600 ± 24	85.1 ± 6.4	134.6 ± 3.1	12.86 ± 0.97	128.8 ± 3.1	121.9 ± 2.6	14.7 ± 1.0	0.23 ± 0.11	0.75 ± 0.23
4	375 ± 19	72.4 ± 5.9	45.52 ± 1.8	11.26 ± 0.91	107.1 ± 2.8	68.3 ± 1.9	2.44 ± 0.42	0.056 ± 0.056	0.31 ± 0.15
5	145 ± 12	77.3 ± 6.1	7.95 ± 0.76	25.5 ± 1.3	36.7 ± 1.6	17.5 ± 1.0	0.44 ± 0.18	0 ± 0.00	0.33 ± 0.17
6	148 ± 12	75.3 ± 6.0	40.4 ± 1.7	16.2 ± 1.0	14.4 ± 1.0	15.32 ± 0.94	13.7 ± 1.0	0.49 ± 0.18	0.21 ± 0.12
7	759 ± 27	372 ± 13	284.4 ± 4.6	56.5 ± 2.0	81.8 ± 2.4	54.2 ± 1.7	22.6 ± 1.2	0.59 ± 0.18	0.74 ± 0.23
8	890 ± 29	392 ± 13	283.9 ± 4.6	52.9 ± 1.9	81.1 ± 2.4	42.5 ± 1.5	9.84 ± 0.85	0.28 ± 0.12	0.98 ± 0.27
9	496 ± 22	259 ± 11	88.0 ± 2.5	51.7 ± 1.9	31.8 ± 1.5	18.5 ± 1.0	1.80 ± 0.37	0.28 ± 0.13	0.29 ± 0.14
10	443 ± 21	317 ± 12	17.4 ± 1.1	91.0 ± 2.6	7.45 ± 0.74	26.7 ± 1.2	3.02 ± 0.47	0.22 ± 0.11	0.14 ± 0.10
11	119 ± 10	83.7 ± 6.4	31.2 ± 1.5	15.6 ± 1.0	14.1 ± 1.0	10.02 ± 0.76	10.09 ± 0.86	0.22 ± 0.11	0.22 ± 0.12
12	1070 ± 32	600 ± 17	290.8 ± 4.6	87.9 ± 2.5	94.1 ± 2.6	58.7 ± 1.8	23.4 ± 1.3	0.65 ± 0.20	0.96 ± 0.26
13	1612 ± 40	886 ± 20	405.9 ± 5.5	123.4 ± 3.0	93.4 ± 2.6	60.9 ± 1.8	11.7 ± 0.93	0.52 ± 0.17	1.62 ± 0.34
14	1126 ± 33	708 ± 18	217.8 ± 4.0	144.4 ± 3.2	36.9 ± 1.6	45.6 ± 1.6	4.17 ± 0.55	0.29 ± 0.14	0.59 ± 0.20
15	1141 ± 33	869 ± 20	29.27 ± 1.4	262.3 ± 4.4	7.10 ± 0.72	74.9 ± 2.0	3.69 ± 0.52	0.10 ± 0.10	0.0 ± 0.0
16	768 ± 27	409 ± 14	265.8 ± 4.4	71.9 ± 2.3	70.8 ± 2.3	38.1 ± 1.4	23.7 ± 1.3	0.77 ± 0.21	2.06 ± 0.39
17	978 ± 31	446 ± 14	413 ± 5.5	67.6 ± 2.2	65.8 ± 2.2	30.8 ± 1.3	8.99 ± 0.81	0.29 ± 0.12	2.15 ± 0.40
18	840 ± 28	351 ± 13	339.4 ± 5.0	79.7 ± 2.4	31.8 ± 1.5	19.7 ± 1.0	3.99 ± 0.54	0.063 ± 0.063	1.82 ± 0.38
19	673 ± 25	502 ± 15	51.6 ± 1.9	184.6 ± 3.7	8.16 ± 0.77	41.5 ± 1.5	2.45 ± 0.42	0.147 ± 0.087	0.15 ± 0.10
20	597 ± 24	255 ± 11	270.4 ± 4.4	48.5 ± 1.9	60.5 ± 2.1	28.0 ± 1.2	29.9 ± 1.4	0.69 ± 0.19	1.93 ± 0.37
21	896 ± 29	283 ± 11	513.2 ± 6.1	44.1 ± 1.8	71.3 ± 2.3	20.2 ± 1.0	13.01 ± 0.98	0.49 ± 0.17	3.13 ± 0.48
22	1029 ± 32	253 ± 11	656.8 ± 6.9	52.9 ± 1.9	55.9 ± 2.0	14.03 ± 0.90	4.58 ± 0.57	0.073 ± 0.073	2.18 ± 0.40
23	649 ± 25	372 ± 13	161.1 ± 3.4	141.3 ± 3.2	14.6 ± 1.0	22.8 ± 1.1	2.50 ± 0.42	0.30 ± 0.14	0.71 ± 0.22
24	382 ± 19	106.7 ± 7.2	233.5 ± 4.1	26.0 ± 1.3	48.6 ± 1.9	18.6 ± 1.0	30.2 ± 1.4	0.66 ± 0.19	1.79 ± 0.36
25	741 ± 27	139.5 ± 8.2	510.5 ± 6.1	21.3 ± 1.2	63.0 ± 2.1	15.76 ± 0.95	13.7 ± 1.0	0.36 ± 0.15	3.52 ± 0.51
26	1241 ± 35	132.6 ± 8.0	988.2 ± 8.5	26.7 ± 1.4	84.3 ± 2.5	12.00 ± 0.83	9.19 ± 0.82	0.47 ± 0.18	6.20 ± 0.70
27	648 ± 25	186 ± 9.5	415.4 ± 5.5	79.1 ± 2.4	33.0 ± 1.5	10.83 ± 0.79	3.30 ± 0.49	0.137 ± 0.097	2.87 ± 0.46
28	211 ± 14	54.8 ± 5.1	156.5 ± 3.4	10.19 ± 0.87	31.4 ± 1.5	8.65 ± 0.70	26.3 ± 1.4	0.85 ± 0.22	1.77 ± 0.36
29	398 ± 19	50.4 ± 4.9	383.9 ± 5.3	8.92 ± 0.81	50.8 ± 1.9	13.60 ± 0.88	15.1 ± 1.0	0.77 ± 0.21	3.14 ± 0.48
30	1141 ± 33	53.8 ± 5.1	1037.0 ± 8.7	10.62 ± 0.88	90.2 ± 2.5	12.93 ± 0.86	10.13 ± 0.86	0.17 ± 0.10	7.04 ± 0.73
31	791 ± 28	38.1 ± 4.3	718.3 ± 7.3	12.64 ± 0.97	54.3 ± 2.0	2.96 ± 0.41	4.04 ± 0.54	0.21 ± 0.12	5.91 ± 0.68
32	146 ± 12	41.6 ± 4.5	114.8 ± 2.9	15.2 ± 1.0	9.07 ± 0.81	2.03 ± 0.34	0.89 ± 0.25	0.0 ± 0.0	1.10 ± 0.32
33	170 ± 13	33.7 ± 4.0	118.0 ± 2.9	5.85 ± 0.65	23.3 ± 1.3	8.27 ± 0.69	21.8 ± 1.2	0.65 ± 0.21	1.46 ± 0.33
34	312 ± 17	12.7 ± 2.4	315.2 ± 4.8	4.01 ± 0.54	45.9 ± 1.8	18.8 ± 1.0	18.1 ± 1.1	0.59 ± 0.19	2.52 ± 0.43
35	1080 ± 32	12.7 ± 2.4	1046.0 ± 8.8	3.27 ± 0.49	102.6 ± 2.7	22.5 ± 1.1	11.81 ± 0.93	0.79 ± 0.23	10.05 ± 0.88
36	1079 ± 32	15.6 ± 2.7	1207.0 ± 9.4	3.05 ± 0.47	99.1 ± 2.7	6.42 ± 0.61	5.89 ± 0.65	0.28 ± 0.14	13.01 ± 0.99
37	234 ± 15	14.1 ± 2.6	359.9 ± 5.1	4.53 ± 0.58	29.8 ± 1.4	0.98 ± 0.23	1.95 ± 0.37	0.21 ± 0.12	4.86 ± 0.61
38	108 ± 10	11.2 ± 2.3	96.9 ± 2.6	2.85 ± 0.45	18.9 ± 1.1	8.59 ± 0.70	22.4 ± 1.2	0.91 ± 0.23	0.95 ± 0.26
39	243 ± 15	5.3 ± 1.6	232.5 ± 4.1	0.74 ± 0.23	36.4 ± 1.6	22.7 ± 1.1	20.7 ± 1.2	0.91 ± 0.23	3.29 ± 0.49
40	798 ± 28	7.8 ± 1.9	821.2 ± 7.8	0.70 ± 0.22	92.4 ± 2.6	36.2 ± 1.4	13.17 ± 0.97	0.61 ± 0.20	10.81 ± 0.90
41	977 ± 31	2.4 ± 1.0	1223.0 ± 9.5	0.51 ± 0.19	114.6 ± 2.9	24.5 ± 1.1	5.88 ± 0.73	0.073 ± 0.073	20.1 ± 1.2
42	330 ± 18	3.4 ± 1.2	553.5 ± 6.3	0.50 ± 0.19	52.2 ± 1.9	12.54 ± 0.84	2.37 ± 0.41	0.088 ± 0.088	9.81 ± 0.97

Table 7.5: The table shows the number of selected events per $(\cos\theta_\mu, p_\mu)$ reconstructed bin and different categories. Only statistical uncertainties are shown.

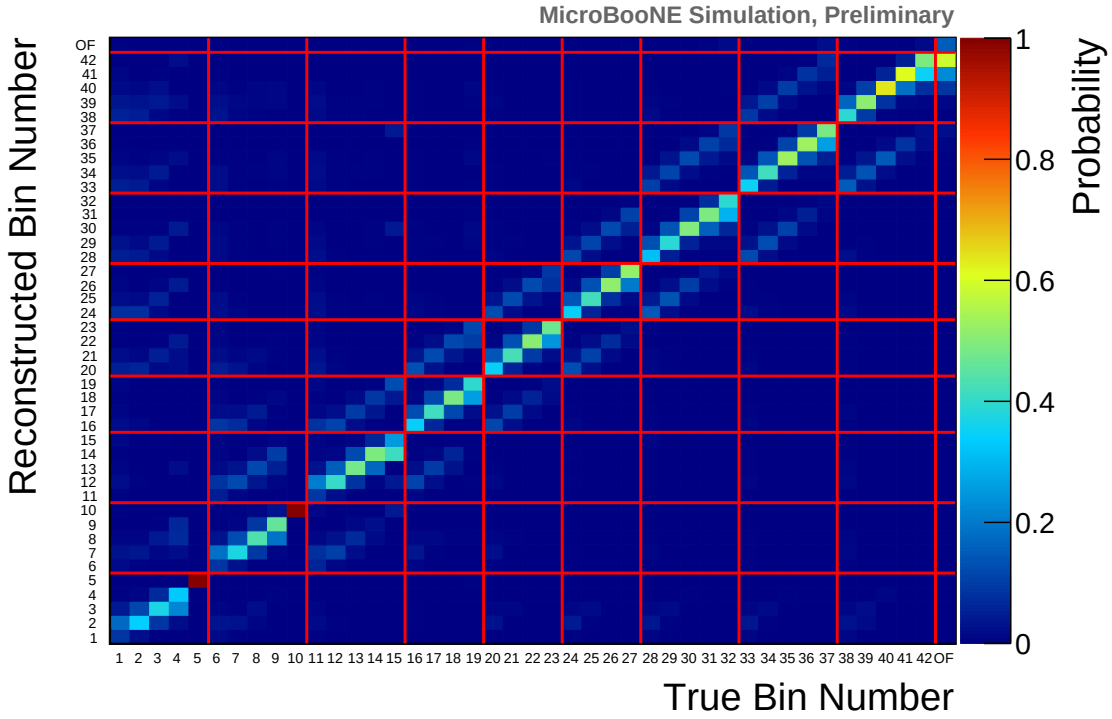

Figure 7.11: Migration matrix for the double-differential cross section in p_μ and $\cos\theta_\mu$. It shows the probability that an event in a certain true bin (y axis) is observed in a reconstructed bin (x axis).

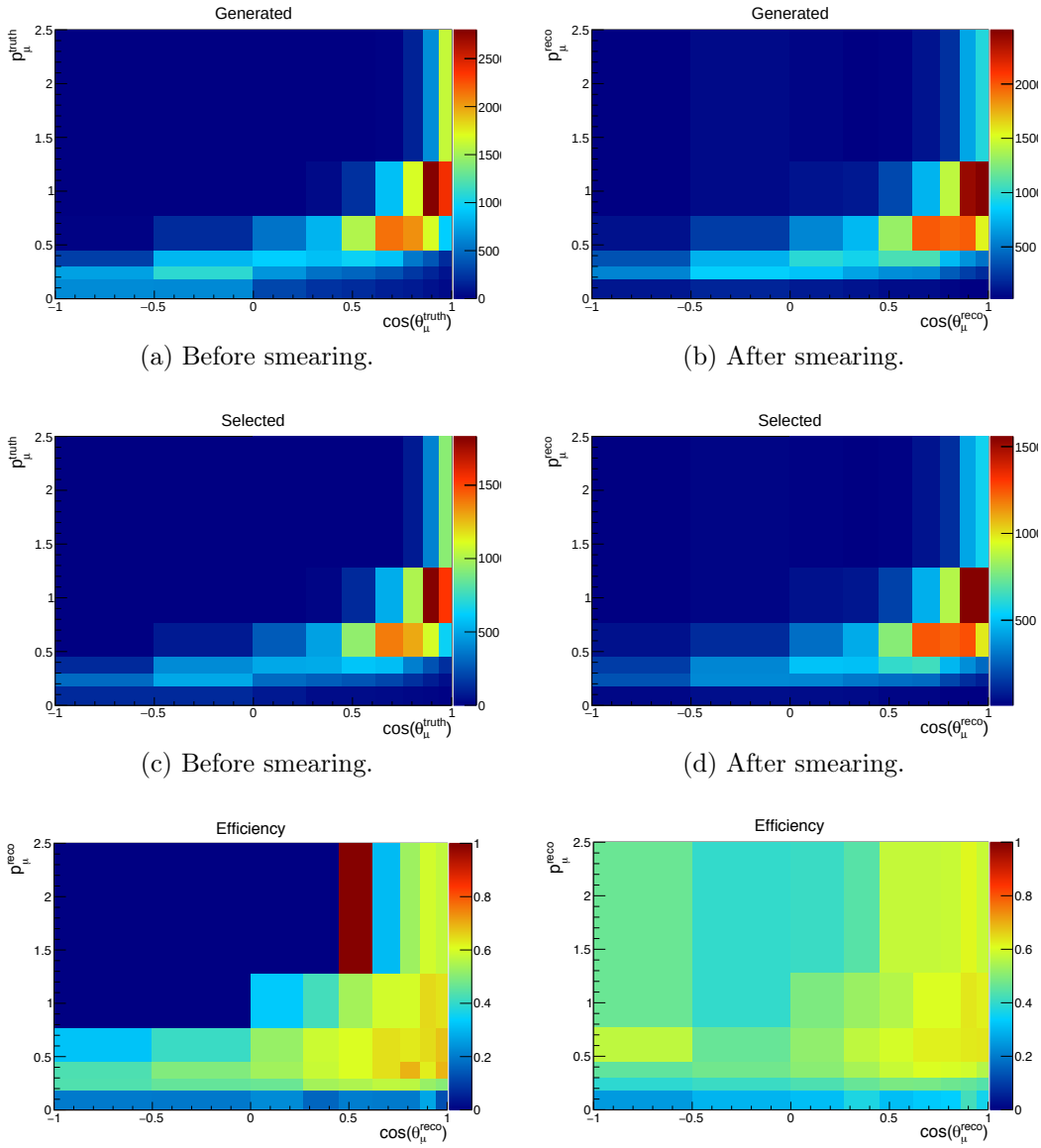

(a) Before smearing. (b) After smearing.

(c) Before smearing. (d) After smearing.

(e) Before smearing. (f) After smearing.

Figure 7.12: Top: distributions of the generated signal events in terms of the simulated variables $(p_\mu^{\text{truth}}, \cos\theta_\mu^{\text{truth}})$ (a) and, after smearing, the reconstructed variables $(p_\mu^{\text{reco}}, \cos\theta_\mu^{\text{reco}})$ (b). Middle: distributions of the selected signal events in terms of the simulated variables $(p_\mu^{\text{truth}}, \cos\theta_\mu^{\text{truth}})$ (c) and, after smearing, the reconstructed variable $(p_\mu^{\text{reco}}, \cos\theta_\mu^{\text{reco}})$ (d). Bottom: ratio of the distributions above, meaning the efficiency in $(p_\mu^{\text{truth}}, \cos\theta_\mu^{\text{truth}})$ (e) and in $(p_\mu^{\text{reco}}, \cos\theta_\mu^{\text{reco}})$ (f).

in Figure 7.13a for data and in Figure 7.13b for simulation. Data and simulation are also compared in Figure 7.14. Here, the data extracted cross section is compared to the default GENIE simulation as well as an alternative GENIE configuration, as previously described in Section 4.5. A more detailed comparison between these two simulations will be made in Chapter 9, once systematic uncertainties are incorporated into the analysis.

7.6 Cross-Section Extraction Summary

This chapter presented the procedure used to extract the total, single- and double-differential cross sections. In order to validate that the analysis framework is functioning correctly and that there are no significant biases in the cross-section results, fake data tests have performed as shown in Appendix C. The next chapter will discuss the systematic uncertainties that affect this measurement, and how they are estimated. The cross section with both statistical and systematic uncertainties will be shown in Chapter 9.

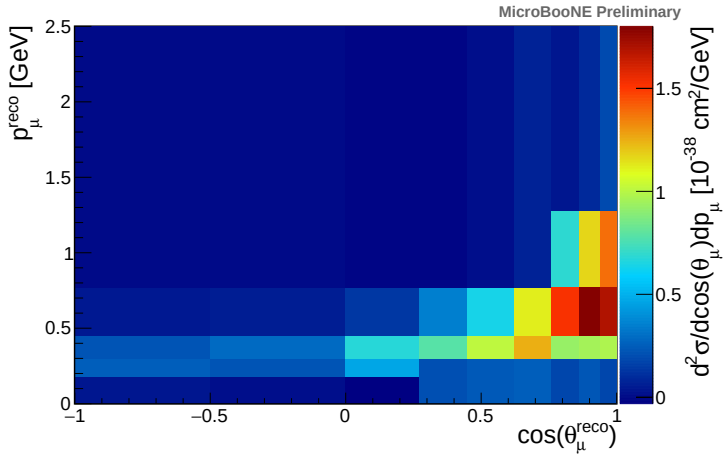

(a) Data.

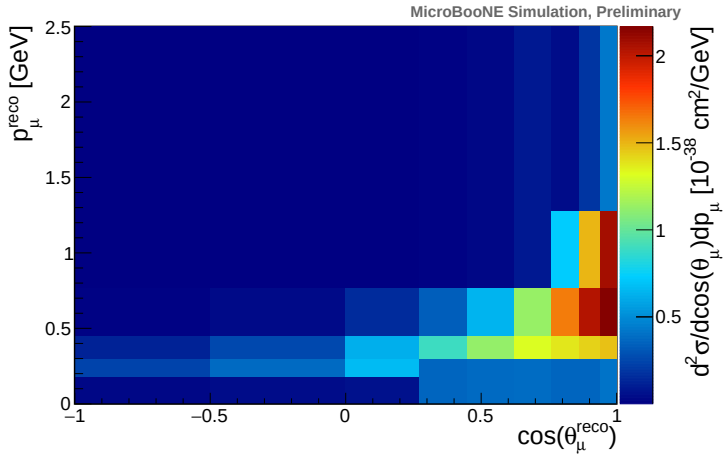

(b) Simulation.

Figure 7.13: ν_μ CC inclusive double-differential cross section on argon per nucleon as a function of the reconstructed muon momentum and cosine of the reconstructed muon polar angle (angle with respect to the incoming neutrino direction). The data extracted cross section is shown in Figure (a), while the MC prediction is shown in Figure (b). Only central values are shown in these plots.

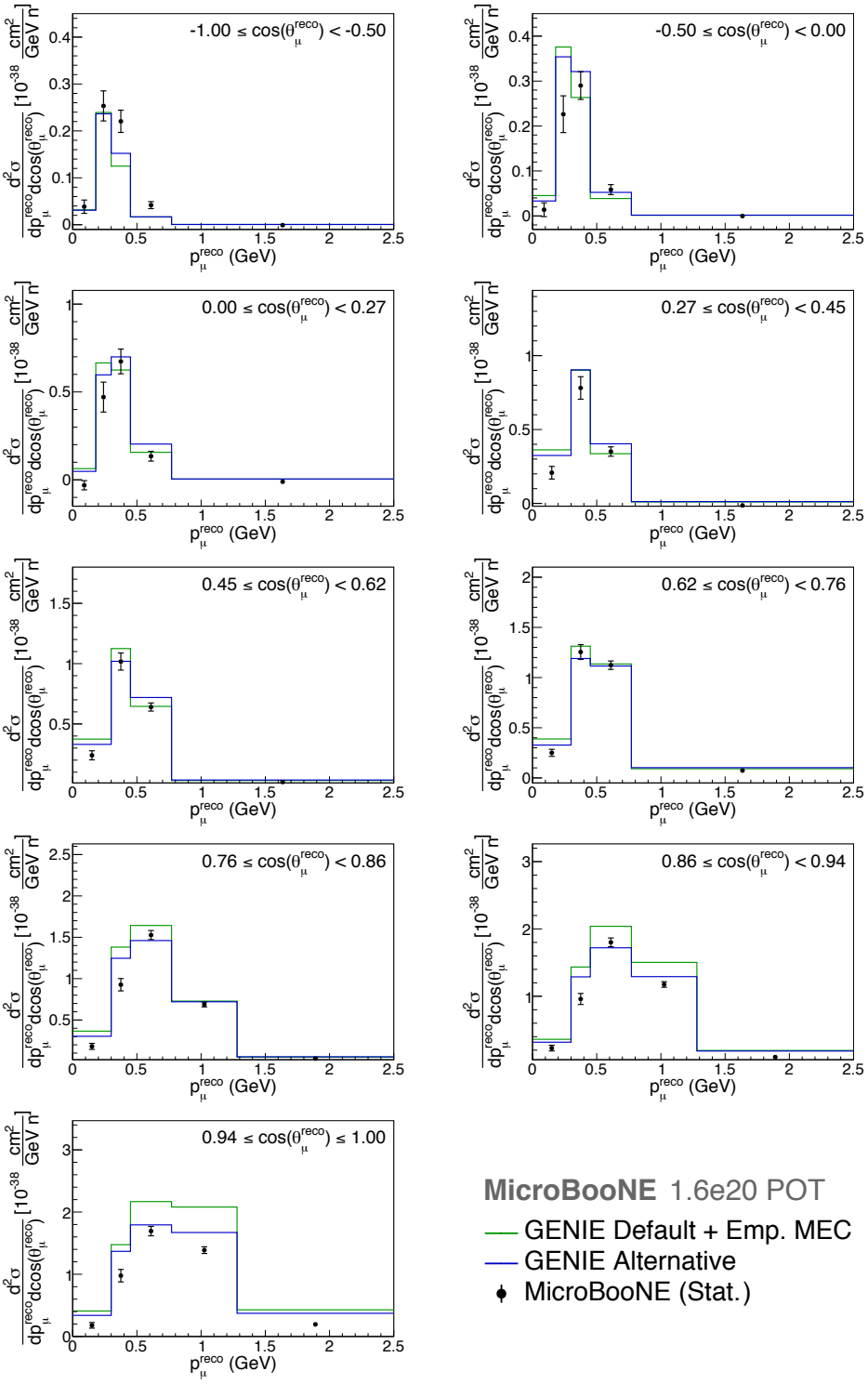

Figure 7.14: ν_μ CC inclusive double-differential cross section on argon per nucleon as a function of the reconstructed muon momentum and cosine of the reconstructed muon polar angle (angle with respect to the incoming neutrino direction). The error bars show statistical uncertainties only. The "Default GENIE + Emp. MEC" prediction prediction is shown in green, while the "GENIE Alternative" prediction is shown in blue. The error bars show statistical uncertainties only.

Chapter 8

Systematic Uncertainties

The precision of the cross section measurement depends not only on the statistics of the data but also on the understanding of the models and detector limitations, which are encoded in the systematic uncertainties. This chapter starts by describing how systematic uncertainties are propagated to the data extracted cross section, in Section 8.1, and then describes all the contributions to the systematic uncertainties that affect this measurement, which are summarised here:

Cross-Section Modelling Uncertainties on the parameters used to model neutrino interactions (used to estimate the number of background events and the efficiency) must be propagated to the final cross-section measurement. This is discussed in Section 8.2.

Neutrino Beam Flux Modelling Uncertainties on the parameters used to model the neutrino beam flux (used for simulating the initial neutrino energy, direction and location, and in the denominator of Equation (7.1)) must be propagated to the final cross-section measurement. This is discussed in Section 8.3.

Detector Modelling Detector limitations and uncertainties in detector param-

eters must be propagated to the final cross-section measurement. Detector parameter uncertainties primarily affect reconstructed quantities which, in turn, affect the measured vs. the predicted event rates. This is discussed in Section 8.4.

Simulated Cosmic Background Modelling The simulated CR rate at MicroBooNE can be different compared to the observed one. The impact of this effect must be included in the final cross-section uncertainties. This is discussed in Section 8.5.

Simulated Dirt Background Modelling Neutrino interactions happening outside the cryostat, in the dirt surrounding the detector, are difficult to simulate and an additional uncertainty must be included for this type of background. This is discussed in Section 8.6.

Simulation Statistical Uncertainty A finite simulated sample is used to estimate the number of background events and the efficiencies per bin. This leads to an uncertainty in the extracted data cross section. The impact of the simulation statistical uncertainties is discussed in Section 8.7.

Finally, Section 8.8 summarises all the systematic uncertainties.

8.1 Uncertainty Propagation

Uncertainties, both statistical and systematic, are encoded in a covariance matrix E. The total error matrix is a combination of the statistical and systematic uncertainties:

$$E = E^{\text{stat}} + E^{\text{syst}}, \tag{8.1}$$

where E^{stat} is the completely uncorrelated data statistical uncertainty matrix (diagonal), and E^{syst} is the systematic covariance matrix. The latter is a combination of independent matrices constructed for each of the systematic uncertainties considered:

$$E^{\text{syst}} = E^{\text{flux}} + E^{\text{xsec}} + E^{\text{detector}} + E^{\text{cosmic}} + E^{\text{dirt}} + E^{\text{MC stat}}. \tag{8.2}$$

The total systematic covariance matrix E^{syst}, related to the differential cross section in muon momentum and angle, has matrix element units of cm^4/GeV^2 or cm^4. The evaluation of these six systematic covariance matrices depends on the technique used to evaluate such uncertainties.

For both cross-section and flux systematics this analysis uses a *multisim* technique [123], which consists of generating several MC replicas, each one called "universe", where the model parameters are varied within their uncertainties. These universes are constructed by reweighting the baseline MC. A number N of such universes are created and combined to construct the covariance matrix:

$$E_{ij} = \frac{1}{N}\sum_{n=1}^{N}(\sigma_i^n - \sigma_i^{cv})(\sigma_j^n - \sigma_j^{cv}), \tag{8.3}$$

where σ is a shorthand notation for either the total, the single-, or the double-differential cross sections, shown in Equations (7.1), (7.2) and (7.3) respectively, and i and j correspond to bins in measured quantities, σ_i^{cv} is the central value cross section in bin i, and σ_i^n is the cross section evaluated in systematic universe n. The beam-on and beam-off data is untouched in every universe. What changes in the cross-section computation is the MC, i.e. efficiency, migration matrix and subtracted background events (and integrated flux in the case of flux systematics only).

A different strategy is followed for the detector modelling systematics. In this case *unisim* samples [123] are generated, where only one detector parameter at a time is changed by its uncertainty. Each parameter variation corresponds to a different MC run. The difference between the central value cross section and the cross section calculated with the new MC runs gives an indication of the systematic uncertainty on the cross section. For M detector parameters, the covariance matrix is [123]:

$$E_{ij}^{det} = \sum_{m,n=1}^{M} C_{mn}(\Delta\sigma_{mi} + S_{mi}) \cdot (\Delta\sigma_{nj} + S_{nj}), \tag{8.4}$$

where $\Delta\sigma_{mj} = \sigma_j^m - \sigma_j^{cv}$ is the observed cross-section number difference for the cross-section value in bin j due to a change in systematic parameter m. The derivative matrix $\Delta\sigma_{mj}$ can be considered as a change of variable matrix going from the systematic error indices m to the bin indices j. S_{mi} is the statistical fluctuation from the mean in unisim m in bin i. C_{mn} is the normalised covariance matrix (ones in the diagonal) for systematic uncertainties m and n. The experiment has currently no knowledge on C_{mn}, and the matrix is set to $C_{mn} = \delta_{mn}$, where δ_{mn} is the Kronecker delta. The exact same GENIE simulated events are used in all the different MC replicas, only the detector simulation changes, so that the statistical fluctuations S_{mi} are negligible. The systematic covariance matrix between bins i and j becomes:

$$E_{ij} = \sum_{m=1}^{M} (\sigma_i^m - \sigma_i^{cv})(\sigma_j^m - \sigma_j^{cv}). \tag{8.5}$$

The fractional covariance matrix is generally a more useful result as it indicates the fractional uncertainty per bin, and is defined as

$$F_{ij} = \frac{E_{ij}}{\sigma_i^{cv}\sigma_j^{cv}}. \tag{8.6}$$

From E_{ij} the linear correlation matrix can also be calculated as

$$\rho_{ij} = \frac{E_{ij}}{\sqrt{E_{ii}}\sqrt{E_{jj}}}, \qquad \text{where } -1 \leqslant \rho \leqslant 1. \tag{8.7}$$

The matrix in Equation (8.3) is statistically meaningful only if σ_i^{cv} approximately corresponds to the mean of the cross sections among all the universes:

$$\sigma_i^{cv} \sim m_i \qquad \text{where } m_i = \frac{1}{N}\sum_{s=1}^{N} \sigma_i^s. \tag{8.8}$$

Moreover, the uncertainties that are derived per bin i, $\sqrt{E_{ii}}$, have a coverage of 68% only if the distribution of the cross sections σ^s is a normal distribution. If any of the above is not true, one should consider a different approach for estimating the systematic uncertainties, for example based on a likelihood containing all the underlying probability distributions for all the different model parameters, and then constructing a 68% coverage region based on the likelihood itself. Where this is not possible, one may consider to keep using Equation (8.3) as an approximation of the real uncertainty. In this specific case, the conditions above are satisfied in the case of the GENIE systematics, but are not for the flux systematics. For the flux systematics, the mean m_i differs from the central value cross section σ_i^{cv}, for reasons that will be discussed in Section 8.3. In this case one may decompose the definition in Equation (8.3) into a proper covariance matrix V_{ij}, and a bias matrix, which measures the bias between the central value and the mean of the distribution, to obtain $E_{ij} = V_{ij} + B_{ij}$, where

$$\begin{aligned} V_{ij} &= \frac{1}{N}\sum_{s=1}^{N}(\sigma_i^s - m_i)(\sigma_j^s - m_j), \\ B_{ij} &= (m_i - \sigma_i^{cv})(m_j - \sigma_j^{cv}), \end{aligned} \tag{8.9}$$

in fact:

$$
\begin{aligned}
V_{ij} + B_{ij} = \\
&= \frac{1}{N}\sum_{s=1}^{N}(\sigma_i^s\sigma_j^s - \sigma_i^s m_j - m_i\sigma_j^s + m_i m_j) + m_i m_j - m_i\sigma_j^{cv} - \sigma_i^{cv} m_j + \sigma_i^{cv}\sigma_j^{cv} \\
&= \frac{1}{N}\sum_{s=1}^{N}(\sigma_i^s\sigma_j^s - \sigma_i^s\sigma_j^{cv} - \sigma_i^{cv}\sigma_j^s + \sigma_i^{cv}\sigma_j^{cv}) \\
&= \frac{1}{N}\sum_{s=1}^{N}(\sigma_i^s - \sigma_i^{cv})(\sigma_j^s - \sigma_j^{cv}) \equiv E_{ij}.
\end{aligned}
\tag{8.10}
$$

In an ideal scenario, $B_{ij} = 0 \ \forall \ i, j$.

Except for the cross-section modelling uncertainty, the following sections will not show the covariance matrices for all systematics, which are instead collected in Appendix B. For the cross-section modelling all the matrices are shown and explained. The total covariance matrix is shown in the next chapter, together with the cross-section results.

8.2 Cross-Section Uncertainties

The GENIE simulator provides a built-in framework of event reweighting for evaluating systematic uncertainties in an analysis [62, 52]. Given a certain physics parameter P with estimated prior uncertainty δP, the effect on the final cross section if this parameter is changed to $P' = P + x_p\delta P$, where x_P is a systematic parameter, is shown in this section. A list of the systematic parameters is given in Table 8.1.

Here, the effect of reweighting all GENIE parameters at the same time is studied in order to evaluate the systematic uncertainty on the measurement. For each

Parameter P	Description of P	Value	$\delta P/P$
M_A^{NCEL}	Axial mass for NC elastic	0.990 GeV	$\pm 25\%$
η^{NCEL}	Strange axial form factor η for NC elastic	0.120 GeV	$\pm 30\%$
M_A^{CCQE}	Axial mass for CC QE	0.990 GeV	$-15\% + 25\%$
M_A^{CCRES}	Axial mass for CC resonance neutrino production	1.120 GeV	$\pm 20\%$
M_V^{CCRES}	Vector mass for CC resonance neutrino production	0.840 GeV	$\pm 10\%$
M_A^{NCRES}	Axial mass for NC resonance neutrino production	1.120 GeV	$\pm 20\%$
M_V^{NCRES}	Vector mass for NC resonance neutrino production	0.840 GeV	$\pm 10\%$
$M_A^{COH\pi}$	Axial mass for CC and NC coherent pion production	1.000 GeV	$\pm 50\%$
$R_0^{COH\pi}$	Nuclear size param. controlling π absorption in RS model	1.000 fm	$\pm 10\%$
CCQE-PauliSup (p)	CCQE Pauli suppression (via changes in Fermi level k_F)	0.242 GeV	$\pm 35\%$
CCQE-PauliSup (n)	CCQE Pauli suppression (via changes in Fermi level k_F)	0.259 GeV	$\pm 35\%$
A_{HT}^{BY}	A_{HT} higher-twist param in BY model scaling variable ξ_w	0.538	$\pm 25\%$
B_{HT}^{BY}	B_{HT} higher-twist param in BY model scaling variable ξ_w	0.305	$\pm 25\%$
C_{V1u}^{BY}	C_{V1u} u valence GRV98 PDF correction param in BY model	0.291	$\pm 30\%$
C_{V2u}^{BY}	C_{V2u} u valence GRV98 PDF correction param in BY model	0.189	$\pm 40\%$
FZ (pion)	Hadron formation zone	0.342 fm	$\pm 50\%$
FZ (nucleon)	Hadron formation zone	2.300 fm	$\pm 50\%$
$BR(\gamma)$	Branching ratio for radiative resonance decays	-	$\pm 50\%$
$BR(\eta)$	Branching ratio for single-η resonance decays	-	$\pm 50\%$
$R_{\nu p}^{CC1\pi}$	Non-resonance bkg in νp $CC1\pi$ reactions	-	$\pm 50\%$
$R_{\nu p}^{CC2\pi}$	Non-resonance bkg in νp $CC2\pi$ reactions	-	$\pm 50\%$
$R_{\nu n}^{CC1\pi}$	Non-resonance bkg in νn $CC1\pi$ reactions	-	$\pm 50\%$
$R_{\nu n}^{CC2\pi}$	Non-resonance bkg in νn $CC2\pi$ reactions	-	$\pm 50\%$
$R_{\nu p}^{CC1\pi}$	Non-resonance bkg in νp $NC1\pi$ reactions	-	$\pm 50\%$
$R_{\nu p}^{CC2\pi}$	Non-resonance bkg in νp $NC2\pi$ reactions	-	$\pm 50\%$
$R_{\nu n}^{CC1\pi}$	Non-resonance bkg in νn $NC1\pi$ reactions	-	$\pm 50\%$
$R_{\nu n}^{CC2\pi}$	Non-resonance bkg in νn $NC2\pi$ reactions	-	$\pm 50\%$
x_{abs}^{N}	Nucleon mean free path (total rescattering probability)	-	$\pm 20\%$
x_{cex}^{N}	Nucleon charge exchange probability	-	$\pm 50\%$
x_{el}^{N}	Nucleon elastic reaction probability	-	$\pm 30\%$
x_{inel}^{N}	Nucleon inelastic reaction probability	-	$\pm 40\%$
x_{mfp}^{N}	Nucleon absorption probability	-	$\pm 20\%$
x_{pi}^{N}	Nucleon π-production probability	-	$\pm 20\%$
x_{abs}^{PI}	π mean free path (total rescattering probability)	-	$\pm 20\%$
x_{cex}^{PI}	π charge exchange probability	-	$\pm 50\%$
x_{el}^{PI}	π elastic reaction probability	-	$\pm 10\%$
x_{inel}^{PI}	π inelastic reaction probability	-	$\pm 40\%$
x_{mfp}^{PI}	π absorption probability	-	$\pm 20\%$
x_{pi}^{PI}	π π-production probability	-	$\pm 20\%$

Table 8.1: Neutrino interaction model parameters and uncertainties. This information is reproduced here from the GENIE User Manual [52] for convenience.

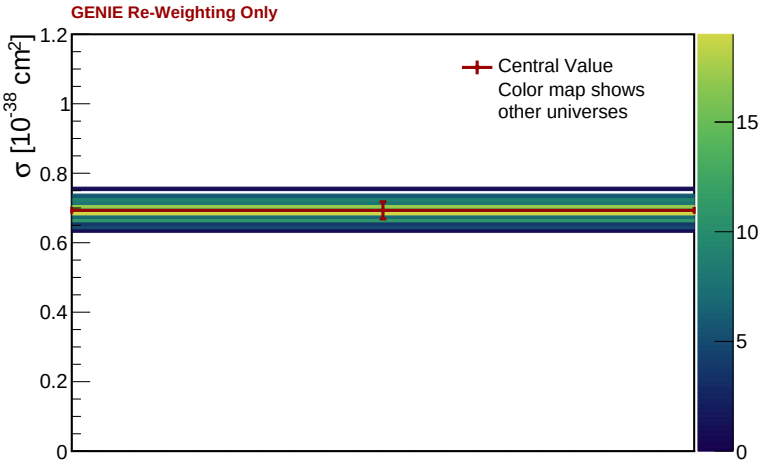

Figure 8.1: *Cross-Section Modelling Uncertainties.* Total data extracted cross sections for all the simulated universes in the colour map. The red graph shows the total data extracted cross section for the nominal MC. The red vertical bars show the GENIE systematic uncertainty derived from the *multisims* according to Equation (8.3). The relative systematic uncertainty on the total cross section is 3.55%.

parameter, a random number is generated following a Gaussian distribution with mean zero and STD one. This number represents the number of Gaussian σ that the parameter will be tweaked to. This is done simultaneously for all parameters. The reweighting code is run in order to generate 100 universes. It is computationally expensive to generate more than 100 universes, as the requested memory grows linearly with the number of universes. The distribution of all these universes is shown in Figure 8.1 for the total cross section and in Figure 8.2a and 8.3a for the two single-differential cross sections in muon momentum and angle, respectively. The universes produce cross sections distributed around the nominal value, without introducing a bias.

The relative uncertainty on the total cross section due to the GENIE variations amounts to 3.55%. Figure 8.2b and 8.3a show the covariance matrices for the muon momentum and $\cos\theta$ cross sections, respectively. In the same figures, the covariance and fractional covariance matrices, as well as the correlation matrices,

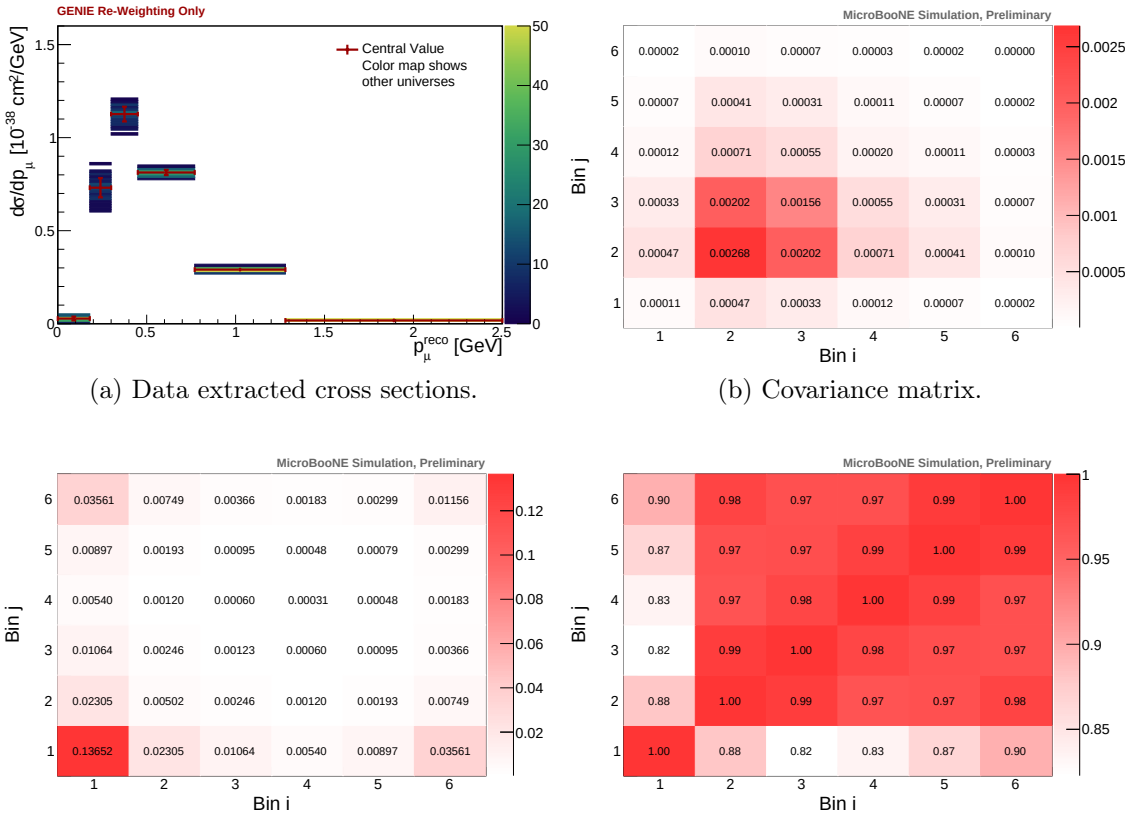

(a) Data extracted cross sections.

(b) Covariance matrix.

(c) Fractional covariance matrix.

(d) Correlation matrix.

Figure 8.2: *Cross-Section Modelling Uncertainties.* (a): data extracted differential cross section in muon momentum for all the simulated universes in the colour map. The red graph shows the data extracted cross section for the nominal MC. The red vertical bars show the GENIE systematic uncertainties derived from the *multisims* according to Equation (8.3). (b), (c) and (d): covariance, fractional covariance, and correlation matrices, respectively.

all calculated according to Equations (8.3), (8.6) and (8.7) are shown as well.

In the same way, the reweighting is performed with the double-differential cross section, for which all the universes are shown in Figure 8.4. Here, all the extracted cross sections are displayed with a green line, and the central value cross section is in red. The covariance matrix is also shown in Figure 8.5.

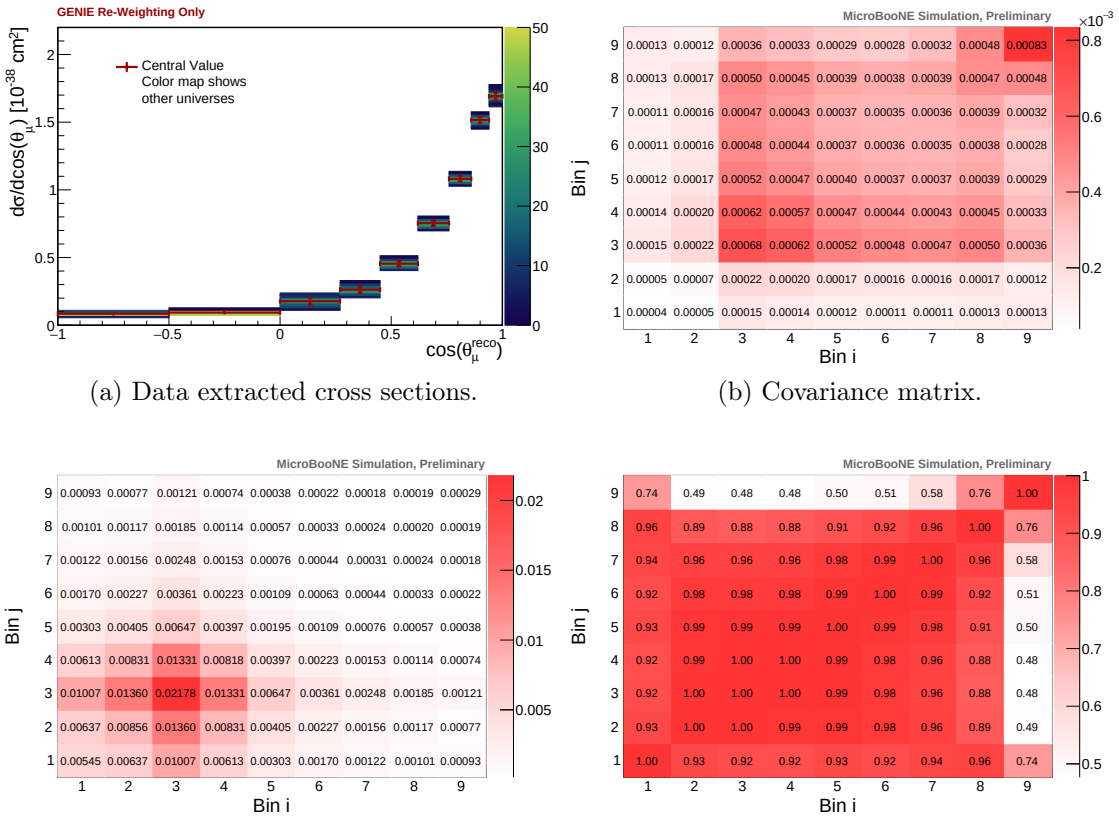

(a) Data extracted cross sections.

(b) Covariance matrix.

(c) Fractional covariance matrix.

(d) Correlation matrix.

Figure 8.3: *Cross-Section Modelling Uncertainties.* (a): data extracted differential cross section in muon angle for all the simulated universes in the colour map. The red graph shows the data extracted cross section for the nominal MC. The red vertical bars show the GENIE systematic uncertainties derived from the *multisims* according to Equation (8.3). (b), (c) and (d): covariance, fractional covariance, and correlation matrices, respectively.

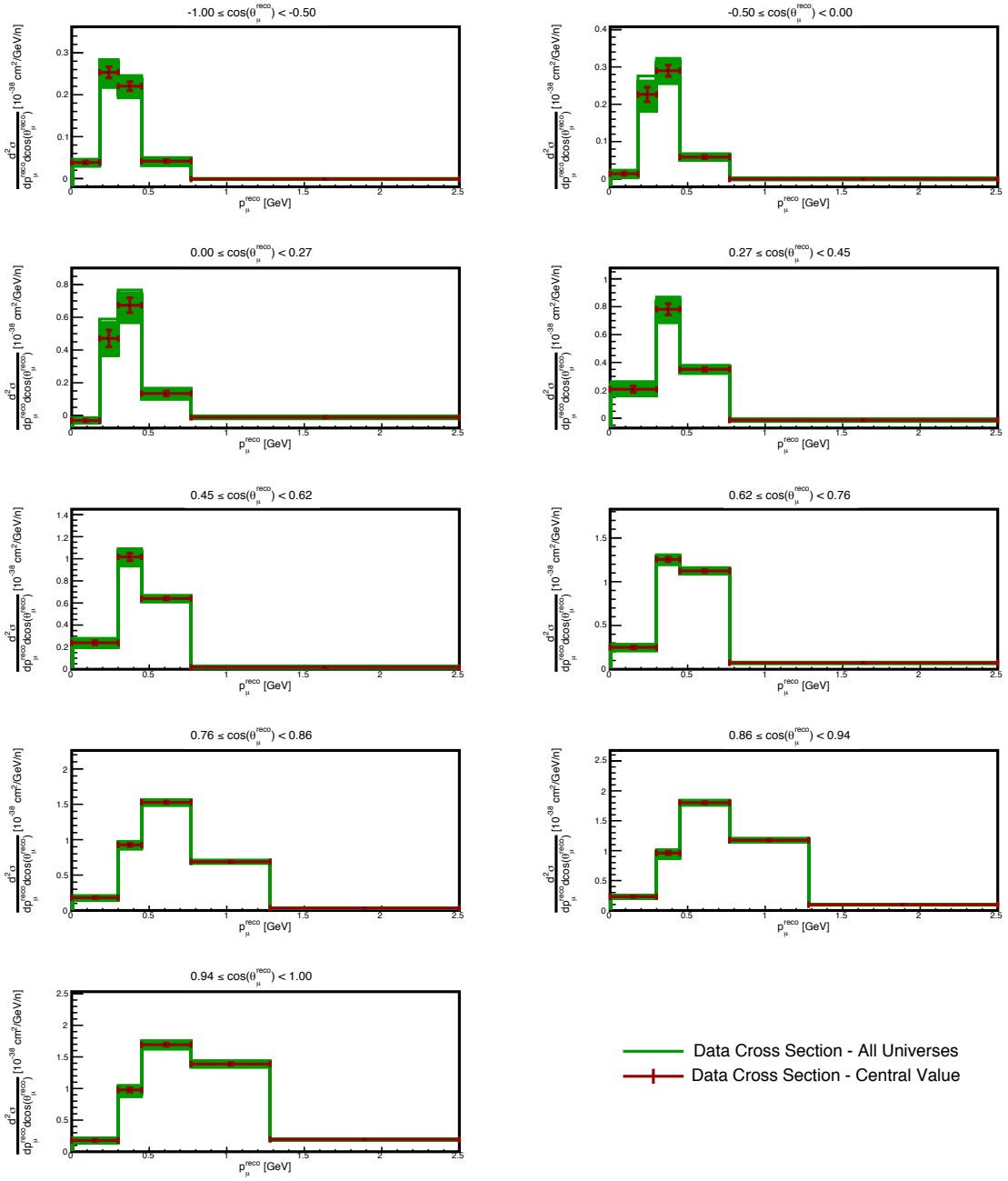

Figure 8.4: *Cross-Section Modelling Uncertainties.* Data extracted cross sections for every universe. The green cross sections show the 100 GENIE universes, while the red cross section shows the central value. The vertical vertical bars show the standard deviation of all the universes with respect to the central value (i.e. the systematic uncertainty).

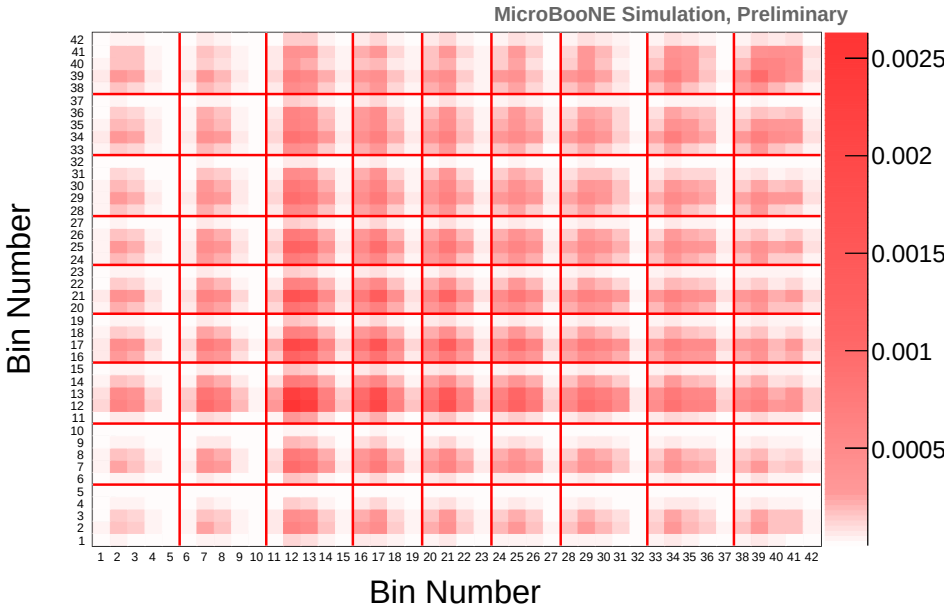

Figure 8.5: *Cross-Section Modelling Uncertainties.* Cross-section modelling covariance matrix, for the double differential cross section.

8.2.1 QE and MEC Cross Section Systematics

This section describes a method to account for uncertainties in the QE cross section model, largely due to RPA effects, and the choice of MEC model. As explained in Chapter 3, RPA refers to long range multi-nucleon correlations which suppress the cross section at low Q^2, while MEC is related to scatters involving correlated pairs of nucleons. The MicroBooNE simulation uses the GENIE "Default GENIE + Emp. MEC" model set (see Section 4.5). These models do not consider RPA, and MEC is handled with an empirical model without associated uncertainties. To assess systematic uncertainties related to these two limitations, the baseline model is compared to an alternative model set (called "GENIE Alternative" in Section 4.5). This uses the "Valencia" model for QE interactions [67, 68], which includes RPA effects, and a more theory-driven MEC model. Ratios of the "Valencia" model with respect to the "default" model are treated in exclusive interaction channels as an uncertainty on the cross section, and a reweighing of the default MC in relevant truth-level kinematic variables is performed. The cross sections for the two different models are shown in Figure 8.6.

These uncertainties are additional to the default parameter variations built within GENIE, which are based on fits to historical neutrino scattering data. The reweighing is done in the q^0/q^3 space, the ratio of area-normalised q^0/q^3 distributions is treated as a shape uncertainty, and the ratio of flux-integrated CCQE or CCMEC cross sections as a normalisation uncertainty.

This uncertainty is handled through a *multisim* approach which moves the default MC toward the "Valencia" model by a Gaussian normal distributed random amount, in a set of model variation universes, providing a measure of off-diagonal correlations. In this approach, the upper half of a standard normal is used to draw a normalisation scaling for a given universe, and multiplying this by the ratio

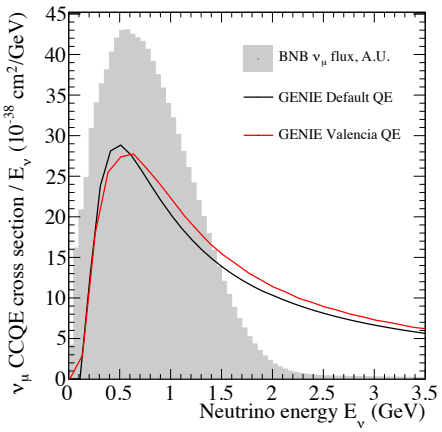

(a) CC QE cross sections.

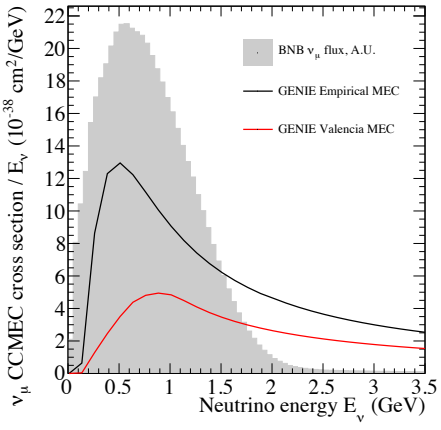

(b) CC MEC cross sections.

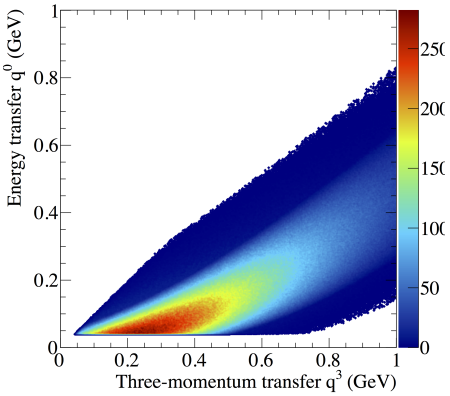

(c) Default model, kinematics of CC QE events.

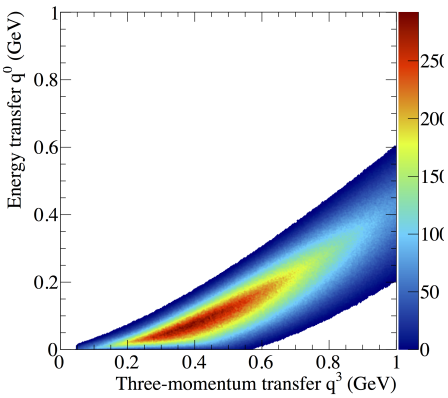

(d) Valencia model, kinematics of CC QE events.

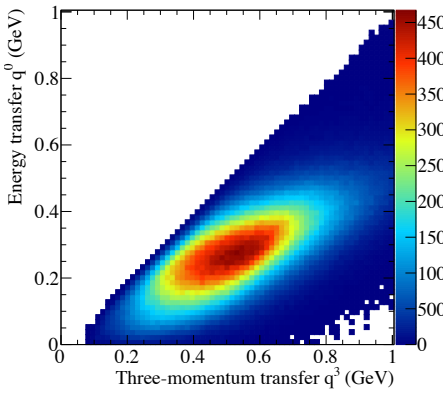

(e) Default model, kinematics of CC MEC events.

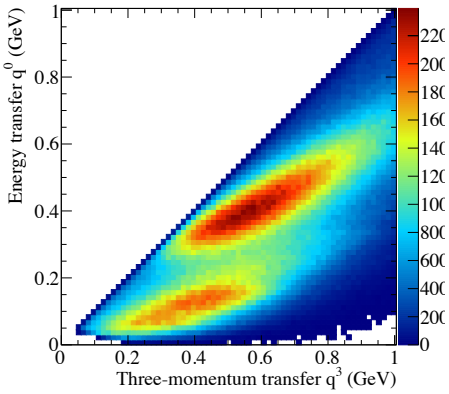

(f) Valencia model, kinematics of CC MEC events.

Figure 8.6: (a) and (b): CC QE and MEC cross sections for the "Valencia" and "Default" GENIE models (as extracted from GENIE splines), together with the BNB ν_μ flux. (c), (d), (e) and (f): kinematics of CCQE distributions. Image source: [124].

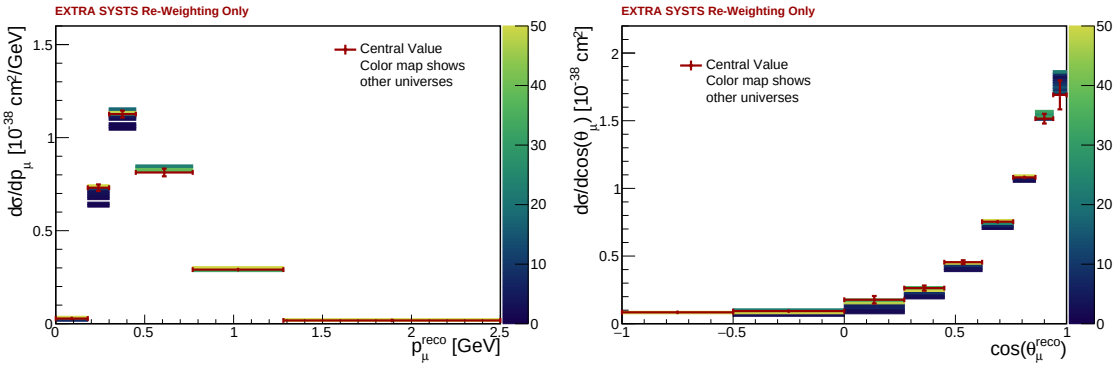

(a) $d\sigma/dp_\mu$ extracted cross sections. (b) $d\sigma/d\cos\theta_\mu$ extracted cross sections.

Figure 8.7: *CC QE and MEC Uncertainties.* Data extracted differential cross sections in muon momentum (a) and cosine of the muon angle (b) for all simulated universes in the colour map. Only CCQE and CCMEC variations are included in these plots. The red graph shows the data extracted cross section for the nominal MC. The red vertical bars show the uncertainties derived from the *multisims* according to Equation (8.3).

between the "Valencia" and the "default" models for each event.

Figure 8.7 shows the universes distributions and the central value cross sections. The relative systematic uncertainty on the total cross section, only due to these CCQE and CCMEC uncertainties, amounts to 1.44%.

8.2.2 Hadronic Re-Interaction Systematics

This section describes the method used to account for uncertainties in the hadron interaction cross-section model that is used in GEANT4. Protons, charged pions, and neutrons all lose energy through ionisation but also hadronic scatters with argon nuclei. Hadronic scatters lead to "hard" direction changes, or production of new particles. The interaction length at a given energy is given by:

$$\lambda(E) = \frac{1}{\sigma(E) \cdot \rho}, \tag{8.11}$$

where $\sigma(E)$ is the interaction cross section and ρ is the particle number density. For any small piece of pion track, the survival probability (the probability that does not interact) is

$$P_{\text{surv}}(E, E + \Delta E) = e^{-\Delta L/\lambda(E)}, \tag{8.12}$$

where ΔL is the length of a slice $\Delta L = \Delta E/(dE/dx)$. Multiplying $P_{\text{surv}}(E, E+\Delta E)$ for al the pion track segments, the total survival probability at a given initial energy $P_{\text{surv}}(E_{\text{init}})$ can be obtained. The interaction probability is then $P_{\text{int}}(E_{\text{init}}) = 1 - P_{\text{surv}}(E_{\text{init}})$. To account for uncertainty in the cross section $\sigma(E)$, such cross section is changed according to its uncertainty and the survival probability is recalculated for a given start momentum, obtaining P'_{surv}. A conservative estimate to the fractional hadron interaction cross section has been estimated to be 30%, by looking at data from [125, 126, 127]. The weight given to an interacting hadron is:

$$w = \frac{1 - P'_{\text{surv}}(E_{\text{init}})}{1 - P_{\text{surv}}(E_{\text{init}})}, \tag{8.13}$$

while the weight given to a non-interacting hadron is:

$$w = \frac{P'_{\text{surv}}(E_{\text{init}})}{P_{\text{surv}}(E_{\text{init}})}. \tag{8.14}$$

This reweighting is performed on a per-event basis and the results is shown in Figure 8.8. The relative systematic uncertainty on the total cross section, only due to particle re-interaction uncertainties, amounts to 0.612%.

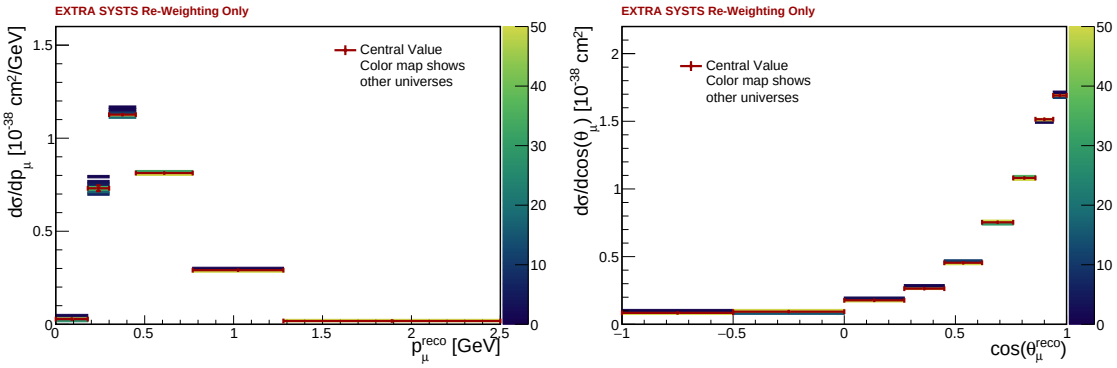

(a) $d\sigma/dp_\mu$ extracted cross sections. (b) $d\sigma/d\cos\theta_\mu$ extracted cross sections.

Figure 8.8: *Particle Re-Interaction Uncertainties.* Data extracted differential cross sections in muon momentum (a) and cosine of the muon angle (b) for all simulated universes in the colour map. Only particle reinteraction variations are included in these plots. The red graph shows the data extracted cross section for the nominal MC. The red vertical bars show the uncertainties derived from the *multisims* according to Equation (8.3).

8.3 Beam Flux Uncertainties

This section describes the implementation of the beam flux uncertainties, which are divided into two main categories:

- uncertainties related to secondary hadron particles (π^+, π^-, K^0, K^+, K^-) due to the collision of protons with the beryllium target;
- "non-hadron" uncertainties, arising from uncertainties in the estimation of the current running in the horn conductor, as well as the estimation of the depth of the conductor traversed by such current ("skin effect"), and the estimation of the pion and nucleon cross sections (total, inelastic, and QE) on aluminium and beryllium.

In total, there are six uncertainties due to flux modelling: five on hadron production and one on non-hadron production. 1000 *multisims* are generated where the flux parameters are varied. The non-hadron uncertainties are estimated by varying the effect by plus or minus one standard deviation. In the case of the "skin effect", the model is switched on and off to create a second universe. The two universes are used to generate weights to assess the overall systematic uncertainties by assuming they follow a Gaussian distribution around the central value. The covariance matrix is calculated according to Equation (8.3).

The re-weighting of the hadron production cross sections is described in [88, 89]. This section focuses on the evaluation of the π^+ uncertainties, as they have the largest impact on the final cross-section uncertainty. The beam simulation used at MicroBooNE uses as a central value a Sanford-Wang [88] parameterisation based on fits to data provided by the HARP experiment [128]. HARP provided double-differential charged pion production cross sections at the Booster energies, with a full covariance matrix. The systematic uncertainties are assessed performing

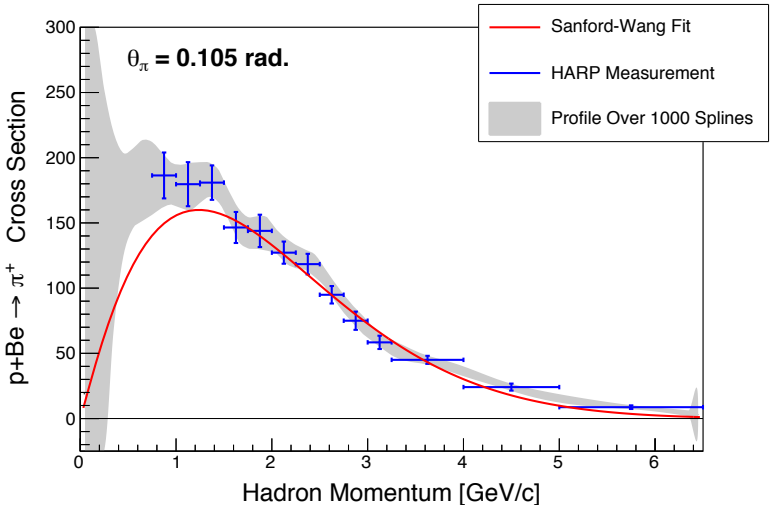

Figure 8.9: HARP pion production cross section measurements as a function of outgoing hadron momentum at a fixed hadron angle (θ_π = 0.105 rad.). The plot includes the measurements, in blue, the Sanford-Wang parameterisation, in red, and the profile of 1000 spline fits to correlated variations in the HARP measured cross sections, in grey. Image source: [129].

a splined fit to the HARP cross-section data. Figure 8.9 shows the HARP data, the spline fits, and the central value fit. A visible bias is introduced such that the average of the universes drawn from the splining is offset from the nominal central value. This creates a bias between the cross-section central value and the average of the cross section among all the universes. Figure 8.10, illustrating the total cross section for all the universes, and the nominal cross section, clearly shows the bias described above, where almost all the universes predict a cross section smaller than the nominal central value. As already discussed in the introduction to this chapter, in this case Equation (8.3) is still used to evaluate the covariance matrix, as this includes the proper covariance matrix V and the bias B as shown in Equation (8.10). Including the bias allows having a conservative estimate for the flux systematic uncertainties. The red vertical bars in this plot are the cross-section systematic uncertainties derived from these universes.

The relative uncertainties on the total cross section for all the flux systematic

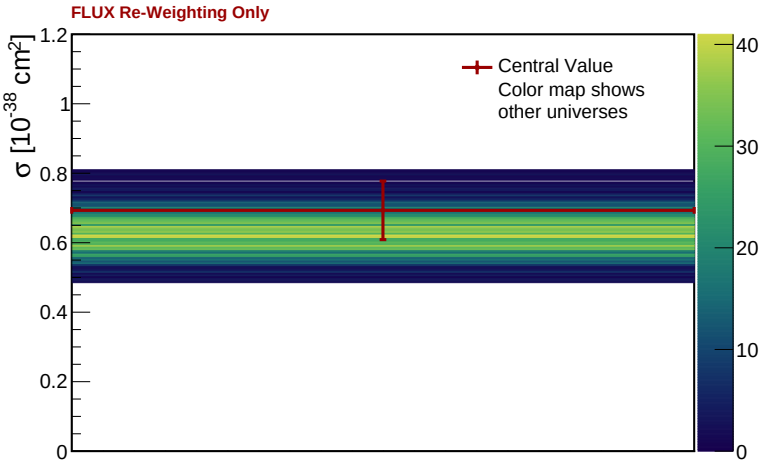

Figure 8.10: *Beam Flux Uncertainties.* Total cross section extracted from data for all the simulated universes in the colour map. The red graph shows the total data extracted cross section for the nominal MC. The red vertical bars show the flux systematic uncertainty derived from the *multisims* according to Equation (8.3). The relative systematic uncertainty on the total cross section is 12.16%.

categories are shown in Table 8.2. The overall relative flux systematic uncertainty amounts to 12.16%, where the main contributions arise from the π^+ production cross section and the non-hadron systematics.

An additional uncertainty is due to the POT counting. The primary proton beam is monitored using two toroids measuring its intensity (protons-per-pulse). According to the MiniBooNE flux paper [88], the proton flux measured in the two toroids agree within 2% . This is included as an additional uncertainty on the normalisation of the cross section, added in quadrature to all the elements of the final total covariance matrix.

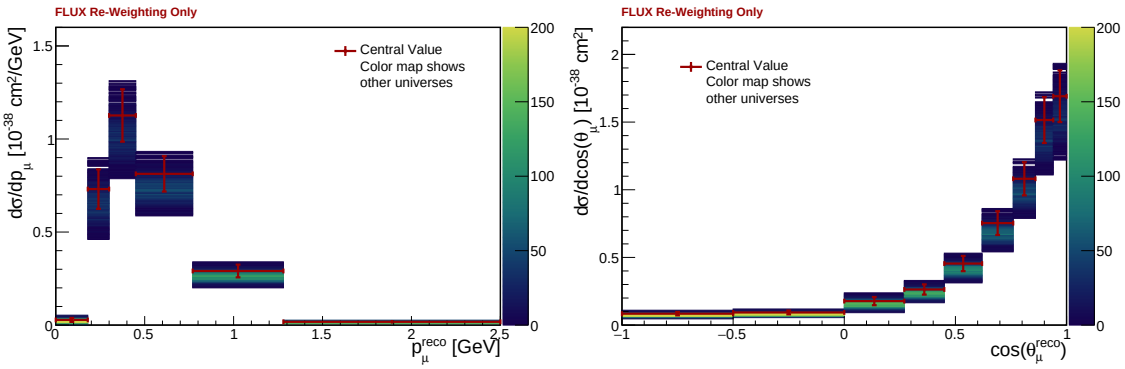

(a) $d\sigma/dp_\mu$ extracted cross sections. (b) $d\sigma/d\cos\theta_\mu$ extracted cross sections.

Figure 8.11: *Beam Flux Uncertainties.* Data extracted differential cross sections in muon momentum (a) and cosine of the muon angle (b) for all simulated universes in the colour map. Only flux variations are included in these plots. The red graph shows the data extracted cross section for the nominal MC. The red vertical bars show the uncertainties derived from the *multisims* according to Equation (8.3).

Parameter	Total Cross Section Relative Uncertainty
Non-Hadron	5.46%
K^- production cross section	0.52%
K^+ production cross section	0.54%
K^0 production cross section	0.57%
π^- production cross section	0.75%
π^+ production cross section	9.59%
Combined uncertainty	12.16%

Table 8.2: Flux systematics parameters and their contribution to the relative cross-section uncertainty.

8.4 Detector Uncertainties

In this section, the detector-related systematic uncertainties are described. While the understanding of the LArTPC detectors have been improved significantly in the past few years, there are still areas where further refinements in the simulation are required. At this point, conservative estimates of the possible systematic biases in the MicroBooNE simulation are made, and are treated as symmetric 1σ uncertainties. The detector systematic uncertainties are evaluated via *unisims* and Equation (8.5) is used to calculate the covariance matrix. Variation samples for a set of 13 detector parameters have been generated. Variations of the central value were created by using a $\pm 1\sigma$ range for parameters where constraints from data were available, or otherwise by simulating an alternative model. The list of parameters is given in Table 8.3. Work is currently ongoing to improve the knowledge on proper uncertainty ranges and detector systematics uncertainties are expected to be improved in the next iteration of this analysis. The uncertainty on the total cross section related to the above-listed detector effects has been calculated and the covariance matrices are shown in Figure 8.12 and 8.13. Here, the covariance matrix is evaluated using Equation 8.5. The relative detector systematic uncertainty on the total cross section currently amounts to 16%. Contributions of individual effects are listed in Table 8.3. For parameters with both plus and minus 1σ variations, the larger of the relative deviations from the central value cross section is chosen as an uncertainty to use in the total uncertainty budget. The largest effect is due to the simulation of induced charge on neighbouring wires.

The following points describe why some effect produce a large cross-section variation, and discuss on future improvements:

- *Induced-Charge Effect.* A charge is induced on neighbouring wires when electrons provoke a signal on an induction plane wire, or are deposited on

Detector Systematic Sample	Description	Type	Total Cross Section Relative Uncertainty [%]
Space Charge	A simple data-driven calibration is applied to the space charge simulation to make it better match measured space charge effects [99].	Modified Model	3.7
Induced Charge	Charge induction is simulated on a longer spatial range than in the default MC, so that more distant wires see the effect of drifting charge.	Alternate Model	13
Light Yield	An improved light production simulation model is used.	Alternate Model	4.7
Remove Channels Prone to Saturating	Turning off channels that frequently become saturated as charge builds up on capacitors in the ASIC circuits, resulting in deadtime.	Alternate Model	4.3
Remove Misconfigured Channels	Turning off the misconfigured channels associated with ASICs that have a different gain and shaping time than desired	Modified Model	1.8
Wire Response Function	The wire response functions used during deconvolution are stretched by 20% based on MicroBooNE data.	$\pm1\sigma$	0.25
Longitudinal Diffusion	The amplitude of longitudinal diffusion is varied based on world data [130, 131].	$\pm1\sigma$	1.7
Transverse Diffusion	The amplitude of transverse diffusion is varied based on world data [132, 133, 134].	$\pm1\sigma$	1.6
Wire Noise	The amplitude of the wire noise model varied.	$\pm1\sigma$	0.089
PE Noise	The single-PE noise of the PMTs is varied.	$\pm1\sigma$	0.38
TPC Visibility	The light yield in the cryostat but outside the TPC is increased by 50%.	Alternate Model	3.7
Electron Lifetime	The electron lifetime is reduced to 10 ms. (This condition affects only about ∼10% of data taken with lower purity).	Alternate Model	2.9
Electron Recombination	The Birks recombination model, with parameters derived from ICARUS [135], is used instead of the default modified box model, with parameters derived from ArgoNeuT [108].	Alternate Model	0.060
Total combined relative uncertainty			16

Table 8.3: List of parameters varied for the detector systematic studies.

a collection plane wire. In the simulated sample that includes the induced-charge effect, the 13% cross section difference comes from a change in the number of selected signal events that affect the efficiency in Equation (7.1). In this simulation there are less reconstructed neutrino-induced muons at the Pandora stage before any selection takes place. This effect is currently being implemented and will be included in the default simulation with a reasonable parameter range of variation, with an expected significant reduction of its effect on the measurement.

- *Space-Charge Effect.* Space charge refers to the presence of positively charged ions that are formed when the argon is ionised. These ions influence the recombination of ionisation electrons from new interactions, and can cause distortions in the readout. In the simulated sample where the space charge effect is decreased, the main difference with respect to the nominal simulation arises in the number of OUTFV background events being selected. There are less OUTFV selected events in the variation sample. In the nominal simulation, many events happening outside the FV are pushed in the FV by space-charge distortion, and appear as OUTFV background. The number of such events decreases if the space charge is turned off.
- *Light Yield, Saturating and Misconfigured Channels, TPC Visibility and Electron Lifetime.* All these effect, that produce an uncertainty of the order of 4%, will decrease in a future iteration of this analysis, when a more data-driven model of the detector will be available. This is achieved by overlaying beam-off data, and the GENIE neutrino simulation, without the need to simulate the CR background.

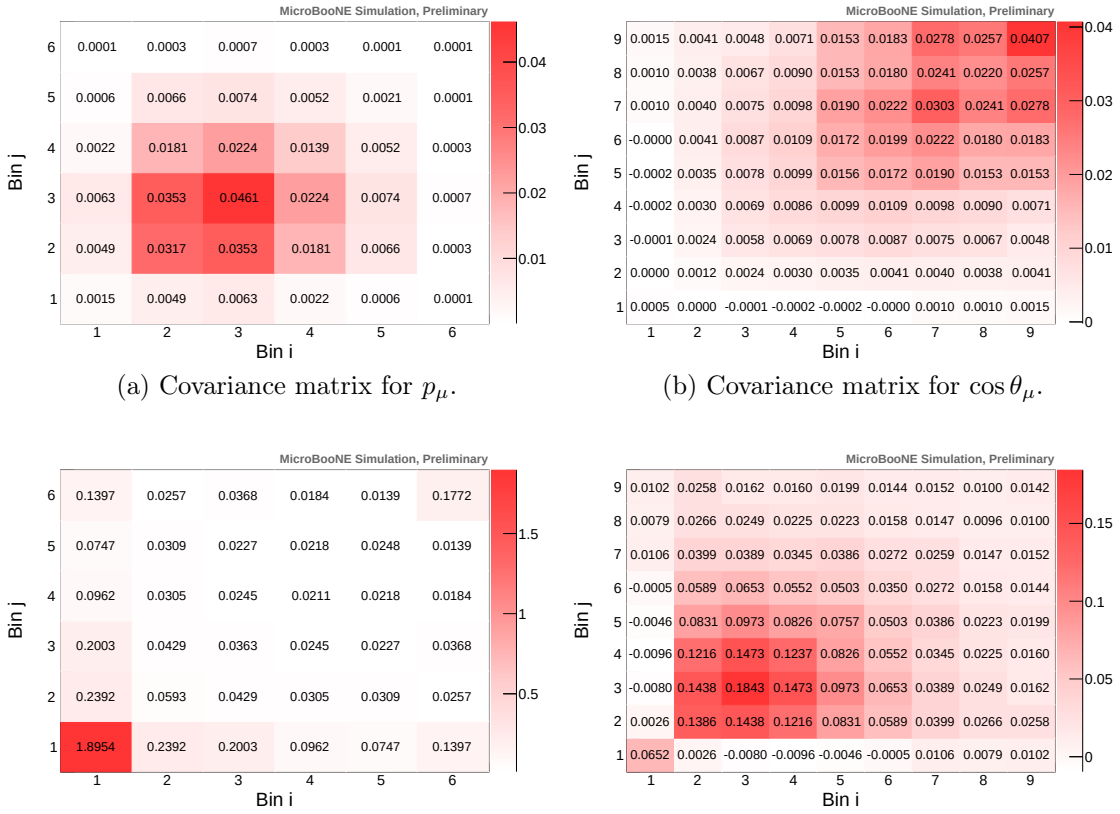

(a) Covariance matrix for p_μ.

(b) Covariance matrix for $\cos\theta_\mu$.

(c) Fractional covariance matrix for p_μ.

(d) Fractional covariance matrix for $\cos\theta_\mu$.

Figure 8.12: *Detector Response Uncertainties.* The detector response systematic covariance matrices for muon momentum (a) and muon angle (b) bins, respectively and the fractional covariance matrices for muon momentum (c) and muon angle (d) bins, respectively.

8.4.1 Uncertainty on the Number of Targets

The two contributors to a potential variation on the calculated number of targets are argon density and FV. To understand the uncertainty on the density, the temperature and pressure of the detector during the period in which the data was taken must be considered. These values are extracted from sensors in the detector and the cryogenic system. During the beam-on data taking, temperature and pressure were measured to be 89.2 ± 0.3 K and 1.241 ± 0.004 bar, respectively. Accounting for variations of these values, the liquid argon density with its uncertainty is $1.3836^{+0.0019}_{-0.0002}$ g/cm^3: it is a 0.1% effect. This effect is

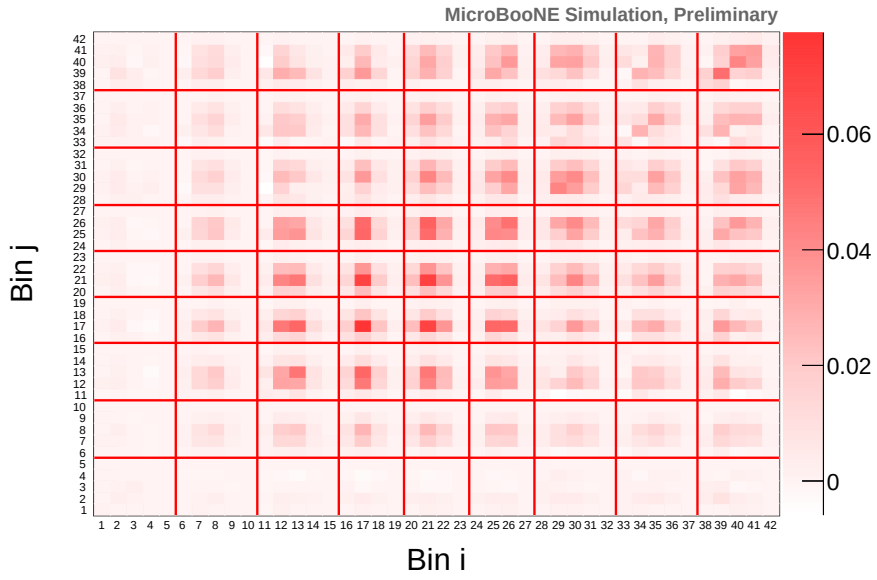

Figure 8.13: *Detector Response Uncertainties.* Covariance matrix for the double-differential cross section. Only detector variations are included.

safely negligible considering the size of the other uncertainties currently taken into account.

8.5 Uncertainty on the Simulated Cosmogenic Background

This section addresses the uncertainty with the simulated CR background. To understand the systematic associated with this background, the full analysis was run over a sample of BNB simulated neutrinos overlaid with CR from data, here called the "overlay" sample. This is different with respect to the nominal MicroBooNE simulation, where CR are also simulated using CORSIKA (see Section 4.5). The event distributions of the selected events obtained from this new sample are then compared with the nominal distributions, in order to estimate an additional systematic uncertainty. Figure 8.14 shows the distribution of the muon track length

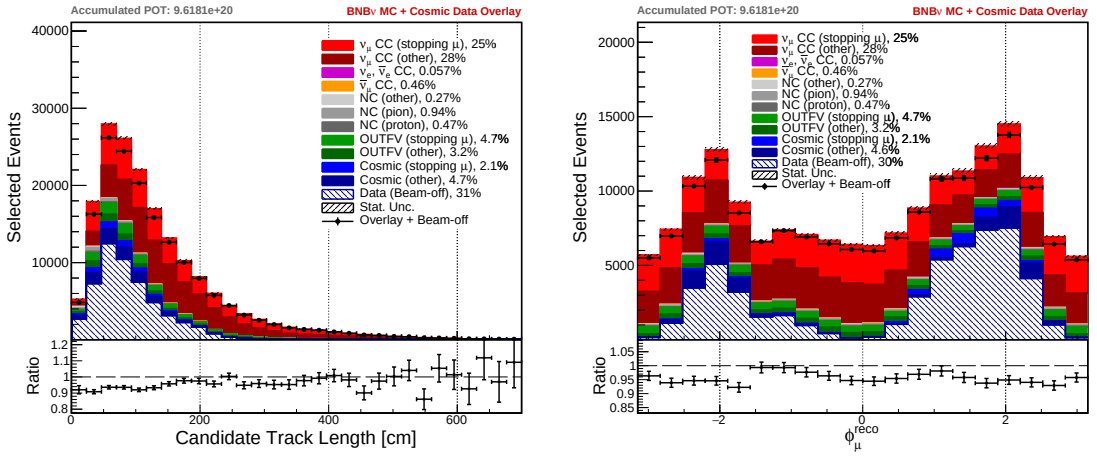

(a) (b)

Figure 8.14: Distributions of candidate muon track length (a) and ϕ angle (b) for selected events. The black points are not from data, but come from the "overlay" sample. The coloured histograms show simulated events according to the nominal MicroBooNE simulation. There is good agreement between the two MC samples, except in the regions were there are more CR in BNB background events (blue). This difference is used to estimated the systematic uncertainty due to the simulated cosmogenic background.

and ϕ angle, obtained with the "overlay" samples. An overall agreement except in the bins that have a relevant CR background contribution is observable. A scaling factor is estimated and applied to the CR background only, such that the ratio between the nominal and the "overlay" simulations corresponds to unity in every bin. The measured scaling factor is 0.60. To estimate what impact this may have on the total cross section, this scaling factor is applied to the simulated CR cosmic background, and a new cross section is extracted with this scaling applied. The difference between this new cross section and the nominal cross section is taken as an additional systematic uncertainty of the cross-section measurement. The relative uncertainty on the total cross section due to the simulated cosmogenic background amounts to 4.1%.

8.6 Uncertainty on the Simulated Dirt Background

The dirt background is used to estimate events where neutrinos interact outside of the cryostat, and either a CR or a neutrino-induced track entering the TPC is selected. Due to the many unknowns in generating this background, that strongly depends on the building geometry, the dirt composition and the ability of GENIE in simulating interactions with the dirt, the MicroBooNE collaboration agreed to assign a 100% systematic uncertainty on this sample.

8.7 MC Statistical Uncertainties

This section describes how the MC statistical uncertainties are estimated. MC statistical uncertainties are considered as an additional systematic uncertainty. The cross section is evaluated as:

$$\left(\frac{d\sigma}{dx_\mu}\right)_i = \frac{N_i - B_i}{\tilde{\epsilon}_i \cdot T \cdot \Phi_{\nu_\mu} \cdot (\Delta x_\mu)_i}, \qquad \tilde{\epsilon}_i = \frac{\sum_j S_{ij} N_j^{\text{sel}}}{\sum_j S_{ij} N_j^{\text{gen}}},$$

and similarly for the double-differential cross section. Since the same MC sample is used to evaluate N_j^{gen}, N_j^{sel} and S_{ij}, it is then not possible to propagate statistical uncertainties as if those quantities were independent. The smearing matrix S makes it hard to analytically propagate the statistical uncertainties.

For this reason, a *multisim* approach was followed for the MC statistical uncertainties. The idea is to generate Poisson random numbers for each event, and for several universes, and to extract the cross section for every universe. The distribution of cross sections for every universe will then give an estimation for the MC statistical uncertainties. All possible correlations introduced by using the same events for N_j^{gen}, N_j^{sel} and S_{ij} will be automatically taken into account by this

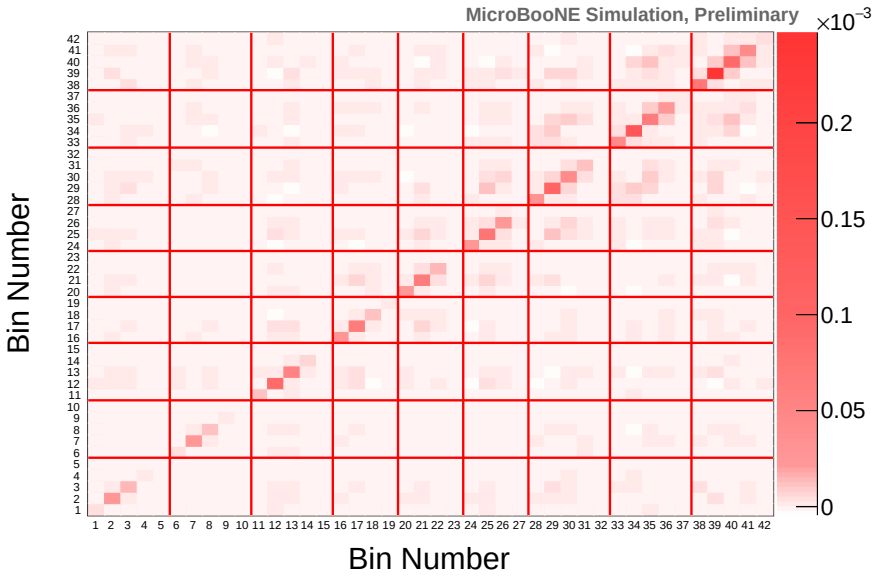

Figure 8.15: *MC Statistical Uncertainties.* MC statistics fractional covariance matrix, for the double differential cross section.

method. This method is also referred to as the "bootstrap method" [136].

In the bootstrap method, toy MC samples are drawn for each event. Poisson random numbers are generated with $\mu = 1$ such that the average over bootstrap replicas for a given event yields one event. The weights are integer numbers, such that each event can be taken 0, 1, 2, ... N times. The fractional covariance matrix is shown in Figure 8.15, and relative uncertainty on the total cross section amounts to 0.2%

8.8 Systematic Uncertainties Summary

This chapter has described the estimation and implementation of the systematic uncertainties that affect the ν_μ CC inclusive cross-section measurement. The systematic uncertainties due to cross-section modelling and flux have been estimated using a *multisim* approach, where several universes have been generated, and the cross section was extracted for every universe. The variance of this distribution gives the systematic uncertainty on the cross section, which amounts to 3.6% for the cross-section modelling and 12.2% for the beam flux modelling. For the systematic uncertainties coming from the detector simulation, a *unisim* approach was used instead, where an MC sample was generated for each single detector parameter variation. The difference between the nominal cross section and the cross section obtained in each of these MC runs is the estimation for the detector systematic uncertainty. The estimated systematic uncertainty amounts to 16.2%, dominated by the induced charge effect (13%). Other systematic uncertainties arise from CCQE and CCMEC uncertainties (1.4%), particle re-interaction uncertainties (0.6%), the POT counting (2%), the simulated cosmic background (4%), the dirt background (11%) and the MC statistics (0.2%). These are summarised in Table 8.4. The total systematic uncertainty, obtained by summing all the mentioned uncertainties in quadrature, adds up to 23.8%. The next chapter will show the cross section with both statistical and systematic uncertainties.

Uncertainty Source	Estimated Relative Uncertainty
Beam Flux	12.2%
Cross Section Modelling	3.6%
CCQE and CCMEC Modelling	1.4%
Particle Re-Interaction	0.6%
Detector Response	16.2%
POT Counting	2.0%
Dirt Background	10.9%
Cosmic Ray Background (CORSIKA)	4.1%
Cosmic Ray Background (Beam-off data)	0.7%
MC Statistics	0.2%
Total Combined	23.8%

Table 8.4: The table shows the different contributions to the total cross section systematic uncertainty.

Chapter 9

Cross-Section Results and Interpretations

Chapter 7 presented the cross-section extraction with statistical uncertainties only and Chapter 8 described the treatment and estimation of the systematic uncertainties that affect the cross-section measurement. This Chapter presents the final results: the muon-neutrino charged current inclusive cross section on argon with statistical and systematic uncertainties.

Section 9.1 shows the total, single- and double-differential cross sections and the comparison with two different GENIE configurations, and Section 9.2 shows a χ^2 testing between these two hypotheses.

9.1 Final Cross Sections

All the systematic uncertainties are summed in quadrature to obtain the total flux-integrated CC inclusive cross section on argon per nucleon:

$$\sigma(\nu_\mu + \mathrm{Ar} \to \mu^- + X) = 0.693 \pm 0.010\,(\mathrm{stat.}) \pm 0.165\,(\mathrm{syst.}) \times 10^{-38}\,\mathrm{cm}^2. \quad (9.1)$$

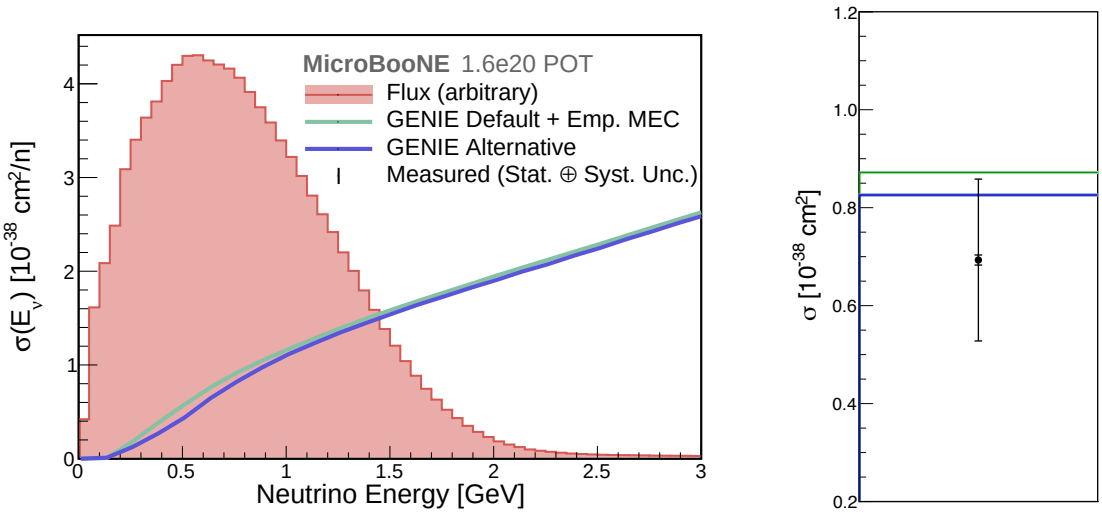

(a) (b)

Figure 9.1: Predicted ν_μ CC inclusive cross section on argon per nucleon n as a function of neutrino energy (a). The "Default GENIE + Emp. MEC" MC prediction is shown in green, while the "GENIE Alternative" prediction is shown in blue. For comparison, the neutrino flux at MicroBooNE (with an arbitrary scale) is shown in red. The total measured cross section is shown in (b) with a black point. The inner vertical bars show statistical uncertainties, while the outer ones show the quadrature sum of the statistical and systematic uncertainties.

The total cross section is also shown in Figure 9.1, which shows its comparison with the two GENIE configurations described in Section 4.5. Figure 9.2 shows the measured total cross section compared to data from other experiments.

The single differential cross sections in muon momentum and angle are shown in Figure 9.3. The uncertainties shown in this figure are the square root of the diagonal elements of the total covariance matrix in Equation (8.1). The total covariance matrices are shown in Figure 9.4.

The double-differential cross section in muon momentum and angle is shown in Figure 9.5 and in Figure 9.6 for different muon angle bins. The total covariance matrix for the double-differential is shown in Figure 9.7.

Tabulated values for the measured cross sections are reported in Appendix A.

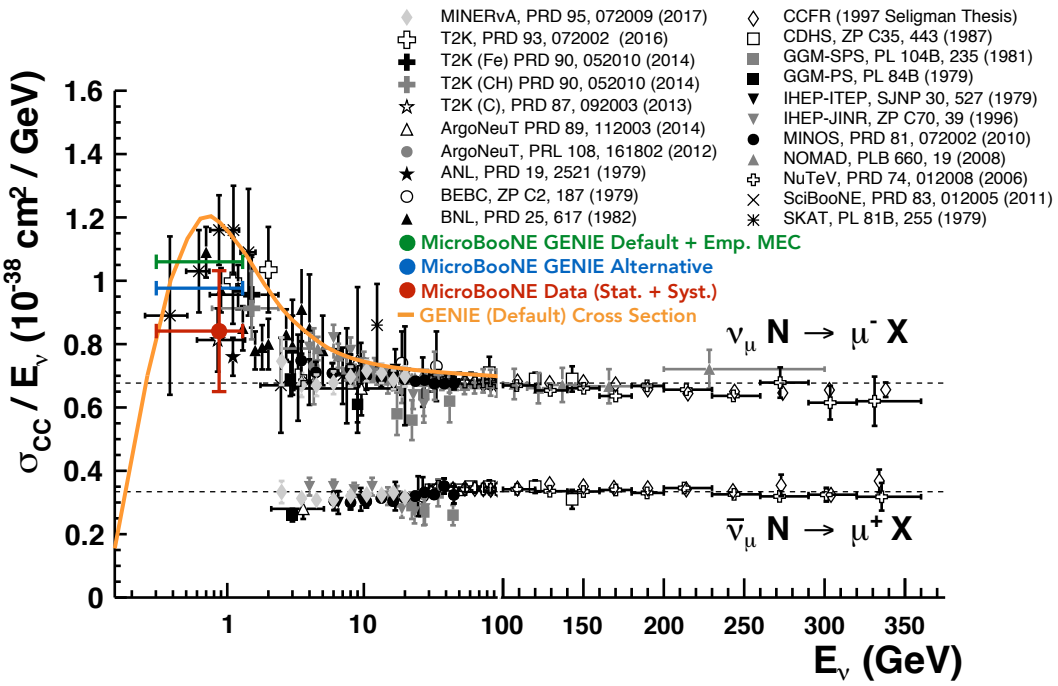

Figure 9.2: CC inclusive measurements for ν_μ and $\bar{\nu}_\mu$ from different experiments with different nuclear targets in black and grey. The coloured points represent the result and MC predictions from this analysis. The green point shows the MC extracted cross section according to the "Default GENIE + Emp. MEC" configuration, the blue point according to the "GENIE Alternative" configuration, and the red one shows the data extracted cross section. The vertical bars on the data cross section show the sum in quadrature of the statistical and systematic uncertainties. The orange curve shows the GENIE predicted cross section as a function of neutrino energy according to "Default GENIE + Emp. MEC".

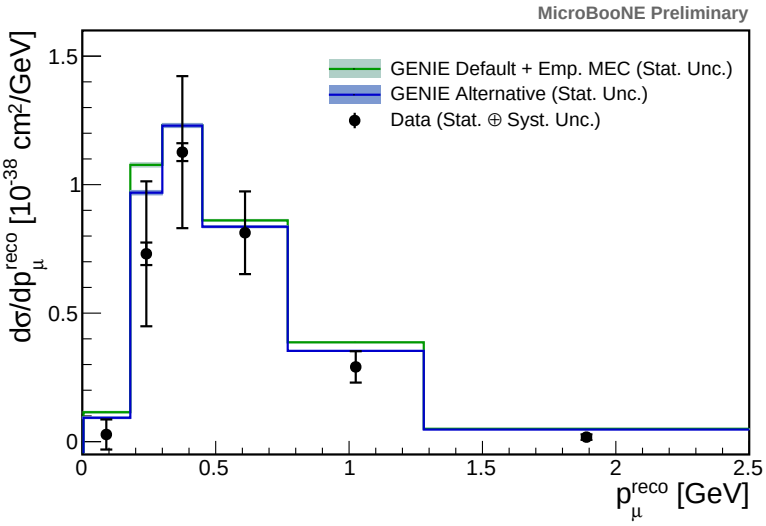

(a)

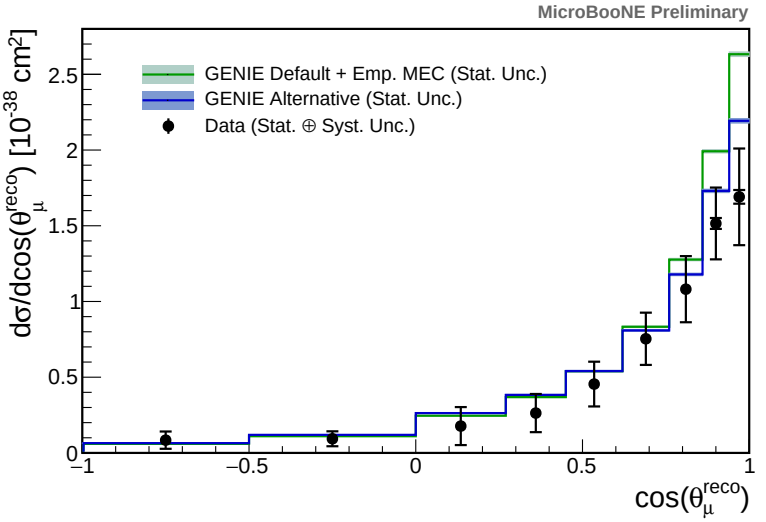

(b)

Figure 9.3: ν_μ CC inclusive single-differential cross section on argon per nucleon as a function of the reconstructed muon momentum (a) and cosine of the muon polar angle (b). The data (black) is compared to the default GENIE prediction (green) and the alternative GENIE prediction (blue), as described in the text. The inner vertical bars show statistical uncertainties, while the outer ones show the quadrature sum of the statistical and systematic uncertainties.

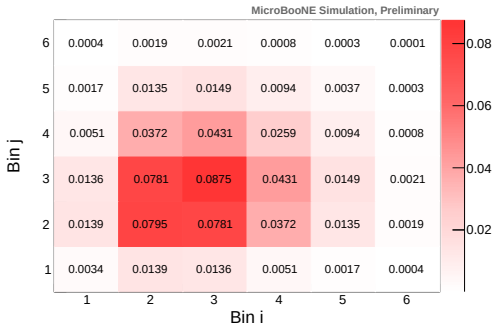

(a) Covariance matrix, p_μ bins.

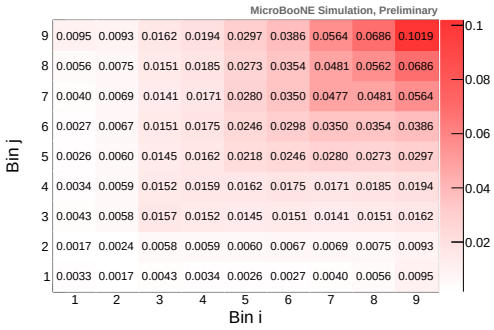

(b) Covariance matrix, $\cos\theta_\mu$ bins.

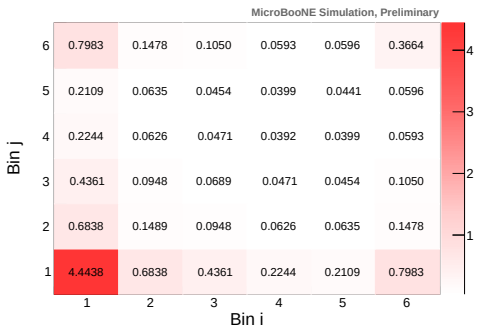

(c) Fractional covariance matrix, p_μ bins.

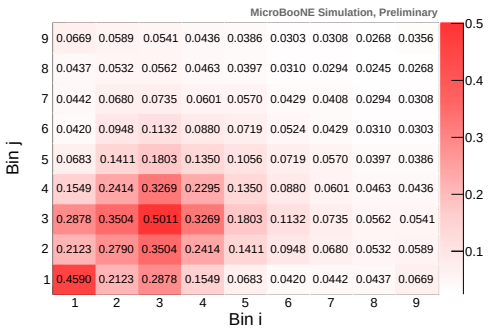

(d) Fractional covariance matrix, $\cos\theta_\mu$ bins.

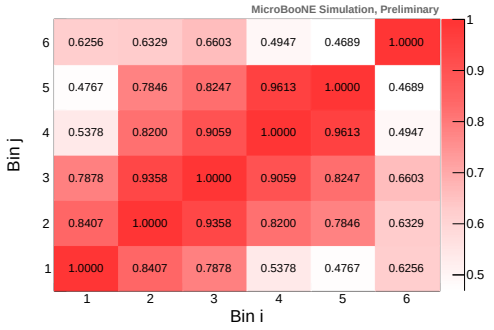

(e) Correlation matrix, p_μ bins.

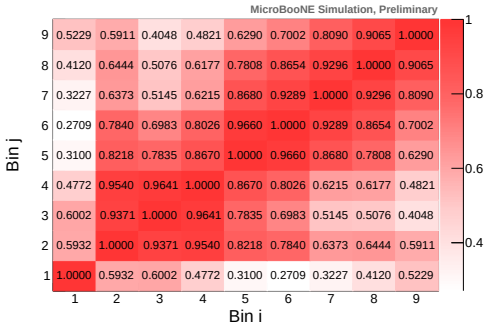

(f) Correlation matrix, $\cos\theta_\mu$ bins.

Figure 9.4: Total covariance ((a), (b)), fractional covariance ((c), (d)) and correlation ((e), (f)) matrices for the p_μ and $\cos\theta_\mu$ bins. For the bin definition, see Section 7.1.3.

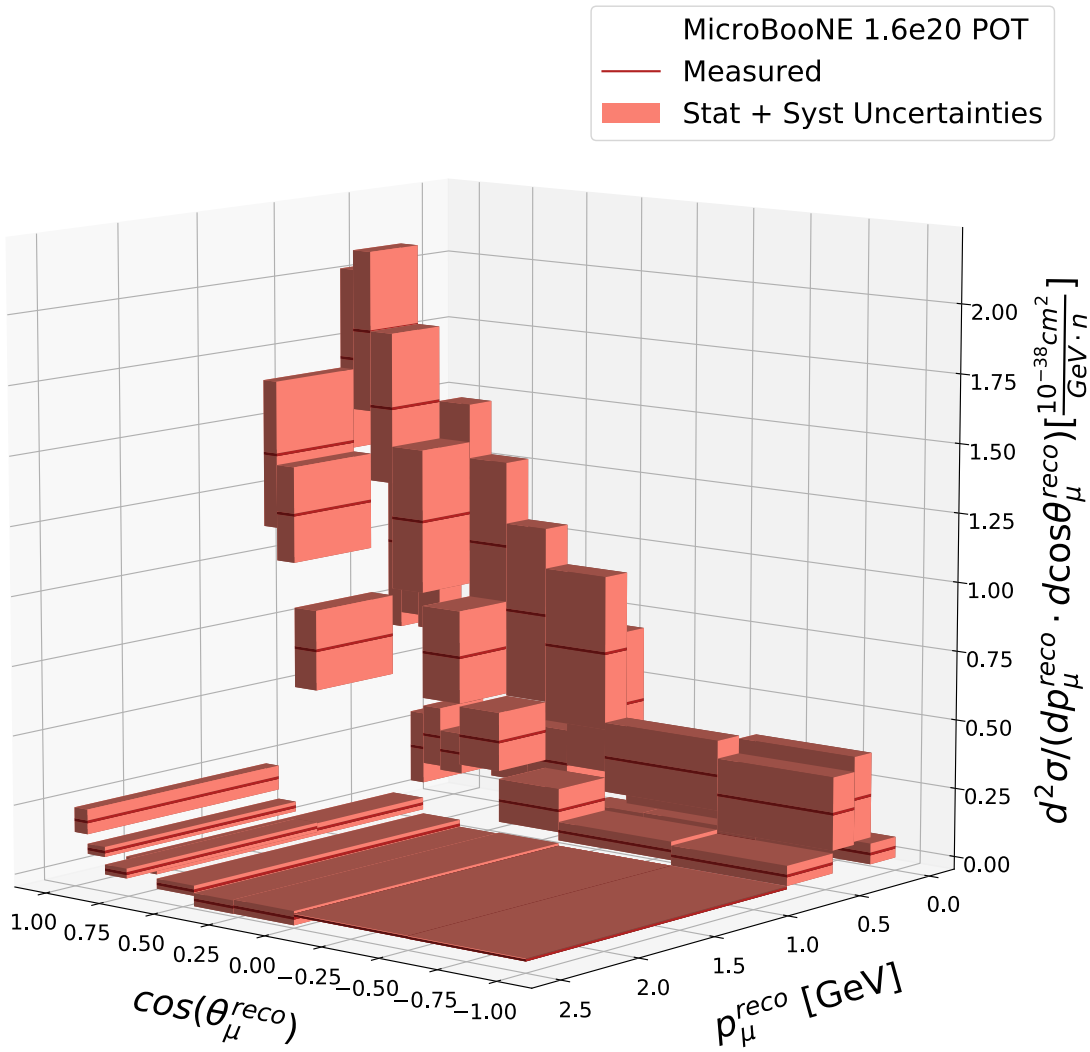

Figure 9.5: ν_μ CC inclusive double-differential cross section on argon per nucleon as a function of the reconstructed muon momentum p_μ and cosine of the reconstructed muon polar angle $\cos\theta_\mu$ (angle with respect to the incoming neutrino direction).

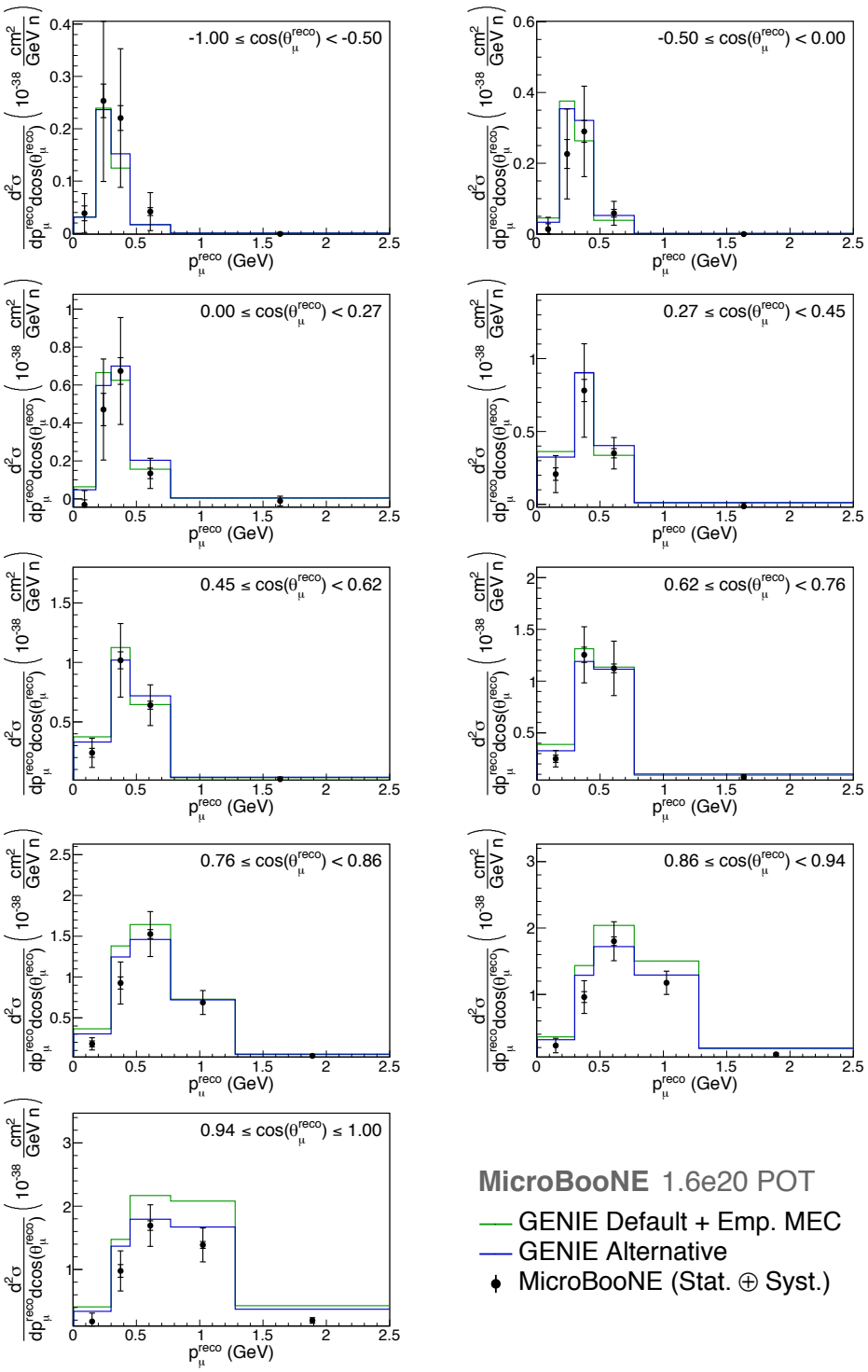

Figure 9.6: ν_μ CC inclusive double-differential cross section on argon per nucleon as a function of the reconstructed muon momentum and cosine of the reconstructed muon polar angle (angle with respect to the incoming neutrino direction). The data (black) is compared to the default GENIE prediction (green) and the alternative GENIE prediction (blue), as described in the text. The inner vertical bars show statistical uncertainties, while the outer ones show the quadrature sum of the statistical and systematic uncertainties.

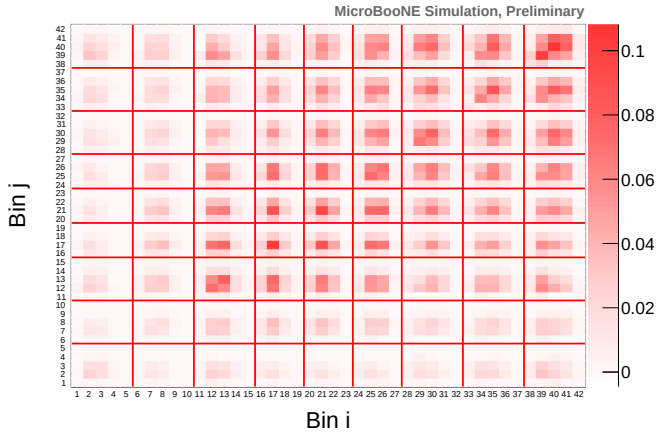

(a) Covariance matrix.

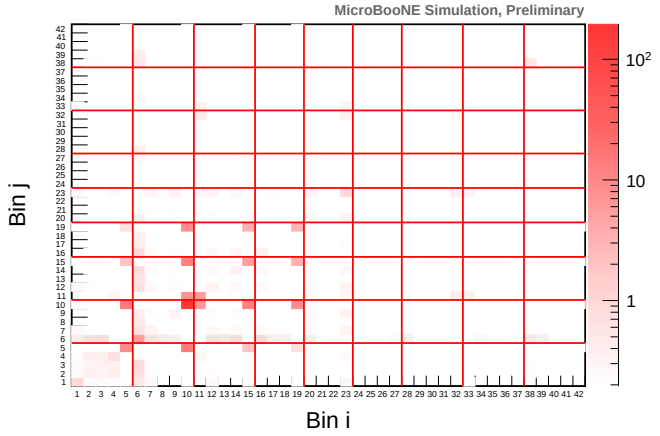

(b) Fractional covariance matrix.

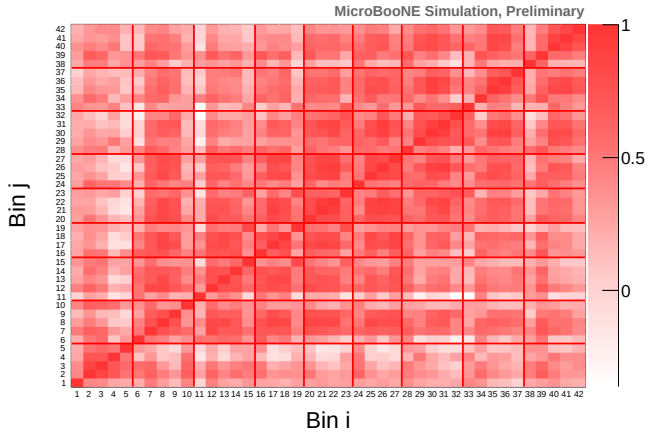

(c) Correlation matrix.

Figure 9.7: Total covariance (a), fractional covariance (b) and correlation (c) matrices for the $(p_\mu, \cos\theta_\mu)$ bins. For the bin definition, see Section 7.1.3.

9.2 Hypotheses Testing

In this Section, the two set of neutrino interaction models ("Default GENIE + Emp. MEC" and "GENIE Alternative") will be quantitatively compared with the double differential cross-section measurement. A chi-squared χ^2 test statistic is used assuming a multi-dimensional Gaussian approximation [137]:

$$\chi^2 = \sum_{ij}(x_i - \mu_i) \cdot E_{ij}^{-1} \cdot (x_j - \mu_j), \tag{9.2}$$

where $x_{i(j)}$ is the measured double-differential cross section in bin $i(j)$, $\mu_{i(j)}$ is the predicted cross section in bin $i(j)$ and E_{ij} is the total covariance matrix defined in Equation (8.1) and shown in Figure 9.7a. The measured χ^2 under the GENIE default, $\chi^2_{\text{def.}}$, and alternative, $\chi^2_{\text{alt.}}$, are calculated:

$$\begin{aligned} \chi^2_{\text{def.}} &= 246, \\ \chi^2_{\text{alt.}} &= 210. \end{aligned} \tag{9.3}$$

With 42 degrees of freedom, the p-values turn out to be extremely small ($\sim 2\times10^{-30}$ and $\sim 5 \times 10^{-24}$ respectively) which means both hypotheses can be rejected given the measured data and the estimated systematic uncertainties. The χ^2 result is mainly driven by off-diagonal entries in the covariance matrix, especially in the detector systematic covariance matrix, for which the induced-charge is the dominant effect, as shown in Chapter 8.

Moreover, the measured data is also able to discriminate between the two models. This is shown by the difference between the χ^2 calculated under the GENIE alternative and default hypotheses, resulting in

$$\Delta\chi^2 = \chi^2_{\text{alt.}} - \chi^2_{\text{def.}} = -36.8. \tag{9.4}$$

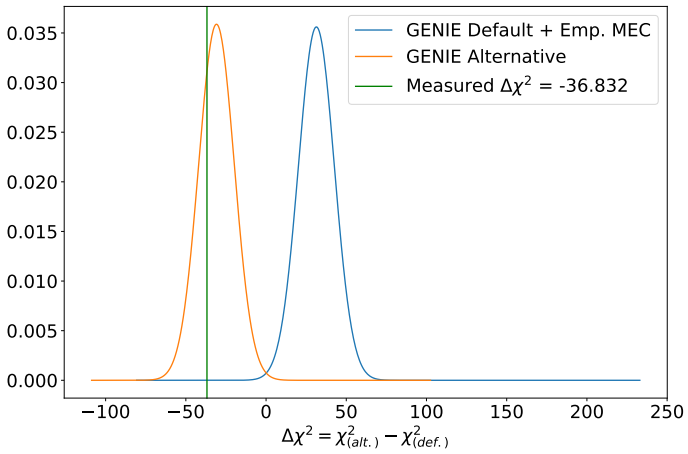

Figure 9.8: Expected distributions for $\Delta\chi^2 = \chi^2_{\text{alt.}} - \chi^2_{\text{def.}}$ under the "Default GENIE + Emp. MEC" (blue) and "GENIE Alternative" (orange) hypotheses. The measured delta chi-squared ($\Delta\chi^2 = -36.8$) is also shown with a green line.

To understand the statistical significance of this result, the expected distributions of the $\Delta\chi^2$ variable must be calculated. This can be done by using the Gaussian approximation as described in [138, 139], where it is shown that the $\Delta\chi^2$ distribution can be approximated by a Gaussian with mean $\overline{\Delta\chi^2_{\text{def.}}} = \chi^2_{\text{alt.}}(x^{\text{Asimov}}_{\text{def.}})$ and standard deviation $2\sqrt{|\overline{\Delta\chi^2_{\text{def.}}}|}$ under GENIE default, and mean $\overline{\Delta\chi^2_{\text{alt.}}} = \chi^2_{\text{def.}}(x^{\text{Asimov}}_{\text{alt.}})$ and standard deviation $2\sqrt{|\overline{\Delta\chi^2_{\text{alt.}}}|}$ under GENIE alternative . Here, $x^{\text{Asimov}}_{\text{def.(alt.)}}$ is the Asimov dataset under GENIE default (alternative), which is taken to be the GENIE default (alternative) simulation itself.

The Asimov $\Delta\chi^2$ under the default and alternative hypotheses amounts to $\overline{\Delta\chi^2_{\text{def.}}} = 31.3$ and $\overline{\Delta\chi^2_{\text{alt.}}} = -30.9$, respectively. The $\Delta\chi^2$ expected distributions under the two hypotheses are shown in Figure 9.8. The two-side p-value is estimated to be 1.1×10^{-9} under the default hypothesis, which in Gaussian standard deviation σ gives more than a 6σ exclusion of the default model set. Also here the discriminating power comes from the non-diagonal entries in the covariance matrix, which do not allow much freedom for shape adjustments.

This result implies that the GENIE default model is excluded given the current data in favour of the alternative one. Statistics are highest in the most forward-going region of muon phase-space, where both the default and alternative model appear to over-predict the signal. This region is dominated by MEC events, and shows a stronger preference for the alternative model than the more QE dominated regions. This is expected as the "Valencia" model folds interaction of correlated pairs and RPA to describe many-body interactions into the calculation, versus an empirical correction to the CC QE events in the default configuration. Nevertheless, the measured cross section is slightly lower than the predicted GENIE cross section, even in the more theory-driven alternative GENIE configuration.

Chapter 10

Conclusions and Outlook

The current and next generation precision neutrino oscillation experiments aim to determine the neutrino mass ordering, to measure the extent of CP violation in the lepton sector, and to probe beyond Standard Model physics, such as sterile neutrinos. These experiments rely on models for neutrino interactions with matter complicated by the existence of nuclear effects and final state interactions. Moreover, neutrino oscillation experiments measure the oscillation probability which depends on the neutrino energy, and therefore requires a link between the energy of reconstructed secondary hadrons and leptons emerging from the neutrino's interaction to its initial energy. This link is also affected by the existence of nuclear effects and final state interactions, which to date cannot be modelled exactly, especially for heavy target nuclei typically used in modern neutrino experiments. As shown in Chapter 3, neutrino interaction modelling uncertainties are already the dominant systematic on current measurements of the oscillation parameters and will soon become the principal limitation if an improved understanding will not be achieved. In particular, it is essential to better understand the nuclear effects that obfuscate any attempt to measure the cross section of interactions between neutrinos and free nucleons.

Over the past years, many experiments have measured the total inclusive charge-current cross section for neutrino ($\nu_\mu N \rightarrow \mu^- X$) scattering off nucleons covering a broad range of neutrino energies. To provide a more complete picture, differential cross sections for inclusive scattering processes are preferred. Inclusive differential measurements have been performed on iron by NuTeV [140], on lead, iron, and carbon by MINERvA [141], on carbon by T2K [142] and on argon by ArgoNeuT [76, 77]. ArgoNeuT is the only experiment that published cross sections for neutrino-argon scattering to date, at a neutrino energy around 5 GeV. Many future experiments will employ liquid argon time projection chambers as detectors. As a consequence, neutrino-argon cross-section measurements are of paramount importance, especially given the relative scarcity of neutrino-argon data.

This thesis presented the first measurement of differential muon-neutrino charged-current inclusive cross sections on argon at a mean neutrino energy of 0.8 GeV. Data were collected using the MicroBooNE liquid argon time projection chamber in the Fermilab Booster neutrino beam for a period of six months and corresponding to 1.6×10^{20} protons on target of exposure. The measured cross section is presented as a function of muon momentum and muon angle with respect to the beam direction, making it a double-differential cross section. This analysis has full angular coverage, achieved thanks to the 4π acceptance of liquid argon time projection chamber detectors and uses multiple Coulomb scattering for measuring the muon momentum. The results for the double-differential cross section are in Figure 9.5 and 9.6. The measured cross section is compared with two different configurations of the GENIE neutrino event generator, and better agreement is found with theory calculations that include a nuclear effect modelling. Additionally, single-differential cross sections in muon momentum and angle have also been presented separately, and a total flux integrated cross section $\sigma(\nu_\mu + \mathrm{Ar} \rightarrow \mu^- + X)$

per nucleon of $0.693 \pm 0.010\,(\text{stat.}) \pm 0.165\,(\text{syst.}) \times 10^{-38}\,\text{cm}^2$ is obtained. An estimation of the discriminating power between theoretical models was also provided, through a χ^2 test between data and two different predictions.

Improvements to the analysis are planned for future iterations, together with a more precise understanding of the detector systematic uncertainties, which will improve the precision of this measurement. New data samples are currently being prepared with the aim to reduce both statistical and systematic uncertainties, by using a data-driven model of the detector and by exploiting an external cosmic-ray tagger, recently installed [103]. Further structural changes in the analysis could also lead to improvements. The smearing matrices are binned in momentum and angle, but more information could be included by binning variables that affect reconstruction, for example the angular separation of tracks or total particle multiplicity. Moreover, model parameters can be constrained in a fit to the measured cross section.

Besides the physics itself, this inclusive measurement has a huge value for the development of reconstruction and selection tools in MicroBooNE. Since the detector is located on the surface, it is constantly pierced by cosmic rays, which constitute the main background when looking for neutrino-induced muon tracks. In Chapter 5, many techniques were described to distinguish neutrino-induced particles from cosmic-ray muons for a sample with full angular coverage. The matching between optical and track information was also described. This is the first time that such flash matching is performed in an automated way in a liquid argon time projection chamber detector demonstrating the capability of such detector technology. Moreover, the final neutrino enriched sample used for this analysis (selected using the event selection described in Section 6) is currently being used as a pre-selection for more exclusive channels.

Appendix A

Cross-Section Tabulated Values

This appendix shows tabulated values for the extracted cross sections. Table A.1 and A.2 show the measured ν_μ CC flux-integrated differential cross section (per nucleon) in muon momentum p_μ and cosine of the muon angle $\cos\theta_\mu$, respectively.

Measurement Bin $[p_\mu]$ [GeV]	$d\sigma/dp_\mu$ $[10^{-38}\text{cm}^2/\text{GeV}]$	Total Uncertainty $[10^{-38}\text{cm}^2/\text{GeV}]$
$[0.00, 0.18)$	2.8×10^{-2}	5.9×10^{-2}
$[0.18, 0.30)$	7.3×10^{-1}	2.8×10^{-1}
$[0.30, 0.45)$	11.3×10^{-1}	3.0×10^{-1}
$[0.45, 0.77)$	8.1×10^{-1}	1.6×10^{-1}
$[0.77, 1.28)$	29.1×10^{-2}	6.1×10^{-2}
$[1.28, 2.50]$	1.8×10^{-2}	1.1×10^{-2}

Table A.1: Measured ν_μ CC flux-integrated differential cross section (per nucleon) in muon momentum p_μ.

Measurement Bin $[\cos\theta_\mu]$	$d\sigma/d\cos\theta_\mu$ $[10^{-38}\text{cm}^2]$	Total Uncertainty $[10^{-38}\text{cm}^2]$
$[-1.00, -0.50)$	8.4×10^{-2}	5.7×10^{-2}
$[-0.50, 0.00)$	9.3×10^{-2}	4.9×10^{-2}
$[0.00, 0.27)$	1.8×10^{-1}	1.3×10^{-1}
$[0.27, 0.45)$	2.6×10^{-1}	1.3×10^{-1}
$[0.45, 0.62)$	4.5×10^{-1}	1.5×10^{-1}
$[0.62, 0.76)$	7.5×10^{-1}	1.7×10^{-1}
$[0.76, 0.86)$	10.8×10^{-1}	2.2×10^{-1}
$[0.86, 0.94)$	15.2×10^{-1}	2.4×10^{-1}
$[0.94, 1.00]$	16.9×10^{-1}	3.2×10^{-1}

Table A.2: Measured ν_μ CC flux-integrated differential cross section (per nucleon) in cosine of the muon angle $\cos\theta_\mu$.

The total covariance matrix for the single differential cross section in p_μ:

$$E_{ij} = \begin{bmatrix} 3.430\text{e-}03 & 1.388\text{e-}02 & 1.365\text{e-}02 & 5.067\text{e-}03 & 1.704\text{e-}03 & 3.894\text{e-}04 \\ 1.388\text{e-}02 & 7.953\text{e-}02 & 7.805\text{e-}02 & 3.721\text{e-}02 & 1.350\text{e-}02 & 1.897\text{e-}03 \\ 1.365\text{e-}02 & 7.805\text{e-}02 & 8.748\text{e-}02 & 4.311\text{e-}02 & 1.488\text{e-}02 & 2.076\text{e-}03 \\ 5.067\text{e-}03 & 3.721\text{e-}02 & 4.311\text{e-}02 & 2.589\text{e-}02 & 9.439\text{e-}03 & 8.460\text{e-}04 \\ 1.704\text{e-}03 & 1.350\text{e-}02 & 1.488\text{e-}02 & 9.439\text{e-}03 & 3.724\text{e-}03 & 3.041\text{e-}04 \\ 3.894\text{e-}04 & 1.897\text{e-}03 & 2.076\text{e-}03 & 8.460\text{e-}04 & 3.041\text{e-}04 & 1.130\text{e-}04 \end{bmatrix}. \tag{A.1}$$

The total covariance matrix for the single differential cross section in $\cos\theta_\mu$:

$$E_{ij} = \begin{bmatrix} 3.261\text{e-}03 & 1.671\text{e-}03 & 4.300\text{e-}03 & 3.436\text{e-}03 & 2.617\text{e-}03 & 2.669\text{e-}03 & 4.024\text{e-}03 & 5.576\text{e-}03 & 9.530\text{e-}03 \\ 1.671\text{e-}03 & 2.432\text{e-}03 & 5.798\text{e-}03 & 5.931\text{e-}03 & 5.989\text{e-}03 & 6.671\text{e-}03 & 6.862\text{e-}03 & 7.531\text{e-}03 & 9.302\text{e-}03 \\ 4.300\text{e-}03 & 5.798\text{e-}03 & 1.574\text{e-}02 & 1.525\text{e-}02 & 1.453\text{e-}02 & 1.511\text{e-}02 & 1.409\text{e-}02 & 1.509\text{e-}02 & 1.621\text{e-}02 \\ 3.436\text{e-}03 & 5.931\text{e-}03 & 1.525\text{e-}02 & 1.589\text{e-}02 & 1.615\text{e-}02 & 1.746\text{e-}02 & 1.711\text{e-}02 & 1.846\text{e-}02 & 1.940\text{e-}02 \\ 2.617\text{e-}03 & 5.989\text{e-}03 & 1.453\text{e-}02 & 1.615\text{e-}02 & 2.184\text{e-}02 & 2.463\text{e-}02 & 2.801\text{e-}02 & 2.735\text{e-}02 & 2.966\text{e-}02 \\ 2.669\text{e-}03 & 6.671\text{e-}03 & 1.511\text{e-}02 & 1.746\text{e-}02 & 2.463\text{e-}02 & 2.977\text{e-}02 & 3.499\text{e-}02 & 3.539\text{e-}02 & 3.856\text{e-}02 \\ 4.024\text{e-}03 & 6.862\text{e-}03 & 1.409\text{e-}02 & 1.711\text{e-}02 & 2.801\text{e-}02 & 3.499\text{e-}02 & 4.767\text{e-}02 & 4.811\text{e-}02 & 5.637\text{e-}02 \\ 5.576\text{e-}03 & 7.531\text{e-}03 & 1.509\text{e-}02 & 1.846\text{e-}02 & 2.735\text{e-}02 & 3.539\text{e-}02 & 4.811\text{e-}02 & 5.617\text{e-}02 & 6.857\text{e-}02 \\ 9.530\text{e-}03 & 9.302\text{e-}03 & 1.621\text{e-}02 & 1.940\text{e-}02 & 2.966\text{e-}02 & 3.856\text{e-}02 & 5.637\text{e-}02 & 6.857\text{e-}02 & 1.019\text{e-}01 \end{bmatrix}. \tag{A.2}$$

The binning used for the measurement of the ν_μ CC flux-integrated double-

differential cross section in cosine of the muon angle $\cos\theta_\mu$ and muon momentum p_μ is shown in Table A.3, and the cross section per bin is shown in Table A.4.

Bin Number	$\cos\theta_\mu$ Range	p_μ Range [GeV]
1	[-1.00, -0.50)	[0.00, 0.18)
2	[-1.00, -0.50)	[0.18, 0.30)
3	[-1.00, -0.50)	[0.30, 0.45)
4	[-1.00, -0.50)	[0.45, 0.77)
5	[-1.00, -0.50)	[0.77, 2.50]
6	[-0.50, 0.00)	[0.00, 0.18)
7	[-0.50, 0.00)	[0.18, 0.30)
8	[-0.50, 0.00)	[0.30, 0.45)
9	[-0.50, 0.00)	[0.45, 0.77)
10	[-0.50, 0.00)	[0.77, 2.50]
11	[0.00, 0.27)	[0.00, 0.18)
12	[0.00, 0.27)	[0.18, 0.30)
13	[0.00, 0.27)	[0.30, 0.45)
14	[0.00, 0.27)	[0.45, 0.77)
15	[0.00, 0.27)	[0.77, 2.50]
16	[0.27, 0.45)	[0.00, 0.30)
17	[0.27, 0.45)	[0.30, 0.45)
18	[0.27, 0.45)	[0.45, 0.77)
19	[0.27, 0.45)	[0.77, 2.50]
20	[0.45, 0.62)	[0.00, 0.3)
21	[0.45, 0.62)	[0.30, 0.45)
22	[0.45, 0.62)	[0.45, 0.77)
23	[0.45, 0.62)	[0.77, 2.50]
24	[0.62, 0.76)	[0.00, 0.30)
25	[0.62, 0.76)	[0.30, 0.45)
26	[0.62, 0.76)	[0.45, 0.77)
27	[0.62, 0.76)	[0.77, 2.50]
28	[0.76, 0.86)	[0.00, 0.30)
29	[0.76, 0.86)	[0.30, 0.45)
30	[0.76, 0.86)	[0.45, 0.77)
31	[0.76, 0.86)	[0.77, 1.28)
32	[0.76, 0.86)	[1.28, 2.50]
33	[0.86, 0.94)	[0.00, 0.30)
34	[0.86, 0.94)	[0.30, 0.45)
35	[0.86, 0.94)	[0.45, 0.77)
36	[0.86, 0.94)	[0.77, 1.28)
37	[0.86, 0.94)	[1.28, 2.50]
38	[0.94, 1.00]	[0.00, 0.30)
39	[0.94, 1.00]	[0.30, 0.45)
40	[0.94, 1.00]	[0.45, 0.77)
41	[0.94, 1.00]	[0.77, 1.28)
42	[0.94, 1.00]	[1.28, 2.50]

Table A.3: Binning used for the measurement of the ν_μ CC flux-integrated double-differential cross section in cosine of the muon angle $\cos\theta_\mu$ and muon momentum p_μ.

Bin Number	$d^2\sigma/dp_\mu d\cos\theta_\mu$ $[10^{-38}\text{cm}^2/\text{GeV}]$	Total Uncertainty $[10^{-38}\text{cm}^2/\text{GeV}]$
1	3.8×10^{-2}	3.8×10^{-2}
2	2.5×10^{-1}	1.5×10^{-1}
3	2.2×10^{-1}	1.3×10^{-1}
4	4.1×10^{-2}	3.6×10^{-2}
5	-0.9×10^{-3}	2.9×10^{-3}
6	1.4×10^{-2}	3.3×10^{-2}
7	2.2×10^{-1}	1.3×10^{-1}
8	2.9×10^{-1}	1.3×10^{-1}
9	5.9×10^{-2}	3.4×10^{-2}
10	-0.2×10^{-3}	3.2×10^{-3}
11	-3.1×10^{-2}	7.5×10^{-2}
12	4.7×10^{-1}	2.7×10^{-1}
13	6.7×10^{-1}	2.8×10^{-1}
14	1.3×10^{-1}	0.8×10^{-1}
15	-1.1×10^{-2}	2.5×10^{-2}
16	2.1×10^{-1}	1.3×10^{-1}
17	7.8×10^{-1}	3.2×10^{-1}
18	3.5×10^{-1}	1.1×10^{-1}
19	-1.3×10^{-2}	2.4×10^{-2}
20	2.4×10^{-1}	1.2×10^{-1}
21	10.2×10^{-1}	3.1×10^{-1}
22	6.4×10^{-1}	1.7×10^{-1}
23	1.8×10^{-2}	1.8×10^{-2}
24	25.0×10^{-2}	7.9×10^{-2}
25	12.5×10^{-1}	2.7×10^{-1}
26	11.2×10^{-1}	2.6×10^{-1}
27	7.4×10^{-2}	2.2×10^{-2}
28	18.1×10^{-2}	7.5×10^{-2}
29	9.3×10^{-1}	2.6×10^{-1}
30	15.3×10^{-1}	2.8×10^{-1}
31	6.9×10^{-1}	1.5×10^{-1}
32	3.4×10^{-2}	1.8×10^{-2}
33	2.3×10^{-1}	1.1×10^{-1}
34	9.6×10^{-1}	2.5×10^{-1}
35	18.0×10^{-1}	2.9×10^{-1}
36	11.8×10^{-1}	1.8×10^{-1}
37	9.7×10^{-2}	1.8×10^{-2}
38	1.8×10^{-1}	1.3×10^{-1}
39	9.8×10^{-1}	3.2×10^{-1}
40	16.9×10^{-1}	3.3×10^{-1}
41	13.9×10^{-1}	2.7×10^{-1}
42	19.4×10^{-2}	4.5×10^{-2}

Table A.4: The measured ν_μ CC flux-integrated double-differential cross section (per nucleon) in cosine of the muon angle $\cos\theta_\mu$ and muon momentum p_μ.

Appendix B

Systematic Covariance Matrices

This appendix collects all the covariance matrices for all the systematic uncertainties that affect the cross section measurement presented in this thesis, that have not already been shown in Chapter 8. For instance, this appendix shows covariance matrices

- including only CCQE and CCMEC uncertainties in Figure B.1;
- including only particle re-interaction uncertainties in Figure B.2;
- including only beam flux uncertainties in Figure B.3;
- including only simulated cosmic background uncertainties in Figure B.4;
- including only simulated dirt background uncertainties in Figure B.5;
- including only MC statistical uncertainties in Figure B.6.

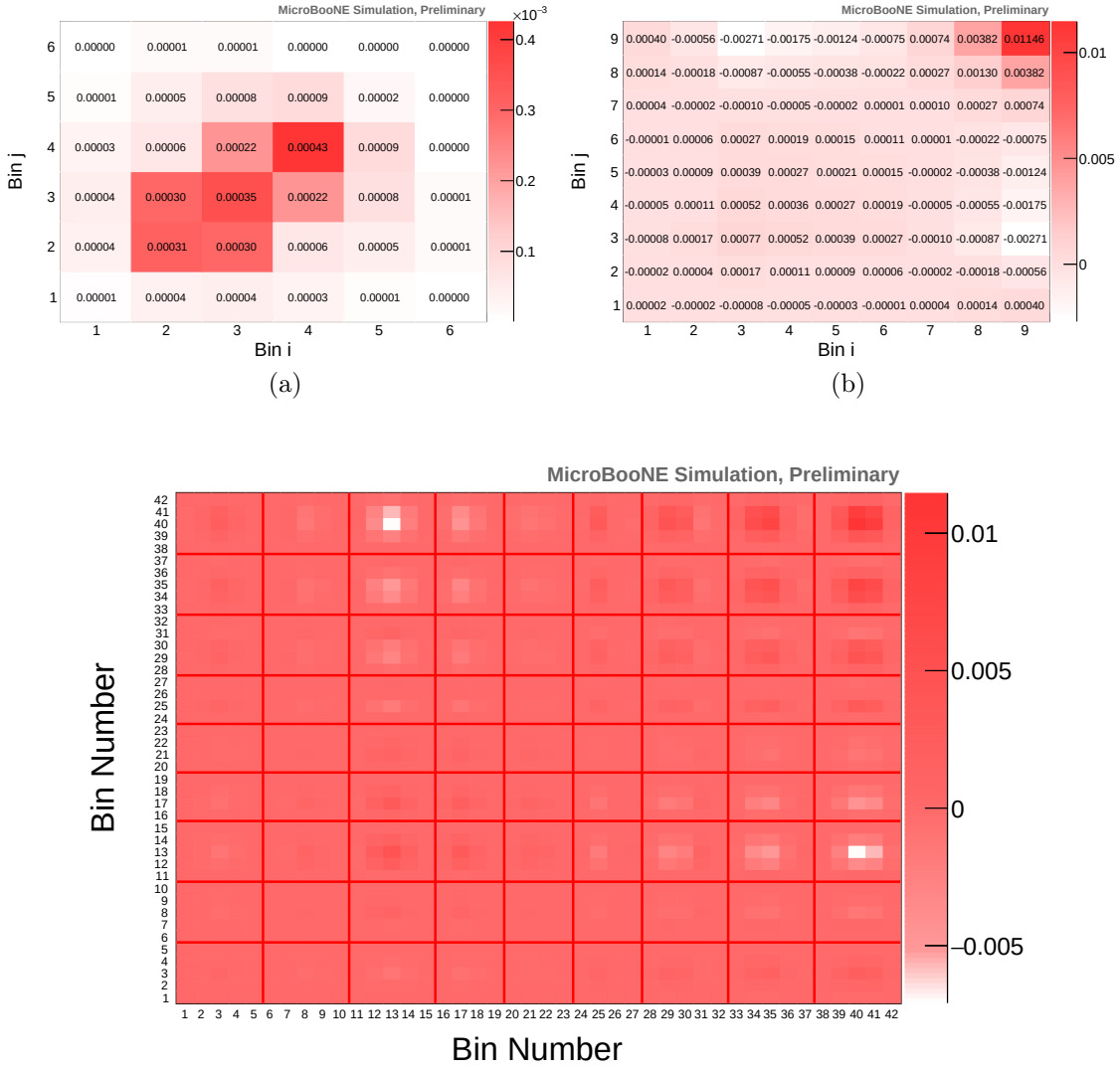

Figure B.1: *CC QE and MEC Uncertainties.* Covariance matrices for the single differential cross section in p_μ (a), in $\cos\theta_\mu$ (b) and the double differential cross section in $(p_\mu, \cos\theta_\mu)$ (c). Only CC QE and MEC related uncertainties are included.

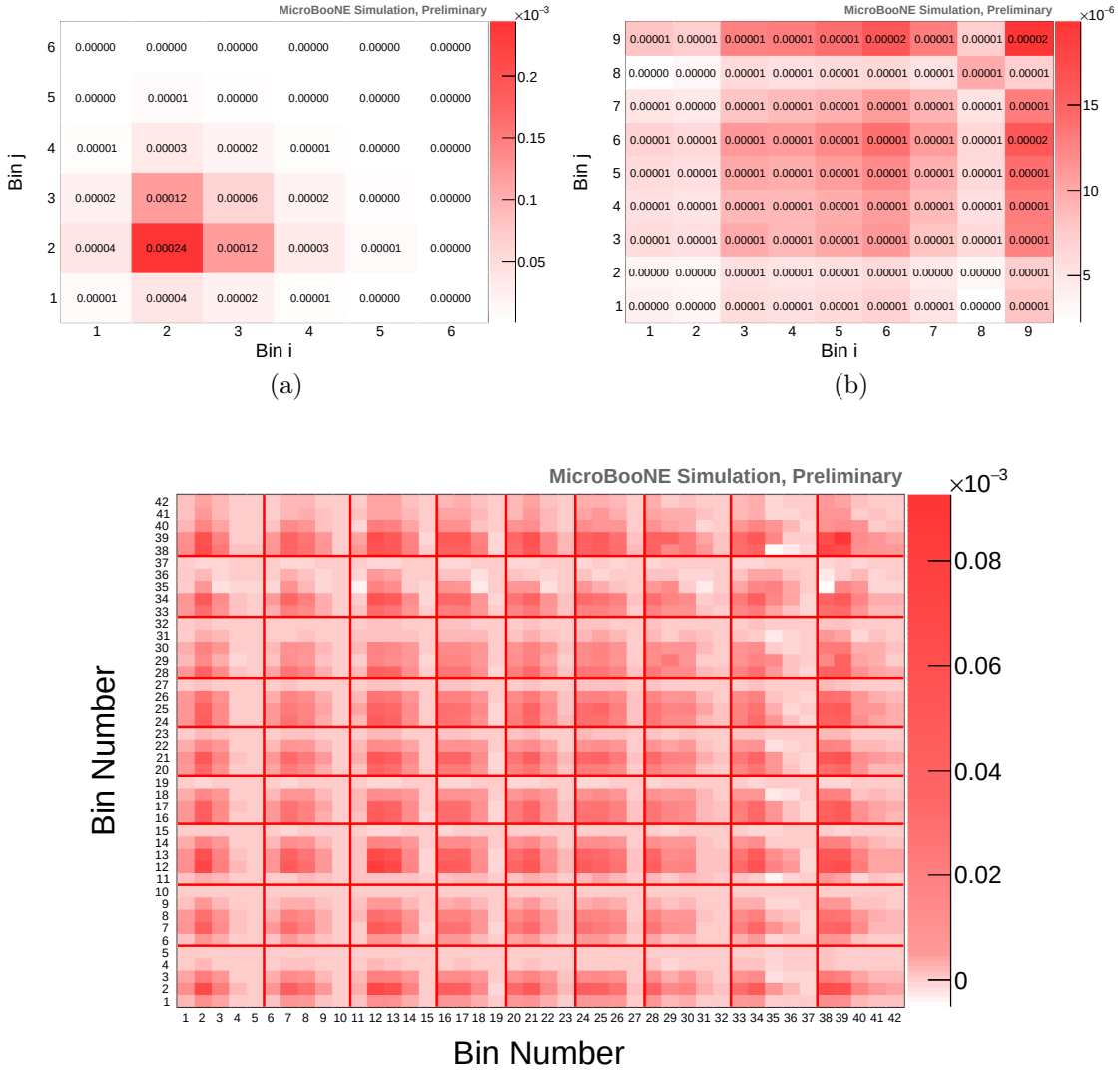

(a) (b) (c)

Figure B.2: *Particle Re-Interaction Uncertainties.* Covariance matrices for the single differential cross section in p_μ (a), in $\cos\theta_\mu$ (b) and the double differential cross section in $(p_\mu, \cos\theta_\mu)$ (c). Only particle re-interaction related uncertainties are included.

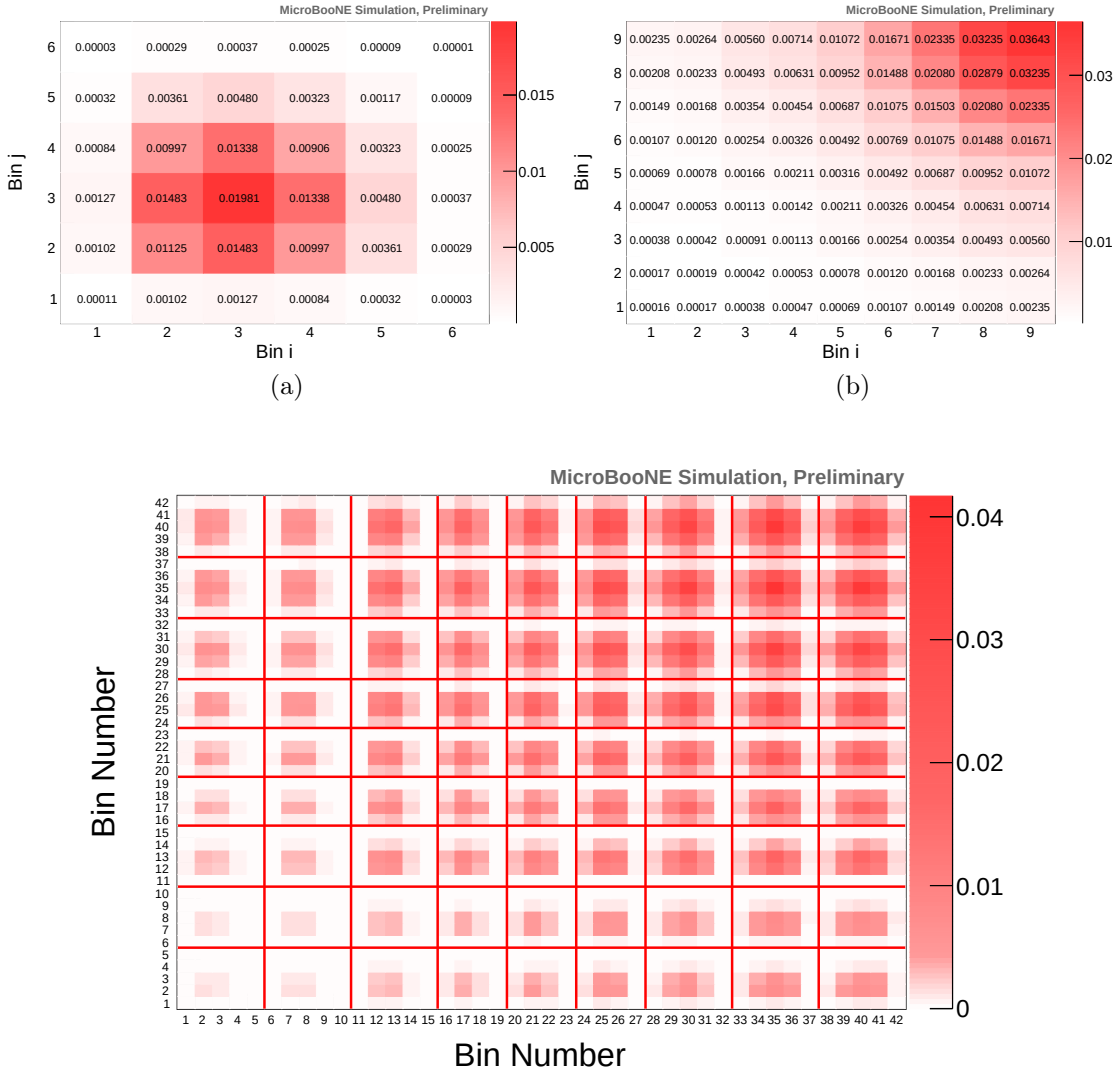

(a) (b) (c)

Figure B.3: *Beam Flux Uncertainties.* Covariance matrices for the single differential cross section in p_μ (a), in $\cos\theta_\mu$ (b) and the double differential cross section in $(p_\mu, \cos\theta_\mu)$ (c). Only beam flux related uncertainties are included.

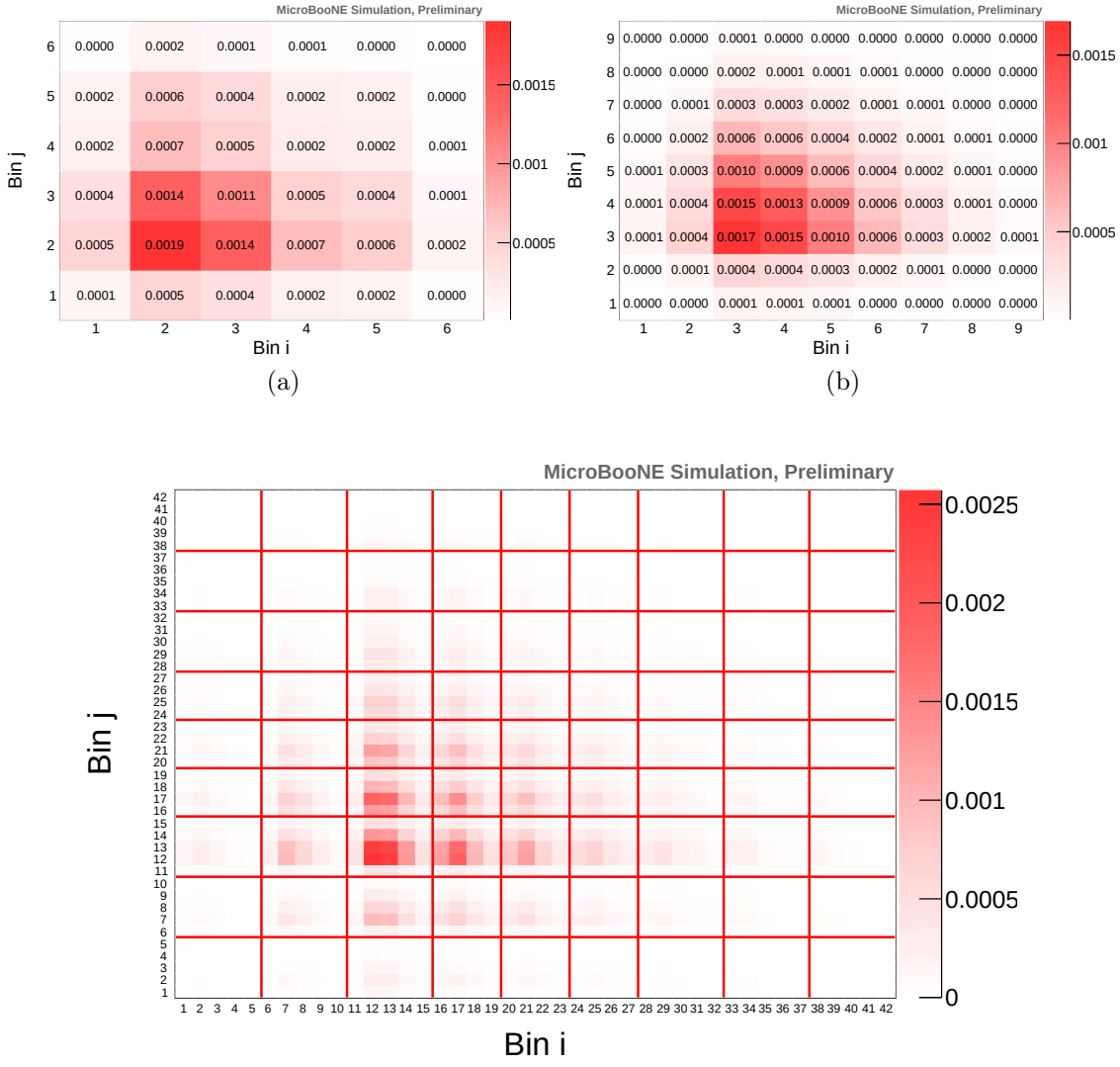

Figure B.4: *MC Cosmic Background Uncertainties.* Covariance matrices for the single differential cross section in p_μ (a), in $\cos\theta_\mu$ (b) and the double differential cross section in $(p_\mu, \cos\theta_\mu)$ (c). Only MC cosmic background related uncertainties are included.

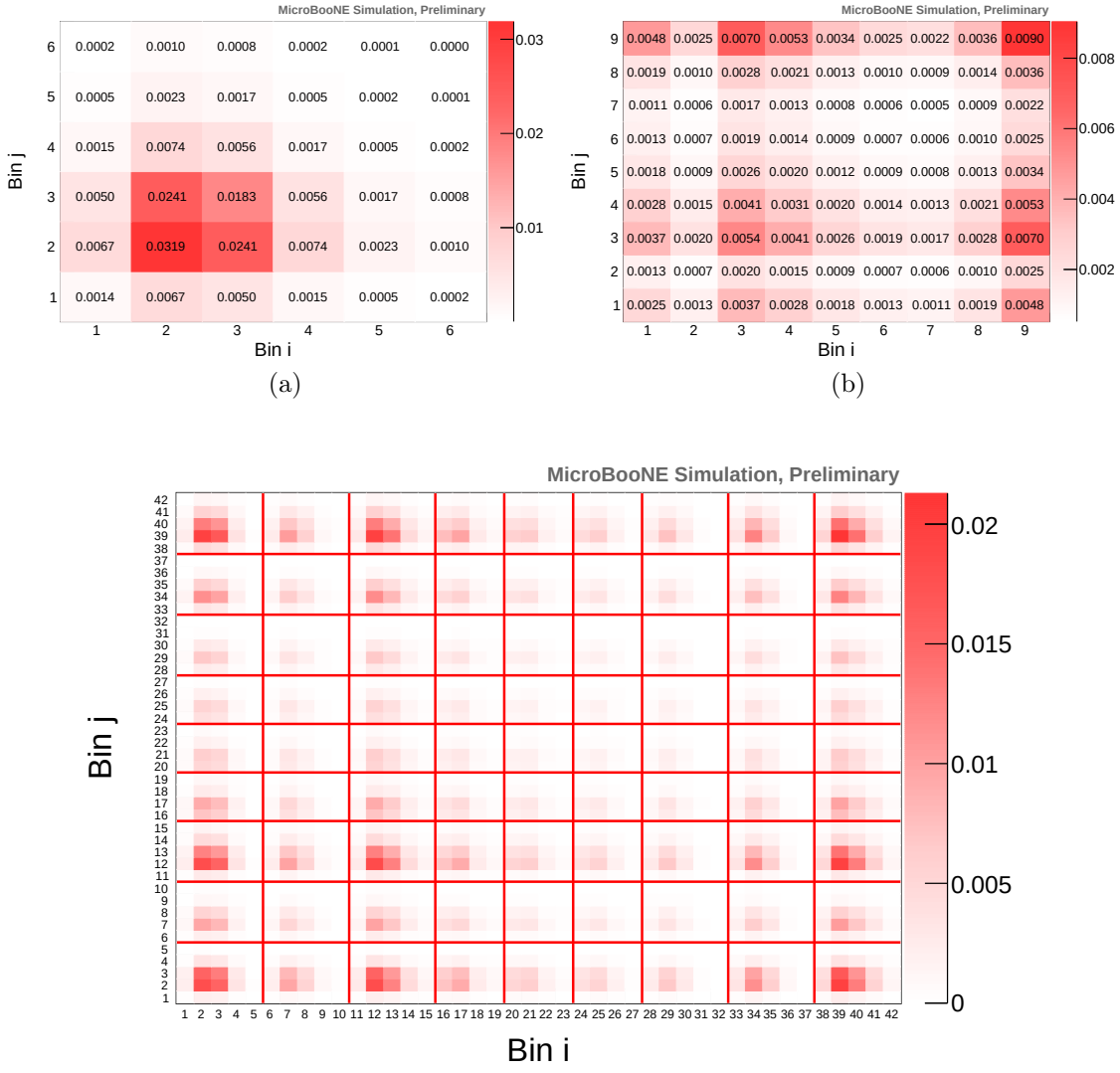

(a) (b)

(c)

Figure B.5: *Dirt Background Uncertainties.* Covariance matrices for the single differential cross section in p_μ (a), in $\cos\theta_\mu$ (b) and the double differential cross section in $(p_\mu, \cos\theta_\mu)$ (c). Only dirt background related uncertainties are included.

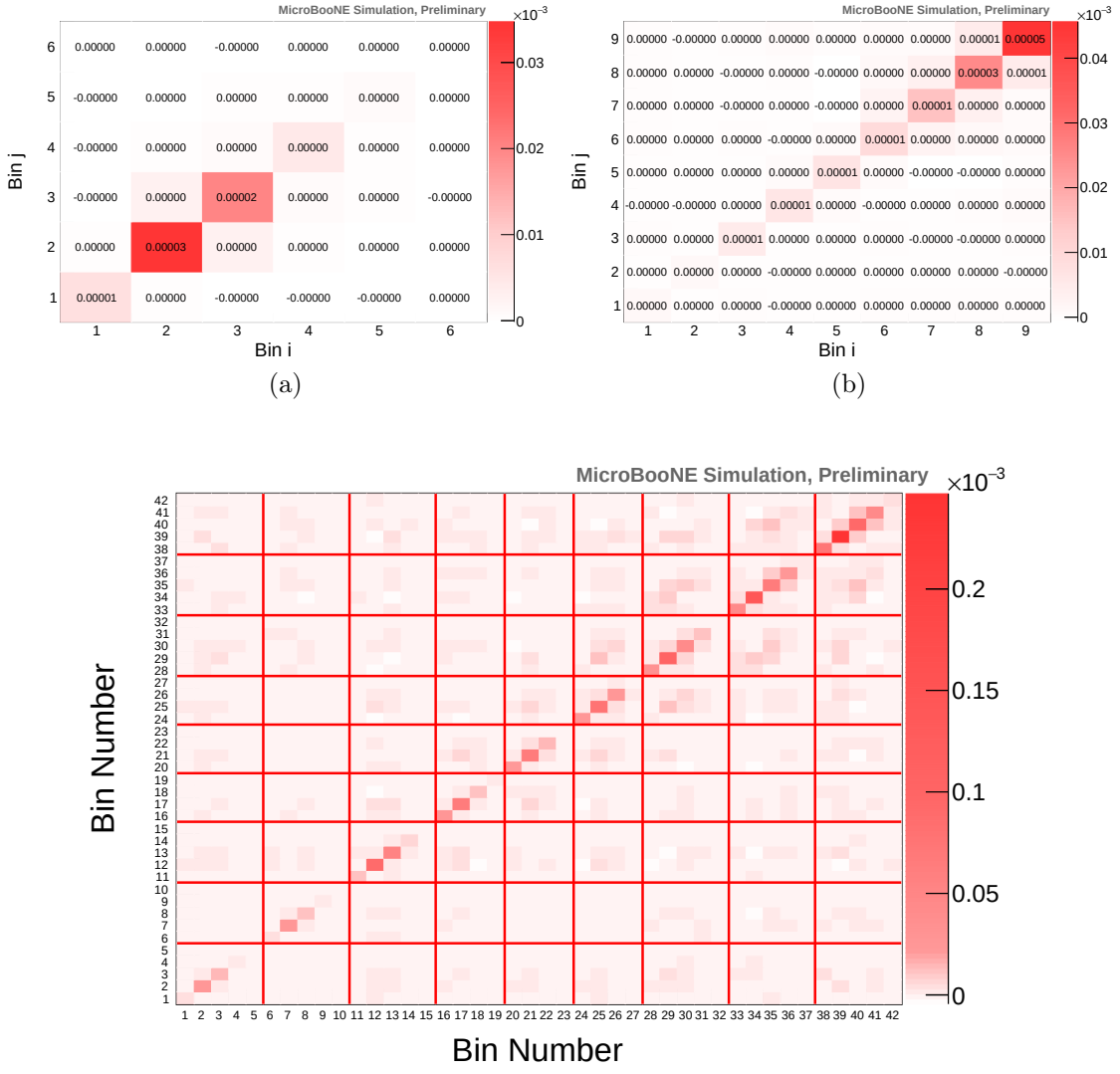

(a) (b) (c)

Figure B.6: *MC Statistical Uncertainties.* Covariance matrices for the single differential cross section in p_μ (a), in $\cos\theta_\mu$ (b) and the double differential cross section in $(p_\mu, \cos\theta_\mu)$ (c). Only MC statistics related uncertainties are included.

Appendix C

Analysis Validation

In this appendix studies are performed to validate that the analysis framework is functioning correctly and that there are no significant biases in the cross-section results. In Chapter 7 the default GENIE configuration was used to extract the cross section. This simulation is used for the estimation of the efficiency and some of the backgrounds. Here, the alternative GENIE configuration is used (described in Section 4.5) to check that the same result (within cross section modelling systematic uncertainties) is obtained. The default data extract cross section from Eq. 7.15 was

$$\sigma = 0.693 \pm 0.010\,(\text{stat.}) \times 10^{-38}\,\text{cm}^2. \tag{C.1}$$

Using the alternative GENIE configuration the cross section is calculated as

$$\sigma^{\text{alt.}} = 0.714 \pm 0.010\,(\text{stat}) \times 10^{-38}\,\text{cm}^2. \tag{C.2}$$

The systematic uncertainty due to cross section modelling amount to (see Table 8.4) $0.025\ \times 10^{-38}\,\text{cm}^2$ and covers the value of the cross section extracted with the

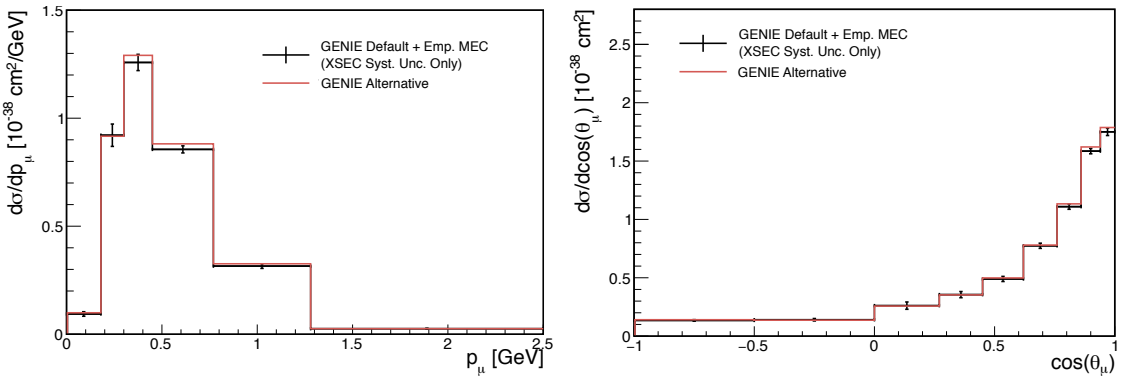

(a) (b)

Figure C.1: Single-differential cross section in p_μ (a) and $\cos\theta_\mu$ (b) extracted using two different simulations for background and efficiency estimations. The black points shows the data cross section extracted using the "Default GENIE + Emp. MEC" simulation (default MicroBooNE simulation). The error bars show systematic uncertainties from cross section modelling only. The red shows the data cross section extracted using the "GENIE Alternative" simulation.

alternative model set in less than 1σ range:

$$\text{Number of STD } \sigma \text{ differs from } \sigma^{\text{alt.}} = \frac{0.714 - 0.693}{0.025} = 0.84. \tag{C.3}$$

The comparison is also done for the two single differential cross sections (similar results are obtained with the double-differential cross section), as shown in Figure C.1. The plots show the data cross section extracted using the "Default GENIE + Emp. MEC" configuration in black, and using the "GENIE Alternative" configuration in red. Also here, the data cross section doesn't change drastically going from one model set to another, confirming that the cross section extraction is robust. The vertical bars show the systematic uncertainties on the default extracted cross section, only from cross-section modelling. This is done in order to show that the error bars cover the difference between the two cross sections in every bin.

Moreover, a fake data test is used to validate the analysis framework. For this test, the GENIE alternative MC is used as fake data. This is shown in Figure C.2

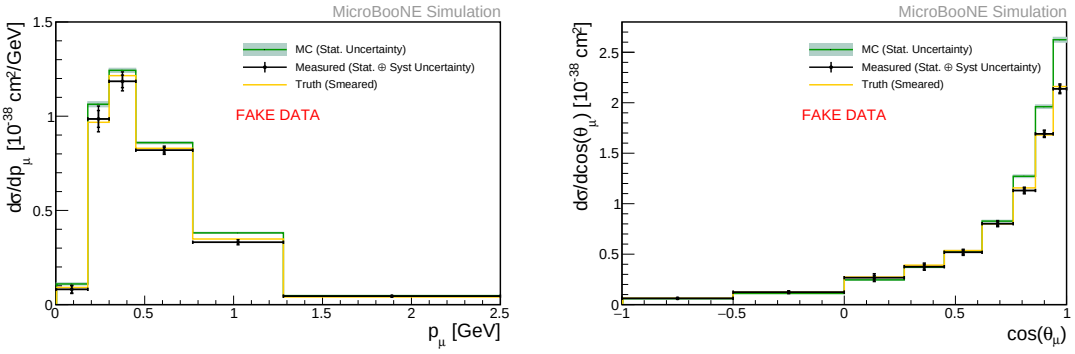

(a) (b)

Figure C.2: Single-differential cross section in p_μ (a) and $\cos\theta_\mu$ (b) extracted using using a sample of fake data from an alternative simulation. The green shows the MC only extracted cross section from the "Default GENIE + Emp. MEC" simulation (default MicroBooNE simulation)s. The black points are a fake data simulation. They are obtained from a sample generated with the "GENIE Alternative" model configuration. The orange shows the truth GENIE cross section from "GENIE Alternative", smeared using the migration matrix from Figure 7.5 and 7.8. Only systematic uncertainties from cross section modelling are included here (vertical bars).

for the two single -differential cross sections (similar results are obtained with the double-differential cross section). The green is pure MC from GENIE default, while the black data points show the fake data (GENIE alternative) extracted cross section. To ensure that the cross section extraction is done properly, the GENIE alternative cross section, simulated in true momentum and angle bins, has been smeared using the smearing matrices from Figure 7.5 and 7.8, and compared to the black data point. This is shown with the yellow line in Figure C.2. The fake data points match the true prediction within the cross section modelling systematic uncertainties (vertical bars) which validates the cross section extraction.

Acronyms

ACPT Anode or Cathode Piercing Track. 80, 88, 96

ADC Analog-to-Digital Converter. 64, 65, 71, 75

BNB Booster Neutrino Beamline. ii, v, 48, 49, 52, 54, 61, 62, 98, 119, 122, 128, 131, 132, 136, 137, 139, 143, 148, 167, 179, 180

CC Charged Current. vi–viii, 8–11, 16, 17, 22–29, 32–35, 45–47, 57–59, 68, 89–91, 103, 105–107, 110, 112, 113, 122, 123, 125–127, 137–140, 142–144, 146–148, 152, 153, 160, 166–168, 183–188, 190, 191, 195, 199, 200, 202–205

CMOS Complementary Metal–Oxide–Semiconductor. 63

COHNR Coherent Noise Removal. 120

CP Charge and Parity Symmetry. 3, 10, 12, 17, 20

CR Cosmic Ray. 10, 18, 62–68, 70, 72, 74–82, 84–89, 91, 92, 110, 112–115, 119–121, 123, 125, 155, 177, 179–181

CRPA Continuum Random-Phase Approximation. 121

CVC Conserved Vector Current. 30

DIS Deep Inelastic Scattering. 26–28, 34, 35, 123

ES Elastic Scattering. 8, 9

FM Flash Matching. 90, 92, 94–96, 106

FSI Final State Interactions. 24, 40, 41, 65, 68

FV Fiducial Volume. 78, 80, 81, 85, 86, 88, 90, 103, 112, 114, 119, 122, 123, 125, 126, 132, 139, 144, 147, 177, 178

GQE Global Quantum Efficiency. 92, 93

IA Impulse Approximation. 36, 37, 40

INC Intra-Nuclear Cascade. 40, 41

LArTPC Liquid Argon Time Projection Chamber. 3, 4, 27, 36, 45, 48, 54–56, 60, 61, 64, 75, 97, 175

LFG Local Fermi Gas. 38, 39

MC Monte Carlo. v–vii, 44, 65, 94–96, 115–118, 120, 121, 123, 126, 133, 136–139, 142, 143, 146, 148, 152, 156, 157, 161–163, 166, 168, 170, 173, 174, 176, 180–184, 186, 187, 204, 208, 210, 212, 213

MCS Multiple Coulomb Scattering. v, 81, 85–87, 98–102, 111–113, 123

MEC Meson Exchange Current. vi, vii, 43, 45, 123, 166–168, 183, 184, 195, 204, 205

MIP Minimum Ionising Particle. 92, 123

MSW Mikheyev-Smirnov-Wolfenstein. 16

NC Neutral Current. 8–10, 16, 26, 29, 32–35, 107, 122, 137, 139, 143, 148, 160

OUTFV Out Of Fiducial Volume. 119, 120, 122, 137, 139, 143, 148, 177

PDG Particle Data Group. 99

PE Photo Electron. v, 63, 65, 72, 73, 78, 79, 92–97, 104–106, 176

PMT Photo Multiplier Tube. 8, 54, 55, 60–64, 67, 70–73, 78, 79, 90–97, 121, 176

POT Protons on Target. 50, 68, 87, 113, 115–118, 123, 126, 128, 131, 132, 136, 137, 173, 183, 184

QCD Quantum Chromodynamics. 29, 30

QE Quasi-Elastic. vi, vii, 22, 23, 25–29, 32, 33, 40, 43, 68, 123, 160, 166–168, 171, 183, 184, 195, 204, 205

RFG Relativistic Fermi Gas. 37–39

RMS Root Mean Square. 73, 99, 100

RPA Random Phase Approximation. 44, 45, 166, 195

SF Spectral Function. 37–39

SM Standard Model. 1–3, 6, 10, 13, 18

STD Standard Deviation. 71, 84, 110, 111, 161

SVM Support Vector Machine. 108, 109

TPB tetraphenyl-butadiene. 61, 92

TPC Time Projection Chamber. ii, 54, 56, 57, 59, 61, 63, 64, 67, 70, 73–75, 77, 78, 80, 84, 86, 92, 93, 95, 97, 98, 106, 107, 114, 115, 119, 176, 177, 181

Bibliography

[1] D. Hanneke, S. Fogwell Hoogerheide, and G. Gabrielse. "Cavity control of a single-electron quantum cyclotron: Measuring the electron magnetic moment". In: *Phys. Rev.* A.83 (2011), p. 052122. URL: https://link.aps.org/doi/10.1103/PhysRevA.83.052122.

[2] Laurent Canetti, Marco Drewes, and Mikhail Shaposhnikov. "Matter and antimatter in the universe". In: *New Journal of Physics* 14.9 (Sept. 2012), p. 095012. DOI: 10.1088/1367-2630/14/9/095012. URL: https://doi.org/10.1088%2F1367-2630%2F14%2F9%2F095012.

[3] Y. Fukuda et al. "Evidence for Oscillation of Atmospheric Neutrinos". In: *Phys. Rev. Lett.* 81 (1998), p. 1562. URL: https://doi.org/10.1103/PhysRevLett.81.1562.

[4] Q. R. Ahmad et al. "Direct Evidence for Neutrino Flavor Transformation from Neutral-Current Interactions in the Sudbury Neutrino Observatory". In: *Phys. Rev. Lett.* 89.011301 (1998). URL: https://doi.org/10.1103/PhysRevLett.89.011301.

[5] K. Winter. *Neutrino Physics*. Cambridge University Press, 2000.

[6] H. Bethe and R. Peierls. In: *Nature* 133 (1934), p. 532.

[7] F. Reines et al. "Detection of the Free Antineutrino". In: *Phys. Rev.* 117 (1 Jan. 1960), pp. 159–173. DOI: 10.1103/PhysRev.117.159. URL: https://link.aps.org/doi/10.1103/PhysRev.117.159.

[8] G. Danby et al. "Observation of High-Energy Neutrino Reactions and the Existence of Two Kinds of Neutrinos". In: *Phys. Rev. Lett.* 9 (1 July 1962), pp. 36–44. DOI: 10.1103/PhysRevLett.9.36. URL: https://link.aps.org/doi/10.1103/PhysRevLett.9.36.

[9] F. J. Hasert et al. "Observation of neutrino-like interactions without muon or electron in the gargamelle neutrino experiment". In: *Physics Letters B* 46.1 (1973), pp. 138–140. ISSN: 0370-2693. DOI: https://doi.org/10.1016/0370-2693(73)90499-1. URL: http://www.sciencedirect.com/science/article/pii/0370269373904991.

[10] K. Kodama et al. "Observation of tau neutrino interactions". In: *Physics Letters B* 504.3 (2001), pp. 218–224. ISSN: 0370-2693. DOI: https://doi.org/10.1016/S0370-2693(01)00307-0. URL: http://www.sciencedirect.com/science/article/pii/S0370269301003070.

[11] C. Giunti et al. "Pragmatic view of short-baseline neutrino oscillations". In: *Phys. Rev. D* 88 (7 Oct. 2013), p. 073008. DOI: 10.1103/PhysRevD.88.073008. URL: https://link.aps.org/doi/10.1103/PhysRevD.88.073008.

[12] K. S. Hirata, T. Kajita, M. Koshiba, et al. "Experimental study of the atmospheric neutino flux". In: *Physics Letters B* 205.2 (1988), pp. 416–420. ISSN: 0370-2693. DOI: https://doi.org/10.1016/0370-2693(88)91690-5. URL: http://www.sciencedirect.com/science/article/pii/0370269388916905.

[13] Y. Fukuda et al. "Evidence for Oscillation of Atmospheric Neutrinos". In: *Phys. Rev. Lett.* 81 (8 Aug. 1998), pp. 1562–1567. DOI: 10.1103/PhysRevLett.81.1562. URL: https://link.aps.org/doi/10.1103/PhysRevLett.81.1562.

[14] A. Yu. Smirnov. "Solar neutrinos: Oscillations or No-oscillations?" In: *preprint* (2016). arXiv: 1609.02386 [hep-ph].

[15] T. Araki et al. "Measurement of Neutrino Oscillation with KamLAND: Evidence of Spectral Distortion". In: *Phys. Rev. Lett.* 94 (8 Mar. 2005), p. 081801. DOI: 10.1103/PhysRevLett.94.081801. URL: https://link.aps.org/doi/10.1103/PhysRevLett.94.081801.

[16] M. Guler et al. "An appearance experiment to search for $\nu_\mu \to \nu_\tau$ oscillations in the CNGS beam: experimental proposal". In: *CERN-SPSC-2000-028* (2000). URL: https://cds.cern.ch/record/456523?ln=de.

[17] M. Tanabashi et al. "Review of Particle Physics". In: *Phys. Rev. D* 98 (3 Aug. 2018), p. 030001. DOI: 10.1103/PhysRevD.98.030001. URL: https://link.aps.org/doi/10.1103/PhysRevD.98.030001.

[18] F. Halzen and A. D. Martin. *Quarks And Leptons: Introductory Course in Modern Particle Physics*. Wiley, 1984.

[19] W. Xu et al. (Majorana Collaboration). "The Majorana Demonstrator: A Search for Neutrinoless Double-beta Decay of 76 Ge". In: *Journal of Physics: Conference Series* 606.1 (2015), p. 012004. URL: http://iopscience.iop.org/article/10.1088/1742-6596/606/1/012004/meta.

[20] M. Agostini et al. (GERDA Collaboration). "$2\nu\beta\beta$ Decay of 76 Ge Into Excited States With GERDA Phase I". In: *Journal of Physics G: Nuclear and Particle Physics* 42.11 (2015), p. 115201. URL: http://iopscience.iop.org/article/10.1088/0954-3899/42/11/115201/meta.

[21] C. Arnaboldi et al. (CUORE Collaboration). "CUORE: A Cryogenic Underground Observatory for Rare Events". In: *Nuclear Instruments and Meth- ods in Physics Research Section A: Accelerators, Spectrometers, Detectors and Associated Equipment* 518.3 (2004), pp. 775–798. URL: https://doi.org/10.1016/j.nima.2003.07.067.

[22] S. Andringa et al. "Current Status and Future Prospects of the SNO+ Experiment". In: *Advances in High Energy Physics* 2016 (2016). URL: http://dx.doi.org/10.1155/2016/6194250.

[23] V Álvarez et al. "NEXT-100 Technical Design Report (TDR). Executive summary". In: *Journal of Instrumentation* 7.06 (June 2012), T06001–T06001. DOI: 10.1088/1748-0221/7/06/t06001. URL: https://doi.org/10.1088%2F1748-0221%2F7%2F06%2Ft06001.

[24] J. B. Albert et al. "Sensitivity and discovery potential of the proposed nEXO experiment to neutrinoless double-β decay". In: *Phys. Rev. C* 97 (6 June 2018), p. 065503. DOI: 10.1103/PhysRevC.97.065503. URL: https://link.aps.org/doi/10.1103/PhysRevC.97.065503.

[25] L. Wolfenstein. "Neutrino oscillations in matter". In: *Phys. Rev. D* 17 (9 May 1978), pp. 2369–2374. DOI: 10.1103/PhysRevD.17.2369. URL: https://link.aps.org/doi/10.1103/PhysRevD.17.2369.

[26] K. Abe et al. (T2K Collaboration). "Measurements of neutrino oscillation in appearance and disappearance channels by the T2K experiment with 6.6^{20} protons on target". In: *Phys. Rev.* 91.072010 (2015). URL: https://doi.org/10.1103/PhysRevD.91.072010.

[27] R. B. Patterson. "The NOvA experiment: status and outlook". In: *Nuclear Physics B - Proceedings Supplements* 235-236 (2013). The XXV International Conference on Neutrino Physics and Astrophysics, pp. 151–157. ISSN: 0920-5632. DOI: https://doi.org/10.1016/j.nuclphysbps.2013.04.005. URL: http://www.sciencedirect.com/science/article/pii/S0920563213001266.

[28] The DUNE and LBNF collaboration. "Long-Baseline Neutrino Facility (LBNF) and Deep Underground Neutrino Experiment (DUNE) - Conceptual Design Report". In: *LBNE doc-db 10690* (2015). URL: https://lbne.bnl.gov/tmp/volume-project.pdf.

[29] M. G. Aartsen et al. "Determining neutrino oscillation parameters from atmospheric muon neutrino disappearance with three years of IceCube DeepCore data". In: *Phys. Rev. D* 91 (7 Apr. 2015), p. 072004. DOI: 10.1103/PhysRevD.91.072004. URL: https://link.aps.org/doi/10.1103/PhysRevD.91.072004.

[30] C. Angelina et al. "New experimental limits on $\nu_\mu \to \nu_e$ oscillations". In: *Physics Letters B* 179.3 (1986), pp. 307–312. ISSN: 0370-2693. DOI: https://doi.org/10.1016/0370-2693(86)90586-1. URL: http://www.sciencedirect.com/science/article/pii/0370269386905861.

[31] F. Dydak et al. "A search for ν_μ oscillations in the Δm^2 range 0.3–90 eV2". In: *Physics Letters B* 134.3 (1984), pp. 281–286. ISSN: 0370-2693. DOI: https://doi.org/10.1016/0370-2693(84)90688-9. URL: http://www.sciencedirect.com/science/article/pii/0370269384906889.

[32] F. Bergsma et al. "A search for neutrino oscillations". In: *Z. Phys.* C.40 (1988), p. 171. URL: https://link.springer.com/article/10.1007%2FBF01555880.

[33] E. Eskut et al. "New results from a search for $\nu_\mu \to \nu_\tau$ and $\nu_e \to \nu_\tau$ oscillation". In: *Phys. Lett.* B.497 (2001), pp. 8–22.

[34] P. Astier et al. "Search for $\nu_\mu \to \nu_e$ oscillations in the NOMAD experiment". In: *Physics Letters B* 570.1 (2003), pp. 19–31. ISSN: 0370-2693. DOI: https://doi.org/10.1016/j.physletb.2003.07.029. URL: http://www.sciencedirect.com/science/article/pii/S0370269303010505.

[35] C. Athanassopoulos et al. "The liquid scintillator neutrino detector and LAMPF neutrino source". In: *Nuclear Instruments and Methods in Physics Research Section A: Accelerators, Spectrometers, Detectors and Associated Equipment* 388.1 (1997), pp. 149–172. ISSN: 0168-9002. DOI: https://doi.org/10.1016/S0168-9002(96)01155-2. URL: http://www.sciencedirect.com/science/article/pii/S0168900296011552.

[36] A. A. Aguilar-Arevalo et al. (MiniBooNE Collaboration). "First measurement of the muon neutrino charged current quasielastic double differential cross section". In: *Phys. Rev.* D.81 (2010). URL: https://doi.org/10.1103/PhysRevD.81.092005.

[37] P. Aprili et al. "ICARUS : a second generation proton decay experiment and neutrino observatory at the Gran Sasso Laboratory". In: *CERN-SPSC-2002-027* (2002).

[38] P. Adamson et al. "First Direct Observation of Muon Antineutrino Disappearance". In: *Phys. Rev. Lett.* 107 (2 July 2011), p. 021801. DOI: 10.1103/PhysRevLett.107.021801. URL: https://link.aps.org/doi/10.1103/PhysRevLett.107.021801.

[39] M. A. Acero et al. "New constraints on oscillation parameters from ν_e appearance and ν_μ disappearance in the NOvA experiment". In: *Phys. Rev. D* 98 (3 Aug. 2018), p. 032012. DOI: 10.1103/PhysRevD.98.032012. URL: https://link.aps.org/doi/10.1103/PhysRevD.98.032012.

[40] L. Alvarez-Ruso et al. "NuSTEC White Paper: Status and challenges of neutrino–nucleus scattering". In: *Progress in Particle and Nuclear Physics* 100 (2018), pp. 1–68. ISSN: 0146-6410. DOI: https://doi.org/10.1016/j.ppnp.2018.01.006. URL: http://www.sciencedirect.com/science/article/pii/S0146641018300061.

[41] A. Bodek and T. Cai. "Removal Energies and Final State Interaction in Lepton Nucleus Scattering". In: *Eur. Phys. J. C* (2019). DOI: https://doi.org/10.1140/epjc/s10052-019-6750-3. URL: https://arxiv.org/abs/1801.07975.

[42] M. A. Acero et al. (NOvA Collaboration). "New constraints on oscillation parameters from ν_e appearance and ν_μ disappearance in the NOvA experiment". In: *Phys. Rev.* D.98 (2018), p. 032012. URL: https://doi.org/10.1103/PhysRevD.98.032012.

[43] J. A. Formaggio and G. P. Zeller. "From eV to EeV: Neutrino cross sections across energy scales". In: *Rev. Mod. Phys.* 84 (3 Sept. 2012), pp. 1307–1341. DOI: 10.1103/RevModPhys.84.1307. URL: https://link.aps.org/doi/10.1103/RevModPhys.84.1307.

[44] D. Casper. "The nuance neutrino physics simulation, and the future". In: *Nuclear Physics B - Proceedings Supplements* 112.1 (2002), pp. 161–170. ISSN: 0920-5632. DOI: https://doi.org/10.1016/S0920-5632(02)01756-5. URL: http://www.sciencedirect.com/science/article/pii/S0920563202017565.

[45] O. Gayou et al. "Measurement of G_{Ep}/G_{Mp} in $ep \to ep$ to $Q^2 = 5.6\text{GeV}^2$". In: *Phys. Rev. Lett.* 88 (2002), p. 092301. URL: https://journals.aps.org/prl/abstract/10.1103/PhysRevLett.88.092301.

[46] R. Bradford et al. "A New Parameterization of the Nucleon Elastic Form Factors". In: *Nucl. Phys. Proc. Suppl.* B.159 (2006), p. 127132. URL: https://doi.org/10.1016/j.nuclphysbps.2006.08.028.

[47] C. H. Llewellyn Smith. "Neutrino reactions at accelerator energies". In: *Phys. Rept.* 3 (1972), p. 261. URL: https://www.sciencedirect.com/science/article/pii/0370157372900105?via%3Dihub.

[48] D. Rein and L. M. Sehgal. "Neutrino excitation of baryon resonances and single pion production". In: *Ann. Phys.* 133 (1981), p. 79. URL: https://doi.org/10.1016/0003-4916(81)90242-6.

[49] R. P. Feynman, M. Kislinger, and F. Ravndal. "Current Matrix Elements from a Relativistic Quark Model". In: *Phys. Rev.* D.3 (1971), p. 2706. URL: https://doi.org/10.1103/PhysRevD.3.2706.

[50] Ch. Berger and L. M. Sehgal. "Partially conserved axial vector current and coherent pion production by low energy neutrinos". In: *Phys. Rev. D* 79 (5 Mar. 2009), p. 053003. DOI: 10.1103/PhysRevD.79.053003. URL: https://link.aps.org/doi/10.1103/PhysRevD.79.053003.

[51] A Bodek and U K Yang. "Higher twist, wscaling, and effective LO PDFs for lepton scattering in the few GeV region". In: *Journal of Physics G: Nuclear and Particle Physics* 29.8 (July 2003), pp. 1899–1905. DOI: 10.1088/0954-3899/29/8/369. URL: https://doi.org/10.1088%2F0954-3899%2F29%2F8%2F369.

[52] Costas Andreopoulos et al. "The GENIE Neutrino Monte Carlo Generator: Physics and User Manual". In: *arXiv:1510.05494* FERMILAB-FN-1004-CD (2015). URL: http://inspirehep.net/record/1398588?ln=en.

[53] C. M. Marshall et al. "Measurement of K^+ production in charged-current ν_μ interactions". In: *Phys. Rev. D* 94 (1 July 2016), p. 012002. DOI: 10.1103/PhysRevD.94.012002. URL: https://link.aps.org/doi/10.1103/PhysRevD.94.012002.

[54] O. Benhar et al. "Electron- and neutrino-nucleus scattering in the impulse approximation regime". In: *Phys. Rev. D* 72 (5 Sept. 2005), p. 053005. DOI: 10.1103/PhysRevD.72.053005. URL: https://link.aps.org/doi/10.1103/PhysRevD.72.053005.

[55] R. A. Smith and E. J. Moniz. "Neutrino reactions on nuclear targets". In: *Nuclear Physics B* 43 (1972), pp. 605–622. ISSN: 0550-3213. DOI: https://doi.org/10.1016/0550-3213(72)90040-5. URL: http://www.sciencedirect.com/science/article/pii/0550321372900405.

[56] J. Nieves, J. E. Amaro, and M. Valverde. "Inclusive quasielastic charged-current neutrino-nucleus reactions". In: *Phys. Rev. C* 70 (5 Nov. 2004), p. 055503. DOI: 10.1103/PhysRevC.70.055503. URL: https://link.aps.org/doi/10.1103/PhysRevC.70.055503.

[57] P. K. A. de Witt Huberts. "Proton spectral functions and momentum distributions in nuclei from high-resolution (e,e'p) experiments". In: *Journal of Physics G: Nuclear and Particle Physics* 16.4 (1990), p. 507. URL: http://stacks.iop.org/0954-3899/16/i=4/a=004.

[58] D. Rohe et al. "Correlated Strength in the Nuclear Spectral Function". In: *Phys. Rev. Lett.* 93 (18 Oct. 2004), p. 182501. DOI: 10.1103/PhysRevLett.93.182501. URL: https://link.aps.org/doi/10.1103/PhysRevLett.93.182501.

[59] A. Bodek and J. L. Ritchie. "Fermi-motion effects in deep-inelastic lepton scattering from nuclear targets". In: *Phys. Rev. D* 23 (5 Mar. 1981), pp. 1070–1091. DOI: 10.1103/PhysRevD.23.1070. URL: https://link.aps.org/doi/10.1103/PhysRevD.23.1070.

[60] A. Bodek, M. E. Christy, and B. Coopersmith. "Effective Spectral Function for Quasielastic Scattering on Nuclei". In: *Nucl. Phys. Proc.* 273–275 (2016), pp. 1705–1710. URL: https://doi.org/10.1016/j.nuclphysbps.2015.09.275.

[61] J. E. Amaro et al. "Using electron scattering superscaling to predict charge-changing neutrino cross sections in nuclei". In: *Phys. Rev. C* 71 (1 Jan. 2005), p. 015501. DOI: 10.1103/PhysRevC.71.015501. URL: https://link.aps.org/doi/10.1103/PhysRevC.71.015501.

[62] C. Andreopoulos et al. "The GENIE neutrino Monte Carlo generator". In: *Nuclear Instruments and Methods in Physics Research Section A: Accelerators, Spectrometers, Detectors and Associated Equipment* 614.1 (2010), pp. 87–104. ISSN: 0168-9002. DOI: https://doi.org/10.1016/j.nima.2009.12.009. URL: http://www.sciencedirect.com/science/article/pii/S0168900209023043.

[63] T. Golan. "Modeling nuclear effects in NuWro Monte Carlo neutrino event generator". PhD thesis. University of Wroclaw, 2014. URL: http://neutrino.ift.uni.wroc.%20pl/files/phd_tomasz_golan.pdf.

[64] N. Metropolis et al. "Monte Carlo Calculations on Intranuclear Cascades. I. Low-Energy Studies". In: *Phys. Rev.* 110.1 (1958), pp. 185–203. URL: https://link.aps.org/doi/10.1103/PhysRev.110.185.

[65] M. Alam et al. "GENIE Production Release 2.10.0". In: (2015). arXiv: 1512.06882 [hep-ph].

[66] D. Ashery et al. "True absorption and scattering of pions on nuclei". In: *Phys. Rev. C* 23 (5 May 1981), pp. 2173–2185. DOI: 10.1103/PhysRevC.23.2173. URL: https://link.aps.org/doi/10.1103/PhysRevC.23.2173.

[67] J. Nieves, I. Ruiz Simo, and M. J. Vicente Vacas. "Inclusive charged-current neutrino-nucleus reactions". In: *Phys. Rev. C* 83 (4 Apr. 2011), p. 045501. DOI: 10.1103/PhysRevC.83.045501. URL: https://link.aps.org/doi/10.1103/PhysRevC.83.045501.

[68] R. Gran et al. "Neutrino-nucleus quasi-elastic and 2p2h interactions up to 10 GeV". In: *Phys. Rev.* D.88 (2018), p. 113007.

[69] A. Bodek, S. Avvakumov, R. Bradford, et al. "Vector and axial nucleon form factors: A duality constrained parameterization". In: *Eur. Phys. J.* C.53 (2008), p. 349. URL: https://doi.org/10.1140/epjc/s10052-007.

[70] J. Nieves, I. Ruiz Simo, and M.J. Vicente Vacas. "The nucleon axial mass and the MiniBooNE quasielastic neutrino–nucleus scattering problem". In: *Phys. Lett.* B.702 (2012), pp. 72–75. URL: https://doi.org/10.1016/j.physletb.2011.11.061.

[71] T. Katori. "Meson Exchange Current (MEC) Models in Neutrino Interaction Generators". In: *AIP Conf. Proc.* 1663 (2015), p. 030001. URL: https://doi.org/10.1063/1.4919465.

[72] B. Abi et al. "The DUNE Far Detector Interim Design Report Volume 1: Physics, Technology and Strategies". In: (2018). arXiv: 1807.10334 [physics.ins-det].

[73] B. Abi et al. "The DUNE Far Detector Interim Design Report, Volume 2: Single-Phase Module". In: (2018). arXiv: 1807.10327 [physics.ins-det].

[74] B. Abi et al. "The DUNE Far Detector Interim Design Report, Volume 3: Dual-Phase Module". In: (2018). arXiv: 1807.10340 [physics.ins-det].

[75] M. Antonello et al. "A Proposal for a Three Detector Short-Baseline Neutrino Oscillation Program in the Fermilab Booster Neutrino Beam". In: (2015). arXiv: 1503.01520 [physics.ins-det].

[76] R. Acciarri et al. "Measurements of Inclusive Muon Neutrino and Antineutrino Charged Current Differential Cross Sections on Argon in the NuMI Antineutrino Beam". In: *Phys. Rev.* D89.11 (2014), p. 112003. DOI: 10.1103/PhysRevD.89.112003. arXiv: 1404.4809 [hep-ex].

[77] C. Anderson et al. "First Measurements of Inclusive Muon Neutrino Charged Current Differential Cross Sections on Argon". In: *Phys. Rev. Lett.* 108 (2012), p. 161802. DOI: 10.1103/PhysRevLett.108.161802. arXiv: 1111.0103 [hep-ex].

[78] K. Abe et al. "Measurement of the muon neutrino inclusive charged-current cross section in the energy range of 1–3 GeV with the T2K INGRID detector". In: *Phys. Rev.* D93.7 (2016), p. 072002. DOI: 10.1103/PhysRevD.93.072002. arXiv: 1509.06940 [hep-ex].

[79] K. Abe et al. "Measurement of the inclusive numu charged current cross section on iron and hydrocarbon in the T2K on-axis neutrino beam". In: *Phys. Rev.* D90.5 (2014), p. 052010. DOI: 10.1103/PhysRevD.90.052010. arXiv: 1407.4256 [hep-ex].

[80] Y. Nakajima et al. "Measurement of inclusive charged current interactions on carbon in a few-GeV neutrino beam". In: *Phys. Rev.* D83 (2011), p. 012005. DOI: 10.1103/PhysRevD.83.012005. arXiv: 1011.2131 [hep-ex].

[81] Q. Wu et al. "A Precise measurement of the muon neutrino-nucleon inclusive charged current cross-section off an isoscalar target in the energy range 2.5 $<$ E(nu) $<$ 40-GeV by NOMAD". In: *Phys. Lett.* B660 (2008), pp. 19–25. DOI: 10.1016/j.physletb.2007.12.027. arXiv: 0711.1183 [hep-ex].

[82] P. Adamson et al. "Neutrino and Antineutrino Inclusive Charged-current Cross Section Measurements with the MINOS Near Detector". In: *Phys. Rev.* D81 (2010), p. 072002. DOI: 10.1103/PhysRevD.81.072002. arXiv: 0910.2201 [hep-ex].

[83] L. Ren et al. "Measurement of the antineutrino to neutrino charged-current interaction cross section ratio in MINERvA". In: *Phys. Rev.* D95.7 (2017), p. 072009. DOI: 10.1103/PhysRevD.95.072009. arXiv: 1701.04857 [hep-ex].

[84] J. Devan et al. "Measurements of the Inclusive Neutrino and Antineutrino Charged Current Cross Sections in MINERvA Using the Low-nu Flux Method". In: *Phys. Rev.* D94.11 (2016), p. 112007. DOI: 10.1103/PhysRevD.94.112007. arXiv: 1610.04746 [hep-ex].

[85] K. Abe et al. "Measurement of the inclusive numu charged current cross section on carbon in the near detector of the T2K experiment". In: *Phys. Rev.* D87.9 (2013), p. 092003. DOI: 10.1103/PhysRevD.87.092003. arXiv: 1302.4908 [hep-ex].

[86] C. Patrignani et al. (Particle Data Group). "Neutrino Cross Section Measurements". In: *Chin. Phys. C* ((2016) and 2017 update), p. 100001.

[87] Mar. 2015. URL: http://science.energy.gov/hep/facilities/user-facilities/fermilab-accelerator-complex/.

[88] A. A. Aguilar-Arevalo et al. "Neutrino flux prediction at MiniBooNE". In: *Phys. Rev. D* 79 (7 Apr. 2009), p. 072002. DOI: 10.1103/PhysRevD.79.072002. URL: https://link.aps.org/doi/10.1103/PhysRevD.79.072002.

[89] The MicroBooNE Collaboration. *Booster Neutrino Flux Prediction at MicroBooNE*. MICROBOONE-NOTE-1031-PUB. 2018. URL: https://microboone.fnal.gov/public-notes/.

[90] R. Acciarri et al. "Design and construction of the MicroBooNE detector". In: *Journal of Instrumentation* 12.02 (Feb. 2017), P02017–P02017. DOI: 10.1088/1748-0221/12/02/p02017. URL: https://doi.org/10.1088%2F1748-0221%2F12%2F02%2Fp02017.

[91] R. Acciarri et al. "Noise Characterization and Filtering in the MicroBooNE Liquid Argon TPC". In: *Journal of Instrumentation* 12.08 (Aug. 2017), P08003–P08003. DOI: 10.1088/1748-0221/12/08/p08003. URL: https://doi.org/10.1088%2F1748-0221%2F12%2F08%2Fp08003.

[92] Tadayoshi Doke et al. "Let dependence of scintillation yields in liquid argon". In: *Nuclear Instruments and Methods in Physics Research Section A: Accelerators, Spectrometers, Detectors and Associated Equipment* 269.1 (1988), pp. 291–296. ISSN: 0168-9002. DOI: https://doi.org/10.1016/0168-9002(88)90892-3. URL: http://www.sciencedirect.com/science/article/pii/0168900288908923.

[93] Shinzou Kubota et al. "Dynamical behavior of free electrons in the recombination process in liquid argon, krypton, and xenon". In: *Phys. Rev. B* 20 (8 Oct. 1979), pp. 3486–3496. DOI: 10.1103/PhysRevB.20.3486. URL: https://link.aps.org/doi/10.1103/PhysRevB.20.3486.

[94] T Katori. "The MicroBooNE light collection system". In: *Journal of Instrumentation* 8.10 (Oct. 2013), pp. C10011–C10011. DOI: 10.1088/1748-0221/8/10/c10011. URL: https://doi.org/10.1088%2F1748-0221%2F8%2F10%2Fc10011.

[95] D. Caratelli. "Study of Electromagnetic Interactions in the MicroBooNE Liquid Argon Time Projection Chamber". In: *PhD Thesis* (2018). URL: http://inspirehep.net/record/1654724.

[96] D. Heck et al. "CORSIKA: A Monte Carlo Code to Simulate Extensive Air Showers". In: *Forschungszentrum Karlsruhe Report FZKA* (1998). URL: https://www.ikp.kit.edu/corsika/70.php.

[97] The MicroBooNE Collaboration. *Cosmic Shielding Studies at MicroBooNE*. MICROBOONE-NOTE-1005-PUB. 2016. URL: https://microboone.fnal.gov/public-notes/.

[98] S. Agostinelli et al. "Geant4—a simulation toolkit". In: *Nuclear Instruments and Methods in Physics Research Section A: Accelerators, Spectrometers, Detectors and Associated Equipment* 506.3 (2003), pp. 250–303. ISSN: 0168-9002. DOI: https://doi.org/10.1016/S0168-9002(03)01368-8. URL: http://www.sciencedirect.com/science/article/pii/S0168900203013688.

[99] The MicroBooNE Collaboration. "Study of Space Charge Effects in MicroBooNE". In: *MICROBOONE-NOTE-1018-PUB* (2016). URL: http://microboone.fnal.gov/public-notes/.

[100] R. Pordes and E. Snider. "The Liquid Argon Software Toolkit (LArSoft): Goals, Status and Plan". In: *PoS ICHEP* 182 (2016). URL: http://inspirehep.net/record/1497601/.

[101] A. Bodek and J. L. Ritchie. "Further studies of Fermi-motion effects in lepton scattering from nuclear targets". In: *Phys. Rev. D* 24 (5 Sept. 1981), pp. 1400–1402. DOI: 10.1103/PhysRevD.24.1400. URL: https://link.aps.org/doi/10.1103/PhysRevD.24.1400.

[102] K. S. Vladimir Kuzmin, V. Lyubushkin, and V. A. Naumov. "Lepton polarization in neutrino nucleon interactions". In: *Mod. Phys. Lett.* A19 (2004), pp. 2815–2829. URL: https://www.worldscientific.com/doi/abs/10.1142/S0217732304016172.

[103] M. Auger et al. "A Novel Cosmic Ray Tagger System for Liquid Argon TPC Neutrino Detectors". In: *Instruments* 1.1 (2017), p. 2. DOI: 10.3390/instruments1010002. arXiv: 1612.04614 [physics.ins-det].

[104] C. Adams et al. "Ionization electron signal processing in single phase LArTPCs. Part I. Algorithm Description and quantitative evaluation with MicroBooNE simulation". In: *Journal of Instrumentation* 13.07 (July 2018), P07006–P07006. DOI: 10.1088/1748-0221/13/07/p07006. URL: https://doi.org/10.1088%2F1748-0221%2F13%2F07%2Fp07006.

[105] C. Adams et al. "Ionization electron signal processing in single phase LArTPCs. Part II. Data/simulation comparison and performance in MicroBooNE". In: *Journal of Instrumentation* 13.07 (July 2018), P07007–P07007. DOI: 10.1088/1748-0221/13/07/p07007. URL: https://doi.org/10.1088%2F1748-0221%2F13%2F07%2Fp07007.

[106] The MicroBooNE Collaboration. "The Pandora multi-algorithm approach to automated pattern recognition of cosmic-ray muon and neutrino events in the MicroBooNE detector". In: *Eur. Phys. J.* C.78 (2018), p. 1. URL: https://link.springer.com/article/10.1140/epjc/s10052-017-5481-6.

[107] The MicroBooNE Collaboration. "Detector calibration using through going and stopping muons in the MicroBooNE LArTPC". In: *MICROBOONE-NOTE-1048-PUB* (2018). URL: http://microboone.fnal.gov/public-notes/.

[108] R Acciarri et al. "A study of electron recombination using highly ionizing particles in the ArgoNeuT Liquid Argon TPC". In: *Journal of Instrumentation* 8.08 (Aug. 2013), P08005–P08005. DOI: 10.1088/1748-0221/8/08/p08005. URL: https://doi.org/10.1088%2F1748-0221%2F8%2F08%2Fp08005.

[109] H. Primakoff. "Theory of Muon Capture". In: *Rev. Mod. Phys.* 31 (3 July 1959), pp. 802–822. DOI: 10.1103/RevModPhys.31.802. URL: https://link.aps.org/doi/10.1103/RevModPhys.31.802.

[110] J. C. Sens. "Capture of Negative Muons by Nuclei". In: *Phys. Rev.* 113 (2 Jan. 1959), pp. 679–687. DOI: 10.1103/PhysRev.113.679. URL: https://link.aps.org/doi/10.1103/PhysRev.113.679.

[111] A. Bertin, A. Vitale, and A. Placci. "Nuclear Capture of Muons in Argon and Neon". In: *Phys. Rev. A* 7 (6 June 1973), pp. 2214–2217. DOI: 10.1103/PhysRevA.7.2214. URL: https://link.aps.org/doi/10.1103/PhysRevA.7.2214.

[112] P. Abratenko et al. "Determination of muon momentum in the MicroBooNE LArTPC using an improved model of multiple Coulomb scattering". In: *JINST* 12.10 (2017), P10010. URL: http://stacks.iop.org/1748-0221/12/i=10/a=P10010.

[113] S.F. Pate et al. "A model for the Global Quantum Efficiency for a TPB-based wavelength-shifting system used with photomultiplier tubes in liquid argon in MicroBooNE". In: *Journal of Instrumentation* 13.02 (Feb. 2018), P02034–P02034. DOI: 10.1088/1748-0221/13/02/p02034. URL: https://doi.org/10.1088%2F1748-0221%2F13%2F02%2Fp02034.

[114] *Muons in liquid argon (Ar)*. URL: http://pdg.lbl.gov/2012/AtomicNuclearProperties/MUON_ELOSS_TABLES/muonloss_289.pdf.

[115] V. L. Highland. "Some practical remarks on multiple scattering". In: *Nuclear Instruments and Methods* 129.2 (1975), pp. 497–499. ISSN: 0029-554X. DOI: https://doi.org/10.1016/0029-554X(75)90743-0. URL: http://www.sciencedirect.com/science/article/pii/0029554X75907430.

[116] G. R. Lynch and O. I. Dahl. "Approximations to multiple Coulomb scattering". In: *Nuclear Instruments and Methods in Physics Research Section B: Beam Interactions with Materials and Atoms* 58.1 (1991), pp. 6–10. ISSN: 0168-583X. DOI: https://doi.org/10.1016/0168-583X(91)95671-Y. URL: http://www.sciencedirect.com/science/article/pii/0168583X9195671Y.

[117] H. Bichsel, D. E. Groom, and S.R. Klein. "Passage of Particles Through Matter". In: *PDG Chapter 27* (2005). URL: http://pdg.lbl.gov/2005/reviews/passagerpp.pdf.

[118] I. Guyon, B. Boser, and V. Vapnik. "Automatic Capacity Tuning of Very Large VC-dimension Classifiers". In: *Neural Information Processing* (1993). URL: http://citeseerx.ist.psu.edu/viewdoc/summary?doi=10.1.1.17.7215.

[119] V. Pandey et al. "Low-energy excitations and quasielastic contribution to electron-nucleus and neutrino-nucleus scattering in the continuum random-phase approximation". In: *Phys. Rev. C* 92 (2 Aug. 2015), p. 024606. DOI: 10.1103/PhysRevC.92.024606. URL: https://link.aps.org/doi/10.1103/PhysRevC.92.024606.

[120] N. Van Dessel et al. "A dependence of quasielastic charged-current neutrino-nucleus cross sections". In: *Phys. Rev. C* 97 (4 Apr. 2018), p. 044616. DOI: 10.1103/PhysRevC.97.044616. URL: https://link.aps.org/doi/10.1103/PhysRevC.97.044616.

[121] Robert D. Cousins, Samuel J. May, and Yipeng Sun. "Should unfolded histograms be used to test hypotheses?" In: *arXiv* (2016). arXiv: 1607.07038 [physics.data-an].

[122] The MicroBooNE Collaboration. *Measurement of the Electronegative Contaminants and Drift Electron Lifetime in the MicroBooNE Experiment*. MICROBOONE-NOTE-1003-PUB. 2016. URL: https://microboone.fnal.gov/public-notes/.

[123] B. P. Roe. "Statistical errors in Monte Carlo estimates of systematic errors". In: *NIM* A 50 (2007), pp. 159–164. URL: https://www.sciencedirect.com/science/article/pii/S0168900206018055.

[124] A. Mastbaum. *QE & MEC Cross Section Reweighting in MCC8*. MicroBooNE Internal Database 15393. 2018.

[125] B. Kotlinski et al. "Pion absorption reactions on N, Ar and Xe". In: *Eur. Phys. J. A* 9 (2000), pp. 537–552. URL: https://epja.epj.org/articles/epja/abs/2000/12/epja3238/epja3238.html.

[126] Kotliński B. "Multinucleon Pion Absorption Cross Sections on N, Ar and Xe in the Delta Resonance Region". In: *ACTA PHYSICA POLONICA B* 29.11 (1998), p. 3065. URL: https://www.actaphys.uj.edu.pl/fulltext?series=Reg&vol=29&page=3065.

[127] E. Gramellini. "Measurement of the Negative Pion and Positive Kaon Total Hadronic Cross Sections on Argon at the LAr". PhD thesis. FERMILAB-THESIS-2018-24: Yale U., 2018. URL: http://lss.fnal.gov/archive/thesis/2000/fermilab-thesis-2018-24.pdf.

[128] D. W. Schmitz. "A Measurement of Hadron Production Cross Sections for the Simulation of Accelerator Neutrino Beams and a Search for ν_μ to ν_e Osscillations in the δm^2 about equals $1 - eV^2$ Region". PhD thesis. Columbia U., 2008. DOI: 10.2172/935240. URL: http://lss.fnal.gov/cgi-bin/find_paper.pl?thesis-2008-26.

[129] J. Zennamo and Z. Pavlovic. *MicroBooNE Flux and Flux Uncertainties*. MicroBooNE DocDB 8622. 2017. URL: https://microboone-docdb.fnal.gov/cgi-bin/private/ShowDocument.

[130] Y. Li et al. "Measurement of Longitudinal Electron Diffusion in Liquid Argon". In: *Nucl. Instrum. Meth.* A816 (2016), pp. 160–170. DOI: 10.1016/j.nima.2016.01.094. arXiv: 1508.07059 [physics.ins-det].

[131] P. Cennini et al. "Performance of a 3-ton liquid argon time projection chamber". In: *Nucl. Instrum. Meth.* A345 (1994), pp. 230–243. DOI: 10.1016/0168-9002(94)90996-2.

[132] V. M. Atrazhev and I. V. Timoshkin. "Transport of electrons in atomic liquids in high electric fields". In: *Trans. Dielectrics and Electrical Insulation* 5 (3 1998), pp. 450–457.

[133] S. E. Derenzo et al. "Test of a Liquid Argon Chamber with 20-Micrometer RMS Resolution". In: *Nucl. Instrum. Meth.* 122 (1974), p. 319.

[134] Eido Shibamura et al. "Ratio of diffusion coefficient to mobility for electrons in liquid argon". In: *Phys. Rev. A* 20 (6 1979), p. 2547.

[135] S. Amoruso et al. "Study of electron recombination in liquid argon with the ICARUS TPC". In: *Nuclear Instruments and Methods in Physics Research Section A: Accelerators, Spectrometers, Detectors and Associated Equipment* 523.3 (2004), pp. 275–286. ISSN: 0168-9002. DOI: https://doi.org/10.1016/j.nima.2003.11.423. URL: http://www.sciencedirect.com/science/article/pii/S0168900204000506.

[136] B. Efron. "Bootstrap Methods: Another Look at the Jackknife". In: *Ann. Statist.* 7.1 (1979), pp. 1–26. URL: https://doi.org/10.1214/aos/1176344552.

[137] Glen Cowan. *Statistical Data Analysis*. Oxford University Press, 1998.

[138] X. Qian et al. "Statistical evaluation of experimental determinations of neutrino mass hierarchy". In: *Phys. Rev. D* 86 (11 Dec. 2012), p. 113011. DOI: 10.1103/PhysRevD.86.113011. URL: https://link.aps.org/doi/10.1103/PhysRevD.86.113011.

[139] X. Qian et al. "The Gaussian CLs method for searches of new physics". In: *Nucl. Instrum. Meth.* 827 (2016), p. 63. ISSN: 0168-9002. DOI: https://doi.org/10.1016/j.nima.2016.04.089. URL: http://www.sciencedirect.com/science/article/pii/S016890021630314X.

[140] M. Tzanov et al. "Precise measurement of neutrino and antineutrino differential cross sections". In: *Phys. Rev. D* 74 (1 July 2006), p. 012008. DOI: 10.1103/PhysRevD.74.012008. URL: https://link.aps.org/doi/10.1103/PhysRevD.74.012008.

[141] P. A. Rodrigues et al. "Identification of Nuclear Effects in Neutrino-Carbon Interactions at Low Three-Momentum Transfer". In: *Phys. Rev. Lett.* 116 (7 Feb. 2016), p. 071802. DOI: 10.1103/PhysRevLett.116.071802. URL: https://link.aps.org/doi/10.1103/PhysRevLett.116.071802.

[142] K. Abe et al. "Measurement of inclusive double-differential ν_μ charged-current cross section with improved acceptance in the T2K off-axis near detector". In: *Phys. Rev. D* 98 (1 July 2018), p. 012004. DOI: 10.1103/PhysRevD.98.012004. URL: https://link.aps.org/doi/10.1103/PhysRevD.98.012004.